Structure and Assembly of *Bacillus* Spore Proteins

By Qiang Wan

Submitted For the degree of Doctor of Philosophy

Department of Molecular Biology and Biotechnology
The University of Sheffield, UK

July 2013

Acknowledgements

Foremost, I would like to express my deepest gratitude to my supervisor Professor Per Bullough for giving me the opportunity to work on such a great group and introducing me into such a fascinating project. Thanks for your continuous support of my PhD study and research, for your patience, guidance, motivation and immense knowledge. I would also like to thank Professor Anne Moir, whose expertise in all aspects of *Bacillus* benefits me so much.

I would like to thank all members of the EM group (E36) I have worked with over the past years. I would very much like to thank Dr Svetomir Tzokovfor your everywhere help. Thanks Dr Lekshmi Kailas and Dr David Radford for useful scientific discussions and experiment help. The great time in Bruges and Paris with you is unforgettable. Thanks Dr Pu Qian for talking about anything to me, for your encouragement, insightful comments, and hard questions. My sincere thanks also go to Dr Masao Yamashita, Nathan Chan, Cassie Terry, Shuo Jiang, Dr Tham Janganan and Dr Chris Glove. All your guys are so nice to work with.

Last but not least, I would like to thanks my beloved family for their loving considerations and great confidence in me all through my oversea study. My sincere gratitude to my wife Yi Mei and my beloved baby Hanzhang (Adrian). I feel so lucky to have all of you in my life.

Many thanks to Chinese Scholarship Council for providing funding through my PhD. It is a so great project to make students, like me have chance to study abroad.

Contents

Abbreviations

Å	Angstrom
AFM	Atomic Force Microscopy
APS	Ammonium Persulfate
BclA	*Bacillus* collagen-like protein of *anthracis*
BCA	Bicinchoninic acid
BSA	Bovine Serum Albumin
Cryo-EM	Cryo–Electron Microscopy
CTD	C-Terminal Domain
DTT	Dithiothreitol
dH_2O	Distilled water
FEG	Field Emission Gun
FFT / FT	Fast Fourier Transform / Fourier Transform
FPLC	Fast protein liquid chromatography
IPTG	Isopropyl-β-D-thiogalactoside
kDa	Kilodalton(s)
kV	Kilovolt(s)
LB	Luria Bertani
LN_2	Liquid nitrogen
mbar	Millibar(s)
mg	Milligram(s)
MW	Molecular weight
nm	Nanometer(s)
NTD	N-terminal Domain
OD	Optical Density
*p*3	*p*3 Symmetry (Three-fold)
*p*6	*p*6 Symmetry (Six-fold)
Psi	Pounds per square inch
RH	Relative humidity
Rpm	Revolutions per minute
SDS-PAGE	Sodium Dodecyl Sulphate Polyacrylamide Gel Electrophoresis
SEC	Size exclusion chromatograph

TEMED	N,N,N',N'-Tetramethylethylenediamine
TEM/EM	Transmission Electron Microscope/Electron Microscope
Tris	Tris(hydroxymethyl)aminomethane
w/v, v/v	weight /volume, volume /volume

ABSTRACT

The remarkable enzymatic and chemical resistance of bacterial endospore is essentially conferred by the proteinaceous coat. Endospores of *Bacillus subtilis* and members of the *Bacillus cereus* family have many features in common. In this work, we study the assembly properties of spore coats in both organisms. In *B. subtilis,* despite most of the spore coat proteins having been identified, we have only a poor understanding of how such coat structural components are assembled in an ordered fashion; moreover we know little about the structure of the individual components. In order to gain structural insights into the spore coat of *B. subtilis* we have attempted to purify a number of recombinant coat proteins including CotY, CotE, CotZ, CotV, CotW, SafA and SpoVID. We have discovered a number of self-assembled structures including two-dimensional crystals and helical fibres. We will focus on the application of image processing techniques including single particle analysis and electron crystallography in order to characterise the self-assembly properties of some of these proteins.

Moreover, we screened a number of *Bacillus* spores to find the most suitable for generating well-order crystalline exosporium samples. With the same data analysis applied, we constructed the 2D/3D model of exosporium of *B. circulans* 42G1 and *B. fusiformis* ATCC 7055 species. Our preliminary results suggest that the exosporium samples from these *Bacillus* bacteria represent a material of choice ideal for structural analyses.

CHAPTER 1
Introduction

1.1 The genus *Bacillus*

The genus *Bacillus* consists of a wide variety of Gram-positive, rod-shaped aerobic or facultatively anaerobic bacteria that are ubiquitous in the environment. The ability of *Bacillus* to grow in the presence of air makes a distinction between them and the strictly anaerobic *Clostridium* spp. The majorities of species of the *Bacilli* are mesophilic and found in the soil. The genus includes more than 60 species and represents a significant genetic diversity since the different range of base composition in the genus *Bacillus* (36% G+C for *B. cereus* to more than 60% G+C for various thermophiles), indicates the genus is not a group of very closely related organisms. A major contribution of the systematics of the genus *Bacillus* was initiated by Nathan R. smith, together with Francis E. Clark and Ruth E. Gordon (smith, R.E et al. 1952). The subsequently revised and supplemented descriptions of these *Bacillus* species were published by Gordon (Gordon, Haynes *et al*. 1973). These studies lay a foundation for the current classification framework of the genus in *Bergey's Manual Systematic Bacteriology* (Claus and Berkeley 1986).

When confronted with unfavorable environments, *Bacilli* are able to enter into a developmental cycle to yield a highly resistant, metabolically dormant endospore through a process called sporulation. The endospores are able to withstand extreme conditions such as heat, toxic chemicals, desiccation, radiation, acids, and lytic enzymes where few other organisms can survive. Inside the endospore, there is little or no metabolic activity. They can keep in the dormant state through prolonged periods of environmental stress with some even suggesting millions of years (Horneck, Bucker *et al*. 1994; Cano and Borucki 1995). Once the conditions become favourable for growth, the spore can germinate in a matter of minutes and rapidly resume vegetative growth. The spores are everywhere in nature, including both free-living and pathogenic species. Spores are able to escape the acid and heat preservation treatments which are commonly used in food industries, resulting in food spoilage and food-borne illness. For example, *Bacillus cereus* is a known cause of food-borne illness and food spoilage (Ohye and

Murrell 1973). *Bacillus anthracis* is the actual infectious agent of anthrax that can enter the human body and cause clinical symptoms (Popham 2002).

The endospore offers an ideal model system for the molecular biology of differentiation as well as a range of biotechnologically important products such as insect toxins and peptide antibiotics (Katz and Demain 1977). Among the *Bacillus* species, *B. subtilis* has been extensively studied as a model system in physiology, molecular biology and cell biology.

1.2 *Bacillus subtilis*

Bacillus subtilis is a gram-positive, rod-shaped bacterium commonly found in the soil. It has simple growth requirements and is also capable of growth within many biospheres although being commonly found in the soil. *B. subtilis* is able to form endospores as strategy that allows the organism to survive extreme environmental conditions. Another strategy evolved by *B. subtilis* is its capability to uptake DNA from the external environment (Anagnostopoulos and Spizizen 1961), which allows the bacteria to adapt by recombination. *B. subtilis* is considered to be non-pathogenic and non-toxicogenic (FDA partial list of microorganisms, 2002). It rarely causes food poisoning (Ryan KJ and CG 2004) but can cause disease in patients with weakened immune systems (Oggioni, Pozzi *et al*. 1998).

Since *B. subtilis* is highly amenable to genetic manipulations, it has been the model organism for a wide range of studies, especially in the field of cellular development and differentiation, and endospore formation in bacteria. Due to extensive studies in all aspects of *B. subtilis*, it has been the best understood species of the *Bacillus* genus. *B. subtilis* has one circular chromosome, and the entire genome has been sequenced (Kunst, Ogasawara *et al*. 1997).

1.3 The *Bacillus cereus* group

The *Bacillus cereus* includes *B. anthracis, B. cereus*, *B. mycoides* and *B. thuringiensis*. These organisms represent microbes of medical, economic and bio-defence importance. that *B. anthracis*, *B. cereus*, and *B. thuringiensis* are genetically related and could be classified as members of the same species on the basis of their 16s rRNA sequences

(Ash, Farrow *et al.* 1991). All four organisms can generate endospore when confronting starvation. Unlike the spore formed by *B. subtilis*, the spores formed by *B. anthracis, B. cereus, B. mycoides* and *B. thuringiensis* possess an additional large balloon-like outer layer called the exosporium.

1.3.1 *Bacillus cereus*

B. cereus is an ubiquitous soil-dwelling, Gram-positive, rod-shaped endospore-forming bacterium that is a known cause of food spoilage. *B. cereus* may be pathogenic to human and animals (Granum and Lund 1997; Kotiranta, Lounatmaa *et al*. 2000; Schoeni and Wong 2005; Stenfors Arnesen, Fagerlund *et al*. 2008). *B. cereus* is an opportunistic human pathogen that can also cause a number of non-gastrointestinal infections including meningitis in newborn infants (Tokieda, Morikawa *et al.* 1999).

The genome of the *B. cereus* ATCC 14579 was completely sequenced (Ivanova, Sorokin *et al*. 2003). Another *B. cereus* ATCC 10987 (Rasko, Ravel *et al.* 2004)， *B. cereus* G9241 (Hoffmaster, Ravel *et al.* 2004)，*Bacillus cereus* Zk (Han, Xie et al. 2006) and *Bacillus cereus* subsp. cytotoxis NVH 391-98 (Lapidus, Goltsman et al. 2008) have also been completely sequenced.

1.3.2 *Bacillus anthracis*

B. anthracis is a Gram-positive, endospore-forming, non-motile, rod-shaped bacterium. *B. anthracis* is the causative agent of anthrax in humans and animals, resulting in a serious disease. The endospores of *B. anthracis* are the infectious form of anthrax and can be used as a potential bioweapon (Inglesby 1999; Makino 2002). The spores can be engulfed by host organism macrophages and are transported into the host body and life cycle almost exclusively occurs in the host (Inglesby, Henderson *et al*. 1999). The three toxin genes of *B. anthracis* are located on a large (181.7 kDa) plasmid, pXO1 and the gene responsible for capsule synthesis is located on a small plasmid (96.2 kDa) (Welkos 1991).

In 2001, the first anthrax-related bioterrorist attack took place in the USA, which resulted in a boost to anthrax research. The threat of bio-terrorism has brought *B.*

anthracis into the public eye. Many more *B. anthracis* strains have been sequenced such as *B. anthracis* Ames strain (Read, Peterson *et al*. 2003; Ravel, Jiang *et al*. 2009). Due to its high pathogenicity, more efforts are underway to understand *B. anthracis* physiology and virulence and to develop a specific vaccine.

1.3.3 *Bacillus thuringiensis*

B. thuringiensis is a Gram-positive, soil-dwelling, endospore-forming bacterium, commonly used as a biological pesticide. *B. thuringiensis* differs from *B. cereus* in producing a crystal protein toxin that is pathogenic to various insects. In most cases, the toxin genes of *B. thuringiensis* are located on large conjugative plasmids (Dean 1984). Two types of insecticidal crystallised protein inclusion are produced and classified into two functional classes called Cry and Cyt toxin (Koni and Ellar 1994). Cry toxins have specific activities against insect species. Thus, *B. thuringiensis* is used as an important reservoir of Cry toxins for the production of biological insecticides. The Cyt toxins are yielded by the growing cells and have pore forming cytolytic activity *in vitro*. The tertiary structures of six different three-domain Cry proteins, Cry1Aa, Cry2Aa, Cry3Aa, Cry3Bb, Cry4Aa and Cry4Ba have been determined by X-ray crystallography (Yudina, Konukhova et al. 2003; Bravo, Gill et al. 2007; Soberon, Lopez-Diaz et al. 2012).

Spores and crystalline insecticidal proteins produced by *B. thuringiensis* have been commercially used to control insect pests and are often applied as liquid sprays. Thus, because of its insecticidal properties *B. thuringiensis* has been exploited as an industrial biological pesticide.

1.4 *Bacillus* endospores

Endospores are produced during a process called sporulation. Endospores were first described by Cohn in *B. subtilis* and later by Koch in the pathogen, *B. anthracis*. The endospore is a dormant, robust, and non-reproductive structure surrounded by a very tough outer proteinaceous coat, which provides much of the chemical and enzymatic resistance. In *B. subtilis*, the coat is composed of more than 70 polypeptides plus an insoluble protein fraction arranged in multilayers (Zhang, Fitz-James *et al*. 1993; Kuwana, Kasahara *et al.* 2002; Kim, Hahn *et al*. 2006). Although the endospores are in a dormant state, they are continually monitoring nutrient availability in their surrounding environment (Driks 2004). When the surrounding environment becomes

favourable, the spore can germinate and initiate vegetative growth. Endospores represent the dormant stage of a bacterial life cycle. Endospores can be easily transferred or dispersed by wind, water or through the animal gut.

Several genera of endospore-forming bacteria have been distinguished in terms of cell morphology, shape and cellular position of the endospore. The two genera that have been studied most are *Bacillus* and *clostridium*. All endospore-forming bacteria are ecologically related because they are commonly found in nature primarily in soil and water.

1.4.1 Endospore formation and germination

Endospore formation is a representative example of a complex bacterial developmental program. Endospores do not normally form during the active growth of vegetative cells and cell division. Their formation is triggered when environmental conditions are becoming unfavourable, usually as a result of nutrient depletion. An endospore-forming bacterium ceases vegetative growth and activates sporulation process. A single endospore is formed per vegetative cell. Once a vegetative cell is converted into a non-growing spore, it becomes resistant to most agents that would normally kill the vegetative cells. When the environment becomes favourable, reactivation of the endospores occurs which involves activation, germination and outgrowth. It is regulated by a complex network of protein-protein and protein-DNA interactions where events of regulatory modules signalling pathways, and post translational regulation participate (Errington 1993; Stragier and Losick 1996; Errington 2003; Kroos 2007). Activated spores can be prepared for germination by placing them in the presence of specific nutrients. As germination initiates, the spore becomes less resistant and series of events occur which will be depicted below. The final step is outgrowth, during which swelling occurs due to water uptake and the synthesis of DNA, RNA and proteins. Eventually, the cell grows out of the broken spore and resumes all the function as a normal cell. The vegetative cells continue to grow into its own life cycle until unfavourable surrounding conditions once again trigger the sporulation process (Fig 1.1) (Driks 1999; Henriques and Moran 2007; de Hoon, Eichenberger *et al.* 2010).

1.4.2 Sporulation

Spore formation, referred to as sporulation, is a differentiation process that results from sporulation firstly described on *B. anthracis* spore (Koch 1876). It is sequentially governed by a cascade of transcriptional sigma factors (Losick and Stragier 1992). The sporulation process takes about 8 hours to complete once the asymmetric cell division initiates and has been extensively studied in *B. subtilis* as a model organism (Kay and Warren 1968; Warren 1968; Dawes, Kay *et al.* 1969; Stragier and Losick 1996; Feucht, Evans *et al*. 2003; Eichenberger, Fujita *et al.* 2004; Piggot and Hilbert 2004; de Hoon, Eichenberger *et al*. 2010). Seven successive morphological stages of sporulation of *B. subtilis* have been defined as shown in Fig 1.1 (Stragier and Losick 1996).

Stage 0-I: sporulation commences only after DNA replication has been completed, ensuring two copies of chromosome are available in the pre-divisional cells (Veening, Murray *et al*. 2009). Two chromosomes are anchored at the distal ends of cells (Teleman, Graumann *et al*. 1998).

Stage II: asymmetric division starts by forming a septum to produce two unequal compartments, a large mother cell compartment and a smaller forespore chamber. Septation is governed by the tubulin-like protein FtsZ, which forms a Z-ring (Lutkenhaus and Addinall 1997; Rothfield and Justice 1997; Grantcharova, Lustig *et al.* 2005). Only about one third of the forespore chromosome is partitioned into the small chamber of the dividing cell (Pogliano, Sharp *et al*. 2002). SpoIIIE, located at the centre of the polar septum is required to translocate the rest of chromosome across the septum after division (Wu and Errington 1994; Wu and Errington 1998; Ptacin, Nollmann *et al*. 2008).

Stage III: this stage is the engulfment of the forespore by the mother cell. Once this occurs, the sporulation is well underway. This stage is driven by mother cell proteins. It begins with peptidoglycan hydrolysis near the central part of the septal disc, resulting in membrane migration around the forespore (Pogliano, Osborne *et al*. 1999; Morlot, Uehara *et al*. 2010). The edge of the septum migrates to the cell pole till they meet and the membrane fuses. As engulfment completes, the forespore is fully covered by its inner and outer membranes. The cytoplasm is enclosed by inner membrane and forespore is pinched off as a free protoplast in the mother cell cytoplasm (Driks, Roels *et al.* 1994).

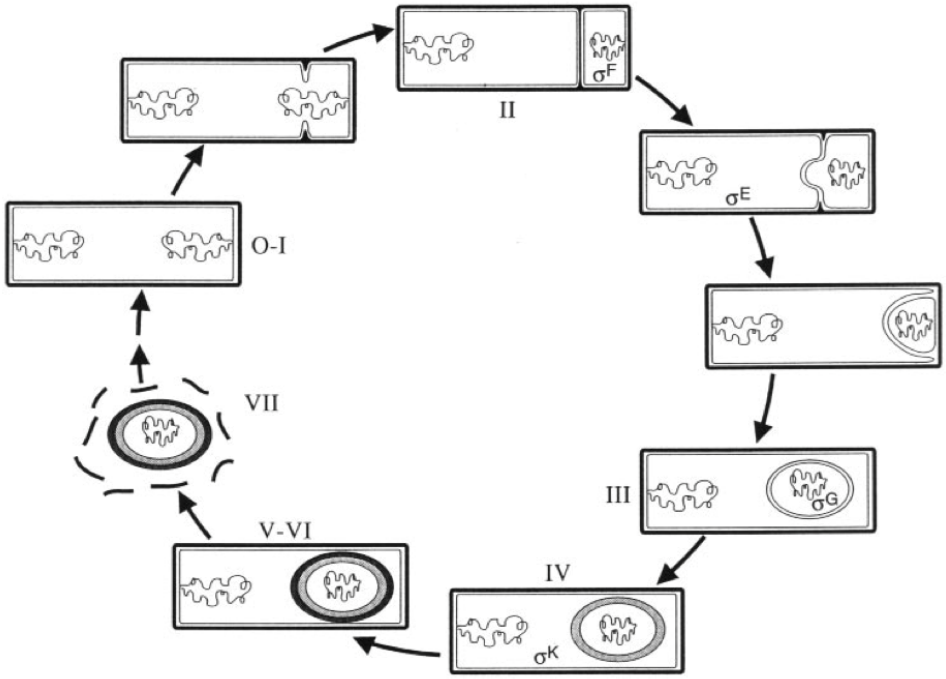

Figure 1.1 The morphological stages of *Bacillus subtilis* endospore formation. In stage 0-I the chromosomes are anchored at the cell poles. Stage II: asymmetric cell division, two membrane bounded compartments are segregated by asymmetric septation, and two identical chromosomes are segregated to two unequal compartments. Stage III: engulfment of the forespore by the mother cell. Stage IV: the cortex that is composed of modified peptidoglycan is synthesized between two membranes surrounding the forespore. Stage V: the coat that is a complex structure encircling the forespore. VI: Spore maturation. Stage VII: mother cell lysis, the mature spore is released into the environment. After sporulation, the spore can stay dormant for an extended period of time until nutrient become available to initiate vegetative growth. Figure from (Stragier and Losick 1996).

Stage IV: in this stage, a series of protective structures is formed. The cortex that is a modified peptidoglycan is formed between the inner and outer membranes (Popham 2002). The forespore is encircled first by the cell wall and then by the cortex. The spore apparently takes shape. Also, the formation of the exosporium is thought to develop in the mother cell at this stage (Ohye and Murrell 1973).

Stage V: coat proteins are simultaneously produced in the mother cell to enclose the forespore forming a multilayered structure (Henriques and Moran 2007; McKenney, Driks *et al.* 2010). The coat that is composed of over 70 distinct proteins assembling around the forespore surface as cortex continues. The coat formation protects the forespore from chemical and enzymic assaults. During this stage, the spore's resistance and germination properties develop, such as lysozyme resistance (Henriques and Moran 2000).

Stage VI: in this stage, the spore continuously gets mature. The spore acquires all resistance properties in this stage.

Stage VII: the final stage, the spore dehydrates cytoplasm and the mother cell lyses; the mature spore is liberated into surrounding environment.

1.5 Spore structure

The basic structure of the endospore consists of a central core surrounded by the inner spore membrane, a cortex layer, a germ cell wall, the outer spore membrane and finally a multilayer proteinaceous coat (Fig 1.2). The outer proteinaceous coat provides much of the resistance to enzymatic and chemical attacks and influences the spore response to germinant. Beneath the coat lies a thick layer of peptidoglycan called the cortex, which conveys resistance to high temperature. A germ cell wall lies under the cortex and its major component peptidoglycan will become the cell wall of the bacterium when germination occurs. Under the germ cell wall resides the inner membrane, a semi-permeable barrier against potentially chemical threats. The core is in the centre of the endospore, exists in a very dehydrated state and contains the spore chromosomal DNA, ribosomes, enzymes and dipicolinic acid. It is noteworthy that in some spore species such as the *B. cereus* family there is an additional external layer, a loose-fitting structure called the exosporium. Spores of *Bacillus anthracis* for example, are enclosed by an exosporium composed of a basal layer and an external hair like nap. A schematic map

of a representative endospore structure is shown in Fig 1.2, the spores of all species of *Bacillus* are formed as a set of concentric structures.

1.5.1 The spore core

The spore core is the innermost part of the spore containing the cellular components such as DNA, RNA, ribosomes and metabolic enzymes that are necessary for establishment of a vegetative cell cytoplasm once germination occurs, but it is not metabolically active (Beaman and Gerhardt 1986). The core contains the chromosomal DNA, which forms tight nucleoprotein complexes with small acid-soluble proteins (SASPs) that make up 3-6% of total spore protein (Francesconi, MacAlister *et al.* 1988; Nicholson, Setlow *et al*. 1990; Setlow, Sun *et al.* 1992; Setlow 1992). SASPs and their DNA-binding properties provide protection to the spore DNA from UV radiation and heat (Fairhead and Setlow 1992; Setlow, Randesi *et al.* 1992; Setlow 2006).

The most notable feature in the spore core is the water content, which largely determines spore resistance to wet heat (Beaman, Pankratz *et al.* 1989; Setlow 2006). Compared to the 75-80% of the wet weight of the vegetative cell, water makes up only 27-55% of the spore core wet weight depending on the species. Lower core water content generally conveys more wet heat resistance to spores, and plays an important role in the spore's enzymatic dormancy and longevity (Gerhardt and Marquis 1989).

About 5-15% of the dry weight of the total spore is made up pyridine-2, 6-dicarboxylic acid (DPA) (Driks and Setlow 1999). DPA only attributes in the spore core, where it is chelated with divalent cations, largely Ca^{2+} contained within the spore core (Gerhardt and Marquis 1989). Although the precise state of the DPA in the core is still unknown a lack of DPA may lead to core hydration suggesting that the large accumulation of DPA in the spore core is responsible for water reduction during sporulation (Driks and Setlow 1999).

1.5.2 The inner and outer spore membranes

The outer membrane lies under the spore coat. Although the outer membrane is an essential structure in the spore, the precise function is poorly understood (Piggot and Hilbert 2004). It has been reported that the outer membrane is a permeability barrier (Driks 1999; Driks 2002). However, the removal of the outer membrane together with

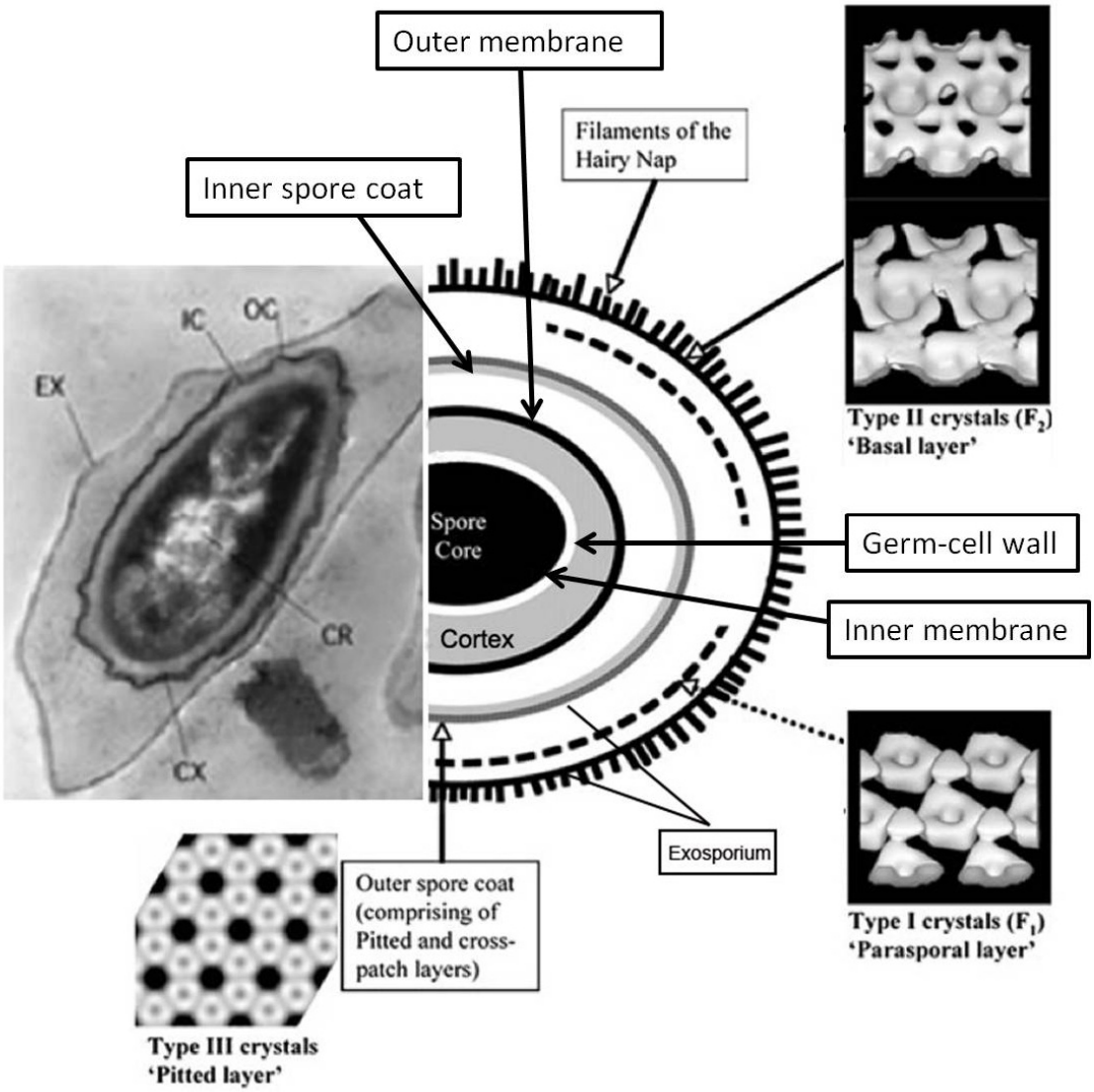

Fig. 1.2 A schematic diagram and electron micrograph of a *B.cereus* spore showing the basic spore structure and proposed localization of the various crystalline layers on the exosporium. The exosporium, spore coat, outer membrane, cortex, germ cell wall, inner-membrane and spore core are clearly indicated. The location of type I, type II and type III layer was tentatively assigned on the exosporium multilayer structure along with 2D/3D representative images (Figure from Ball, Taylor *et al.* 2008). EX: exosporium; IC: Inner coat; OC: Outer coat; CX: Cortex; CR: Core.

much spore coat protein has no significant effect on spore resistance to heat, radiation and chemicals (Nicholson, Munakata *et al*. 2000).

Compared with the outer spore membrane, the inner spore membrane acts as a functional barrier and plays an important role in spore resistance to many chemicals. The inner membrane exists in a specialised compressed state in the dormant spore (Cowan, Olivastro *et al*. 2004). After spore germination, the inner membrane becomes the vegetative cell membrane with its volume increasing approximately two-fold (Freer and Levinson 1967; Cowan, Olivastro *et al.* 2004). Lipid exists in the inner membrane in tightly packed state and largely immobile. Upon spore germination, the lipid becomes fully mobile (Cowan, Olivastro *et al.* 2004).

1.5.3 The germ cell wall and cortex

The germ cell wall is a thin layer of peptidoglycan covering the outer surface of inner forespore membrane. The germ cell wall considerably expands during the spore germination and becomes the cell wall of outgrowing spore (Setlow 2003).

The cortex is a thick layer lying externally to the germ cell wall. The cortex of the spore is composed of peptidoglycan whose structure is slightly different to that of the vegetative cell in cross-linking pattern (Popham 2002). Peptidoglycan chains contain far fewer cross-links in the spore in contrast with the vegetative cell wall. The cortex is thought to be of importance during the formation of a dehydrated core (Setlow 2006). The cortex is hydrolyzed upon spore germination followed by expansion of the germ cell wall which allows full spore core hydration and resumption during spore metabolism (Setlow 2003).

1.5.4 The spore coat

The spore coat is a multilayered structure around the outer membrane and is the outermost layer in many species of *Bacillus*. The proteinaceous coat endows the spore with resistance to lytic enzymes and chemical attack, and plays an important role in the spore response to germinants.

Different species have different numbers of layers and fine structure as well as protein composition. In *B. subtilis*, the coat is made up of 70 or more polypeptides that organize

into multilayers (Holt, Gauther *et al.* 1975; Driks 1999; Riesenman and Nicholson 2000; Kim, Hahn *et al.* 2006). Under electron microscopy, the spore coat appears as a string of concentric layers that is composed of three layers: an amorphous undercoat, an electron-translucent, lamellar inner structure and an electron-dense, striated outer coat (Driks, Roels *et al*. 1994; Driks 1999; Henriques and Moran 2000; Kim, Hahn *et al*. 2006). The coat width differs in different *Bacillus* species, for example *B. cereus* has a visibly thinner layer of coat than that of *B. subtilis*. These species-specific differences in structure may be explained by their functional differences in the spore coat that help bacteria to survive in the harsh environment. It can act as a filter, only allowing small compounds such as germinants through into the interior spore and constantly protect spore from the macromolecules such as lytic enzymes that may kill the spore (Driks 1999).

1.5.5 The exosporium

The exosporium is a large loose-fitting balloon-like layer found surrounding the whole spore. In the *B. cereus* family, the spore coat is encased by an exosporium composed of a basal layer and an external hairy nap (Driks 2002; Lai, Phadke *et al*. 2003; Redmond, Baillie *et al.* 2004; Waller, Fox *et al*. 2004). Microscopy of thin sections indicates that the basal layer fully embraces the endospore but is not connected to the spore coat (Henriques and Moran 2007). The hairy nap is mainly composed of a layer of hair-like projections ranging in size up to 600 Å (Gerhardt and Ribi 1964; Sylvestre, Couture-Tosi *et al*. 2003) that consists of one single collagen-like protein called BclA, while the basal layer is formed by many different proteins and enzymes (Sylvestre, Couture-Tosi *et al.* 2002; Redmond, Baillie *et al*. 2004; Boydston, Chen *et al.* 2005). Some proteins identified as coat proteins in *B. subtilis* are also found in the exosporium of spores of *B. anthr*acis (Lai, Phadke *et al*. 2003; Todd, Moir *et al.* 2003; Redmond, Baillie *et al*. 2004). The exosporium may contribute to the attachment and colonization as it exposed to the outside environment. In addition, the exosporium may confer resistance to chemical and enzymatic treatments, and its hydrophobic surface is responsible for spore surface properties, including adhesion (Kozuka and Tochikubo 1985; Wiencek, Klapes *et al*. 1990; Zolock, Li *et al*. 2006; Henriques and Moran 2007; Chen, Driks *et al*. 2010). It also contains several enzymes that play roles during spore germination. The exosporium is also the first site of contact with host cells of the immune system and a potential site of spore surface antigen (Henriques and Moran 2007; Ball, Taylor *et al*.

2008). 3D reconstruction of the exosporium of *Bacillus* suggested the exosporium could be a semi-permeable selective barrier to potential harmful compounds like lytic enzymes whilst favorable germinants are allowed to pass through (Ball, Taylor *et al.* 2008; Kailas, Terry *et al*. 2011). In spite of the importance of the exosporium, the functions of these individual proteins and the assembly mechanism of the exosporium are still poorly understood.

Electron microscopy showed that some of the spore of *B. cereus* family members have a structurally identical exosporium which is composed of a crystalline basal and a hairy outer layer (Gerhardt and Ribi 1964; Hachisuka, Kojima *et al.* 1966; Beaman, Pankratz *et al*. 1971). Structurally, the exosporium is poorly understood, probably due to the fact that the model organism *B. subtilis* for spore research does not have one. Extensive studies have concentrated on the protein compositions, functionality of each component, and physical properties of the exosporium. Using electron microscopy and image analysis, Ball *et al* have characterized crystalline fragments from the exosporium of *B. cereus, B. thuringiensis* and *B. anthracis* spores and three distinct crystal types were identified (Ball, Taylor *et al.* 2008), namely type I, type II and type III. The three types of crystalline fragments found in the exosporium preparations, which respectively correspond to parasporal layer, basal layer and pitted layer (Fig 1.2) (Ball, Taylor *et al.* 2008). A possible model for the exosporium of the *B. cereus* family at the subnanometer scale has been mapped out by Kailas *et al* (Kailas, Terry *et al.* 2011). Through crystallographic analysis of exosporium of *Bacillus* family, in combination with AFM identification, 2D/3D high resolution structure of the exosporium basal layer has been resolved (Kailas, Terry *et al.* 2011). With the knowledge of putative components of exosporium accumulating, how proteins localize to the whole exosporium has attracted much attention. To understand precise mechanisms of spore exosporium morphology, it is helpful to study the structure of other related *Bacilli* spore's exosporium. It might be possible to discover more suitable well-ordered crystalline exosporium samples for higher resolution analysis and present common features among different spore's exosporium in structure.

1.5.6 Surface appendages of the spore

Some spore species possess additional structures that extend from the spore coat or exosporium surface. In different spores they appear as pilus-like fibres, ribbon-like structures, or other shapes (Graumann 2007).

1.6 Genetic regulation in spore coat assembly

Coat assembly takes place in the mother cell and all the known coat protein genes and coat morphogenetic genes are expressed in this compartment during the sporulation (Fig 1.3). In *B. subtilis*, after asymmetric division, the mother cell nurtures the spore until its formation is complete and the mother cell gene expression is mainly driven by two important transcription factors, RNA polymerase sigma factors σ^E and σ^K (Sun, Stragier *et al.* 1989; Cutting, Driks *et al.* 1991; Losick and Stragier 1992), and three accessory transcription regulatory proteins, SpoIIID (Kroos, Kunkel *et al.* 1989; Kunkel, Kroos *et al.* 1989), GerR (Eichenberger, Fujita *et al.* 2004; Cangiano, Mazzone *et al.* 2010) and GerE (Zheng, Halberg *et al.* 1992; Roels and Losick 1995). The spore formation is strictly driven by a program of sigma factor activation taking place at the right time and place as shown in Fig 1.3.

σE activity results in the engulfment of forespore compartment and remains the specific regulation in mother cell until forespore engulfment completion (Errington 1993; Piggot and Hilbert 2004). Also it directs the activity of an important transcription factor SpoIIID (Kroos, Kunkel *et al*. 1989; Kunkel, Kroos *et al.* 1989). SpoIIID is able to repress gene expression as well as activate it. At the initial stages of coat assembly, σ^E controls a large set of genes that play key roles in initial coat formation including gene *spoVM, spoIVA, spoVID, safA, cotJ, cotE, cotH*, and genes for some of the coat components (Eichenberger, Jensen *et al.* 2003; Feucht, Evans *et al.* 2003; Eichenberger, Fujita *et al*. 2004); SpoIVA is synthesized early in the mother cell under the control of σ^E. SpoIVA localizes near the mother cell side of the division septum (Driks, Roels *et al.* 1994; Price and Losick 1999). The localization of SpoIVA needs a σ^E controlled protein SpoVM which is required for efficient targeting of SpoIVA to the outer surface of the forespore (Price and Losick 1999). SpoIVA is essentially required for spore cortex and coat layer assembly since a *spoIVA* mutant fails to form a cortex but produces a mislocalized coat (Roels, Driks *et al.* 1992). SpoIVA creates a basement layer around the forespore on which coat assembly continuously occurs (Driks, Roels *et al.* 1994).

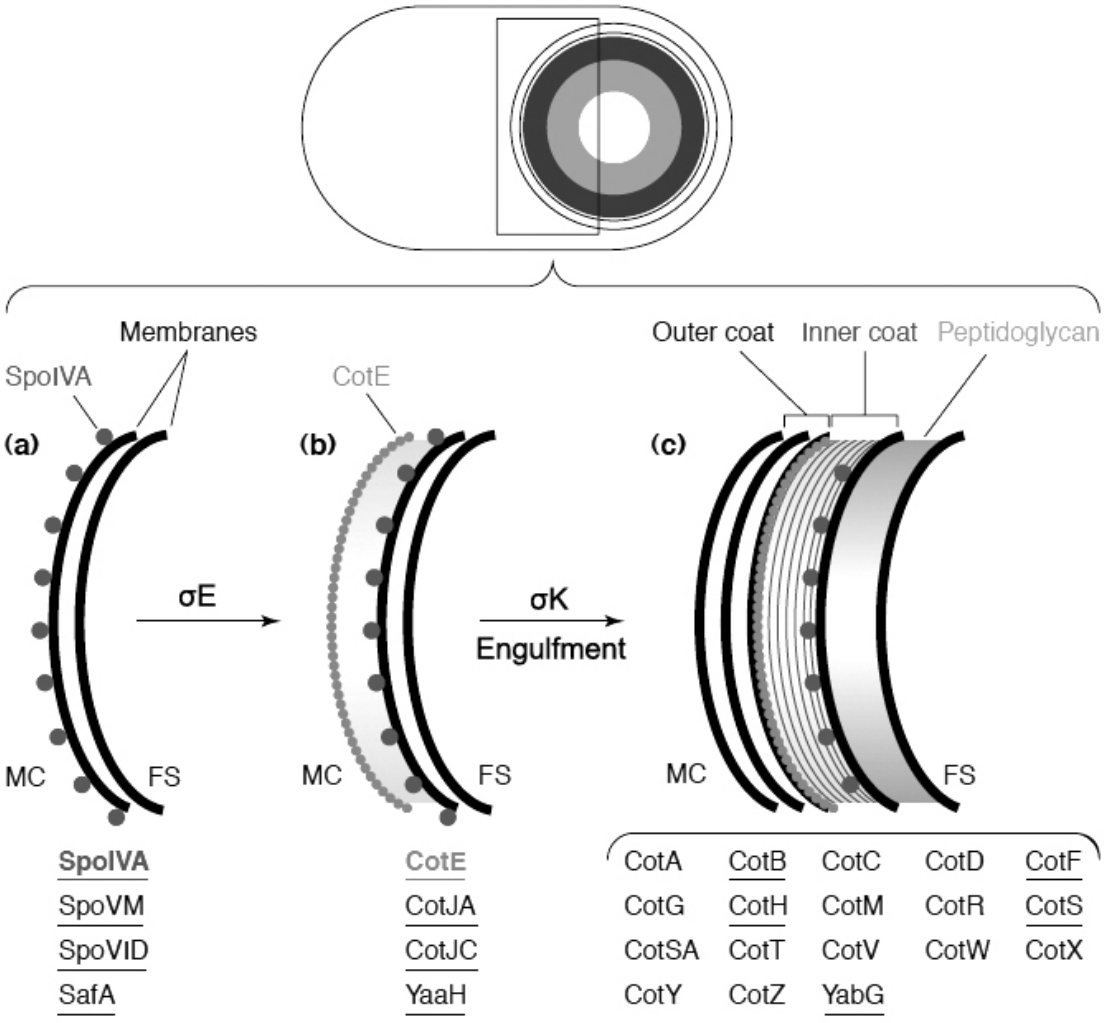

Fig. 1.3 The diagram shows the model for *B. subtilis* spore coat assembly. The upper diagram represents a cell harboring a mature spore before mother cell (MC) lysis. The lower diagram represents an arc of spore surface during spore coat assembly. It shows how spore coat constructed and spore coat proteins involve step by step. The MC and forespore (FC) sides are indicated. (A) In the early stage SpoIVA localizes to the mother cell side of the membranes; (B) CotE is assembled over SpoIVA, localizes to edge of the forespore and connects with SpoIVA via matrix that might be composed by CotJA and CotJC; (C) The assembly of inner and outer coat layers. After engulfment, the cortex appears and a large set of spore coat proteins are expressed and involved into the assembly. The coat-assembly-associated proteins under each stage are shown within the box. Figure from (Driks 2002).

Another important coat morphogenetic protein, SpoVID, also needs SpoIVA to localize to the developing endospore (Beall, Driks *et al.* 1993; Driks, Roels *et al.* 1994; Ozin, Henriques *et al.* 2000). SpoVID expression is under control of σ^E (Beall, Driks *et al.* 1993). *spoVID* mutant have a lysozyme-sensitive spore, suggesting that SpoVID has specific function for spore coat assembly (Beall, Driks *et al.* 1993). SafA is a morphogenetic protein then gets involved in the proper coat assembly (Ozin, Henriques *et al*. 2000). SafA could directly interact with SpoVID and form a complex (Ozin, Henriques *et al.* 2000; Ozin, Samford *et al.* 2001; Costa, Isidro *et al.* 2006), and the interaction between them is essential for the localization and function for SafA. Thus, the initial stages in the coat assembly could be simply summarized as a cascade of interactions, SpoVM-SpoIVA, SpoIVA-SpoVID, and SpoVID-SafA. These proteins form a base layer covering the forespore as engulfment completes.

After engulfment, σ^k controls the expression of a large set of coat protein genes and governs the late stages of development (Cutting, Panzer *et al*. 1989; Zheng and Losick 1990; Ichikawa, Halberg *et al*. 1999; Eichenberger, Fujita *et al.* 2004). *cotA, cotD, cotF, cotH, cotM, cotT, cotV, cotW, cotY,* and *cotZ* are first regulons controlled by σ^k. The transcription factor gene *gerE* is also included to the first regulon. GerE works with σ^k to activate a final regulon that composed of *cotB, cotC, cotG, cotS, cotV, cotW, cotX, cotY*, and *cotZ. cotV, cotW*, and *cotY* are also under the control of σ^k and σ^k+GerE together (Zheng, Halberg *et al*. 1992; Sacco, Ricca *et al*. 1995; Takamatsu, Kodama *et al.* 1999). GerE is able to modulate the gene expression in the σ^k regulon, for example to down-regulate *cotA* (Sandman, Kroos *et al.* 1988) and *cotM* (Henriques, Beall *et al.* 1997). GerE also down-regulates the activity of σ^k (Zheng, Halberg *et al*. 1992).

Another morphogenetic protein, CotE plays a central role in spore coat assembly after engulfment (Fig 1.3). CotE is synthesized early. SpoIVA localization is required for the localization of CotE (Zheng, Donovan *et al*. 1988; Driks, Roels *et al*. 1994; Webb, Decatur *et al.* 1995). After formation of the septum, CotE forms a layer, maintaining a short gap off the septum, after the engulfment, CotE appears as a ring encircling the forespore and localizing about 75 nm from the forepore (SpoIVA) (Fig 1.3) (Driks, Roels *et al.* 1994). The unknown matrix material defines the position between the gap, and later converts into the inner coat (Fig 1.3) (Driks, Roels *et al.* 1994; Henriques and Moran 2000). CotE acts from the edge of the inner coat to nucleate outer coat by

interacting with outer coat proteins (Little and Driks 2001; Kim, Hahn *et al*. 2006; Isticato, Pelosi *et al*. 2010). A large set of coat proteins has been found to assemble in a CotE-independent manner (Kim, Hahn *et al.* 2006). A *cotE* mutant spore that lacks an outer coat layer but retains the lamellar structure of the inner coat suggesting that CotE is essential for outer spore coat assembly and the assembly of the inner and outer coat layer is largely independent (Zheng, Donovan *et al.* 1988). Coat proteins are successively deposited on the spore surface in different patterns. In the maturation stage of coat assembly, the correctly positioned coat proteins are cross-linked and modified.

1.7 Spore coat proteins

The assembly of the spore coat requires a large set of proteins, and it was estimated that the spore coat contained over 70 proteins (Kim, Hahn *et al*. 2006; Abhyankar, Beek *et al.* 2011). Extraction of soluble proteins from the inner and most of the outer coat produced about 40 protein bands on SDS-PAGE (Driks 1999; Henriques and Moran 2000).The insoluble fraction contains cysteine-rich components that are highly cross-linked and are resistant to extraction (Goldman and Tipper 1978; Pandey and Aronson 1979). It has been reported that 55 proteins were found on the insoluble B. subtilis spore coat (Driks 1999; Henriques and Moran 2007).

In this chapter, we will give some information regarding to spore coat proteins that have been specifically investigated in this project.

1.7.1 CotY

In *Bacillus subtilis*, CotY is a 17.9-kDa coat protein that was insoluble fractions of spore coat. CotY is involved in the formation of *B. subtilis* spore coat and its homologues are also found in the exosporium of *B. cereus* and *B. anthracis* (Redmond, Baillie *et al.* 2004; Johnson, Todd *et al.* 2006). *cotY* deletion leads to the production of the spore with a subtle germination defect (Driks 1999).

CotY is cysteine rich protein (15 cysteines out of 161 residues) and shares 54% sequence identity with another insoluble spore coat protein CotZ that contains 10 cysteines out of 147 residues (Zhang, Fitz-James *et al.* 1993). *cotY* and *cotZ* are paralogous genes of a gene cluster *cotVWXYZ* transcribed at the late stage of sporulation

(Zhang, Fitz-James *et al*. 1993; Zhang, Ichikawa *et al*. 1994). Unlike *cotY* and *cotZ*, the first three genes *cotVWX* do not encode cysteine-rich proteins. They are dependent on each other to localize on the spore crust and have critical roles in spore crust formation (Imamura, Kuwana *et al*. 2011). Using genetic and biochemical techniques it was shown that these proteins interact (Krajcikova, Lukacova *et al*. 2009). CotY was found to self-interact, and interact strongly with CotZ (Krajcikova, Lukacova *et al.* 2009). CotY appeared to be multimeric in the spore coat extraction (Zhang, Fitz-James *et al*. 1993). The high content of cysteine residues in both proteins suggests that CotY multimers might be cross-linked by intermolecular or intramolecular disulphide bridges (Zhang, Fitz-James *et al*. 1993). In addition to homologue protein CotZ in *B. subtilis*, there is a gene product of *B. anthracis exsY* is the CotY orthologue identified in exosporium (Redmond, Baillie *et al*. 2004). Likewise, ExsY identified in exosporium of *B. cereus* also thought to be a *B. subtilis* CotY orthlogue (Johnson, Todd *et al*. 2006). ExsY and CotY are required for the correct assembly of the exosporium of *B. anthracis* and *B. cereus* (Redmond, Baillie *et al.* 2004; Johnson, Todd *et al.* 2006). Due to high sequence identity, it is suggested that the spore coat of *B. subtilis* is a cognate of the exosporium of *B. anthracis* and *B. cereus*.

1.7.2 CotE

CotE (MW 24 kDa) is a key morphogenetic protein, which has been shown to play a key role in spore coat formation, directing the correct assembly of a major subset of coat proteins (Zheng, Donovan *et al.* 1988; Roels, Driks *et al.* 1992; Driks, Roels *et al.* 1994; Bauer, Little *et al*. 1999; Little and Driks 2001). In the *B. subtilis* spore coat protein interactions network, the assemblies of many spore coat proteins are CotE dependent, which indicates its pivotal role in spore assembly. CotE is localized at the interface of the inner coat and the outer coat by forming a ring like structure that surrounds the forespore (Driks, Roels *et al.* 1994; Driks and Setlow 1999; Kim, Hahn *et al*. 2006). The formation of the CotE ring was dependent on SpoIVA that localizes to the mother cell side of sporulation septum (Driks, Roels *et al*. 1994; Bauer, Little *et al.* 1999). A small gap between the ring and forespore is believed to be the site where the inner coat forms (Driks, Roels *et al*. 1994). CotE governs the correct formation of outer coat and makes important contributions to the assembly of the inner coat layer as well (Driks, Roels *et al.* 1994).

The functional regions of the *B. subtilis* CotE have been well investigated (Bauer, Little *et al.* 1999; Little and Driks 2001). Within the *cotE* sequence there are specific regions within the C-terminal 28-amino-acid are required for deposition of the coat protein CotA, CotB, CotG, CotSA and CotR. Moreover, 35 amino acids that is required for targeting of CotE to the forespore and an 18-amino-acid stretch of the N-terminus that is responsible for CotE multimers formation (Little and Driks 2001). *cotE* gene disruption was reported to reduce or prevent the assembly of several coat proteins including CotG and CotB (Bauer, Little *et al.* 1999). A *cotE* mutant was created by replacing the chromosomal gene and resulting *cotE* mutant spores lacked outer coat layer and the spore that is heat resistant but sensitive to lysozyme and impaired in germination (Zheng, Donovan *et al*. 1988).

1.7.3 CotZ

CotY and CotZ (MW 16.5 kDa) are homologous, cysteine rich proteins localized to the outermost layer of spore, namely the spore crust. The assembly of CotZ in the spore was previously reported to partially depend on CotE, CotG and CotH (Kim, Hahn *et al.* 2006). In the spore crust formation, CotY and CotZ are dependent on each other to assemble on the spore (Imamura, Kuwana *et a*l. 2010; Imamura, Kuwana *et al*. 2011). Spores missing *cotZ*, *cotX* and *cotY* are phenotypically similar to those harbouring deletions of only *cotX* and *cotY* which indicated that CotZ is unlikely to have a significant contribution to the spore resistance properties (Driks 1999). However, the spore coat thickness with the *cotX*, *cotY* and *cotZ* triple mutant was reduced, which suggested that CotZ may contribute to proper assembly of spore coat. Imamura *et al* proposed that CotZ is at least required for the spore crust to encircle the spore (Imamura, Kuwana *et al.* 2011).

1.7.4 SpoIVA

SpoIVA (MW 57.2 kDa), the crucial morphogenetic protein in the spore coat, is required for the proper assembly of the outer layers of the spore on top of which other spore coat proteins are deposited (Piggot and Coote 1976; Roels, Driks *et al*. 1992; Stevens, Daniel *et al.* 1992; Beall, Driks *et al.* 1993; Driks 1999; Catalano, Meador-Parton *et al.* 2001). *spoIVA* null mutant of sporulating cells are unable to form a cortex and produce a mislocalized coat that misassembles as swirls within the mother cell

rather than a shell around the surface of the forespore (Piggot 1973; Roels, Driks *et al*. 1992). Moreover, the defects in coat and cortex formation introduced by random residues mutation of *spoIVA* were also identified (Catalano, Meador-Parton *et al*. 2001). SpoIVA localizes to the mother cell side of the forespore membrane, anchoring the coat to the spore surface, directing the assembly of CotE in a ring-like structure at a distance from it (Fig 1.3) (Henriques, Beall *et al*. 1997; Driks 1999; Henriques and Moran 2000; McKenney and Eichenberger 2012). The proper localization of SpoIVA was reported to be dependent on SpoVM to efficiently target to the outer surface of the forespore (Price and Losick 1999). Ramamurthi *et al* then found reciprocal dependence that proper localization of SpoVM is dependent on SpoIVA, and they are dependent on each other for proper deployment within the endospore (Ramamurthi, Clapham *et al.* 2006) (Ramamurthi, Clapham *et al.* 2006). However, no direct interaction was found between them, presumably, SpoIVA and SpoVM interact indirectly by participation of an unknown bridging protein. Moreover, as previously described, the formations of CotE rings are also dependent on SpoIVA.

1.7.5 SpoVID

Beall *et al*., cloned and identified *spoVID* in the course of screening for σ^E-dependent promoters (Beall, Driks *et al*. 1993). In *B. subtilis*, expression of the *spoVID* gene occurred around 2h after the commencement of sporulation and increased in abundance during spore development (Beall, Driks *et al*. 1993). SpoVID (MW 65 kDa) localizes near the forespore membrane and plays an essential role at a later stage in spore coat assembly by mediating the process of spore encasement, facilitating a symmetric distribution of individual coat proteins around the spore and thus the formation of the ring pattern typical of normal coat protein localization (Driks and Setlow 1999; Driks 2002; Wang, Isidro *et al*. 2009; McKenney, Driks *et al*. 2010). SpoVID was shown to be involved into the deposition of the coat to the forespore during the earlier shapes of spore formation, but not necessary for the initial attachment of the precoat (Driks 1999). It was previously reported that SpoVID is in close relationship with SpoIVA, SpoVM, SafA and CotE (Ozin, Henriques *et al.* 2000; Ozin, Samford *et al.* 2001; McKenney and Eichenberger 2012). SpoIVA is required for the appearance of SpoVID which is a morphogenetic protein playing a key role in attachment of coat to forespore membrane (Driks 1999; Henriques and Moran 2007). SafA directly associates with SpoVID during the early stage of coat assembly and SafA localization around the forespore was

dependent on SpoVID and SpoIVA (Ozin, Henriques *et al.* 2000; Ozin, Samford *et al*. 2001). SpoVID was found to directly interact with the outer coat morphogenetic CotE, and functions to maintain the integrity of the ring that formed by CotE (Ozin, Samford *et al*. 2001; McKenney and Eichenberger 2012). A *spoVID* mutant appeared to fail to encircle the prespore in the mother cell and resulted in coat defect (Beall, Driks *et al*. 1993).

1.7.6 SafA

SafA (MW 44.6 kDa) is morphogenetic protein required for proper coat assembly of *B. subtilis*. In the *B. cereus* family, ExsA is similar to the SafA in *B. subtilis* (Ozin, Henriques *et al.* 2000). SafA plays a role in controlling deposition of the coat components to the spore coat (Driks, Roels *et al*. 1994; Takamatsu, Kodama *et al.* 1999; Zilhao, Naclerio *et al*. 1999; Zilhao, Serrano *et al.* 2004; Krajcikova, Lukacova *et al.* 2009). SafA is localized at the interface between the coat and cortex in the spore (Ozin, Henriques *et al*. 2000; Ozin, Samford *et al*. 2001). It has been reported that SafA and the other key morphogenetic protein SpoVID might be associated in a complex during the early stages of coat assembly (Ozin, Henriques *et al.* 2000; Ozin, Samford *et al*. 2001; Driks 2002; Costa, Isidro *et al*. 2006; Krajcikova, Lukacova *et al*. 2009). SpoVID has been proved to guide SafA to the spore coat in the *B. subtilis* (Ozin, Samford *et al.* 2001).

Since SafA harbours a LysM domain at its N-terminus and localizes in the cortex/coat interface, it was suggested that SafA ties these two spore layers together by directing protein to the surface of the developing spore (Costa, Isidro *et al*. 2006; Buist, Steen *et al.* 2008). The coat in safA mutant spores is attached rather loosely (Ozin, Henriques *et al*. 2000). Additionally SafA probably controls the assembly of some inner coat proteins.

1.7.7 CotH

CotH (MW 42.8 kDa) is one of the morphogenetic proteins with an intermediate role in outer spore coat assembly. *cotH* lies between *cotB* and *cotG* (Naclerio, Baccigalupi *et al*. 1996). *cotH* expression is controlled by σ^k and CotH localizes in inner layer of coat and controls the assembly of some outer coat proteins, as CotB and CotG (Naclerio, Baccigalupi *et al*. 1996; Zilhao, Naclerio *et al.* 1999; Zilhao, Serrano *et al*. 2004). *cotH* mutant spores were deficient in several coat proteins and a resulting coat structure

appears to peel off the spore (Naclerio, Baccigalupi *et al.* 1996; ZiHao, Naclerio *et al.* 1999). A doubled *cotE* and *cotH* strain caused more severe germination deficiency and was more lysozyme sensitive than a *cotE* mutant alone (Driks 1999). Since it has some functions in germination and spore lysozyme resistance, it raises the possibility that CotH also influences the assembly of the inner coat layers or it is a minor component of this structure.

1.7.8 CotV-CotW

cotVWXYZ genes are clustered on the chromosome and required for the proper formation of the outer spore coat (Zhang, Ichikawa *et al.* 1994). CotY and CotZ, are encoded immediately downstream of the *cotVWX* operon (Zhang, Ichikawa *et al.* 1994). *cotV* is the one most upstream and encodes a very hydrophobic 128 amino acids protein. Due to high hydrophobicity, CotV (MW 14 kDa) was considered to be one of the components on the outer coat surface, with its polar head buried and the hydrophobic portion exposed to the surface (Zhang, Ichikawa *et al.* 1994). *cotW* localizes between *cotV* and *cotX* and encodes a protein with 105 amino acids. CotW (MW 12 kDa) is a very hydrophilic protein with charged residues (Zhang, Ichikawa *et al.* 1994). It was reported that CotW can specifically interact with CotV and the solubility of CotV was remarkably increased when co-produced with CotW (Krajcikova, Lukacova *et al.* 2009).

1.8 Protein composition of the exosporium of the *B. cereus* family

Spores of the *B. cereus* family including *B. anthracis* and *B. thuringiensis* possess an outmost exosporium layer, a balloon-like loose structure consisting of a basal layer where an external hair-like nap attached (Desrosier and Lara 1984; Ball, Taylor *et al.* 2008). It was also found on spores of other *Bacillus* and *Clostridia* species.

1.8.1 BclA

The filament of the hairy nap is formed by trimers of the collagen-like glycoprotein BclA (MW 21 kDa) (Deatherage, Taylor *et al.* 1983; Sylvestre, Couture-Tosi *et al*. 2002; Boydston, Chen *et al.* 2005). The monomers interact with each other through their C-terminus to form a triple helix (Boydston, Chen *et al.* 2005). The C-terminus of BclA is highly conserved and exposed to the environment while the N-terminus anchors to the exosporium (Boydston, Chen *et al*. 2005). BclA consists of three domains: a 38-residue

amino terminal domain (NTD), a glycosylated collagen-like region and a 134-residue carboxy terminal domain (Sylvestre, Couture-Tosi *et al.* 2002; Steichen, Chen *et al.* 2003; Daubenspeck, Zeng *et al.* 2004). Every third residue of the glycosylated collagen-like region is a glycine. The number of collagen-like (GXX)n repeat regions of BclA appears to be strain specific and determines the different length of the filament (Steichen, Chen *et al.* 2003; Sylvestre, Couture-Tosi *et al*. 2003).

BclA may not be the only major component of the hairy nap material. In *B. cereus*, several other glycoproteins may be involved into the nap formation (Henriques and Moran 2007). The exact function of BclA is still unclear. The C-terminal domain (CTD) of BclA is considered to be the immuno-dominant exosporium component (Sylvestre, Couture-Tosi *et al.* 2002; Sylvestre, Couture-Tosi *et al*. 2003). The structure of BclA CTD can interact with a major component of pulmonary surfactant protein C suggesting BclA may get involved in the recognition of specific hydrophobic component in the host (Rety, Salamitou *et al.* 2005). *bclA* mutant results in a lack of filament attached to the exosporium (Sylvestre, Couture-Tosi *et al.* 2002; Boydston, Chen *et al.* 2005). The spore without a nap was more sensitive to lysozyme, suggesting the nap may contribute to its resistance properties (Kozuka and Tochikubo 1985; Steichen, Chen *et al*. 2003).

1.8.2 ExsFA

ExsFA (MW 17 kDa) also termed as ExsF or BxpB (Kozuka and Tochikubo 1985; Steichen, Chen *et al*. 2003) has been characterized in the exosporium of *B. cereus* (Todd, Moir *et al.* 2003) and *B. anthracis* (Steichen, Chen *et al*. 2003; Redmond, Baillie *et al.* 2004). ExsFA has a homologous protein ExsFB identified in *B. anthracis* (Steichen, Kearney *et a*l. 2005). The ExsFB protein has 78% (131 of 168 amino acids) identity with ExsFA (Steichen, Kearney *et al*. 2005). *exsF* is located close to the region of *exsY* and *bclA* in the genome, and ExsFA organized in stable multimeric complexes with ExsFB and BclA (Redmond, Baillie *et al.* 2004; Sylvestre, Couture-Tosi *et al.* 2005). The *ΔexsFA* and *ΔexsFAΔexsFB* respective mutant spores have defective exosporia, and spores surface partially and totally lack filaments (Steichen, Kearney *et al*. 2005). The resulting crystalline basal layer becomes unstable (Steichen, Kearney *et al.* 2005). The results indicate that ExsFA contributes to the localization of BclA targeting to the spore surface and to the stability of exosporium basal layer (Steichen, Kearney *et al*. 2005; Giorno, Mallozzi *et al.* 2009; Thompson, Hoelscher *et al.* 2011). Recently, the

mechanism of BclA attaches directly to BxpB (also called ExsFA) by forming isopeptide bonds and with this bond formation attaches to the exosporium of *B. anthracis* was revealed (Tan, Li *et al*. 2011).

1.8.3 ExsY

ExsY (MW 17 kDa) is a homologue of *B. subtilis* cysteine-rich spore coat proteins CotY and CotZ found in the exosporium of *B. anthracis* and *B. cereus*. High-molecular weight species was formed on exosporium by BclA, ExsFA, and ExsY (Todd, Moir *et al*. 2003; Redmond, Baillie *et al.* 2004; Boydston, Yue *et al*. 2006; Johnson, Todd *et al*. 2006). The *exsY* single mutant *B. cereus* spore failed to have an intact exosporium surrounding the spore, though exosporium fragments were generated (Johnson, Todd *et al.* 2006). The resulted *exsY* mutant spore coat is permeable to lysozyme (Johnson, Todd *et al.* 2006). Double *cotY* and *exsY* mutants of *B. cereus* spore produced the spores that were devoid of exosporium and resulted spores were permeable to lysozyme (Johnson, Todd *et al.* 2006). These exosporium defects suggest ExsY and CotY are required for the correct assembly of the exosporium of *B. anthracis* and *B. cereus* (Redmond, Baillie *et al.* 2004; Johnson, Todd *et al.* 2006). Up to now, three types of 3D structure of exosporium have been reported as well as the protein components like glycoprotein BclA with collagen-like domain and anchoring protein ExsFA and ExsFB (Sylvestre, Couture-Tosi *et al.* 2005; Kailas, Terry *et al*. 2011). *exsFA* and *bclA* mutants were found to produce the spores that were partially and totally devoid of filaments, and the crystalline basal layer was maintained although it appeared unstable (Sylvestre, Couture-Tosi *et al.* 2002; Sylvestre, Couture-Tosi *et al.* 2005). Considering the phenotype associated with inactivation of *exsF* and *cotY*, Kailas *et al*., speculated that ExsY and CotY could be candidates for the major components of the exosporium lattice (Kailas, Terry *et al.* 2011). In combination with high-resolution analysis of exosporium structure, tentative localizations of individual exosporium components were proposed (Kailas, Terry *et al.* 2011). Overall detail of the exosporium structure of *B. cereus* family and its relatively close family is critical to know how the individual components contribute to exosporium formation and integrity.

1.9 Electron microscopy in structural biology

Electron microscopy (EM) is a method using a transmission electron microscope to determine the arrangement of atoms in solids. The advantage of the EM over X-ray crystallography is that it allows studies of small crystals (< 0.1nm), such as membrane proteins, which are not easily assembled into the large 3D crystal required for crystallography and protein structures can be determined from 2D crystal. The electrons emitted by EM could be much more strongly scattered by sample and interact more strongly with atoms than X rays do. For thin 2D crystal samples, X-rays could not able to significantly diffract while electrons can form a micrograph. Conversely, EM enables the collection of both image and a diffraction pattern that provides direct access to the structure factor phase information. This is required to determine the 3D structure of a protein. Difficulties associated with using X-ray crystallography have made electron/cryo-electron microscopy a key technique in structural biology.

In order to improve contrast, negative staining of biology material was firstly used for the imaging of virus (Hall 1955). Staining is done by solutions of heavy metal salts that form a cast of the embedded sample. Heavy ions that surround the sample but excluded from the volume occupied by the sample interacts with electron beam. The deflection of the electron beam through protein is less than that through stain rich region, generating contrast in the image. However, the drawback of negative staining is the limit of the approximately 20 Å in optimal conditions. It also brings artefacts if the stain is uneven. Drying in the staining process may lead material to distortion (Unger 2000).

To minimise radiation damage for biological material and view material structure in a more native hydrated state, cryo-EM was introduced. The samples are studied at cryogenic temperatures (generally liquid nitrogen temperature), without being stained or fixed in any way, presenting them in their native environment. The resolution of cryo-EM maps can reach to near atomic, allowing novel insight into the structure of these large assemblies. Projection structure solved by cryo-EM can provide information and moreover, keep the native information of sample and more structural information in higher resolution such as the location of α-helices perpendicular to the crystal plane.

The first protein structure determined by electron crystallography at atomic resolution was done by Richard Henderson *et al* (Henderson, Baldwin *et al.* 1990). Before that, Henderson and Unwin had determined the first membrane protein structure at molecular

resolution 7Å, which presented its α-helices perpendicular to the crystal plane (Henderson 1975). Since then, electron microscopy related technique has been extensively applied to structural biology, several high resolution structures have been determined such as light-harvesting complex, nicotinic acetylcholine receptor (Kuhlbrandt, Wang *et al.* 1994).

1.10 Aims and objectives

Elucidating the molecular architecture and its structural dynamics is essential to understand the mechanisms of morphology, pathogenesis, environmental resistance, immune response, and provides the means to indentify the spore formation and its components attributes. Using a combination of electron crystallography and biochemical analysis to explore the structure and assembly of a selected number of protein components of *Bacillus* spore coat and exosporium, we aimed to understand how these various components determine function and architecture. This is part of a larger project to describe the structure and assembly of an entire bacterial spore. In the spores of *B. subtilis* and *B. cereus* family, spore coat or exosporium is interacting with the outer environment. The structure of spore coat and exosporium is closely associated with spore's resistance properties, adhesion, dispersal and dormancy, which have important implications for development of decontaminations protocols. Self-assembly is the autonomous building principle of individual or multi-components into ordered pattern of biomolecules with well-defined geometrical, physicochemical and functional surface properties. The ability of coat proteins self-assembly to achieve perfect positional control at the molecular level offers striking advantages in bio-nano manufacturing processes. Comprehensive understanding of spore coat proteins self-assembly may make *B. subtilis* a model to explore the role of self-assembly in cell differentiation.

The main technique to be employed is electron microscopy. Objectives for the project were:

(1) To screen a number of purified *Bacillus subtilis* coat proteins as targets for electron crystallography and single particle analysis.

(2) To do single particle analysis or crystallography of the most promising proteins emerging from the screen.

(3) To screen a number of *Bacillus* spores to find the most suitable for generating well-order exosporium samples for higher resolution cryo-electron microscopy (cryoEM).

CHAPTER 2

Materials and methods

2.1 Culture media, bacterial expression strains, plasmids and growth conditions in this study

2.1.1 Media for strain growth

Luria-Bertani (LB) / LB Agar (Miller 1972)

Bacto tryptone	10 g/l
Yeast extract	5 g/l
NaCl	10 g/l
*Bacto agar	15 g/l

*Bacto agar was only required for solid media preparation.

Prior to sterilization the pH was adjusted to 7.2 using 5 M NaOH.

2.1.2 Stock solution and buffers

$CaCl_2$ solution

60 mM $CaCl_2$

15% glycerol

10 mM PIPES [piperazine-N, N′-bis (2-hydroxypropanesulfonic acid)], pH 7

Solubilisation buffer

25 mM Tris-HCl, pH 8.0

150 mM NaCl

*8 M Urea

*Urea was used in denaturating conditions only.

Washing buffer

40 mM imidazole in solubilisation buffer

Elution buffers

0.1 M imidazole in solubilisation buffer

0.2 M imidazole in solubilisation buffer

0.3 M imidazole in solubilisation buffer

1.0 M imidazole in solubilisation buffer

SDS-PAGE resolving gel buffer (4x, pH 8.8)

1.5 M Tris-HCl

0.4% (w/v) SDS

The buffer pH was adjusted to pH 8.8 and stored at 4 °C.

SDS-PAGE stacking gel buffer (4x, pH 6.8)

0.5 M Tris-HCl

0.4% (w/v) SDS

The buffer pH was adjusted to pH 6.8 and stored at 4 °C.

SDS-PAGE running buffer (10x)

250 mM Tris-HCl

2 M Glycine

1% (w/v) SDS

The pH value of the solution was adjusted to 8.3 and was stored at 4 °C. The working buffer was diluted in deionised water (dH_2O) before use.

SDS-PAGE resolving gel (12%, 7 ml in total)

30% acrylamide/bis	2.8 ml
Resolving gel buffer (4x)	1.75 ml
Ammonium Persulfate (APs 10% m/v)	70 µl
TEMED (N, N, N', N'-tetramethylethylenediamine)	7 µl
dH_2O	2.45 ml

SDS-PAGE stacking gel (4%, 2 ml in total)

30% acrylamide/bis (Bio-Rad)	0.26 ml
Stacking gel buffer (4x)	0.5 ml
Ammonium Persulfate (APs, 10% m/v)	30 µl
TEMED (N, N, N', N'-tetramethylethylenediamine)	3 µl

dH_2O 1.04 ml

Coomassie Billiant Blue stain solution

0.1% (w/v) Coomassie® Brilliant Blue R250

30% (v/v) Methanol

10% (v/v) Acetic acid

dH_2O added to final volume

Destain solution

30% (v/v) Methanol

10% (v/v) Acetic acid

dH_2O added to final volume

All solutions and media used for microbiology experiments were sterilized by autoclave at 120°C (15 psi) for 20 min unless otherwise specified. Buffers were prepared in deionised water and stored at room temperature or 4°C.

2.2 Bacterial expression strains, plasmids, and growth conditions

2.2.1 *E. coli* BL21 (DE3) competent cell preparation

E. coli BL21 cells were streaked on LB agar plates and left to grow at 37°C overnight. Single colonies were inoculated into 5 ml LB media (the antibiotic added depended on resistance) and left at 37°C overnight. 2 ml of culture cells were transferred to 200ml LB media and allowed to grow at 37°C until the OD_{600} reached ~ 0.3. Cells were transferred to centrifuge tubes and cooled on ice for 20 min then centrifuged at 3000g and 4°C for 5 min. The cell pellet was resuspended in pre-chilled 10 ml 0.1 M $CaCl_2$ and left on ice for 30 min. Cells were centrifuged for 5 min at 3000g, and the cell pellet was resuspended in 10 ml pre-chilled $CaCl_2$ solution. Cells were transferred to pre-chilled and sterilized Eppendorf tubes in 100 µl aliquots. All tubes were immediately frozen in liquid nitrogen (LN_2) and stored in -70°C for subsequent use.

2.2.2 Transformation of competent cells with plasmid DNA of spore coat proteins

CotY, CotE and SpoVID expression plasmids were pET28a derivatives (Novagen). CotZ, SafA, CotH and CotV-CotW expression plasmids were pET-Duet derivatives.

The plasmids had been constructed and provided by Bratislava lab, Slovakia (Krajcikova, Lukacova *et al*. 2009).

Competent cells were thawed on ice and gently flicked to homogenize. 1 µl or less of plasmid DNA was added to the competent cells. Plasmid and cells were well mixed and left on ice for 30 min. Cells were heat-shocked at 42°C for about 60s. The tube was placed on ice again for 2 min. 800 µl of LB media was added to the cells and incubated at 220 rpm for 60 min at 37°C. 100 µl cells were transferred to LB agar plates containing the appropriate antibiotics (40 µg/ml kanamycin final concentration for the pET28a vector system). Cells were streaked on the plate and incubated at 37°C overnight and subsequently stored at 4°C.

All recombinant plasmids were transformed into *E. coli* BL21 (DE3). Cells carrying expression plasmids were incubated in LB media containing appropriate antibiotics. Transformed cells were then transferred to larger volumes of media e.g., 200 ml.

2.2.3 Bacterial growth conditions

For protein expression, *E. coli* BL 21 cells containing the plasmids were incubated at 37°C until they reached an OD_{600} ~ 0.6-0.8. The expression of recombinant proteins was induced by adding of IPTG (isopropyl-β-galactoside) to a final concentration of 1mM. The bacteria were incubated at 37°C for 3 hours and then harvested by centrifugation.

2.3 Purification of recombinant spore coat proteins

In our study, 50 ml of cells were induced. Cells were harvested and resuspended in 800 µl solubilisation buffer. Cells were lysed on ice by sonication in 100 sec burst time in total (10 sec bursts with 50 sec chilling period). The cell lysate was centrifuged for 45 min at 30,000 rpm in a Beckman OPTIMA MAX-E ultracentrifuge. The supernatant was loaded on a 1 ml HiTrap affinity column (GE Healthcare). After adsorption by the resin for 10 min, the column was washed with 9 ml of washing buffer and protein was eluted stepwise using 1 ml elution buffers containing 0.1, 0.2, 0.3 and 1 M imidazole in solubilisation buffer with or without urea respectively.

2.4 Protein analysis

2.4.1 Protein analysis by SDS-PAGE

Protein samples and Broad range protein markers (New England Biolabs) were loaded on a 4-12% SDS-PAGE precast gel. Samples were prepared according to the manufacturers instructions (Invitrogen™): with addition of NUPAGE® LDS Sample Buffer (4x) plus NuPAGE® Sample Reducing Agent (10x) (both from Invitrogen™). Mixed samples were heated at 99°C for 10 min and cooled to room temperature. The samples were run at 130 V for about 75 min in a Mini-PROTEAN Tetra Electrophoresis System (Bio-Rad) until the dye front reached the bottom of the gel. The gel was stained with Coomassie Brilliant Blue R250 stain solution and destained with destain solution.

2.4.2 Protein analysis by size exclusion chromatography

Gel filtration was performed on a Superose-6 column (GE healthcare) fitted to the fast protein liquid chromatography (FPLC) system (GE Healthcare). Solubilisation buffer was used as a running buffer. 0.5 ml of protein sample was injected into the loop and eluted at a flow rate of 0.2 ml/min. 0.5 ml fractions were collected. Standard molecular weight markers used for calibration were with thyroglobulin (669 kDa, elution volume is 12.8), apoferritin (443 kDa, elution volume is 14.5 ml), beta-amylase (200 kDa, elution volume is 15.5 ml), alcohol dehydrogenase (150 kDa, elution volume is 16.4 ml), albumin (66 kDa, elution volume is 17.0 ml) and carbonic anhydrase (29 kDa, elution volume is 18.4 ml). The void volume was calibrated by blue dextran at a volume of 7.4 ml (Fig 2.1). All the fractioned proteins were analysed by SDS-PAGE.

2.4.3 Protein concentration determination by BCA protein assay

The concentration of purified proteins was determined by using BCA™ reagent (PIERCE). Working Reagent (WR) was prepared by combining 50 parts of BCA reagent A with 1 part of BCA reagent B (50:1, Reagent A: B) and well mixed. 0.1 ml bovine serum albumin (BSA) and unknown protein samples were separately mixed with 2 ml WR into a labelled tube. All samples were incubated at 60°C for 30 min and cooled to room temperature. The spectrophotometer was blanked to zero with a cuvette that was filled only with water, the absorbance of all the samples were measured at 562 nm by Jenway 67 series UV/visible spectrophotometers. To minimize the error, all protein samples were measured twice and averaged. Protein concentration was estimated using BSA as a standard.

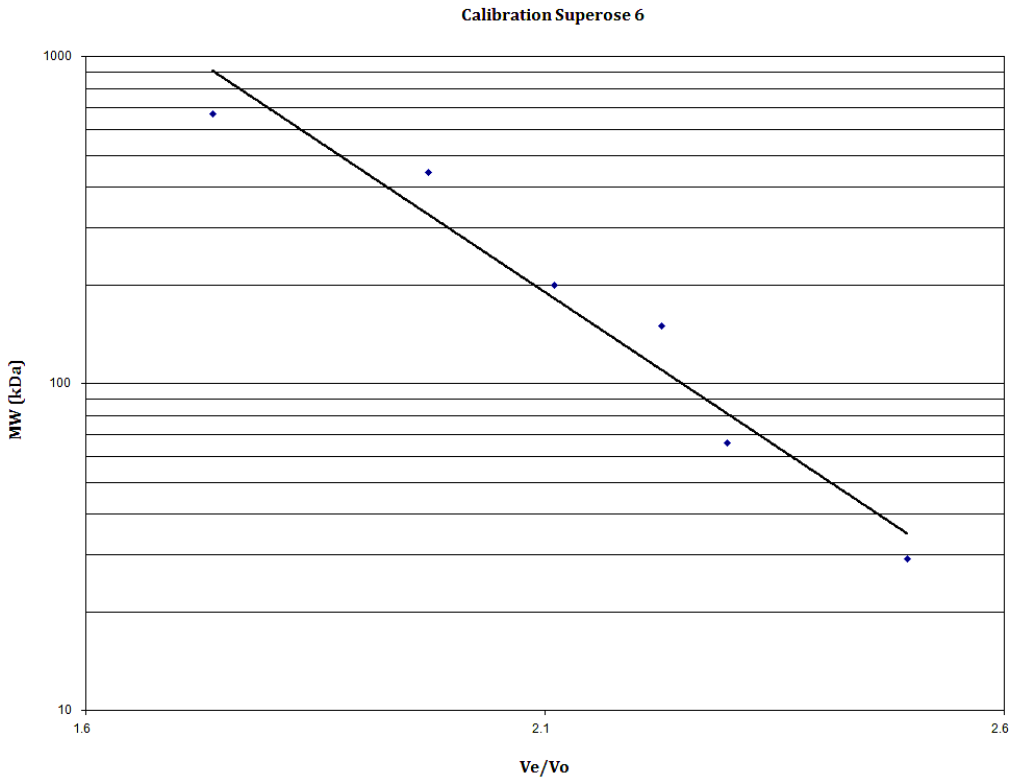

Fig 2.1 The Superose 6 column was calibrated with thyroglobulin (669 kDa), apoferritin (443 kDa), beta-amylase (200 kDa), alcohol dehydrogenase (150 kDa), albumin (66 kDa) and carbonic anhydrase (29 kDa). Molecular weight markers (marked by filled rectangles) were monitored by UV absorption. The void volume was calibrated by blue dextran.

2.4.4 Reducing agent disruption of CotY crystal

Freshly prepared CotY protein (see §2.3) was diluted in Solubilisation Buffer and mixed well with reducing agents 0.05 M DTT and/or then incubated in 99°C for 20 min. Samples were loaded on the grids and observed by TEM (see § 2.6.4).

2.5 Novel *Bacilli* spores for exosporium identification

15 *Bacilli* spores were provided by Adam Driks lab, Loyola University, USA. All the spore samples were kept in sterile water and stored at 4°C prior to use. The samples were periodically spun down every few days and resuspended in fresh water to inhibit germination due to liberated fragments of spore material that can act as germinants. The list of the strains is as below:

Strain number	Name
2214	*B. pumilus* SAFR-032 611
1852	*B. badius* BGSC #23A1
2216	*B. fusiformis* ATCC 7055
1836	*B. lentus* Gibson 165 BGSC #60A1
1346	*Paenibacillus alevei* 1113 DT-1A
1990	*B. vedderi* NRRL B23388
1979	*B. pseudomyciodes* NRRL B-617
1279	*B. megaterium* ATCC 12872
1992	*B. nianci* NRRL B23384
1983	*B. pycnus* NRRL NRS-1691
2211	*B. neidei* NRRL BD101
1130	*B. odysseyi*
1335	*B. circulans* 42G1
2221	*B. mycoides* ES-027
1350	*B. laterosporus* ATCC 64T

2.6 Preparation for transmission electron microscopy

2.6.1 Evaporating carbon onto a mica film

Carbon was evaporated from two sharpened rods (Agar Scientific) through which a high voltage was passed through in short pulses. The whole system was kept under a high vacuum at $1x10^{-4}$ to $1x10^{-5}$ mbar during this operation in a Cressington 208 Carbon Coater. Pulses were kept short by 5 sec as the evaporating carbon degenerated this

vacuum and this must be restabilised before continuing to avoid sparking. Carbon was deposited onto the newly exposed surface of a freshly split sheets of mica as a current was applied through the carbon rods. The intermittent pulses were repeated till the carbon film was about 150-200 Å thickness (thickness measured by a Cressington thickness monitor). The coated mica sheet was then stored in a Petri dish overnight for floating around 24h later.

2.6.2 Floating carbon film onto grids

3.05 mm square copper/palladium grids (Agar Scientific) were coated with the carbon film using a 1-litre tank filled to the brim with water. The carbon film was floated onto the water surface by lowering the mica into the tank at a 45° angle. The water was then siphoned off using a length of rubber tubing that previously had been wedged to the bottom of the tank. During the floating, the carbon film was kept in the right place above the well-arranged grids with the palladium side up using two pairs of tweezers. The coated grids were then stored in a Petri dish to air dry around 24h before use.

2.6.3 Preparation of uranyl formate solution for negative stain

When preparing stain solution it was always kept away from light as much as possible. Uranyl formate (Polysciences Inc) was weighed out to ~37.5 mg and dissolved in boiling distilled water along with an unridged magnetic stir rod in a beaker coated with foil. After 5 min stirring, small drops of 5 M NaOH were added to the solution until a slight colour change was observed. The solution was stirred for a further 2 min. The solution was drawn into 5 ml syringe and forced through a 0.2 µm Minisart® syringe filter unit (Sartorius Stedim Biotech) into a foil-wrapped falcon tube. The stain solution was stored at 4°C for no longer than 10 days.

2.6.4 Negative staining of samples

Carbon coated grids were glow discharged for 30-40 sec in air at $1x10^{-4}$ to $1x10^{-5}$ mbar in the Cressington 208 unit to create a hydrophilic surface in a reduced air environment. 5 µl of sample at a proper concentration was loaded onto the coated side of the grids and left for 1 min to adsorb. Excess sample was blotted using Whatman filter paper and then the grid was quickly washed in one drop of distilled water and blotted again; this was repeated. Grids were finally twice washed in a drop of uranyl formate, blotted, and

waiting 20s before the final blot. Remaining moisture was removed by a small vacuum pump.

2.6.5 Preparation of spore exosporium fragments

Spore samples were diluted to 10 mg/ml by dH_2O. Spores were sonicated on ice for 5-10 sec at amplitude of 10 microns using a MSE Soniprep 150 sonicator. The fragmented spores were loaded on grids (see §2.6.4) and observed by TEM.

2.6.6 Specimen preparation for Cryo-EM

Molybdenum/copper grids (Agar scientific) were glow discharged for 30-40 sec. 5 µl of exosporium suspension was loaded on the grids using an automated Vitrobot plunge-freezing system (FEI Company) and incubated for 30 sec. The working chamber was continuously kept at over 75% humidity to prevent evaporation of the specimen. Grids were plunged into liquid ethane (cooled by LN_2). Blot offset distance was set to -2 mm, blot time to 6-8 sec. Grids were transferred rapidly to LN_2 to protect from ice build-up and placed in a grid holder. The ice-embedded samples were stored in a LN_2-filled Dewar flask before use.

2.7 Electron Microscopy

2.7.1 TEM identification of negatively stained samples

All negatively stained samples including protein samples and spore/exopsorium samples were examined and photographed using a Philips CM100 transmission electron microscope (TEM) at an accelerating voltage of 100 kV. Negatively stained micrographs were typically recorded under Bright field mode at 52,000 x nominal magnification and recorded at a underfocus value around 3000-5000 Å. Digital micrographs were collected at size 1024 x 1024 pixels by Gatan Multiscan 794 CCD camera and initially viewed using Gatan Digital Micrograph (DM, Gatan Inc).

Series of images from specimens tilted by 10 degree steps through a range of up to -55 to 50 degree were also recorded on isolated, large crystal sheets situated in the middle of a grid. For CotY, 113 tilted images in 8 series were collected. All images were recorded at a magnification of ~ 46, 000 x with underfocus value around 3000-5000 Å.

2.7.2 Cryo-EM identification of crystals

Exosporium fragments were embedded in vitreous ice. The evening before the cryo-EM session, the room dehumidifier was set to 20% relative humidity (RH), the cooling water chiller to 17°C and air conditioner to 24°C to help minimise stage drift and ice build-up. The cryostage Dewar flask was evacuated on an Edwards Turbo pumping station overnight prior to cryo-EM session. An Oxford CT3500 cryostage (Oxford Instruments) was transferred to an Oxford loading station consisting of an insulated bath to allow the grid holder to be inserted and grids loaded. Once the specimen holder was inserted, liquid nitrogen was poured into bath and all accessories such as tweezers and screwdriver were pre-cooled. Ice-embedded grids were properly transferred to the cryoholder. The insulated bath was intermittently refilled with LN_2 to maintain vaporization. The clip ring was screwed on the top of grids to secure the sample in place. The sliding cover was slid over the grid to protect it from ice build-up. The cryoholder was drawn from bath and quickly inserted to the CM200 FEG EM. Once inserted, refilled LN_2 to the dewar on the top of the cryostage. The EM was left for 1-2 h for thermal stabilization. Just before starting data collection, set the objective lens water flow to 20 l/h. Images were recorded in Low Dose Bright Field Mode: SEARCH mode was set to a low magnification of 580 x in SEARCH. Aligned beam by adjusting C2 aperture size, usually position 3, which is a 100-micron aperture, spot size was set at "1" (brightest) in EXPOSURE Mode. The objective lens aperture size of 40 microns was inserted. Adjusted beam shift to 2.5 μm and rotation to 0°. Adjusted for FOCUS S2 using rotation of 180° resulting in S1 and S2 positions being 180° to each other and separated by 5 μm. The best specimen area of the grid for imaging was identified at low magnification 770 x in SEARCH mode. Selected S1, set focus level and magnification 100 kx for imaging. Selected and set in S2, reset focus to mean value of S1 and S2. Reset defocus to zero and chose an appropriate defocus value, typically -700 nm for crystal imaging. Films were exposed for 1 sec and a nominal magnification of 50,000 x in EXPOSURE. Images were recorded on Kodak® electron image film SO-163 (Eastman Kodak Company).

All developer and fixer solutions for development were freshly prepared. Films were immersed into D-19 developer solution (Kodak) for 12 min and then rinsed in water. The films were transferred from the water and submerged into fixer solution (ILFORD

HYPAM) for 5 min. Finally the films were rinsed with running water for 30 min and then left to air dry overnight at room temperature.

2.7.3 Preliminary assessment of crystal quality and film scanning

The quality of the crystals was preliminarily evaluated by diffraction identification before film scanning. Films were place on the Optical Diffractometer and optical diffraction for each film was inspected. Films that showed great crystallinity were selected and scanned with a Zeiss SCAI Scanner. Grey scale level with 8-bit depth in Scan mode was set prior to scanning. Low resolution of 112 μm/px was used for initial test scan to determine the best specimen area. The resolution was set to 7μm/px for the final scan. The films were digitised and converted to optical densities. The pixel size on the sample level is 1.46444 Å. All micrographs were converted to ".tif" format files for data processing.

2.8 Image processing

2.8.1 Single particle analysis

Image analysis was carried out within the IMAGIC5 programme suite (Image science software (Vanheel and Keegstra 1981; van Heel, Harauz *et al.* 1996; van Heel, Gowen *et al.* 2000). All the micrographs were converted to IMAGIC format using a program em2em from the IMAGIC software package. Particle views for image processing were selected from individual micrographs manually and the corresponding co-ordinates were stored in a ".plt" file. In order to improve the quality of the dataset, views of particles close to the edges of the micrographs, as well as the particularly noisy views were excluded, and then the views were normalised. For CotY and SafA data processing, 80 x 80 pixel boxes were extracted, centred on the picked particles; this was about three times the particle diameter. "Bad" particle images could be located via their coordinates stored in the .plt file and removed from particle galleries. To determine the centre of mass of an image and obtain a good centring of relatively globular particles, the normalized images were iteratively centred. The cut particles were aligned to a reference file obtained from the total average normalized inside a circular mask, followed by band-pass filtering. Low and high spatial frequencies of images, especially the low spatial frequencies can disturb the result of the alignment and classification

processing procedures. To remove unwanted spatial frequencies, image filtering (band pass filter) was used to reduce the influence of high and/or low spatial frequency information on the alignment. The low frequency cut-off value was calculated by: = 2 x pixel size / particle size. The high frequency cut-off value calculated by: = 2 x pixel size / expected resolution.

Brieflya Gaussian shaped soft-edge mask was used to suppress certain frequency ranges in Fourier transform of the images. The edge of the transform corresponds to the maximum spatial frequency and the centre of the transform is zero. The value is a fraction between 0 and 1. The filtered transforms were then converted back into real space by Fourier transform.

The total average after the first alignment was used for the next round of processing. At this step, the first set of various typical molecular views was obtained. Iterated cycles of averaging and direct alignment identical to the procedure described above were repeated four or five times to get precisely aligned images of single particles for multivariate statistical analysis (MSA). MSA procedure was then used to find images in similar rotational orientations from the whole set of particle images. A MSA mask was created to define the particle area important for analysis. The MSA was applied to masked and aligned images. All images were assigned to the different classes in the classification step. Particles in each class were summed and averaged. The resulting class averages contained similar images in similar orientations. The number of classes were minimised by combining some classes with the same view where possible. For CotY single particle analysis, we initially used 10 classes and reduced to 7 and for SafA we started with 50 and reduced them to 6 classes. The good and characteristic classes were selected out and these were used as references after band-pass filtering. A multi-reference alignment (MRA) procedure was used to align the dataset with respect to reference images. An iterative procedure of MSA, classification and MRA was adopted, whereby selective image averages produced by classification in respective iterations were used as reference images for the subsequent alignment of the whole dataset until stable results were obtained. For CotY and SafA single particle analysis, after 5 cycles of alignment the alignments converged to the final averages.

2.8.2 Computer processing of negatively stained crystal images

Negatively stained crystal images were collected on a CM100 TEM (see §2.7) at size 1024 x 1024 pixels. The crystal images were processed within the *2dx* suite of programs based on the MRC electron crystallography software suite (Henderson, Baldwin *et al.* 1986; Crowther, Henderson *et al*. 1996; Gipson, Zeng *et al*. 2007; Gipson, Zeng *et al.* 2007). *2dx_image* has a high degree of flexibility, customizability and automation, and incorporates programs of the MRC package software. It streamlines the processing procedure of electron microscopy data by providing a friendly graphic user interface. The workflow diagram of the steps involved in image processing of for 2D crystals using the MRC suite of programs is shown in Fig 2.2.

The negatively stained crystal images were recorded in .dm3 format; these were then converted into .tif files with Gatan Digital Micrograph. An individual folder was created for each image since each image should be processed in its own directory in which all image files, parameter files and output files are stored. Initialization was done by *2dx_initialize* script. The nominal magnification (usually 52,000 x) of the microscope measured between sample and image record medium, pixel size on the recording medium, upper resolution limit (20 Å for negatively stained image), Cs (spherical aberration constant of the objective lens in mm, 3.6 for the CM100 microscope and 2 for the CM200 microscope) and high tension (100 kV for CM100 and 200 kV for CM200 microscope) were entered. For images of untilted crystals, tilt geometry determination was disabled while it was enabled for the processing of tilted images.

The fast Fourier transform (FFT) is essentially a computed diffraction pattern of the image in which all the periodic information is stored in discrete diffraction spots, thus allowing determination of the reciprocal lattice, defocus value etc. A FFT of the raw crystal image was generated by executing script *2dx_fftrans*. A couple of programs underlying the *2dx_fftrans* executed their function, like HISTO to produce a histogram of the grey value in the image to detect any pixels with very high or low optical densities (OD) compared to the bulk of the pixels in the rest of image, which can be used to eliminate extreme densities caused by dust particles and scratches both of which would only add to the noise of the image. LABEL was used to down-sample the image by a factor of 2. FFTRANS was used to calculate the Fourier transform of image.

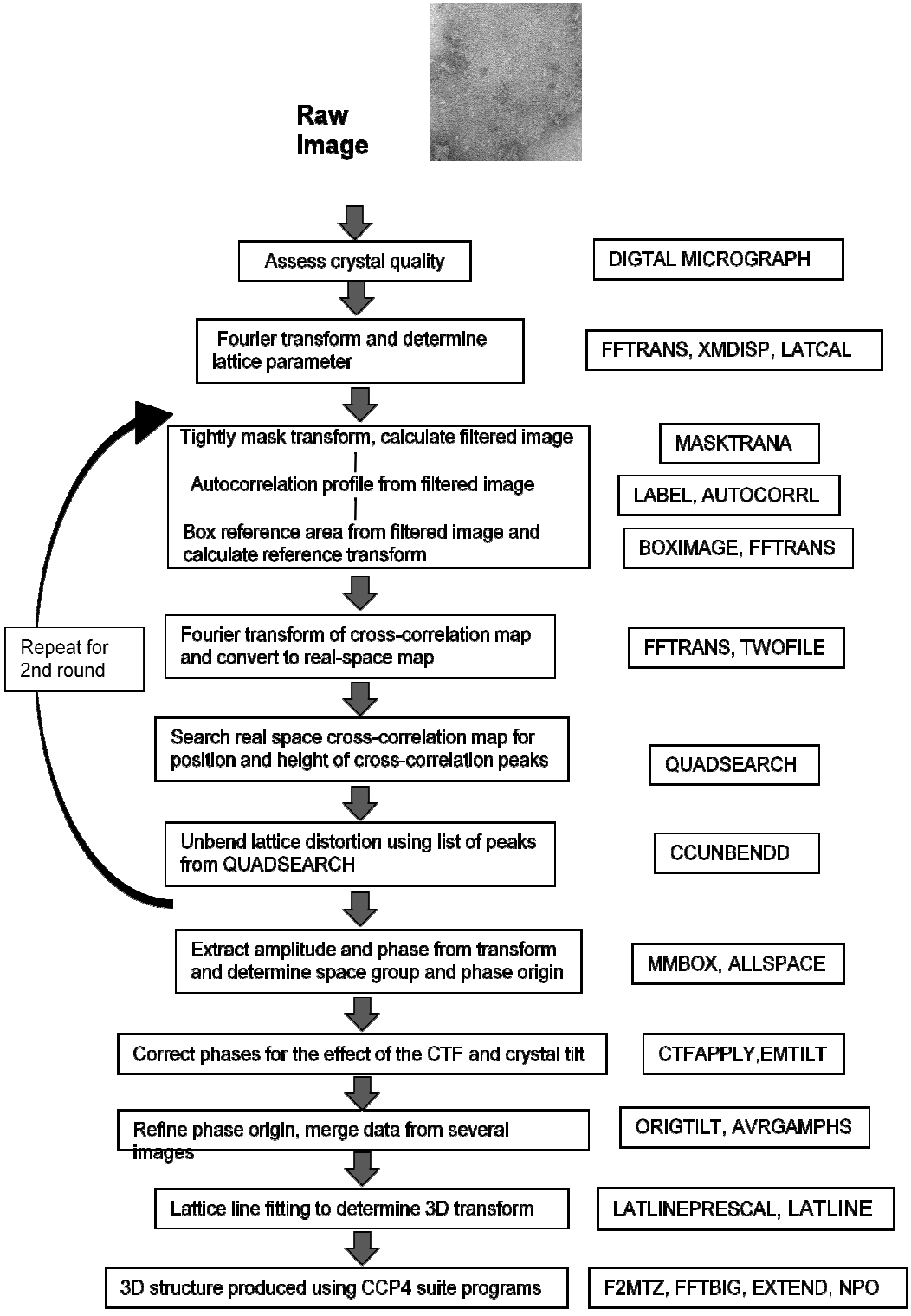

Fig 2.2. Flow diagram for initial 3D-processing steps using the MRC suite of programs (Crowther *et* al., 1996, Henderson *et al*., 1986). Right panels show the corresponding programs involved in processing steps.

To determine the defocus value and astigmatism, the *2dx_getDefocusTilt* script was executed. CTFTILT determines defocus, astigmatism, tilt axis and tilt angle for images of arbitrary size (MRC format). The astigmatic angle is measured from the x axis (same conventions as in the MRC 2D image processing programs). The defocus value was manually adjusted, if necessary, by visual inspection of the Thon rings on FFT image. The *2dx_getLattice* script was run to automatically determine the spot lattice and tilt geometry for tilted images. XIMDISP was called by *2dx_image* to manually do indexing and lattice refinement. To check that most of the spots fall on their predicted positions, if necessary, the spot lattice could be reindexed by visual inspection and refined in lattice refinement mode, which could be accessed via the navigator pull-down menu. When the spot selection and refinement were completed, the spotlist and lattice vectors were saved. For the geometry determination of tilted images, the tilt geometry is defined by five variables:

1. TLTAXIS: defines the angle from X-axis toward the tilt-axis in the image as displayed on the computer screen. The value is given in degree and counted in the mathematically positive sense, meaning that counter-clock wise is positive. TLTAXIS has nothing to do with the 2D crystal.
2. TLTANG: defines the tilt angle of the sample in the microscope. Also this value is valid for the sample support and has nothing to do with the crystal.
3. TLTAXA: defines the angle from the tilt-axis to A^* of the 2D crystal. A^* is the first lattice vector in the real-space image, in degrees. It defines how the 2D crystal lies on the carbon film with respect to the coordinate system.
4. TAXA: defines the angle from tilt-axis to A^* axis of the 2D crystal. TAXA is quite similar to TLTAXA, but usually larger or equal to TLTAXA since TLTAXA is the projection of the TAXA, in grad.
5. TANGL: defines the tilt angle from the point of view of the 2D crystal.

Variation in the lattice parameters of the tilted crystal can be determined the tilt geometry only for large tilt angles, e.g. larger than 30 degrees. EMTILT was used to compare the tilted lattice with that of untilted specimens and hence works best for higher tilt angles (Shaw and Hills 1981). For smaller tilt angles, the method is not sensitive enough, CTFTILT was used to determine defocus gradient for small tilt values.

Prior to unit cell vector calculation, 2dx_refineLattice was run to refine previous resulting parameter including defocus refine, tilt geometry refine (only in tilted image processing) and so on. 2dx_evaluateLattice was run to calculate the unit cell dimension of the crystal. LATCAL was used to determine the real-space dimensions of the vectors that describe the unit cell of the protein crystal. A spot list file was created listing all Miller *h,k* indices for all visible reflections in the Fourier transform.

In the next procedure, a filtered image will be calculated. 2dx_getspots allowed the program MMBOX to get the spot list recording a list of indexed amplitudes and phases at the predicted diffraction spots on the FFT of the image for unbending processing. MASKTRANA was used to filter the Fourier transform by placing maskhole radius of 5 pixels around the diffraction spots and the inverse transformation by FFTRANS yields a filtered image showing the object much more clearly. A small area of 26 x 26 pixels was cut from the filtered image by LABEL. The Fourier transform of the original image and this small reference area are required to form the cross-correlation function by inverse Fourier transformation. This small area was over sampled by 20 times and auto-correlated by AUTOCORRL. An area 100 x 100 pixels was cut from the output autocorrelation map and used as a reference correlation peak then.

An area of 300 x 300 pixels from the centre of crystal was boxed out from the central area of the noise-filtered image that was assumed to be the best crystalline area was boxed out by using BOXIMAGE, and a Fourier transform was calculated by FFTRANS. This area of the crystal was correlated against the rest of the image to define the lattice distortion. This was done in reciprocal space by TWOFILE by multiplying the Fourier transform of the whole filtered image with conjugate of the transform of the 300 x 300 pixels reference area. An output Fourier transform was given. A cross-correlation map describing the lattice disorder in real space was produced by calculating a reverse output Fourier transform. Real space images were used to search the cross correlation map for the position and height of cross-correlation peaks and compared to the reference peak to determine the overall quality of the peak (the 100 x 100 pixels area from the output antocorrelation map). This is done by QUADSEARCHB with a searching radius of 6 pixels from each peak position. CCUNBENDE then used the data from QUADSEARCHB to correct lattice distortions in the raw image by unbending. The unbending correction was applied to the original image to create a corrected Fourier

transform (FFTRANS) and the quality of each spot calculated by MMBOX. In *2dx_image*, unbending was executed in "Unbend I", and then to checked vector plot for distortion and the quality value. The concept of IQ-values was introduced by R. Henderson (Henderson *et al.,* 1986) to describe the intensity ratio between reciprocal spot and background. IQ value ranges from 1-9, with 1 being the best value for its signal to noise ratio of ≥ 7:1 compared to the background. IQ2-1Q8 has signal to noise ratio of 7/IQ grade, so IQ7 has a signal equivalent to the background noise. IQ 8 above background by an amount of signal less than background. IQ9 is less than background.

The second cycle of unbending (Unbend II in *2dx_image*) was required to calculate a highly averaged image using the corrected Fourier transform from the first round giving high signal: noise ratio. A very tight maskhole radius of 1 pixel was used to mask the spots by MASKTRANA, which produced a highly filtered image. The smaller the maskhole radius, the "nicer" the image look since decreasing the radius excludes information about the lattice distortions. The process of preparing a reference peak profile was the same as we did in the first round of unbending except a smaller reference area of 200 x 200 pixels was used to follow the finer details of distortions in the image. All other processing procedures were repeated as in the first round of unbending.

To correct the contrast at all spatial frequencies, a CTF correction procedure was done by running 2dx_applyCTF. CTF correction was applied to modulate the scattered waves by objective lens, which results in periodical contrast reversals across the image. For the individual micrograph we collected, the defocus amount was different; the phase must be corrected to allow the combination of data from several images. Each crystal was then tested against each of the seventeen known 2D crystal and calculated the internal phase residuals for all space group (Holser 1958; Valpuesta, Carrascosa *et al.* 1994).

Plane group symmetry was determined in script 2dx_allspace along with the respective phase origin (Holser 1958; Valpuesta, Carrascosa *et al.* 1994). The most likely plane groups were determined by comparing the phases output after the image unbending by ALLSPACE. The averaged internal phase residual was compared with theoretical phase residual in all 17 plane groups. The most suitable symmetry was then applied to the crystal image to generate the symmetrised grey-level map and density map.

The final step of image processing was to calculate a 2D projection map for the unit cell of individual crystal. 2dx_generateMap was executed and underlying programme ORIGTILT applied the appropriate symmetry and phase shift for each image (Amos, Henderson *et al.* 1982; Henderson, Baldwin *et al*. 1986). Symmetrised image was calculated in Generate SymMap step.

2.8.3 Merging of images from tilted negatively stained specimens

All images were 1024 x 1024 pixels. Individually untilted and tilted images were processed using *2dx_image*. The amplitude and phase (.aph) data derived from individual image by *2dx_image* was contrast transfer function (CTF) corrected and generated lattice line data to yield HKL file (L is 0 in 2D data). The aph was extracted and stored in a directory. 5-7 series of the best crystal images were selected for merging with the MRC programme ORIGTILTK. A UNIX script containing a call to ORIGTILTK was created, to which all required parameters were added and performed the merging of the data. The ORIGTILTK was properly set up with corresponding parameter, such as title, imgdir that contains the HKL file, voltage of beam, spherical aberration, resolution, output file etc. In a first phase origin search we used a coarse step size of 6 degrees with 60 steps. Merging started with images from untilted crystals. The first image used as a reference was the best one judged by its projection map, FFT and processing statistics. This image was set to the correct phase origin and all subsequent images were merged and refined sequentially using this starting reference, exploring phase space in 6.0° steps. The merging of tilted images to the dataset established by untilted images was also accomplished by using the ORIGTILTK programme. Images from low angle tilts were initially merged to dataset, followed by higher tilts. For tilted images merging, except for the general setting as in untilted images merging, additional parameter was required. An estimation of TAXA, an angle value which defines the angle from the tilt axis to a^*-axis of the 2D crystal when measured on the carbon film was required. Tilt angle in degrees defining the tilt angle of the sample in the TEM during data collection was needed as well. TLTAXA that defines how the 2D CotY crystal lies on the carbon film; TLTAXA which is the projection of the TAXA that defines the angle from the tilt axis to A-star axis of the 2D crystal; TANGL defines the tilt angle; TAXA and TANGL are for the 3D reconstruction, and display on the final map. These tilt geometry values were collected from *2dx_image* processing dataset after running standard script Evaluate

Lattice. All the geometry information including TAXA, TANGL, Real space lattice in pixels and phase origin were extracted for 3D merging.

For symmetry *p*6, which has intrinsic twofold symmetry, all phases would be expected to adopt 0° or 180°. That means the unit cell are related by a 180° rotation, while *p*3 is different that has no twofold symmetry and need to be checked by comparing the phase residual value with or without rotation or reverse HK. REVHK and ROT180 were used to investigate and compensate for disagreements caused by inconsistent indexing thus repeat for all non-tilted images with respect to changing ROT180 and REVHK to obtain the optimal phase residual. *h* and *k* indices of reflections were interchanged on input to "flip" the image "upside down" by switching between 0 or 1 on the script. Rotating 180 degrees about Z-axis is useful in *p*1 and *p*3 symmetry where the phases of the Friedel mates are related by $\varphi(h,k,l) = -\varphi(-h,-k,-l)$. Four possible combinations of REVHK and ROT180 input were tested by changing from command (0, 0), (0, 1), (1, 1), (1, 0) and the one resulting minimum phase residual was preferably used.

Moreover, the z*-cutoff value which represents the coordinate along the section perpendicular to the plane of the crystal was determined from the merged amplitude and the phase (Amos, Henderson *et al.* 1982). The Δz^* was limit for including observed reflections for direct comparison of phases. The value of $\Delta z^* = 1/$ (3 x thickness) of crystal. The common phase origin was found by comparing the phases of the reflections on each image within a Δz^* of 0.003 $Å^{-1}$ to those of all the other CotY images.

The absolute hand of the structure needed to be determined before the structure calculation. The absolute hand is to ensure the tilt angle of tilted view is recorded with the correct sign (Amos, Henderson *et al.* 1982). The predicted absolute hand of the tilted crystal in the image would be roughly determined by checking phase granularity on FT of the each tilted image from one series in Digital Micrograph. In FT images of four corners of micrograph that also were the rims of specimen, the difference of defocus value on the four corners helped determine the orientation of the specimen. A suitable diffraction spot from the crystal that was clearly not along the tilt axis was chosen. The z* value for the spot selected was determined from the merged amplitudes and phases by using the definition of axial direction. The z* value of selected spot was determined. Along the tilt axis, the lower end in microscope appears to be more

underdefocused whose z* value is positive +ve, and negative z* value -ve in higher end of specimen. The absolute hand of the structure was correctly confirmed as the sign of the z* value is the same as that for the side of CTF plot where the spot situated (Fig 2.3B)

It is easier to add the image one by one upon inspecting a phase residual in an initially created log file. The log file also output a cross-correlation map that is plotted through a matrix where each entry represents the normalized cross-correlation value between the refined images and the reference. It contains a clear peak, which is indicated by the largest number. A new phase origin for each alignment was generated. Replace the phase origin with one copied from the output log file. Phase residual defines the correlation between the newly added image and the established image database before the new image addition. When the new addition fits well with the database, the phase residual is pretty low. In our merging, the phase residual below 30 was acceptable. The phase origin change should decrease with each iteration and ideally end up being zero. 5-8 series of crystal images were merged by adding tilt data of increasing tilt angle to the previously merged images up to a highest tilt data of +/- 55 degree. Up to this stage, all the images were merged and several output files appeared such as lattice line file which consists of already known reflections with the index.

The merged amplitudes and phases were used to determine interpolated amplitudes and phases due to its irregular sampling in reciprocal space in the z* direction. The merged amplitudes were CTF corrected and the intensity values coming from the same micrograph were scaled by the program LATLINEPRESCAL. Before the dataset can be sampled, the lattice lines have to be fitted along z*. LATLINE program (Agard 1983). A plot of the variation of contrast along z^* axis was generated. The z* sampling interval was set for plotting purpose. The sampling interval for the discretization is calculated from the thickness of the crystal. A small number should be used for a smooth looking lattice line. An estimated real-space envelope of the protein was applied as a constraint. For CotY, the sample interval is set to 1/300 $Å^{-1}$. Weighting of the amplitudes and phases for representative lattice line, showing the experimental data and curves with error bars that set by using a $1/\sigma^2$ where σ is an associated error estimation to each

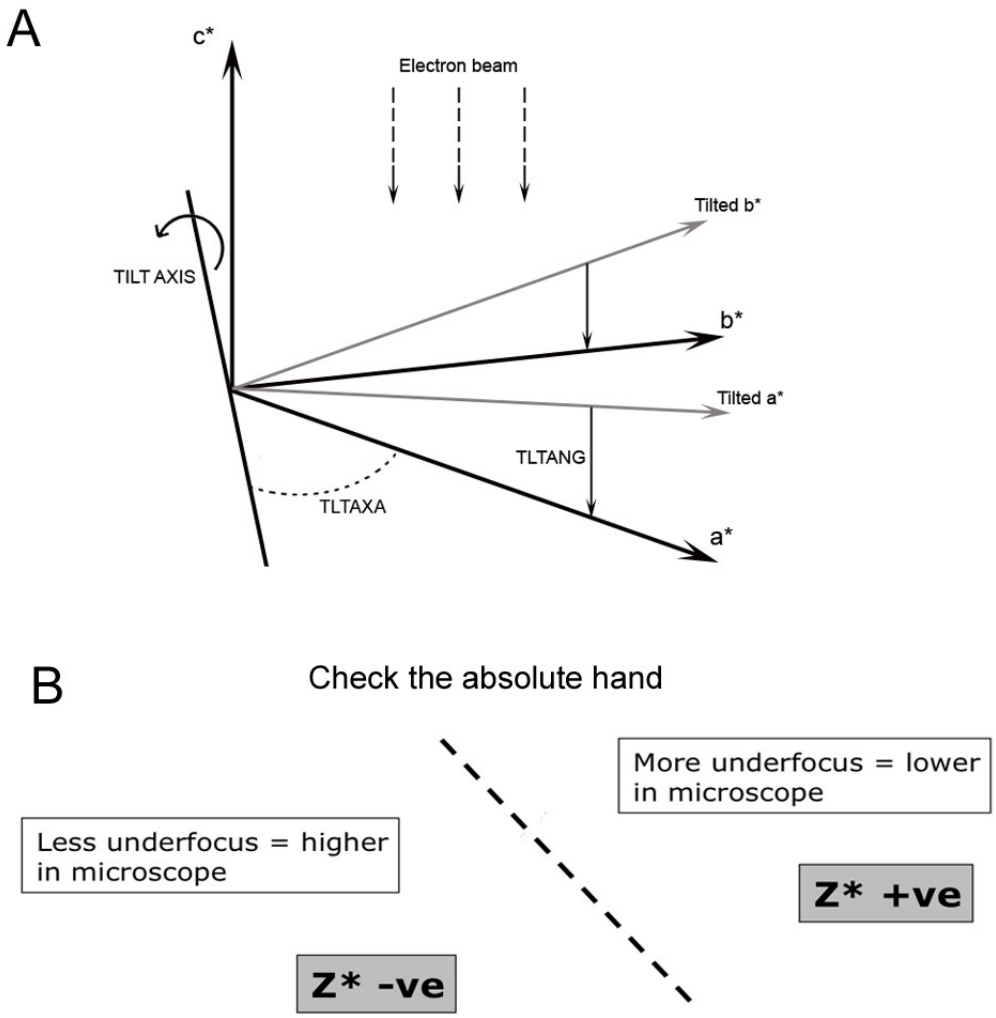

Fig 2.3 (A) A schematic diagram showing the transform of a two-dimensional crystal. It takes the form of a number of lattice lines extending perpendicular to the plane of the crystal. Each micrograph contains an image which, when Fourier transformed, gives the value of amplitudes and phase at points along the lattice line where the central section (perpendicular to the viewing direction) intersects them (Figure from Amos, Henderson *et al*. 1982). (B) A schematic diagram showing absolute hand of tilted crystal in the image. Along the tilt axis, the lower end in microscope appears to be more underdefocused whose z* value is positive +ve, and negative z* value -ve in higher end of specimen.

reflection. σ for amplitudes was the root mean square of the local background and phase error for the phases σ (Agard 1983). The output interpolated lattice lines were converted into an MTZ file by F2MTZ so as to be put into CCP4 programmes (CCP4 1994). CCP4 suite programmes were used to build up a 3D map of crystal with symmetry being applied. The resolution was set from 200-16 Å for the negatively stained image. EXTEND was used to extend the map, NPO to create a contour plot, PLOT to create a post file of contour plot (Smith 1999). The resulting map could be examined in Chimera software. Threshold levels for surface contouring were adjusted to a level so as to indicate continuous connectivity of density throughout the 3D volume.

2.8.4 0, 0, *l* estimation and refinement

Each recorded image produces a set of amplitude and phase with the coordinates (h, k, z*). The next procedure is to densely sample the lattice lines by incorporating as much data as possible with varying orientation and tilt angle, but due to instrumental restrictions of the microscope, we are unable to record an images of tilted higher than ± 60° in our device. However, ideally tilt data collected up to ± 60° would cover 87% of reciprocal space, and for ± 70° it is 94% (Amos, Henderson *et al*. 1982). So there will always be no intensities measured within a missing cone including along the 0, 0, l lattice line. One solution to estimate the 0, 0, l structure factors is to find an image of a folded crystal that gives a side view projected parallel to the crystal plane. The side view from the crystal can be cut out and processed as previously described and a FFT image was calculated. It is possible to roughly calculate the distance in the L direction from the FFT of cut image. Briefly, from the same crystal image, a square section of crystal image from a different area without side view was cut out and a FFT image calculated. The discrete spots of two cut images were compared with each other to help determine the 1, 0 and 0, 1 spot sites. The co-ordinates of 1, 0 spot measured from crystal lattice FFT image by DM, and in combination of the distance for 1, 0 spot Fourier space were input into MMBOX to gain an amplitude and phase for the 1, 0 spot. One unit cell length on X or Y direction could be calculated as well as length in reciprocal space on L direction. The pixel size of in the L direction could be calculated by using the initial plots. The ration of X to L and the reciprocal value of two directions could be used to calculate the value for the L direction. All other 0, 0, *l* was processed in the same way and input to MMBOX to calculate the specific amplitude and phase for

each 0, 0, *l* spot. The output new amplitudes and phases were then integrated into existing amplitude and phase file that was initially generated. The new amplitude and phase file was used to calculate the data point for h, k index in z* direction and these datasets were then used to refine the 3D reconstruction and optimize the initially constructed 3D model. In this thesis, Amplitudes and phases for 0, 0, *l* were estimated from a plot of contrast variation along Z (P. Bullough, personal communication)

2.8.5 Merging of untilted cryo-EM images

Cryo-EM images were taken by film, scanned and digitised as previously described. Cryo-EM crystal images were also processed using 2dx_image. Some parameters such as magnification, pixel size, resolution limit, Cs value and high tension of TEM were changed to correspond to the CM200 TEM settings. The rest of the parameters and processing were similar to those used in negatively stained crystal image processing. 3-5 of the best untilted cryo-images (~11000 by 14000 pixels) were individually processed by 2dx_image. ORIGTILTK was used to merge all untilted cryo-images and the following procedures are similar to that applied to negatively stained images merging. Prior to the completed merging of data from the untilted image, it was necessary to determine a temperature factor by scaling against the reference amplitudes from bacteriorhodopsin (Havelka, Henderson *et al*. 1995). Resolution-dependent factors such as image blurring, intrinsic disorder of the crystal and lack of flatness of specimen, cause the image amplitudes to get weaker (Havelka, Henderson *et al*. 1995). SCALIMAMP3D was carried out to correct the image amplitudes for unstained samples at high resolution. The merging map was eventually calculated by CCP4 suite programs.

CHAPTER 3

Characterisation of self-assembly properties of heterologously expressed *Bacillus subtilis* spore coat and *Bacillus cereus* exosporium proteins

3.1 Introduction

In this chapter, we examine the self-assembly properties of some spore coat proteins by electron microscopy. These proteins were successfully purified with good yield and isolated by gel filtration prior to EM observation. The results reached with the self-assembly properties allowed us to propose a new scheme of spore coat protein assembly.

3.2 CotY

3.2.1 CotY purification

The CotY expression plasmid is a pET28a derivatives. All the expression plasmids described in this chapter have been constructed and provided by Dr. Daniela Krajchikova, Slovak Academy of Sciences, Bratislava. N-terminal His-tagged CotY (predicted MW of 17.9 kDa) was overexpressed and purified in a buffer containing 8 M urea by nickel affinity chromatography and eluted stepwise using a buffer containing increasing concentration of imidazole (0.1, 0.2, 0.3 and 1 M). CotY was mostly expressed mostly as an insoluble protein. The fractions were analysed by 4-12% SDS-PAGE (Fig 3.1). A high yield of CotY in high purity was obtained. As previously described, CotY migration on SDS-PAGE was aberrant, with an apparent MW of 28 kDa instead of the 17.9 kDa expected.

3.2.2 Analysis of CotY by size exclusion chromatography (SEC)

CotY protein collected from 0.3 M imidazole fraction was further separated on a Superose-6 column using solubilization buffer containing 8 M urea as a running buffer. The elution profile revealed three major peaks (Fig 3.2). Peak a was eluted within the void volume of the column. The very broad peak b eluted with an elution time corresponding to an apparent MW of 340 kDa. The smallest peak c was eluted with an apparent molecular weight of 115 kDa (approximately equivalent to a putative hexamer of CotY). The eluted fractions were picked up and then analysed by SDS-PAGE (Fig 3.2b). The fractions collected from peak a were loaded in lanes 2-4. Lanes 5-15 showed

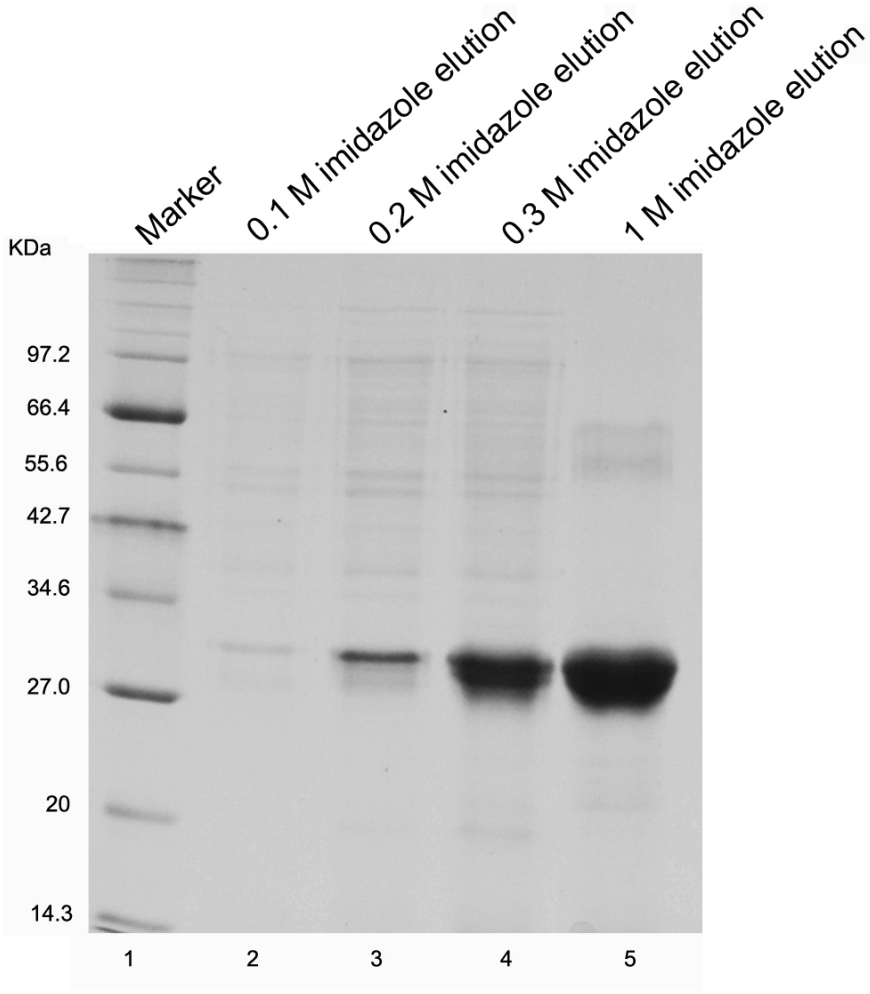

Fig 3.1 Purification of *B. subtilis* coat proteins CotY under denaturating conditions (8 M urea). Eluted proteins were resolved by 4-12% SDS-PAGE. The gel was stained with Coomassie brilliant blue. Lane 1 shows the protein marker. The target proteins were eluted with a stepwise of 0.1 M, 0.2 M, 0.3 M, 1 M imidazole (Lanes 2-5) respectively. The molecular weights of standard markers (in kDa) are indicated on the left.

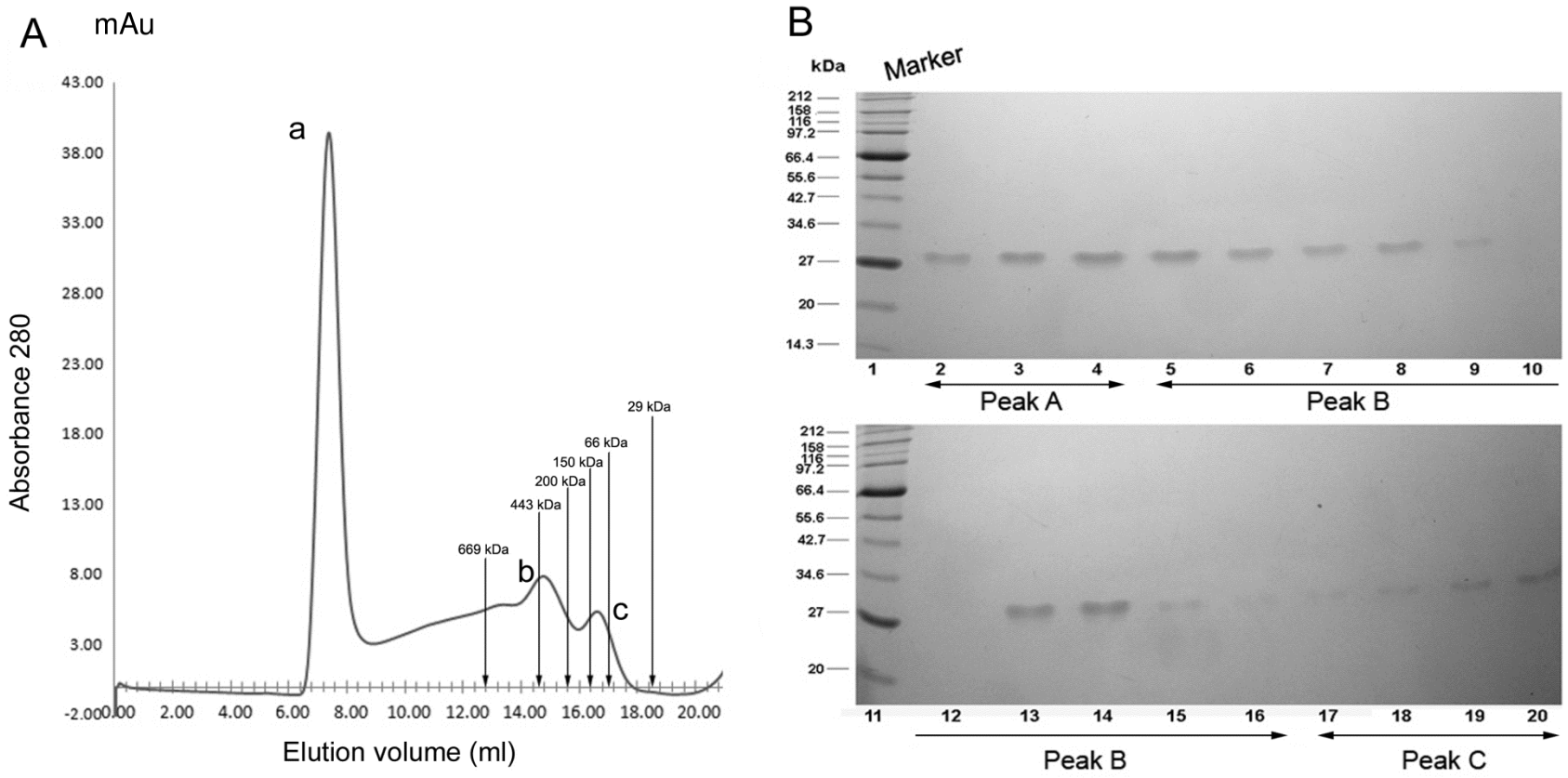

Fig 3.2 Gel filtration chromatography and SDS-PAGE of CotY. (A) Superose-6 chromatogram of CotY. Three main peaks are denoted as a, b and c; (B) The eluted fractions were analysed by SDS-PAGE and visualized by staining with Coomassie brilliant blue. The representative samples broadly cover the three peaks' range. The masses (in kDa) of protein standards are indicated on the left.

the fractions covering volume from peak b to peak a. Lanes 16-20 represented the fractions collected from peak c. The gel profiles indicated single band of approximately 28 kDa in all fractions analysed.

3.2.3 Electron microscopy

Specimens from different peaks were visualized by EM following negative stain. Surprisingly, from the Peak a fractions, large, well-ordered crystalline sheets of up to 0.4 μm arcoss on a side were visible (Fig 3.3). Quite a few small pieces were clearly visible dispersing on the grid as well as some scattered single particles. Peak b and c presented more aggregates with fewer of the crystalline sheets (Fig 3.3B). The size of crystal sheets was smaller than those in peak a and decreased with elution time. More and more particles appeared in the background. Peak b contained amorphous aggregates (Fig 3.3C). In addition to disordered aggregates, overloaded single particles could be seen. Peak c revealed a largely mono-dispersed sample of single particles with about 12 nm in diameter (Fig 3.3D).

3.3 CotE

3.3.1 Purification of CotE

CotE was mostly expressed as an insoluble protein, and only a small fraction of the protein remained soluble in non-denaturating conditions. CotE was purified in two conditions, in 8 M urea and in urea-free buffer. The yield of the protein acquired in urea buffer was significantly higher than in urea-free conditions (Fig 3.4). CotE (predicted MW 23.1 kDa with N-terminal His-tag) was expressed and purified as previously described. Most of the proteins were eluted with 0.2M and 0.3M imidazole with only a few additional protein present in limited amount (Fig 3.4).

CotE isolated in urea was further purified by size exclusion chromatography and analysed by EM. Chromatography on a Superose-6 column revealed 3 peaks (Fig 3.5): peak a was eluted with the void volume of the column which is out of the range of available protein molecular weight standards. Proteins with apparent molecular weight of 485 kDa were eluted in peak b. Most of the protein eluted in peak c had an estimated molecular of about 140 kDa. All the eluted fractions covering the three main peaks were

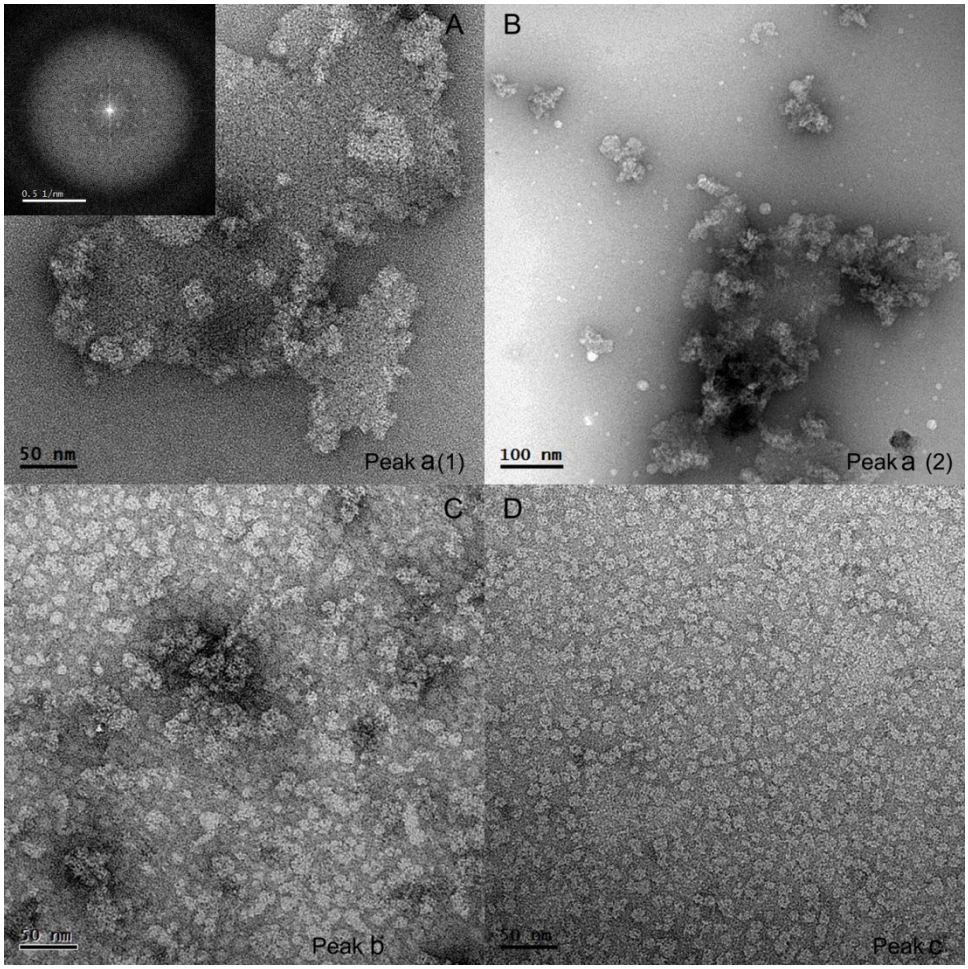

Fig 3.3 Representative micrographs of negatively stained CotY proteins from different size-exclusion chromatography peaks. (A-B) Representative micrographs of crystal sheets and slight aggregations yielded in Peak a. A computer generated Fourier transform in the inset shows the distinct diffraction pattern of CotY crystal; (C) Protein fraction from peak b; (D) Representative micrographs of proteinaceous particles from peak c.

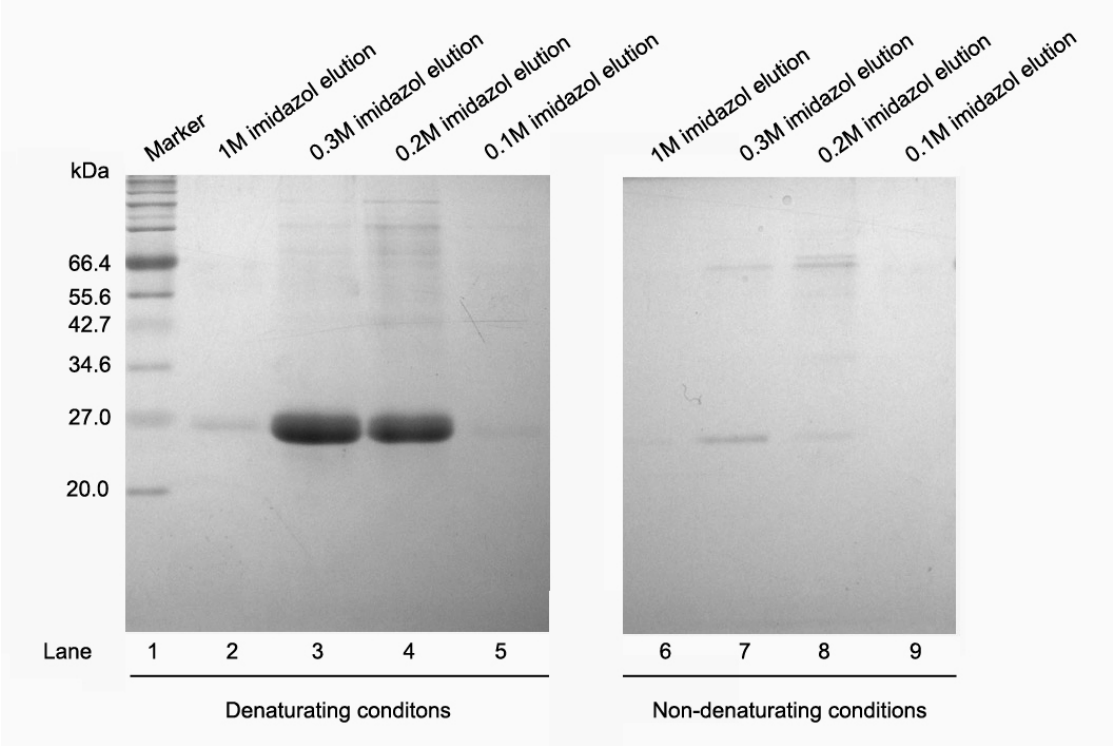

Fig 3.4 Purification of *B. subtilis* coat protein CotE under denaturating (8 M urea) and native conditions. Eluted fractions were resolved by 12% SDS-PAGE. The gel was stained with Coomassie brilliant blue. Lane 1 shows the protein marker. CotE was eluted stepwise with increasing concentrations of imidazole (0.1 M, 0.2 M, 0.3 M, 1M) in urea (Lanes 2-5) respectively. Lanes 6-9 represent samples acquired by equivalent concentrations of imidazole in urea-free conditions.

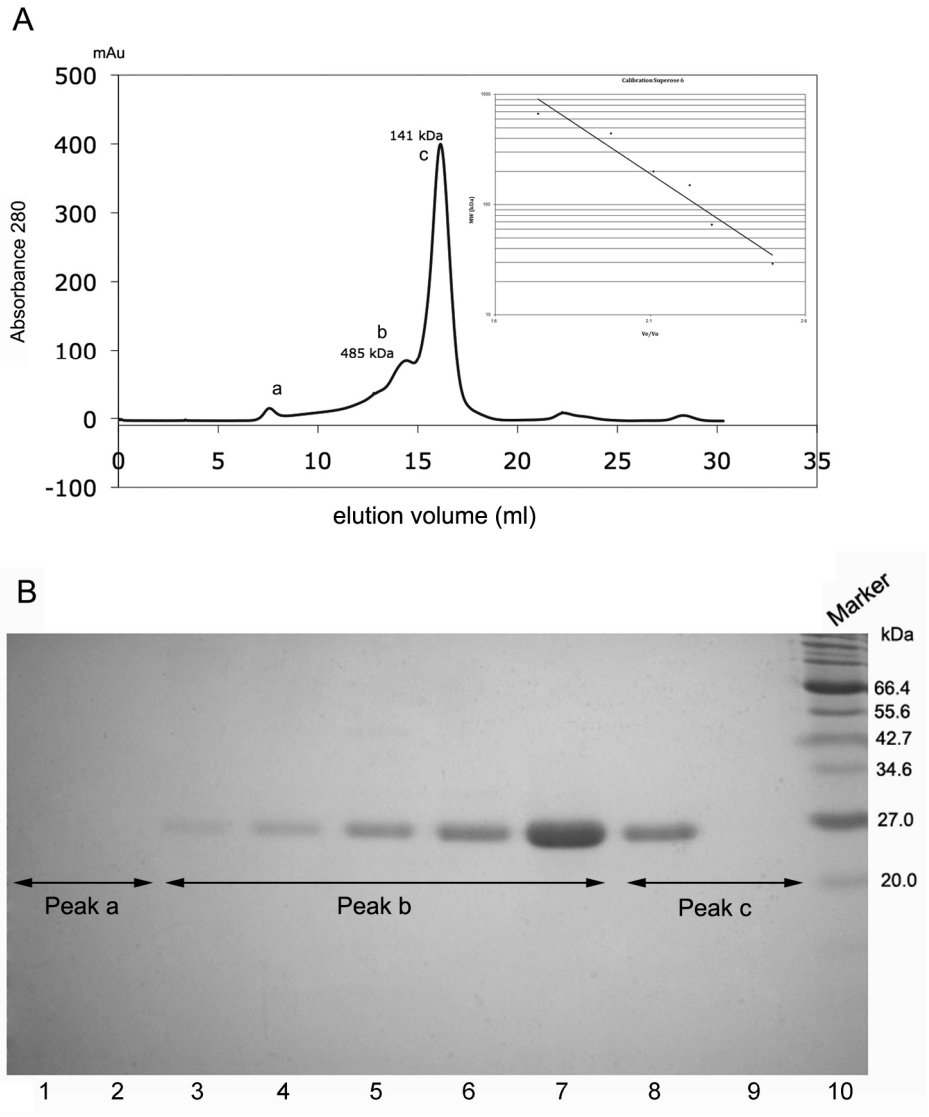

Fig 3.5 Gel filtration chromatography and SDS-PAGE analysis of CotE. (A) Superose-6 chromatogram of CotE. Inset image shows calibrated molecular weights; (B) The eluted fractions were analysed by SDS-PAGE and visualized after staining with Coomassie brilliant blue. The representative samples broadly cover the three peaks' range. The masses (in kDa) of protein standards are indicated on the right. Lanes 1-2 show the protein collected from peak a, lanes 3-7 for volume peak a-b and lanes 8-9 for peak c. Lane 10 shows the protein marker.

selected and loaded on a 12% SDS-PAGE gel. A single band could be seen on the gel (Fig 3.5).

3.3.2 Electron microscopy of purified CotE

In electron micrographs of peak a, (Fig 3.6A-B), vesicle-like species were observed, ranging in diameter from 30 to 200 nm. In peak b, a large number of protein aggregates could be seen, ranging in size from 10 to 35 nm (Fig 3.6C). Peak c showed protein aggregates of smaller size (9-20 nm) than those in the peak b ((Fig 3.6D).

3.4 CotZ

3.4.1 CotZ purification and SEC analysis

Full length CotZ recombinant contains 167 amino acids with a predicted MW of 18.6 kDa. The recombinant protein was purified under denaturating conditions using 8M urea. The resulting SDS-PAGE profile showed only one band with the expected size (Fig 3.7). Most of the protein was isolated from the 0.2 and 0.3 M imidazole elution fractions but the yield was low. Analyzing CotZ protein by gel filtration, we found out that most of the protein eluted in the void volume of the Superose-6 column, followed by several poorly resolved fractions. Finally, two peaks corresponding to proteins with molecular weight of about 143 kDa and 56 kDa could be seen (Fig 3.8).

3.4.2 Electron microscopy

As shown in Fig 3.9A-B, in the peak a, CotZ aggregated into large vesicles with diameters ranging from 35 to 350 nm. Peak b showed protein aggregates giving circular projections with diameter ranging from 12 to 25 nm (Fig 3.9C). The size of the particles was even smaller in peak c (Fig 3.9D). Only a high concentration of protein particles of about 10 nm in diameter with few larger aggregates could be seen.

3.5 CotE-CotZ

3.5.1 Gel filtration

CotE and CotZ were purified separately, mixed in a 1:1 ratio (v/v) and dialyzed against decreasing concentrations of urea. The protein mixture was then subjected to size

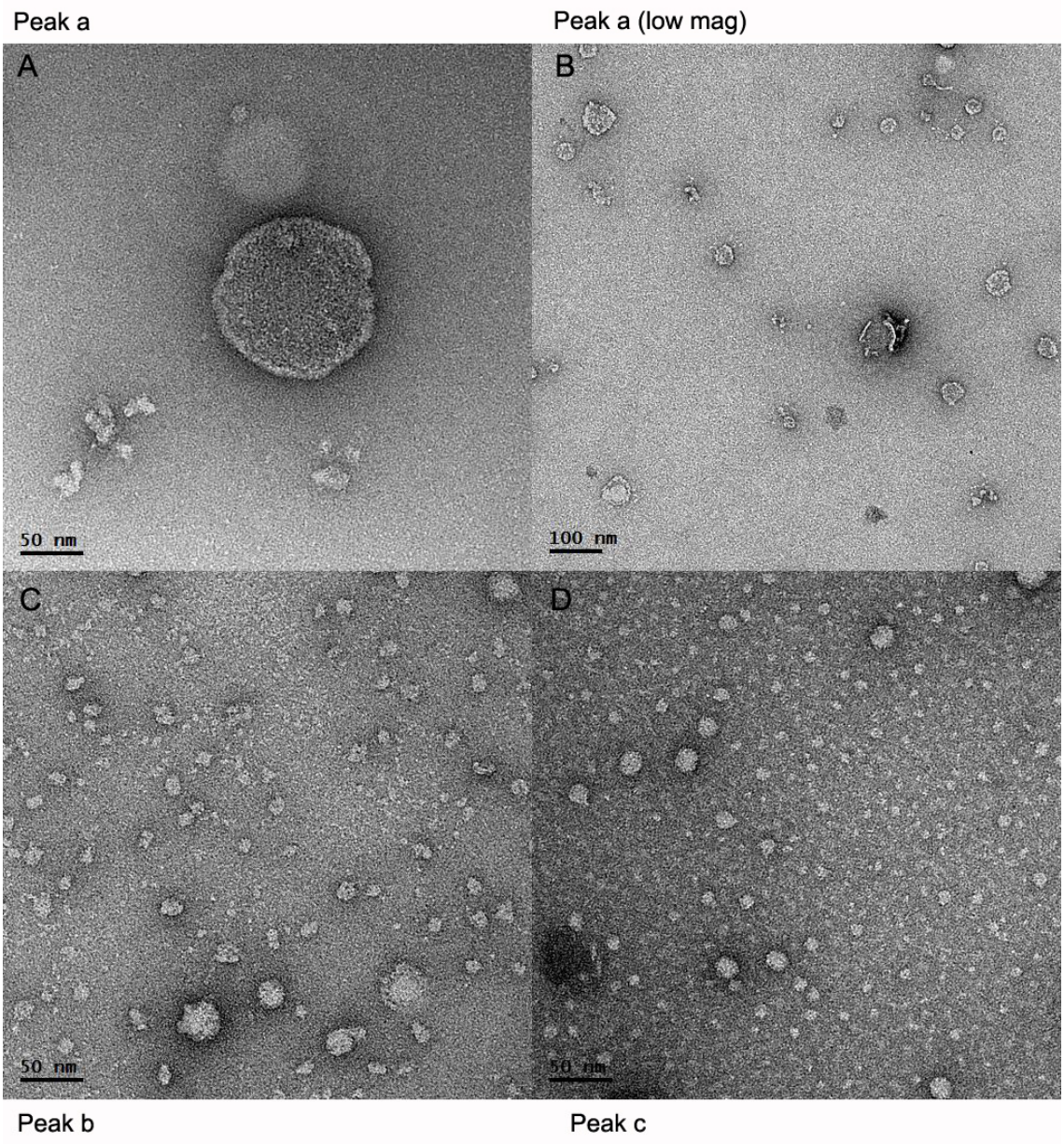

Fig 3.6 Representative micrographs of negatively stained CotE in different peaks separated by Superose-6 column in 8 M urea conditions. (A) Representative micrographs of CotE assemblies found in Peak a; (B) One typical image from the Peak a sample in lower magnification; (C) Heterogeneous protein particles from peak b; (D) Representative image of peak C. The scale bar for each image is shown on the left bottom of each picture.

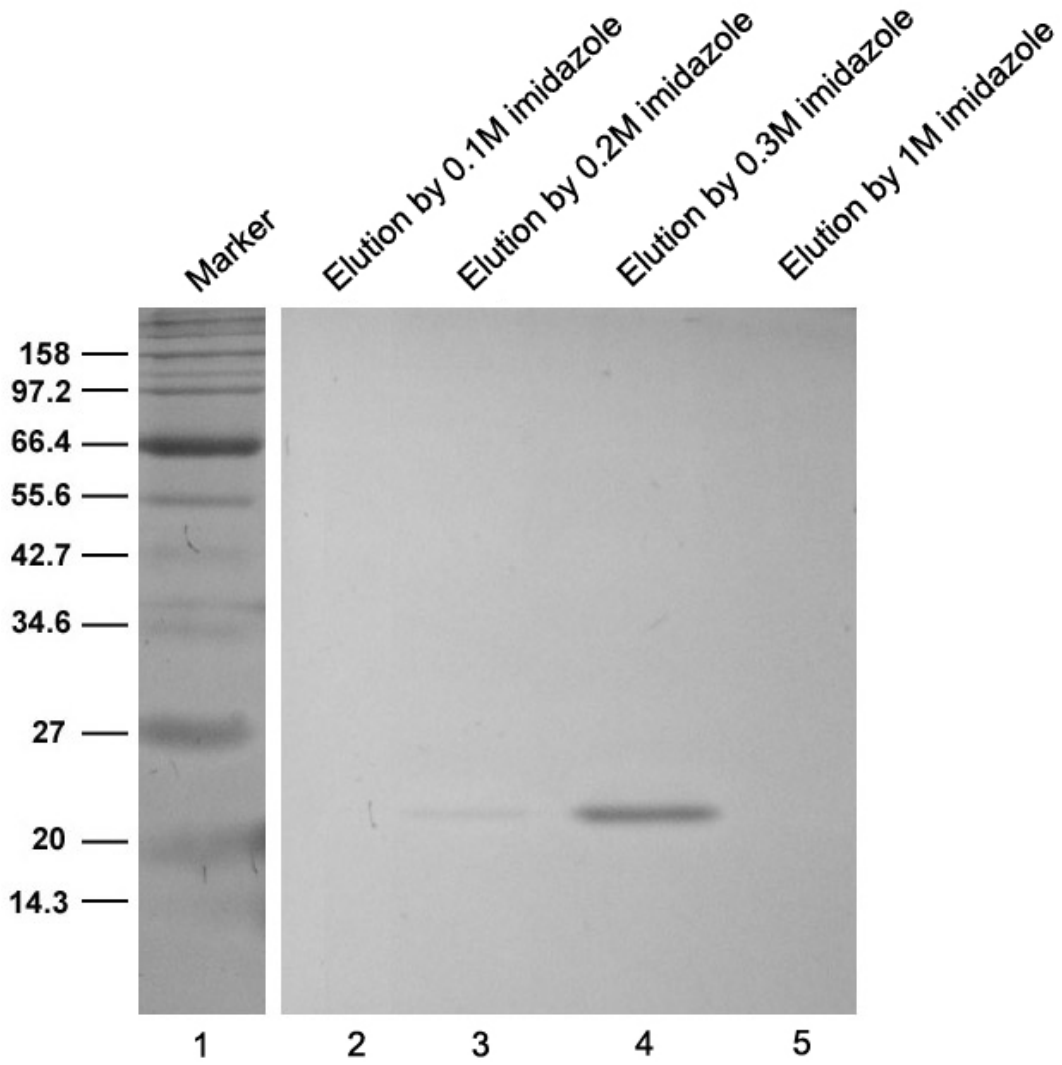

Fig 3.7 Recombinant *B. subtilis* coat protein CotZ was purified under denaturating conditons (8 M urea) and analysed by 4-12% SDS-PAGE. The gel was stained with Coomassie brilliant blue. Lane 1 shows the protein marker. Lanes 2-5 show the protein elution by different concentrations of imidazole.

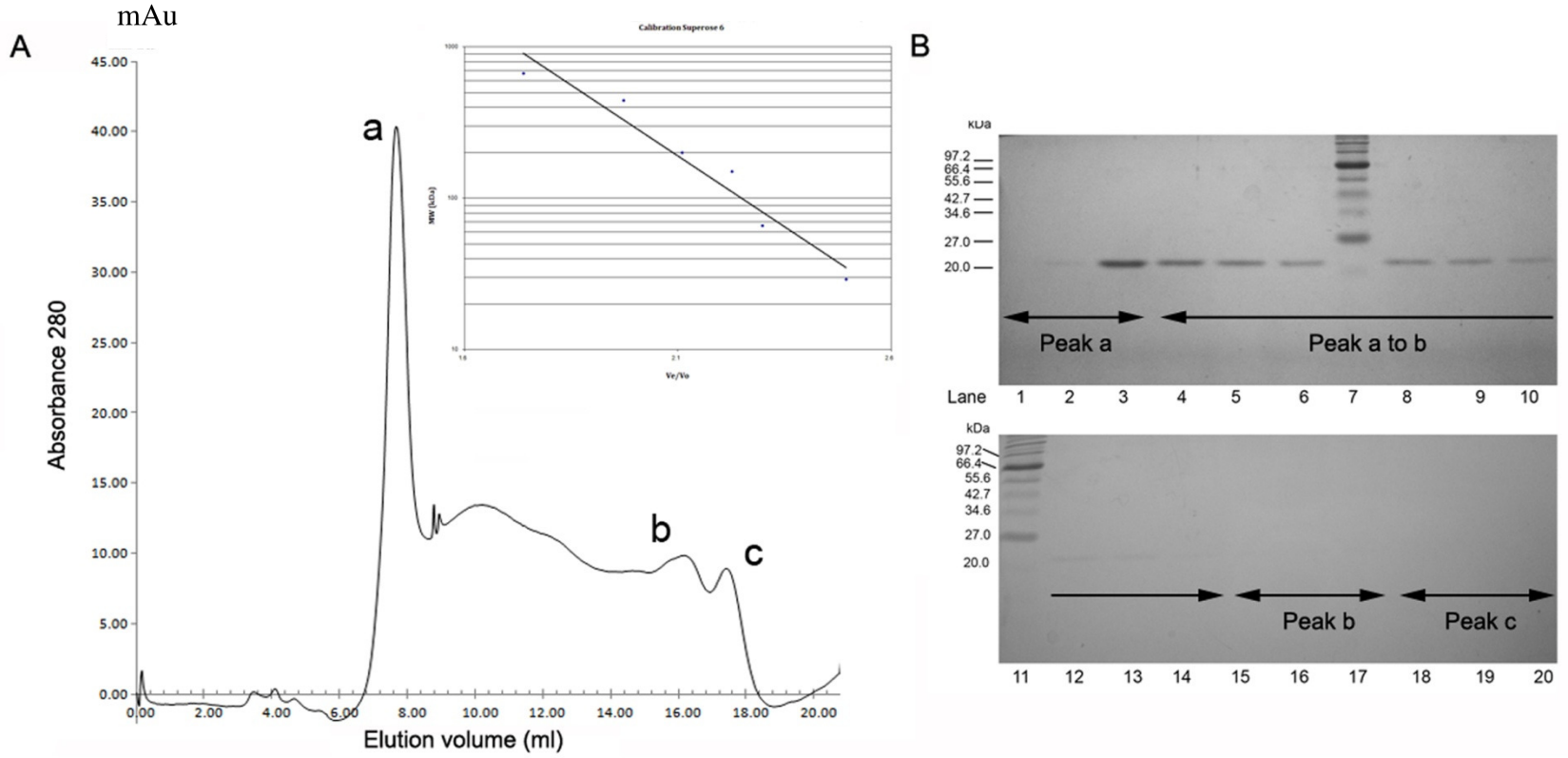

Fig 3.8 Gel filtration chromatography and SDS-PAGE analysis of CotZ. (A) SEC of purified CotZ. Three main peaks are denoted as a, b and c. Inset image shows calibrated molecular weights; (B) The selected fractions covering the three peaks were analysed by 12% SDS-PAGE and visualized after staining with Coomassie brilliant blue. Lanes 1-3 represent samples collected from peak a, lanes 4-14 correspond to fractions from peak a to peak b, lanes 15-17 correspond to fractions in peak b and lane 18-20 fractions from peak c. Lane 7 and 11 are protein marker.

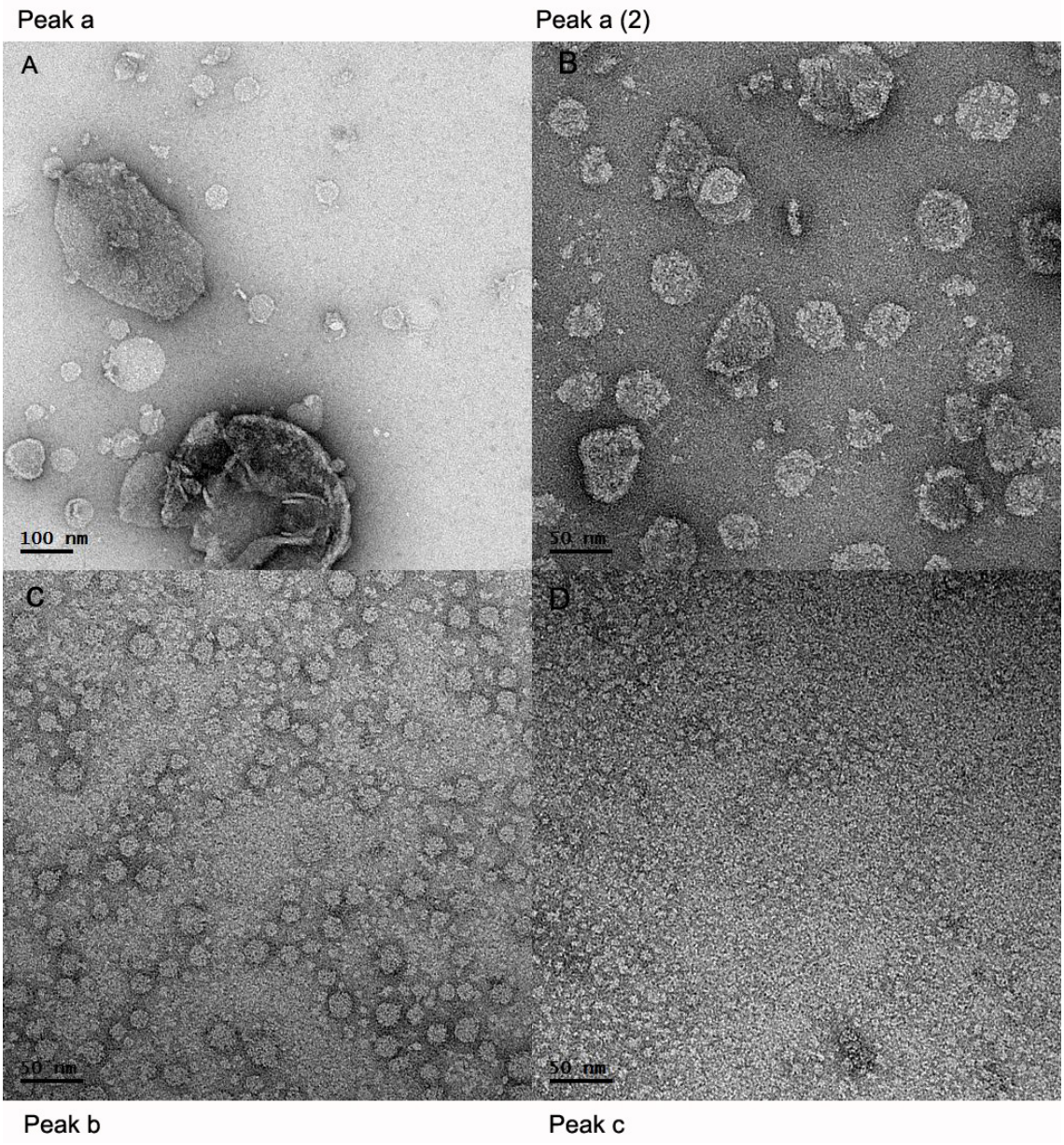

Fig 3.9 Representative micrographs of negatively stained CotZ protein in different peaks separated by Superose-6 column. (A-B) Two typical micrographs of protein fractions from peak a at different magnifications; (C) Protein fraction of peak b; (D) Protein fraction of peak c. The scale bar for each micrographs are indicated on the bottom left.

exclusion chromatography and EM. As shown in Fig 3.10, three elution peaks were resolved. Peak a corresponds to the void volume, indicating enormous proteinaceous complex formation. Peak b contains very high molecular weight aggregates, whilst peak c corresponds to a species with an estimated molecular weight of appoximately 36 kDa (MW of a 1:1 complex of CotE-CotZ expected to be ~ 41 kDa).

3.5.2 Electron microscopy

EM analysis revealed that peak a yielded a population of short ribbon-like assemblies of the order of 100-150 nm in length mixed with extended open-mesh net-like structures (Fig 3.11A-B) with an average repeat spacing of about 20 nm, although the mesh size was not uniform across the arrays. In peak b, large aggregates of irregular morphology could be seen (Fig 3.11C). The diameter of particles seen in this fraction is about 20 nm. Fractions from peak c contained small particles of the order of up to around 11 nm in diameter (Fig 3.11D). CotE or CotZ purified alone did not yield ribbons or net structures.

3.6 SpoIVA

3.6.1 SpoIVA purification, SEC analysis and Microscopy

SpoIVA was isolated in 2 forms: as a full-length protein (N-terminal his-tagged protein 57.2 kDa) and a mutant form, truncated from the C-terminus (N-terminal his-tagged protein 46.8 kDa). Since both full-length and truncated SpoIVA were produced as insoluble proteins, buffers containing urea were used throughout the purification.

Full-length SpoIVA

To increase the purification yield, the supernatant of *E.coli* BL21 lysate was iteratively loaded on the nickel column twice prior to imidazole elution. 0.2 M and 0.3 M imidazole eluted fractions of the protein were pooled, concentrated and analysed by gel filtration (Fig 3.12). The yield of the truncated protein in *E. coli* was significantly higher than the full-length protein. Degraded ~28 kDa forms of an unknown protein (might be a proteolytic cleavage) could be seen (Fig 3.12). 0.2 M and 0.3 M imidazole elutions of full-length SpoIVA were pooled together, concentrated and subjected to size exclusion chromatography.

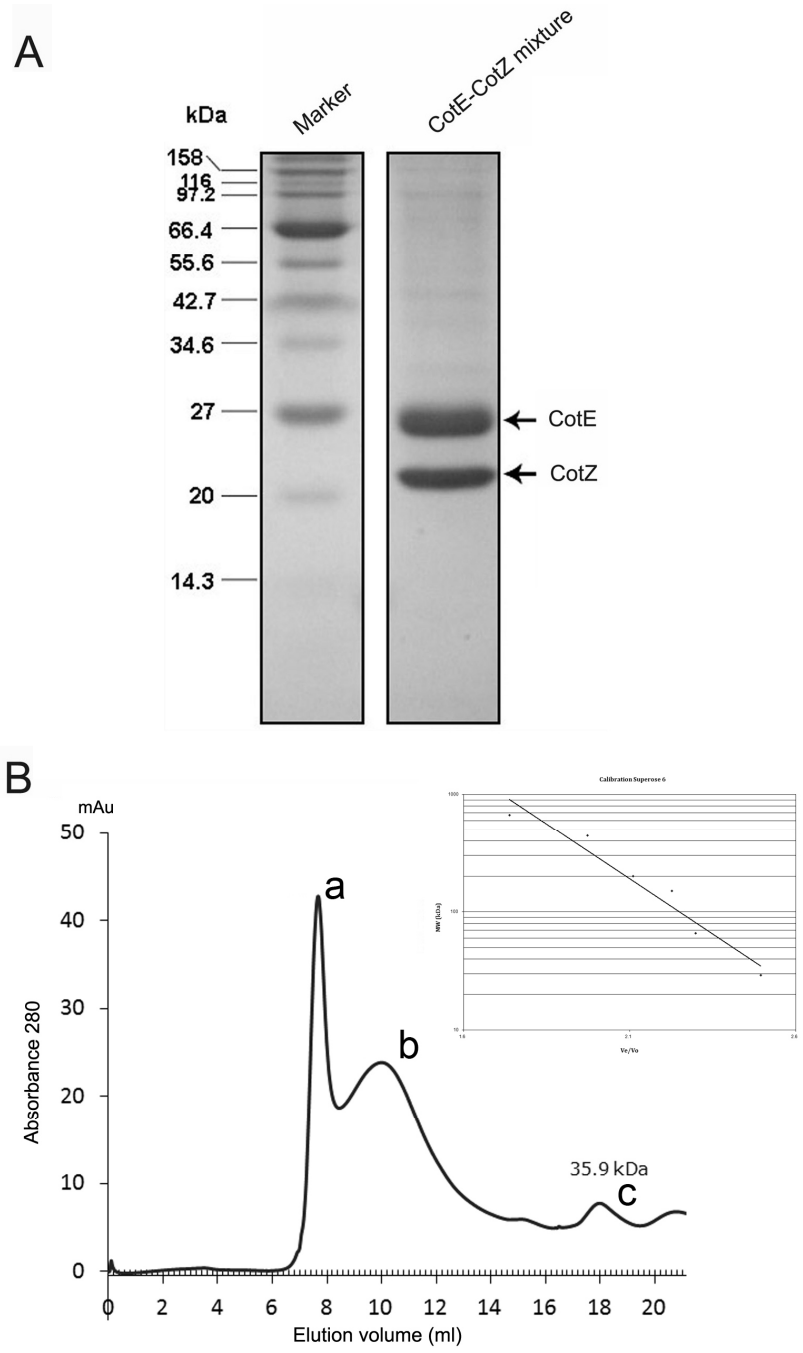

Fig 3.10 CotE-CotZ mixture preparation and size exclusion chromatography. (A) SDS-PAGE profile of a CotE-CotZ mixture dialysed against decreasing concentration of urea. The position for each protein was indicated by arrow. The masses (in kDa) of protein standards are indicated on the left; (B) Superose-6 chromatogram of CotE-CotZ mixture. Inset image shows calibrated molecular weights. Proteins were eluted in 3 major peaks: a, b and c.

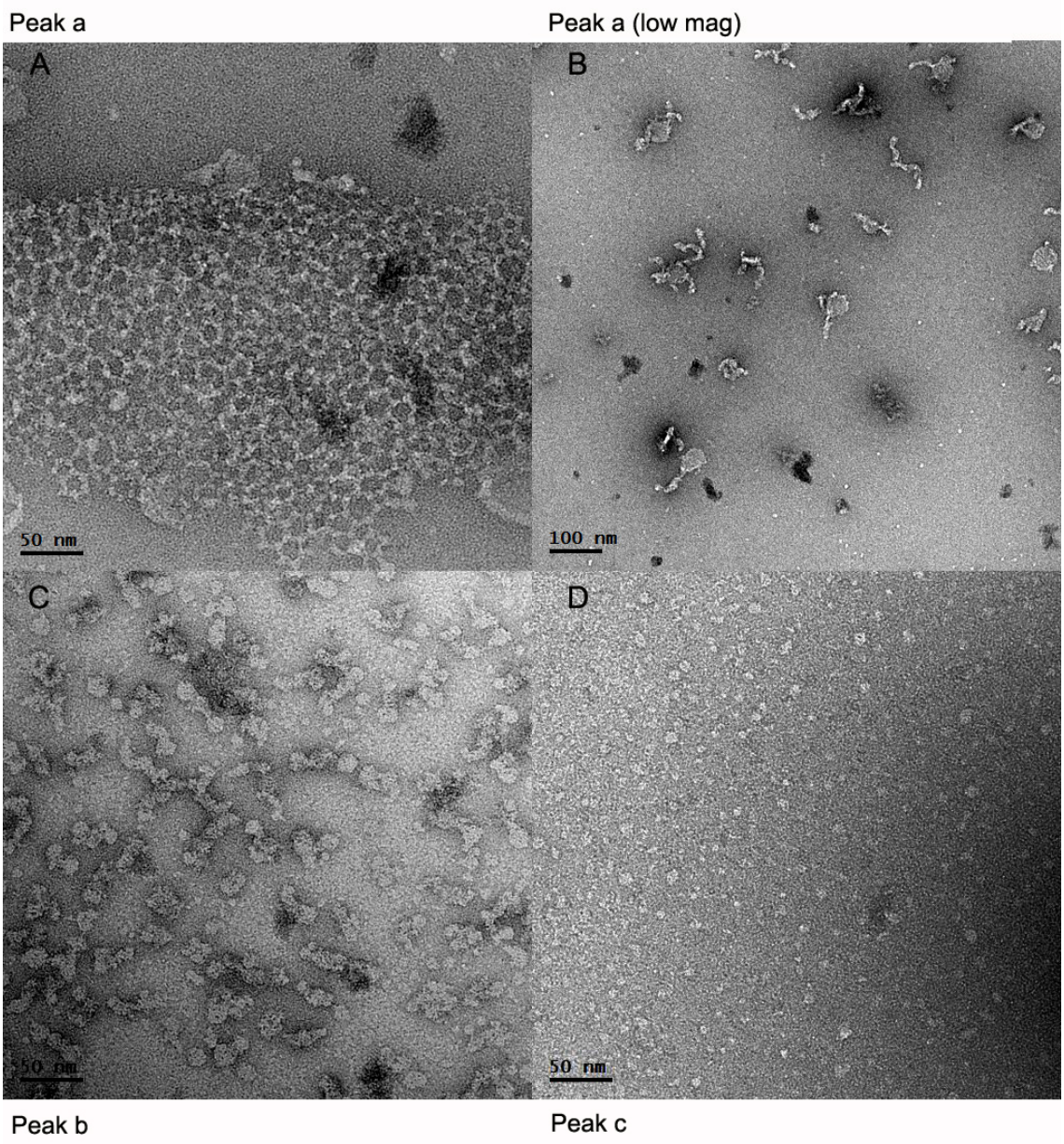

Fig 3.11 Representative micrographs of negatively stained CotE-CotZ mixture in different peaks resolved by Superose-6 column. (A) Open-meshed net-like structure (Peak a); (B) The other typical image from the peak a at lower magnification; (C) Protein fraction of peak b; (D) Representative micrographs of peak c. Scale bar for each image is on the left bottom.

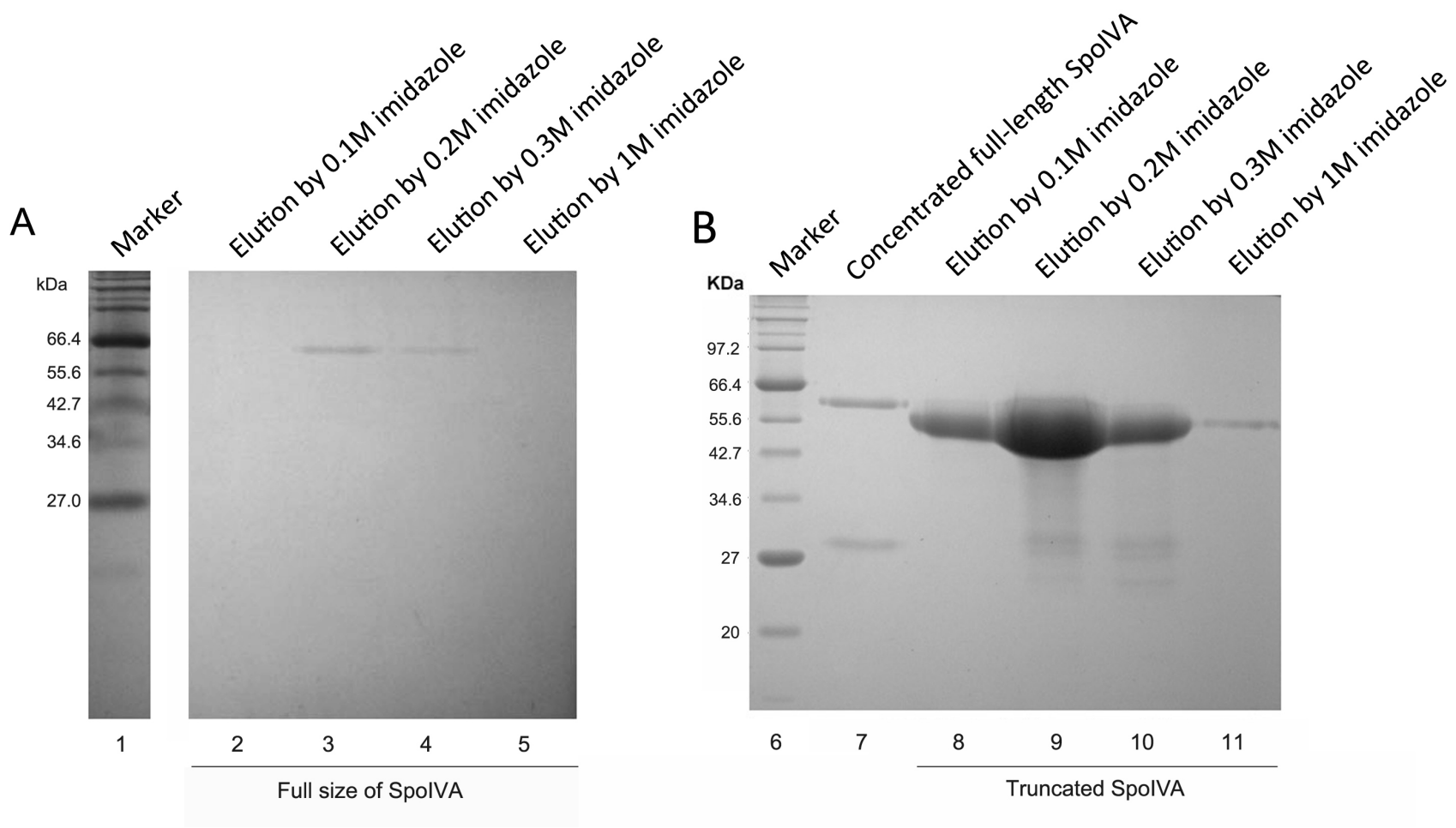

Fig 3.12 Purification of full-length and truncated SpoIVA. Purification products correspond to full length SpoIVA (A) and truncated SpoIVA (B) were analysed by 4-12% SDS-PAGE. The gels were stained with Coomassie brilliant blue. Lanes 2-5 show the full length of SpoIVA (57.2 kDa) eluted by various concetntrations ofof imidazole. Since the yield was low, elutions by 0.2M and 0.3M imidazole were pooled together and concentrated for gel filtration (lane 7). Truncated SpoIVA (46.8 kDa) was eluted stepwise with increasing concentration of imidazole (lanes 8-11). Protein markers are indicated on the left of each panel.

Several peaks eluted from Superose 6 could be observed after gel filtration, but after SDS PAGE only proteins collected from the peak b could be detected (Fig 3.13B). It might be caused by small amount of protein we injected into column. Some proteins with MW around 28 kDa were found in peak c; this could be a degraded form of SpoIVA (see very weak bands in Fig 3.13B, Lanes 14-15).

In the peak a fraction, we could see large vesicle-like aggregates with diameter ranging from 60 to 300 nm (Fig 3.14A). Two minor peaks between peak a and b presented a small population of aggregates (Fig 3.14B). The second minor peak between peak a and b showed similar aggregates (data not shown). SpoIVA in peak b appeared as more uniformly sized particles ranging in diameter from 12 to 15 nm (Fig 3.14C). Peak c and the remaining peaks did not yield any visible particles (Fig 3.14D).

Truncated form of SpoIVA

The yield of the truncated protein expressed in *E. coli* was significantly higher than the full-length protein (Lane 8-11, Fig 3.12). Some unknown ~28 kDa species could be seen again (Fig 3.12). The 0.2 M imidazole-eluted truncated SpoIVA was analysed by Superose 6 column (Fig. 3.15). SpoIVA started to elute in the void volume of the column, followed by some poorly resolved minor peaks like peak a. The main fraction of the protein was eluted in the large peak b corresponding to protein with an apparent molecular weight ~260 kDa. Protein fractions from peaks including the minor peaks to the column volume 30 ml point were selected and resolved by 4-12% SDS-PAGE. The observed bands mainly covered peak b and its shoulder area (Fig 3.15). Only one band corresponding to the expected molecular weight of truncated SpoIVA could be seen. The protein fractions from main peak and some minor peaks till 30ml column volume were analysed by EM.

Fractions from peak a eluted in void volume of the column. EM revealed heterogeneous particles up to 40 nm in diameter (Fig 3.16A). Truncated SpoIVA did not form the vesicle-like structures found in full-length SpoIVA. In the minor peak between peak a and b, a few amorphous aggregates could be seen (Fig 3.16B). Again heterogeneous particles were observed in the biggest peak, peak b (Fig 3.16B). In the fractions after peak b, heterogeneous particles, including some aggregates were seen (Fig 3.16D).

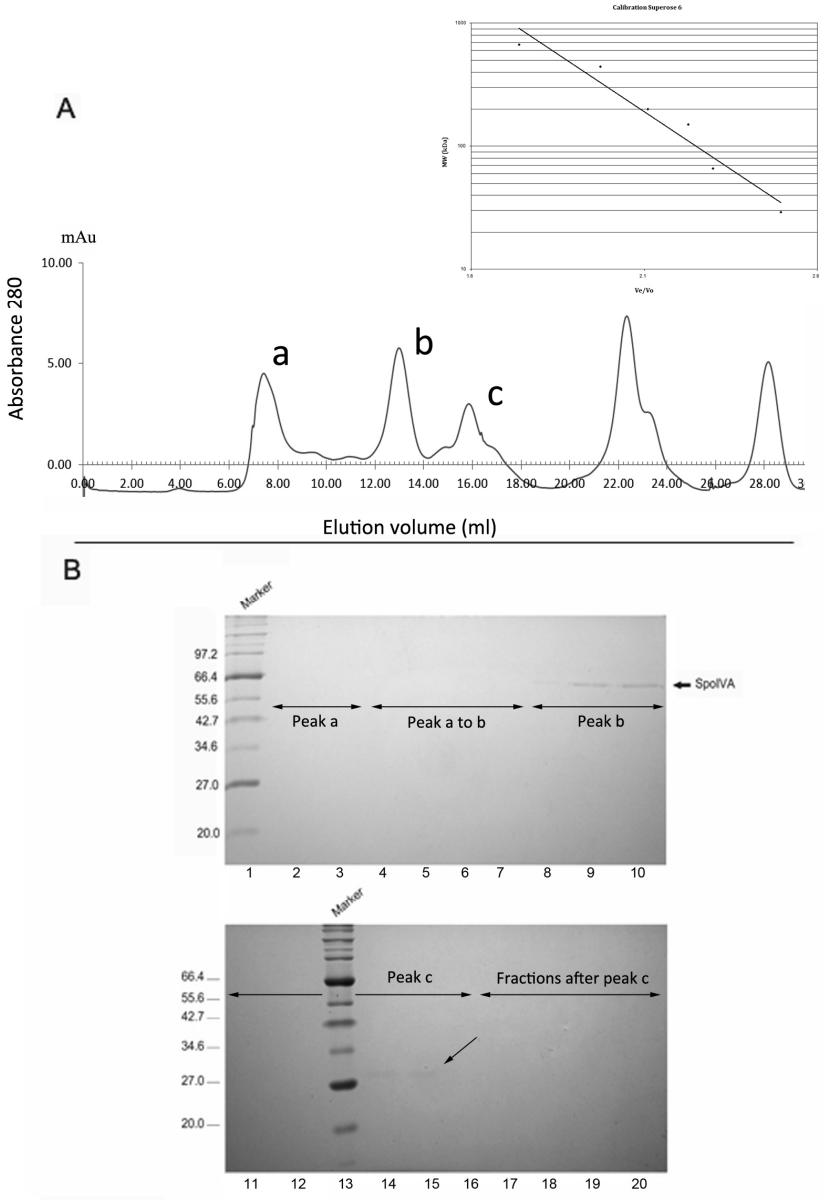

Fig 3.13 Full-length SpoIVA gel filtration chromatography. (A) Superose-6 chromatogram of full-length SpoIVA. Protein was eluted in several peaks. Peaks a, b and c with estimated MW greater than monomer MW were marked. Inset image shows calibrated molecular weights; (B) 4-12% SDS-PAGE analysis of fractions from peaks a, b and c. Samples in lanes 2-3 were collected from peak a, lanes 4-7 correspond to minor peaks between peak a and peak b, lanes 8-10 correspond to peak b, lanes 11-16 (except marker lane 13) correspond to peak c, and lanes 17-20 correspond to unknown fractions after peak c. The position for full SpoIVA is indicated by arrow. Molecular weight (in kDa) of protein standards are indicated.

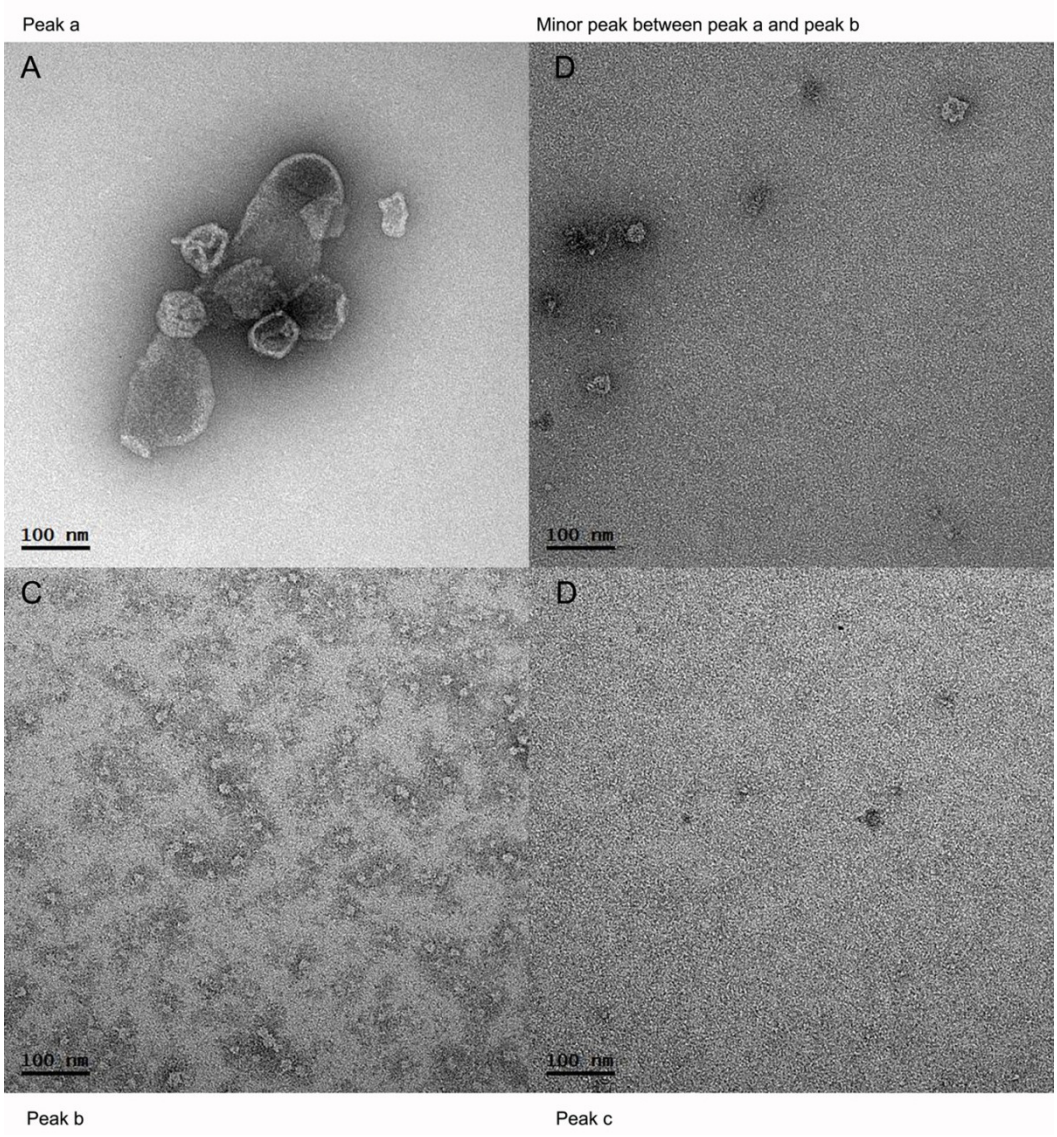

Fig 3.14 Representative micrographs of negatively stained full sized SpoIVA in different peaks resolved by Superose-6 column. (A) Large protein vesicles yielded in peak a; (B) Image from one minor peak between the peak a and peak b; (C) Protein particles detected in peak b; (D) Image of peak c. Scale bar for each image is on the left bottom.

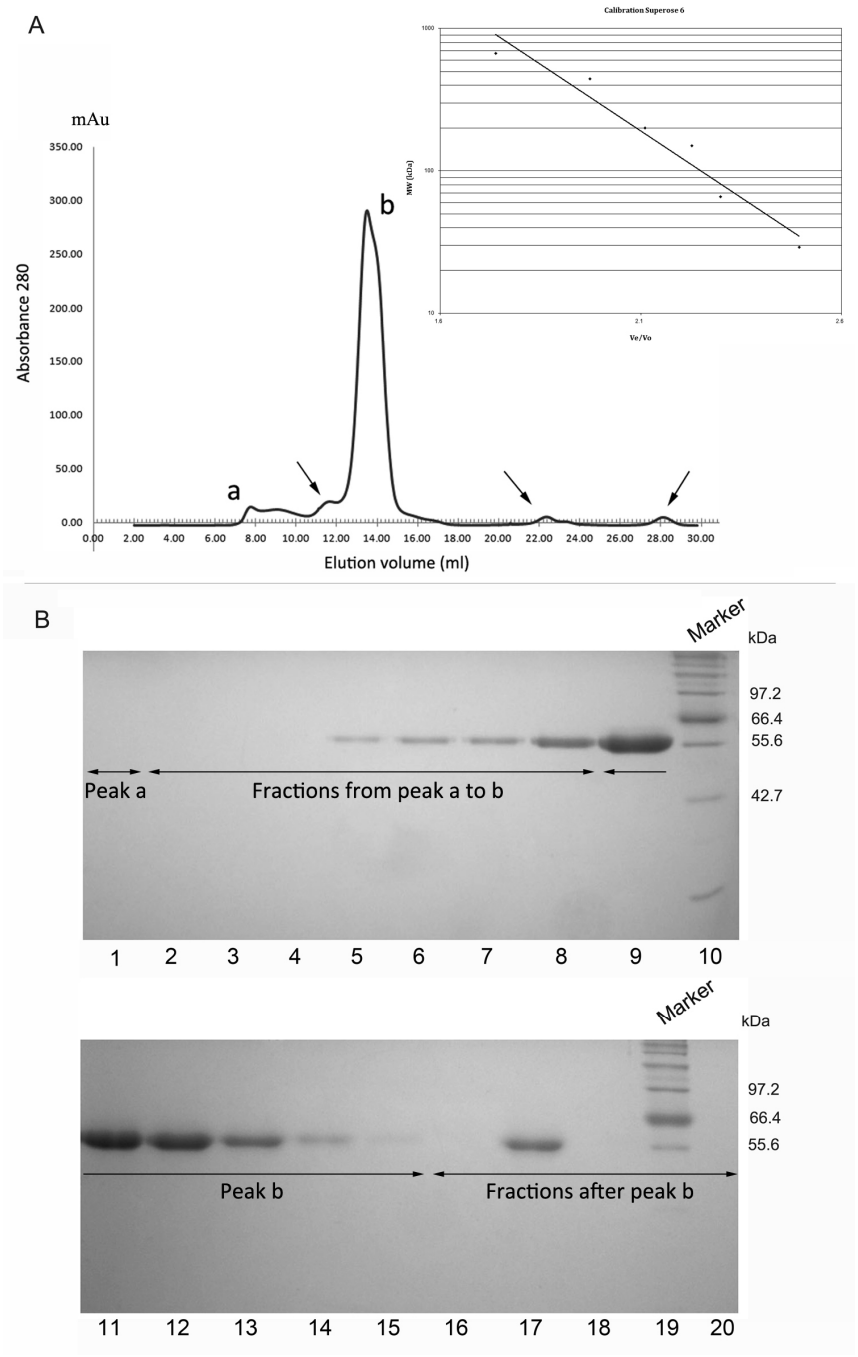

Fig 3.15 Truncated SpoIVA gel filtration chromatography. (A) Superose 6 chromatogram of truncated SpoIVA. Protein was isolated in one main peak and several minor peaks indicated by arrow. Peak a and b were marked. Inset image shows calibrated molecular weights; (B) 4-12% SDS-PAGE analysis of truncated SpoIVA fractions selected from peaks a, b and some minor peaks. Lane 1 corresponds to sample from peak a, lanes 2-8 correspond to fractions from peak a to peak b, lanes 9-15 correspond to peak b and lanes 16-20 correspond to fractions after peak b. Molecular weight (in kDa) of protein standards are indicated.

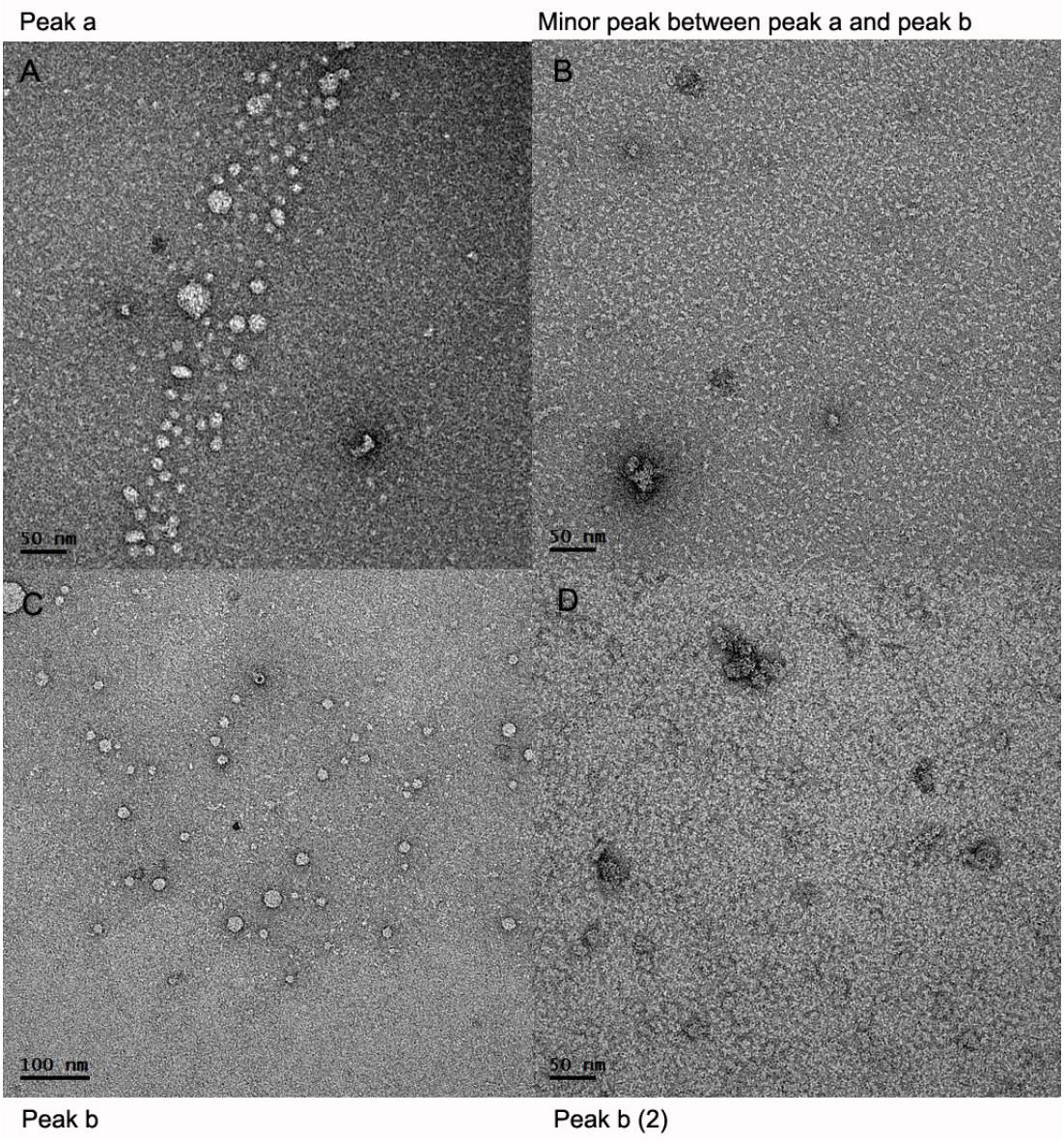

Fig 3.16 Representative micrographs of negatively stained truncated SpoIVA in different peaks separated by Superose-6 column. (A) Fractions in peak a that were eluted in void volume; (B) One representative micrograph from one minor peak between the peak a and peak b; (C) Protein particles detected in peak b; (D) One representative micrograph collected from volume after peak b. Scale bar for each image is on the left bottom.

3.7 SpoVID

3.7.1 SpoVID purification and SEC analysis

SpoVID was overexpressed in *E. coli* BL21 and purified by nickel affinity chromatography. SpoVID was soluble and purified without urea. As shown in Fig 3.17, a large proportion of SpoVID was collected in the 0.2/0.3 M-imidazole elution fractions, carrying a bit of degraded protein (Lanes 2-3, Fig 3.17). To prevent protein aggregation, 20% glycerol was used in all buffers. The protein eluted with 0.2 M imidazole was further analysed by gel filtration. Protein was eluted from the Superose 6 column to yield two major peaks (Fig 3.18A). Peak a corresponds to the void volume, having a wide shoulder; peak b represents proteins with apparent MW of 1250 kDa. Several small peaks could be detected: the protein in peak c and d could be putative dimer (about 145 kDa) and monomer forms (about 50 kDa) of SpoVID respectively.

3.7.2 Electron microscopy of SpoVID

As shown in Fig 3.19, aggregated particles similar to those seen in CotE-CotZ complexes formed in its peak b. In peak c, significantly less aggregation was observed with particles covering a narrow size range of 9 to 11 nm (Fig 3.19D). Peak d was devoid of visible protein (data not shown).

3.8 SafA

3.8.1 SafA purification and electron microscopy

N-terminal His-tagged SafA (predicted MW 44.6 kDa) was expressed in E.coli as a soluble protein. SafA was isolated and analysed under both urea and urea-free conditions (Fig 3.20). The yield of protein when using urea buffers was slightly greater that protein isolated in urea-free conditions. The existence of urea which might influence the protein migration rate of the SafA obtained in urea appeared to have a larger MW, which indicates that the urea condition could slow down the migration rate of protein in SDS-PAGE. The largest yielding fractions, 0.2 M imidazole in urea condition and 0.3 M imidazole in urea-free conditions were respectively used for gel filtration by Superose 6 column.

<u>Purification of SafA under native conditions</u>

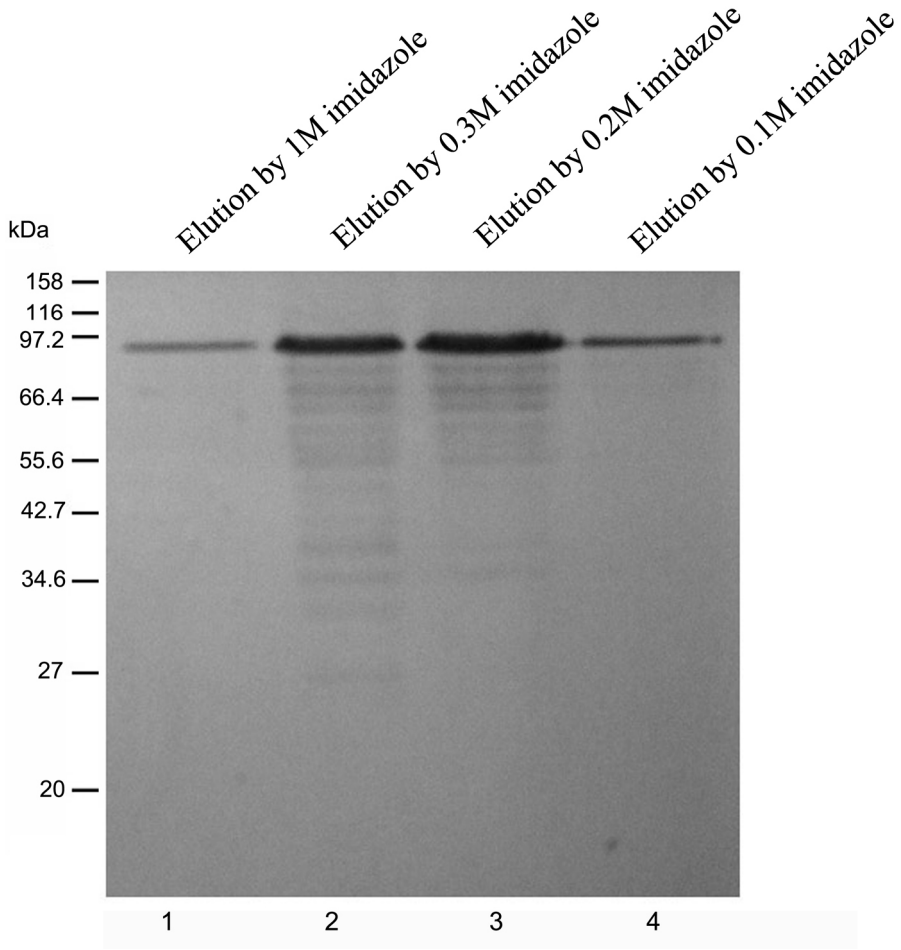

Fig 3.17. Recombinant *B. subtilis* coat protein SpoVID was purified under native conditions and analysed by 4-12% SDS-PAGE. The gel was stained with Coomassie brilliant blue. Lanes 1-4 show the proteins eluted by stepwise concentration of imidazole. Molecular weight markers are indicated on the left.

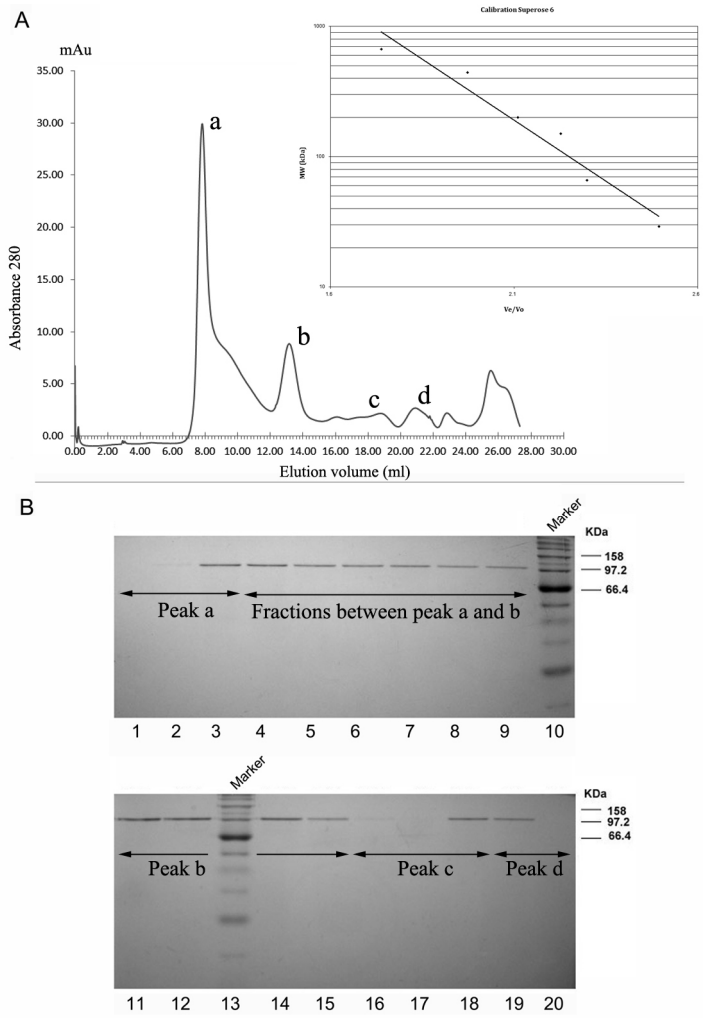

Fig 3.18 SpoVID gel filtration chromatography. (A) Superose 6 chromatogram of SpoVID. Peaks a, b and minor peak c, d are marked. Inset image shows calibrated molecular weights; (B) 4-12% SDS-PAGE analysis of SpoVID fractions selected from peaks a, b and minor peaks c and d. Samples shown in lanes 1-3 were collected from peak a elution, lanes 4-9 from peak shoulder between peak a and peak b, lanes 11-15 except 14 (Marker) from peak b, lanes 16-18 from peak c, and lanes 19-20 from peak d. Molecular weight (in kDa) of protein standards are indicated on the right.

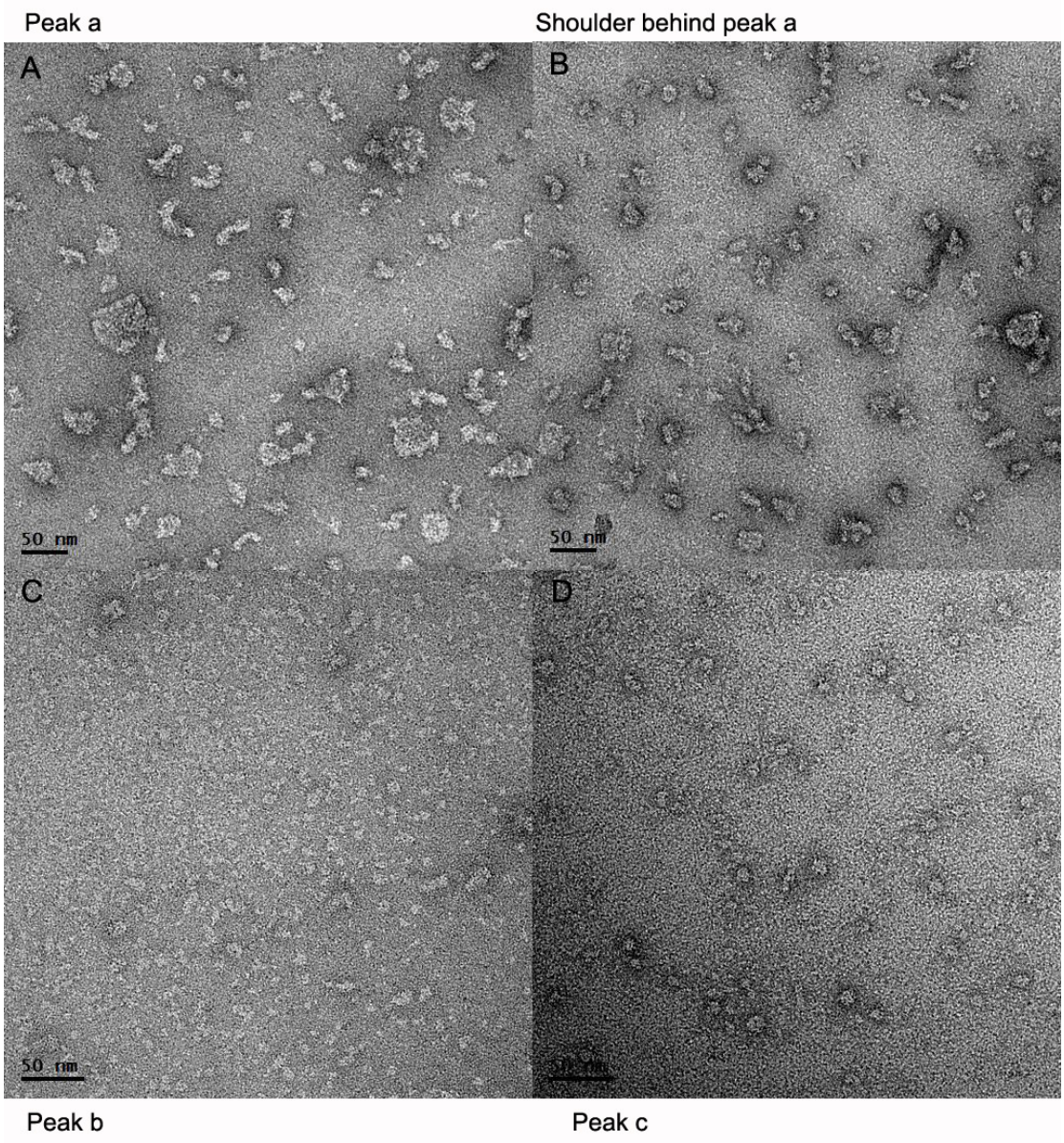

Fig 3.19 Representative images of negatively stained SpoVID in different peaks resolved by Superose-6 column. (A) Fractions in peak a eluted in the void volume of the column; (B) Image from should behind the peak; (C) Protein particles detected in peak b; (D) Image collected from volume point after peak c. Scale bar for each image is on the left bottom.

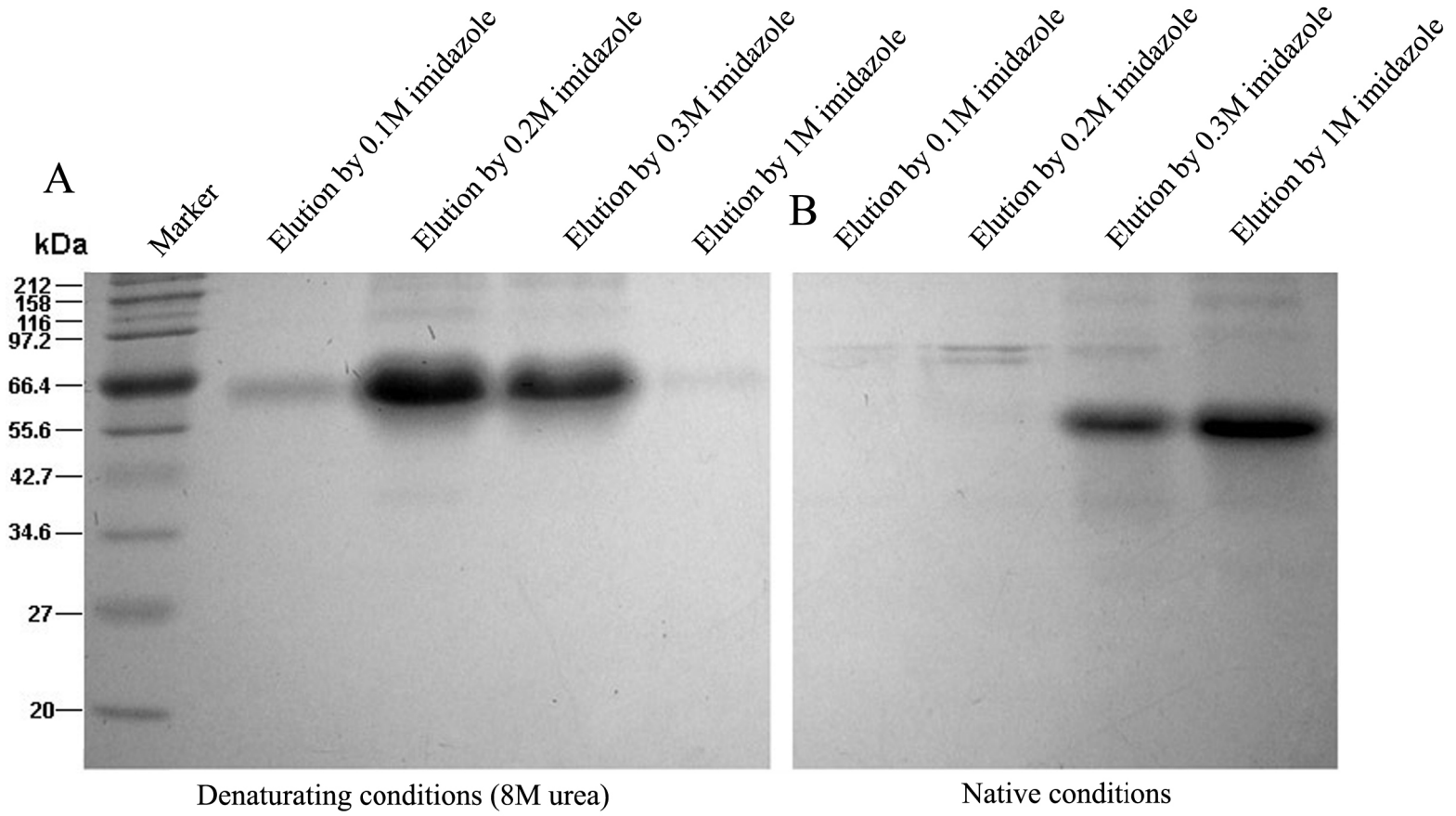

Fig 3.20 4-12% SDS-PAGE analysis of purified SafA. (A) SafA purified under denaturating conditions (8M urea); (B) SafA purified under native conditions. Following 4-12% SDS-PAGE, the gels were stained with Coomassie brilliant blue. Protein markers are indicated on the left.

SafA collected from the 0.3 M imidazole elution was separated by Superose 6 column into 3 peaks (Fig 3.21A). Peak a eluted within the void volume suggesting that they formed large protein complexes of aggragates. The majority of SafA was eluted out in peak b. The MW of complexes in peak b was outside the column calibration suggesting that SafA forms very high MW complexes of aggregates. The MW of SafA in peaks c was predicted to be 44.6 kDa, which is very close to the expected MW of monomeric protein.

The protein fractions eluted into 3 peaks were selected and subjected to SDS-PAGE (Fig 3.21B). Single band could be seen in the gel and that band corresponded to the peak b area. In the two minor peaks a and c, no obvious band could be detected.

The specimens from three peaks were loaded on the grids and observed by EM. In the peak c, the electron micrograph showed a few single particles sparsely distributed (Fig 3.22C). These homogeneous particles of projected diameter ~20 nm were also observed in the peak b micrograph in which much more of protein particles with few of amorphous aggregates appeared (Fig 3.22B). In the peak a, bigger aggregated clusters were seen (Fig 3.22A).

Purification of SafA under denaturating conditions

SafA was also purified in urea in large amounts. The protein elution profile revealed four peaks: peak a – void volume; peak c – the major peak corresponds to protein with molecular weight about 580 kDa, and two minor peaks b and d (Fig 3.23). SDS-PAGE analysis of proteins present in the 4 peaks showed only a single band most abundant in peak c (Fig 3.23).

In peak a, a mix of vesicle-like species was observed with a background of small single particles (Fig 3.24A-B). In peak b, homogeneous particles with a projected diameter around 20 nm were observed (Fig 3.24C). The particle's appearance in the projection is identical to the particles seen in peak c (Fig 3.24D) and also similar to those obtained for SafA without using urea.

3.9 CotH

3.9.1 CotH purification and SEC analysis

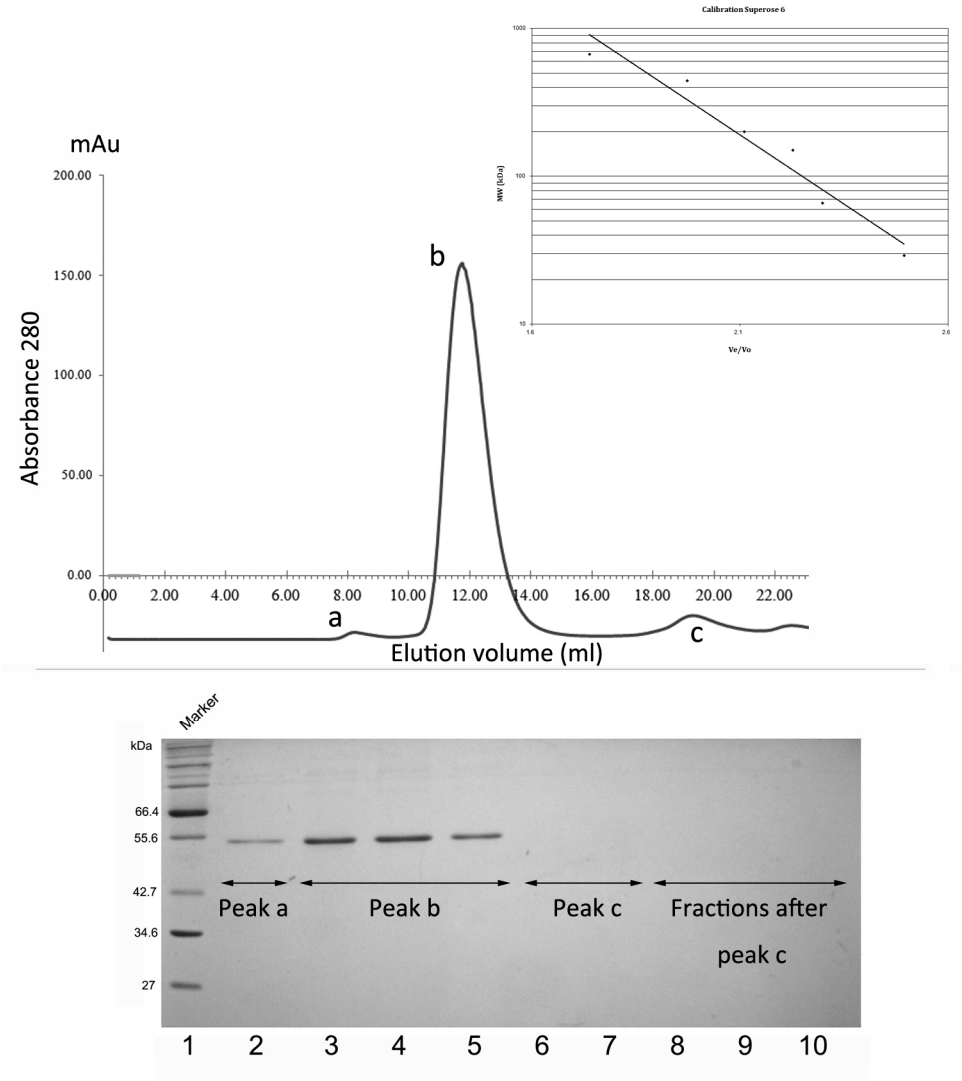

Fig 3.21 Purification of SafA by gel filtration chromatography under native conditions. (A) Superose-6 chromatogram of SafA. Three peaks were separated: peak b, minor peak a and c. Inset image shows calibrated molecular weights; (B) 4-12% SDS-PAGE resolution of SafA elutions selected from peaks a, b and c. The samples shown in lane 1 corresponds to peak a, lanes 2-5 correspond to peak b, lanes 6-7 correspond to peak c, and lanes 8-10 correspond to fractions after peak c. Molecular weight (in kDa) of protein standards are indicated on the left.

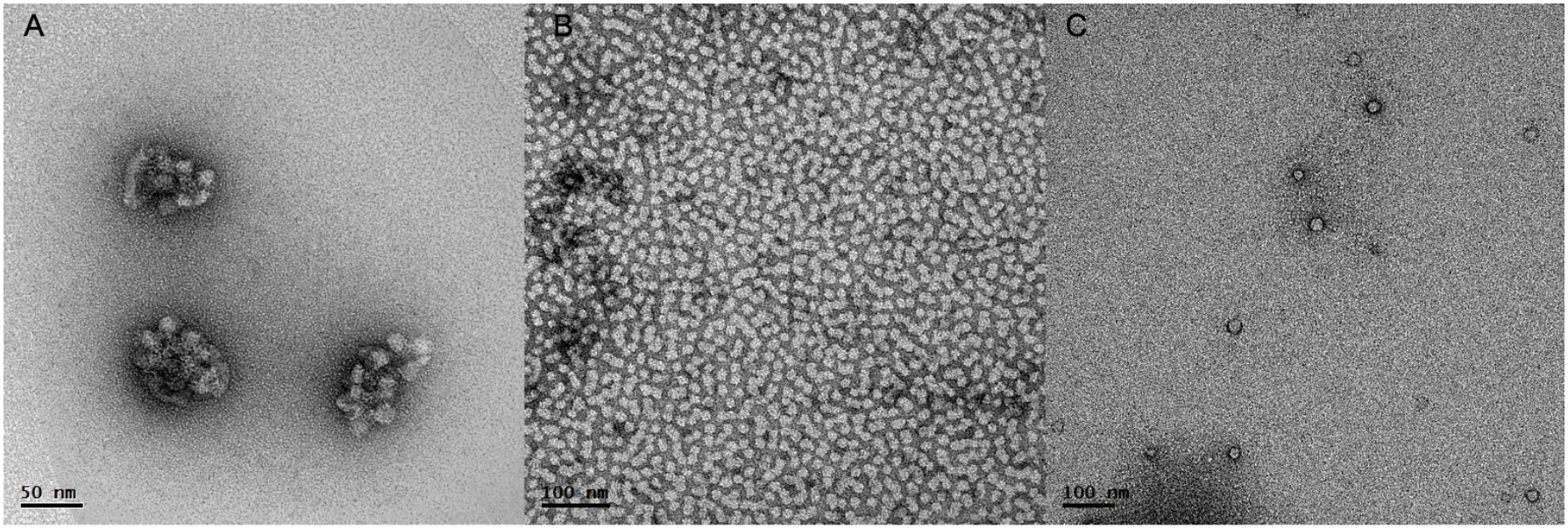

Fig 3.22 Representative images of negatively stained SafA purified under native conditions. (A) Protein fraction of peak a, SafA aggregation clusters dispersed; (B) Protein fraction of peak b, with ball-like structures formed by SafA; (C) Protein fraction of peak c, few showing protein particles. The scale bar for each image is on the left bottom.

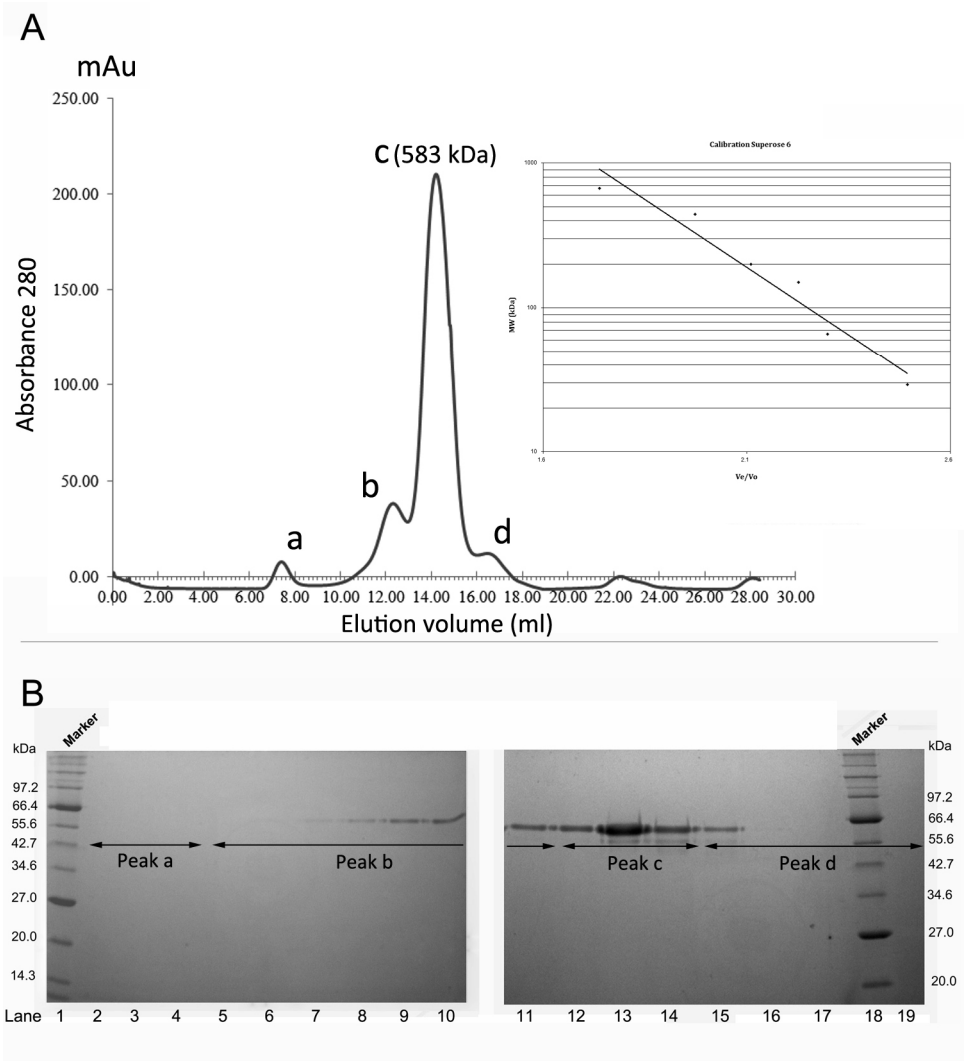

Fig 3.23 SafA purified by gel filtration chromatography under denaturating conditions. (A) Superose 6 chromatogram of SafA. Four peaks were separated: peak c, minor peak a, b and d. Inset image shows calibrated molecular weights. (B) 4-12% SDS-PAGE analysis of SafA fracions selected from peaks a, b, c and d. The samples shown in lanes 2-4 were collected from peak a, lanes 5-11 from peak b, lanes 12-14 from peak c, and lanes 15-19 except lane 18 (Marker) are from peak d. The masses (in kDa) of protein standards are indicated.

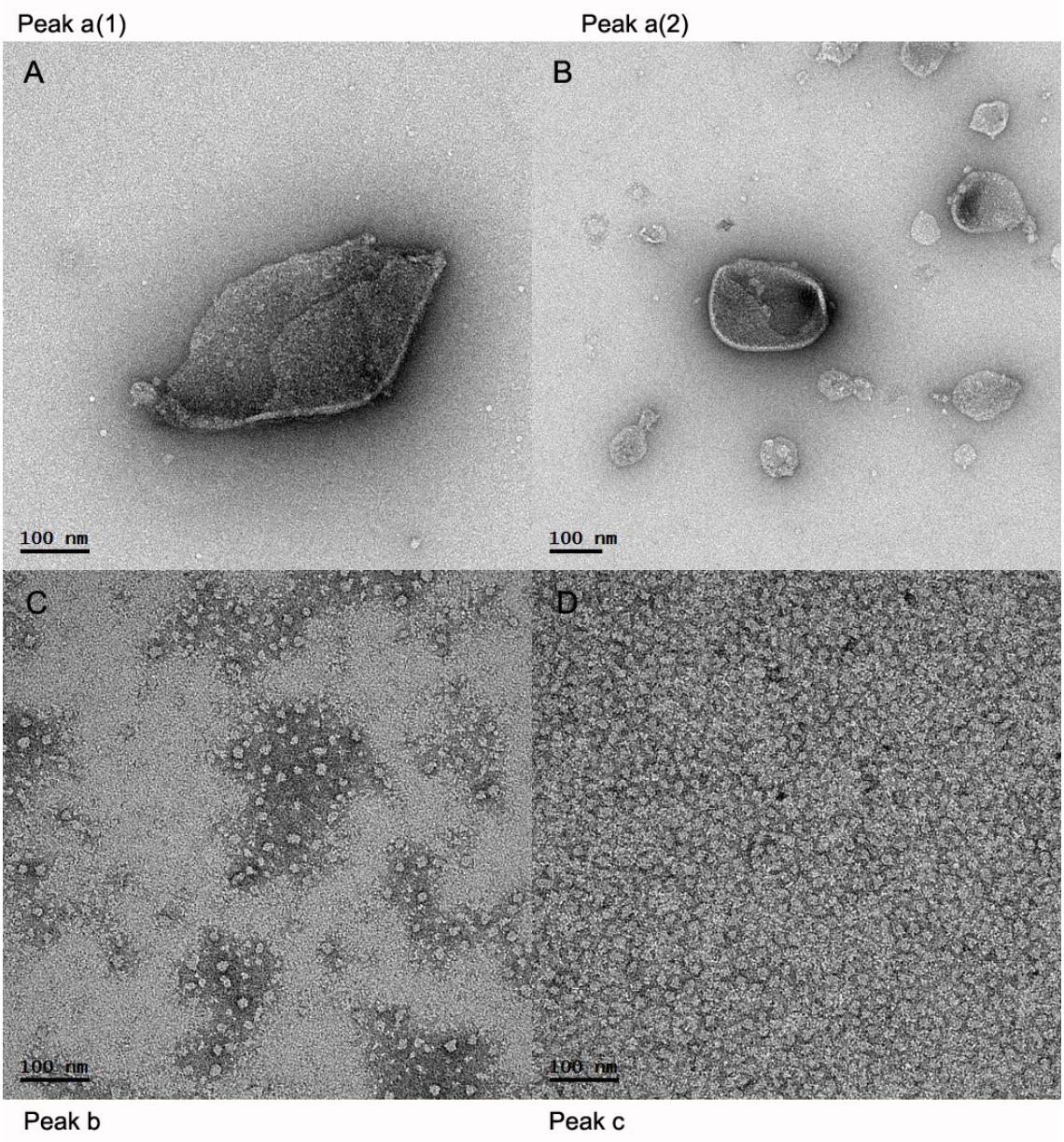

Fig 3.24 Representative micrographs of negatively stained SafA purified under denaturing conditons by SEC. (A-B) Typical images in fractions across peak a in the void volume of the column; (C) Dispersed single particles from peak b; (D) Protein particles detected in peak c. Scale bar for each image is on the left bottom.

N-terminal his-tagged CotH (MW 44.8 kDa) was produced in *E. coli* mostly as a soluble protein and was isolated under both urea and urea-free conditions. The yield when using urea buffers was slightly higher in comparison with native conditions (Fig 3.25). In our study, only CotH obtained in the 0.3 M imidazole elution in urea conditions was used, and the CotH purified protein was separated by Superose 6 column. The CotH protein started to elute in the void volume (peak a) and 2 more peaks, b and c could be observed (Fig 3.26A). The molecular weight of the protein in the highest peak c was estimated at ~470 kDa. SDS-PAGE analyses revealed that all peaks containing a band corresponding to CotH (Fig 3.26B).

3.9.2 Electron microscopy of CotH

Peak a was isolated in the void volume of Superose 6 column with molecular weight outside the column calibration range. Peak a yielded vesicle-like particles not bigger than 100 nm in diameter (Fig 3.27A). Peaks b and c yielded smaller heterogeneous particles (Fig 3.27 B-C). Amorphous aggregations were also found in the peak c sample.

3.10 CotV-CotW

3.10.1 CotV-CotW self assembly analysis by EM and AFM (Atomic force microscopy)

CotV (14 kDa) and CotW (12 kDa) (provided by Daniela Krajcikova, Slovak Academy of Sciences, Bratislava) were co-expressed and purified as previously described (Fig 3.28D) (Krajcikova, Lukacova *et al.* 2009). Negatively stained CotV-CotW preparations were analysed by EM. The most striking feature of these preparations was a network of tangled fibres with a background of more amorphous material (Fig 3.28A). The projected fibres viewed by EM were consistently of ~10 nm diameter. The thickness of the fibres estimated from AFM height images (Fig 3.28C) was similar, indicating that the fibres have a roughly cylindrical cross section. AFM work was done by Jilin Tang, Changchun Institute of Applied Chemistry, China.

We were not able to inspect CotV since the solubility of CotV without coexpression with CotW was extremely low even in urea condtions, but CotW was sufficiently soluble for EM analysis. Negatively stained CotW appeared in projection as a central

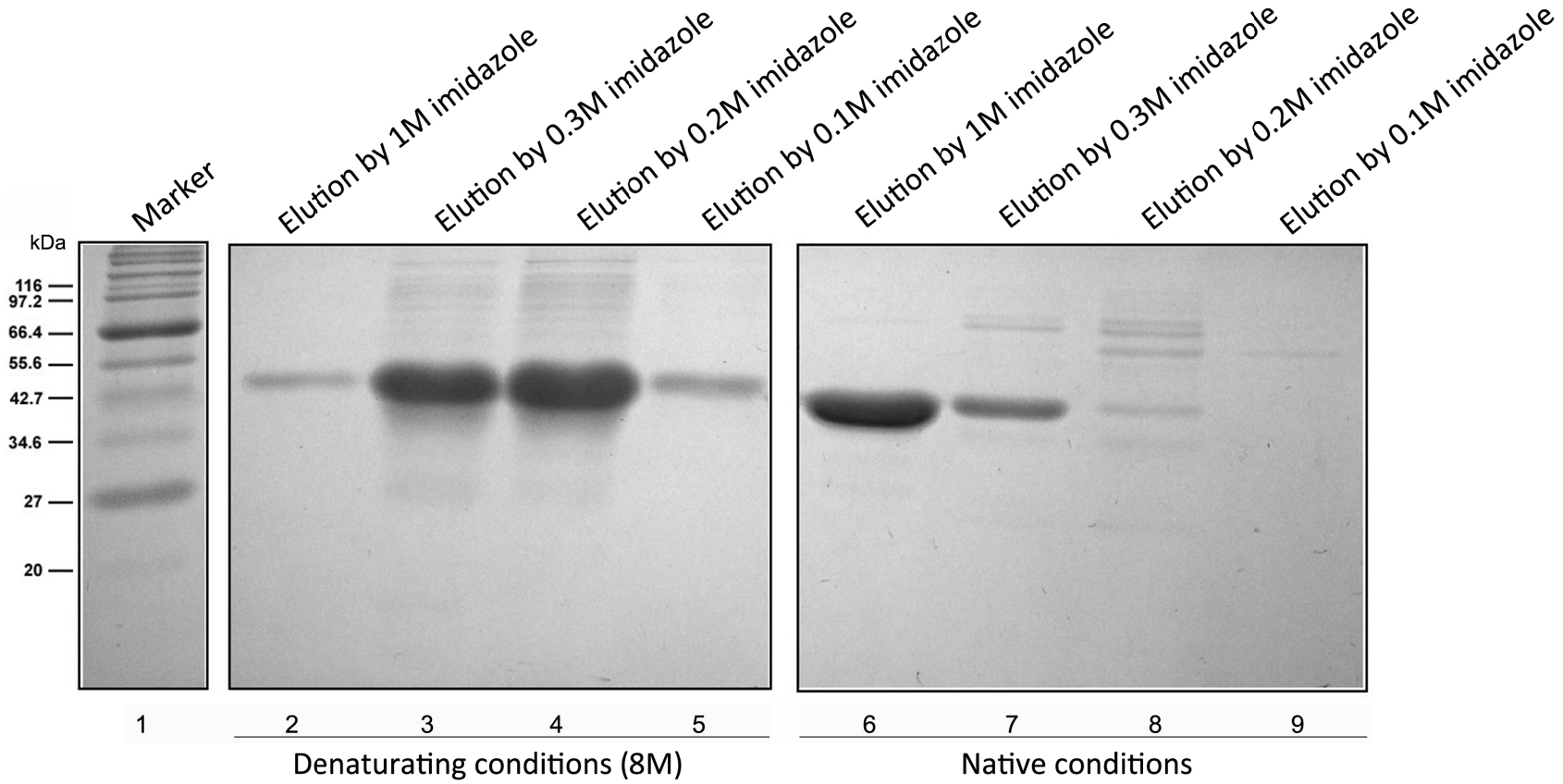

Fig 3.25 Purification of CotH in denaturating conditons (8M urea) and native conditions. Purified proteins were analysis by 4-12% SDS-PAGE. The gels stained with Coomassie brilliant blue. Lanes 2-5 correspond to CotH acquired in 8 M urea conditions and eluted by stepwise concentrations of imidazole. Lanes 6-9 correspond to CotH extracted under native conditions. Protein markers are indicated on the left.

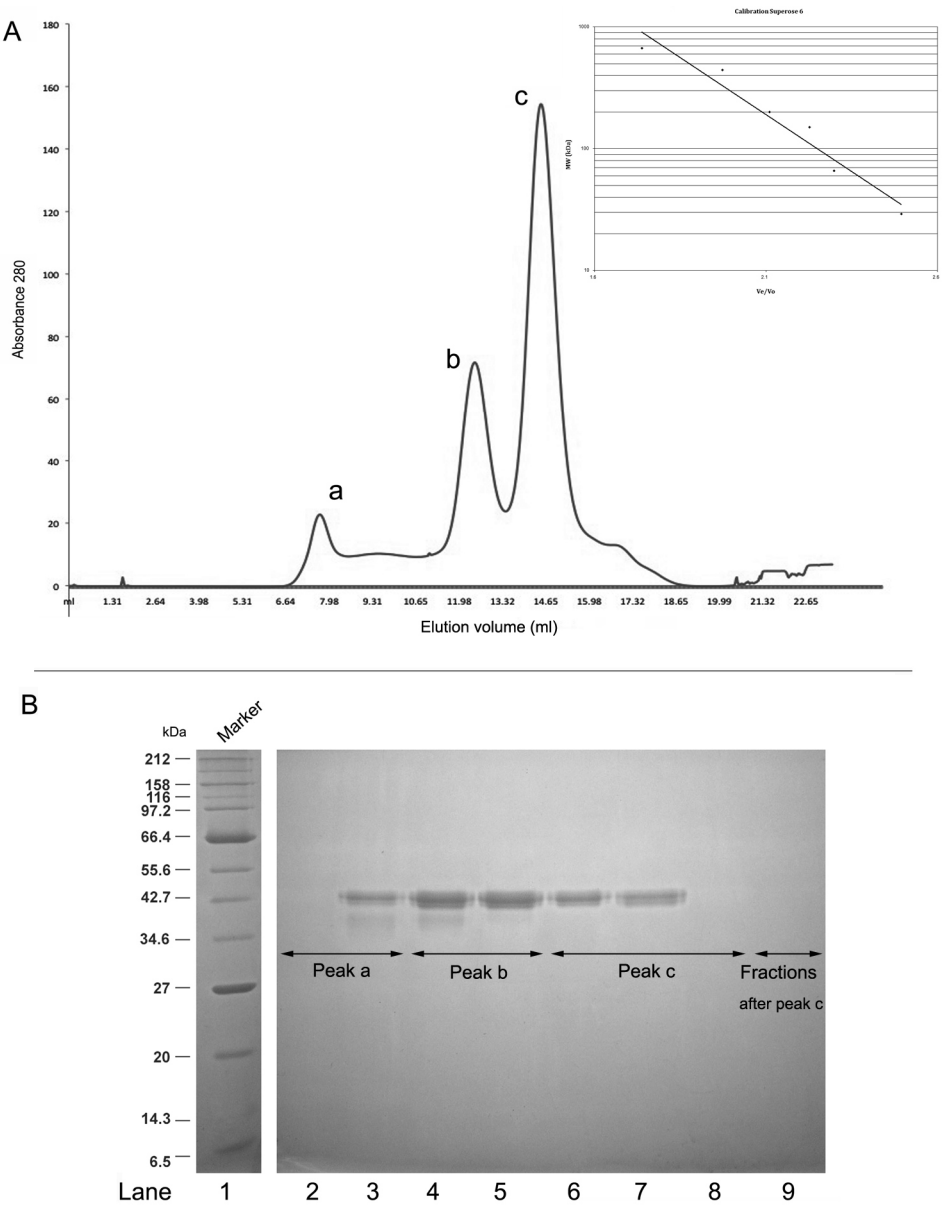

Fig 3.26 SEC analysis of CotH under denaturating conditions. (A) Superose-6 chromatogram of CotH. Three peaks were separated: peak a, b and c. Inset image shows calibrated molecular weights; (B) 4-12% SDS-PAGE analysis of selected CotH fractions from the range over peaks a, b and c. The samples shown in lanes 2-3 were collected from peak a, lanes 4-5 correspond to peak b, lanes 6-8 correspond to peak c, and lane 9 correspond to fractions after peak c. Molecular weight (in kDa) of protein standards are indicated on the left.

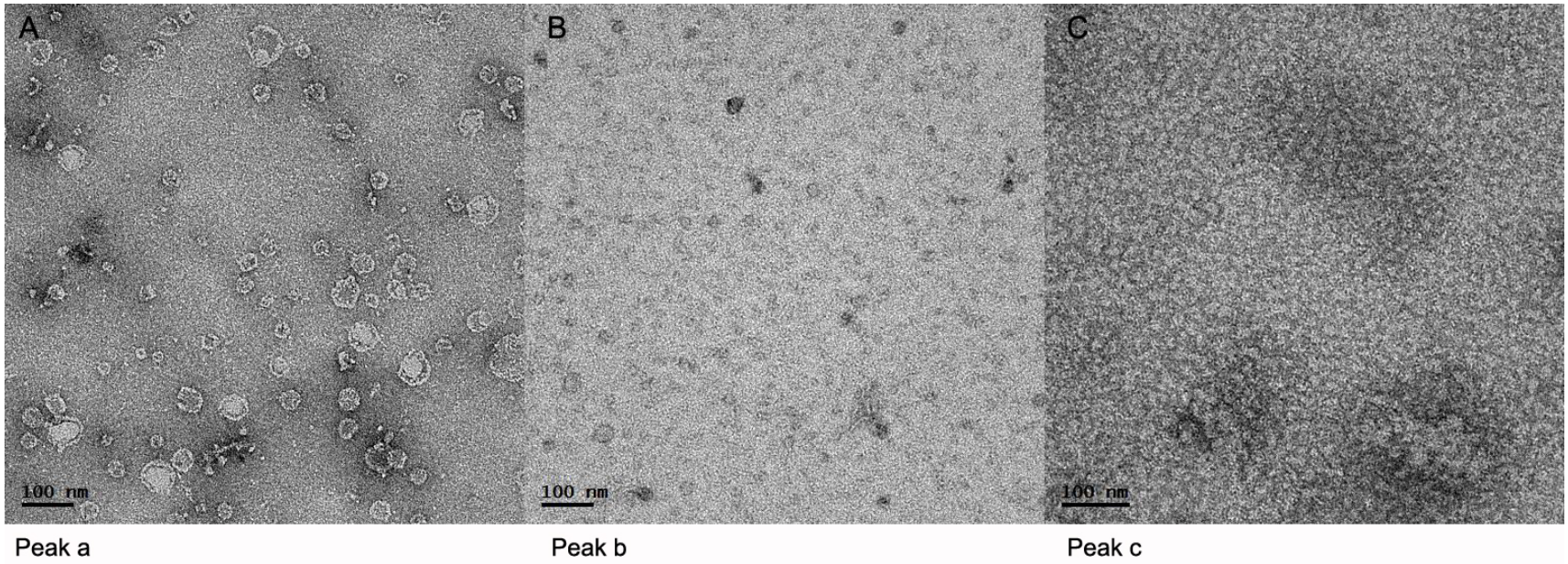

Figure 3.27 Representative images of negatively stained CotH fractions purified by SEC under denaturating conditions. (A) Protein fraction of peak a; (B) Protein fraction of peak b; (C) Protein fraction of peak c. The scale bar for each image is on the left bottom.

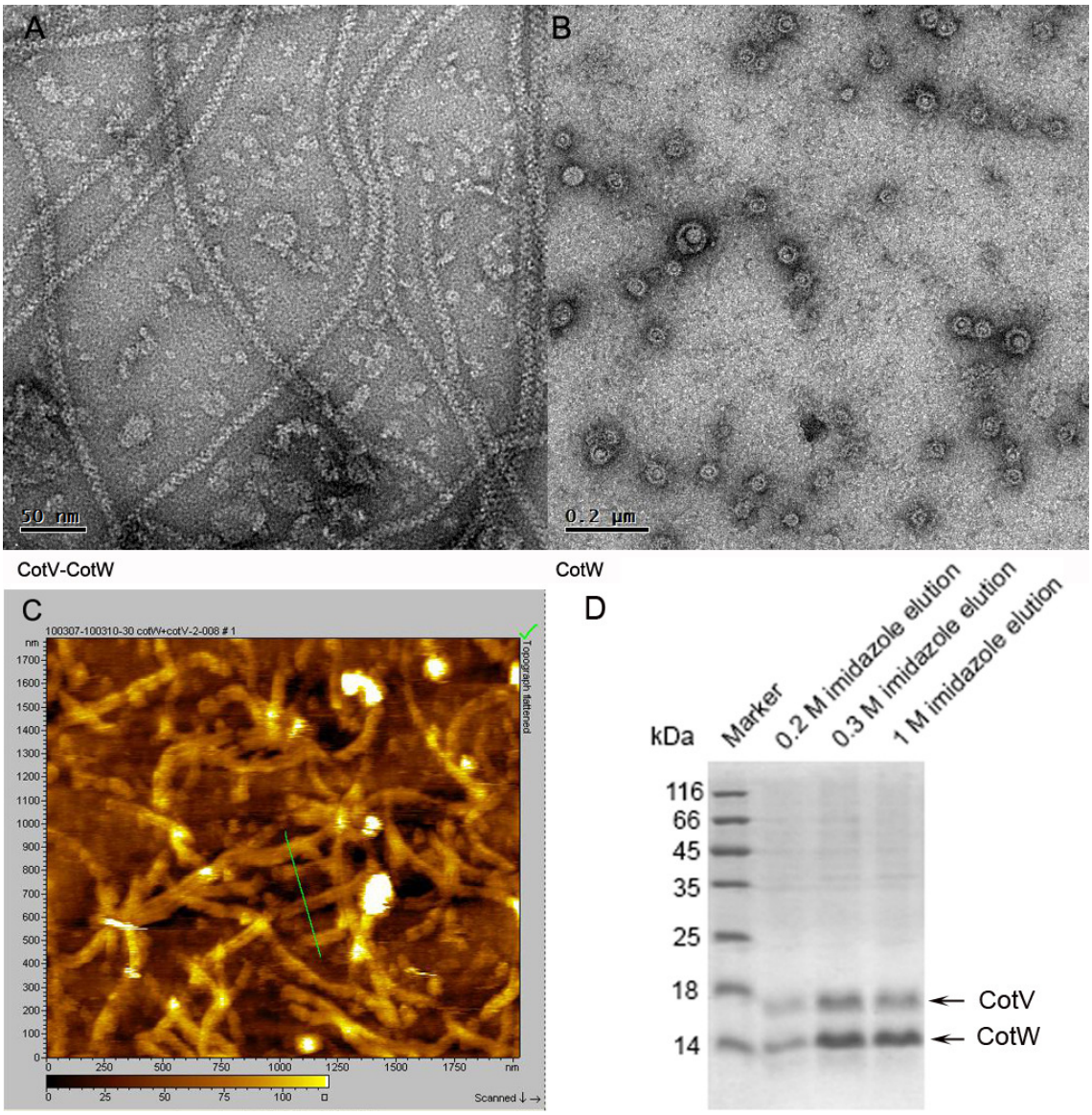

Figure 3.28 Negatively stained image of CotV-CotW and CotW. Co-expressed CotV-CotW shows distinct fibrous assemblies and debris in panel A. Panel B shows bowl-shaped complexes assembled by CotW alone. Panel C shows atomic force microscope analusis (height image) of CotV-CotW surface (Jilin Tang, Changchun Institute of Applied Chemistry, China.). Scale bar for each image is on the left bottom. Panel D shows the coexpression of CotV-CotW. The positions of CotV and CotW were indicated by arrows.

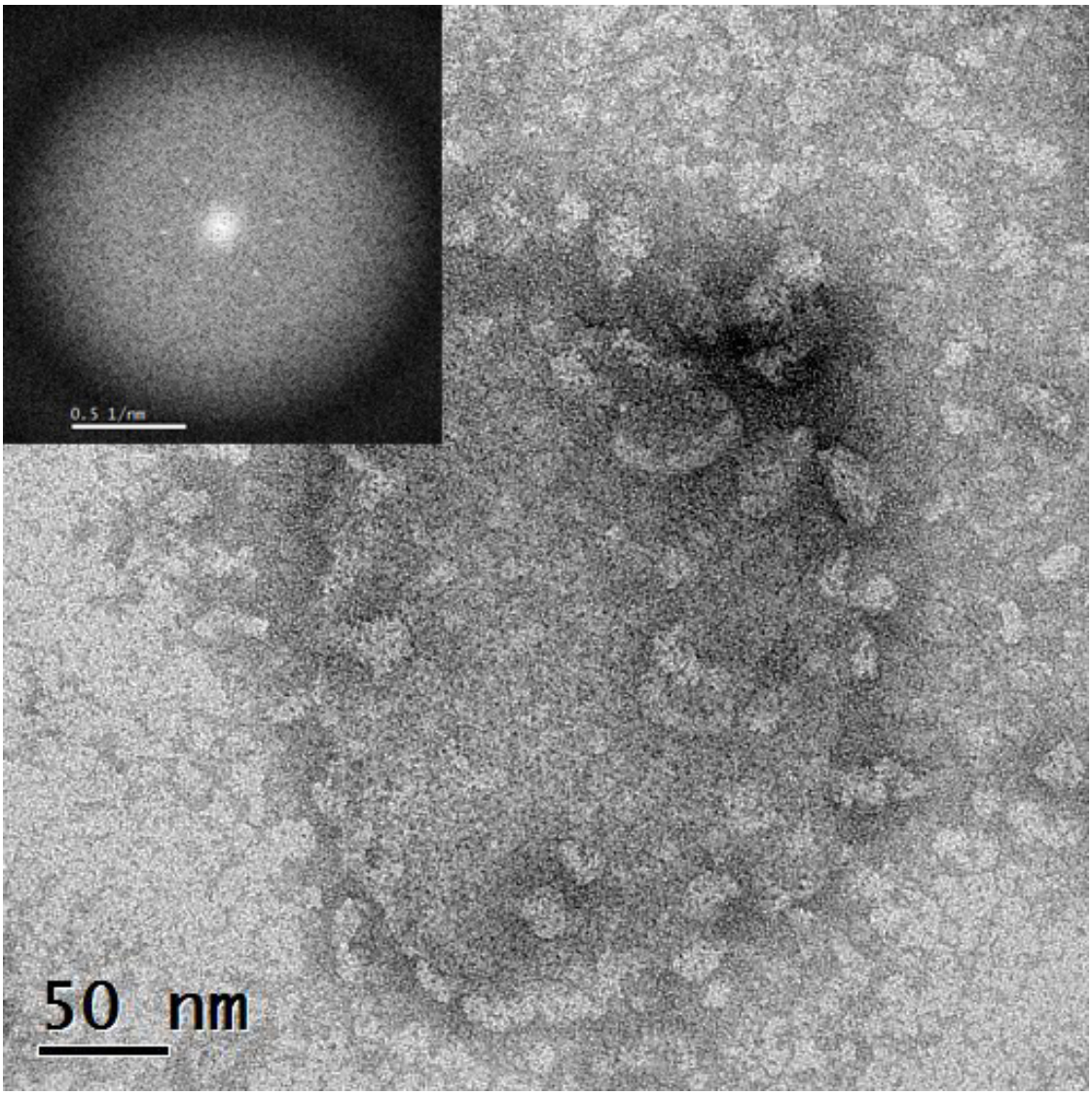

Fig 3.29 Representative images of negatively stained ExsY. Crystal sheets were yielded by ExsY with few aggregates. A computer generated Fourier transform in the inset shows a distinct diffraction pattern of the ExsY crystal. The scale bar for image is on the bottom left.

stain-excluding density encircled by a stain-filled moat and an outer stain-excluding ring (Fig 3.28B). These characteristic particles were absent in images of negatively stained co-expressed CotV-CotW preparations. We did not observe fibres in preparations of pure CotW, suggesting that the fibres are assembled from both proteins in a fixed stoichiometry.

3.11 ExsY

3.11.1 Electron microscopy of ExsY

In our study, the recombinant ExsY protein of *B. cereus* was provided by Dr. David Radford, Sheffield. The ExsY recombinant protein contained two series of his-tag, one in N-terminal and the other one in C-terminal. As CotY, ExsY yielded ordered arrays (Fig 3.29) along with a background of amorphous particles. More detail about 3D model reconstruction will be given in the next chapter.

3.12 Discussion

Most of the protein components of the spore coat are now well established. However, the assembly mechanism and structures of the spore proteins are still poorly understood.

Historically, it has been challenging to extract protein components from the spore, which requires rather harsh treatments. Instead, in our approach, we have focused on defined, heterologously overexpressed polyhistidine-tagged proteins. These proteins were purified with nickel affinity chromatography and initially characterized by size exclusion chromatography and negative stain EM. We examined a number of recombinant *B. subtilis* spore coat proteins CotY, CotE, CotZ, CotE-CotZ, SpoIVA, SpoVID, SafA, CotH, CotV, CotW and the *B. cereus* exosporium protein ExsY, some in the presence or absence of urea (Table 3.1). The chromatography profiles of these proteins generally consisted of multiple peaks, corresponding to a variety of aggregation/ multimer states but some proteins were robust enough to fold into higher ordered structures and were amenable to electron microscopy at molecular resolutions. Spore coat proteins like CotY, SafA, CotE-CotZ, CotV-CotW and *B. cereus* ExsY were found to self-assemble in an ordered manner, in which notably CotY and ExsY were able to assemble into crystal structures. What is quite intriguing is that CotY and ExsY crystals, and CotY protein particles were not denatured even in 8M urea. Probably the

Spore protein	length	Molecular weight	Purification conditions	EM observation
CotY-his	181 aa	19.9 kDa	Denaturating (8 M urea)	Crystal pieces and single particles
CotE-his	201 aa	23.1 kDa	Denaturating (8 M urea)/native	Heterogeneous particles and aggregates in 8M urea conditions
CotZ-his	167 aa	18.6 kDa	Denaturating (8 M urea)	Aggregates and heterogeneous particles
CotE-CotZ				Mesh-net structure
SpoIVA-his	511 aa	57.2 kDa	Denaturating (8 M urea)	Sac-like aggregates and particles
SpoIVA his - truncated	419 aa	46.8 kDa	Denaturating (8 M urea)	Aggregates and particles
SpoVID-his	595 aa	67.1 kDa	Native	Aggregates and particles
SafA-his	399 aa	44.6 kDa	Denaturating (8 M urea)/native	Cluster formed by particles and single particles in both conditions
CotH-his	381 aa	44.8 kDa	Denaturating (8 M urea)/native	Aggregates in 8M urea conditions
CotW-his	125 aa	14.5 kDa	Native	Heterogeneous particles
CotV-CotW				Fibre assemblies
ExsY	154 aa	17.9 kDa	Denaturating (8 M urea)	Crystal pieces and aggregates

Table 3.1 A number of spore coat protein and exosporium ExsY identified in this chapter. The supportive information includes amino acid length of each protein, molecular weight, purification conditions and their assemblies observed by EM.

structures are so compactly folded that urea did not penetrate. Presumably, this is a feature of CotY that is capable of self-assembling into such a rigid structure - to participate in formation of coat which is also very compact and hard to solubilize. In addition to crystals, symmetric single particles were seen for CotY. Some trials have been set by incubating single particles, such as dialysis of CotY single particles against phosphate buffer (Protein concentration is about 0.5 mg/ml) to see if it was able to form crystal. In no condition were we able to induce isolated particles to form two-dimensional array. The reasons for this might be kinetic, perhaps a rare nucleation event or higher protein concentration are required.

SafA appeared to assemble into uniformly sized higher order structures. As an important spore morphogenetic protein, SafA is localized at the interface between the coat and cortex in the spore, associating with SpoVID and CotH and controlling the deposition of spore coat components. For SafA, it has been purified to homogeneity by assembling into uniformly sized, possibly spherical particles of 20 nm in diameter and a possible MW of 4000 kDa (estimated base on assuming SafA a globular protein). Under conditions with or without urea, SafA was purified to particles with consistent projected diameter.

We identified CotW protein complexes by EM observation and it appeared to be a central stain-excluding density encircled by a stain-filled moat and an outer stain-excluding ring (Fig 3.28B). We occasionally noticed similar particles in the CotV-CotW preparation but we have not seen a consistent physical association between particles and fibres.

The exact provenance of these fibres is unclear but fibrous assemblies have been observed *in situ*. The fibres in our study have approximately the same diameter as fibrous structures generated by sonic treatment of spore coat and by renaturation reported by Goldman *et al* (Goldman and Tipper 1978). Furthermore, CotW has been assigned to the outermost regions of the coat, possibly the crust (Kim, Hahn *et al.* 2006; McKenney, Driks *et al.* 2010). This is consistent with the observation, by freeze-etch EM of long fibres traversing the spore in a layer just underneath the outermost shell (Holt and Leadbetter 1969; Aronson and Fitz-James 1976). The lateral spacing of these fibres appears to range from 5 to 10 nm that is close to our measurement of 10 nm diameter for the putative CotV-CotW fibres. In the *B. cereus* family much shorter, ribbon-like

assemblies of diameter 3 to 13 nm were observed forming a layer (cross-patched layer) over the pitted-layer substructure (Aronson and Fitz-James 1976). Using AFM, Plomp *et al*. observed long fibrous structures (rodlets) in a 10 nm thick layer of *B. thuringiensis* spores (8 nm spacing) and smaller, randomly oriented patches of fibres in *B. cereus* (Plomp, Leighton *et al*. 2005). On the other hand, AFM scanning of *B. atropheus* shows rodlets undergoing disassembly (Plomp, Leighton *et al.* 2005) and it is difficult to see how arrays of our CotV-CotW fibres could disassemble in such a fashion, where weaknesses appear to run perpendicular to the rodlets rather than parallel. Whether or not the fibres/rodlets correspond to CotV-CotW remains an open question. Confirmation awaits higher resolution *in situ* data and/or labelling studies.

B. subtilis spores do not have an exosporium; CotY and CotZ are localized in the insoluble outer layer of the *B. subtilis* spore coat, also called the spore crust (Imamura, Kuwana *et al*. 2011). ExsY of *B. cereus* shares 37% identity to the CotY of *B. subtilis*. During spore assembly, ExsY and CotY are required for the correct assembly of the exosporium and spore coat (Boydston, Yue *et al.* 2006; Johnson, Todd *et al.* 2006; Steichen, Kearney *et al.* 2007). Part of the exosporium is naturally crystalline in some of the *Bacillus* spores like *B. anthracis* and *B. cereus.* The native crystalline exosporium leads us to speculate that a large part of the natural two-dimensional crystal may consist of crystalline ExsY (a homologue of CotY) and/or CotY. Although CotY has been proposed as a component of the crust of *B. subtilis*, whether or not CotY forms natural two-dimensional arrays in the *B. subtilis* spore is still unknown.

Since crystallization occurred in purified CotY, we identified its homologous protein ExsY of *B. cereus* to see if it is also capable of crystallizing. Surprisingly, it also formed into two-dimensional arrays in urea conditions. The ability to self-assemble as a crystal might reflect part of its function in the correct formation of the exosporium. We have not looked into other CotY/ExsY orthologues, such as CotY of *B. cereus* but we might anticipate similar results.

Although both CotY and its homologue protein ExsY could self-assemble to 2D-crystal structures, the other homologue, CotZ of *B. subtilis* did not behave as CotY in our purification and EM approach; for example, we were not able to isolate homogeneous single particles or crystalline arrays. Additionally, we tried to analyse fractions from a

CotY/CotZ mixture, but did not observe two-dimensional crystals in the void volume that appeared similar to those seen for pure CotY (data not shown). We were not able to confirm whether the crystals were assembled by CotY alone or a mixture of CotY/CotZ.

For the rest of proteins investigated like CotE, CotE-CotZ, SpoIVA, SpoVID and CotH, they are to some extent able to form protein complexes. We found that the solubility of CotZ could be maintained after dialysis of urea if CotE was present and occasionally noticed in the void volume fraction quasi-crystalline net-like structures with an average repeat of ~ 200 Å. These arrays had much larger and more variable spacing than the CotY crystal. Nevertheless it is possible that these nets represent a type of assembly that might be found at some stage in spore coat construction. Since we were unable to isolate these nets from pure CotE or CotZ preparations, it is possible that they either contain both CotZ and CotE or that CotE is able to catalyse formation of pure CotZ nets, in an alternative path to amorphous aggregation. Such a role has indeed been inferred for CotE *in vivo*.

In both forms of SpoIVA, a small amount of protein particles with varying size could be seen. The correlation of vesicle structure in full SpoIVA and protein particles is still uncertain. With respect to structure analysis, without a well-ordered array, we could not proceed further on them.

CotE, SpoIVA, SpoVID and CotH formed disordered protein aggregates. CotE, CotH, SpoIVA were able to assemble into high molecular weight vesicle-like species with a wide range of sizes. Single particle structure was also detected in CotE, SpoIVA, and SpoVID. The particles from CotE and SpoVID and truncated SpoVIA were not of uniform size, whilst particles from full-sized SpoVIA appeared to be homogeneous, which could be considered to be appropriate for single particle analysis. The interaction network among the spore coat protein has been mapping out, among the spore coat proteins we are currently working on, CotE was found to interact with SpoVID (de Francesco, Jacobs *et al.* 2012), SpoVID and SafA interaction was reported as well (Costa, Isidro *et al.* 2006). These interactions among spore coat proteins may produce protein complexes which are likely their part of function involved into the spore coat assembly. These interactions are also the foundation of the next-stage work: to observe

the complexes formed by protein-protein interactions and elucidate how single component or multi-components contribute to the entire spore coat architecture.

CHAPTER 4

Electron crystallography and single particle analysis of the spore coat proteins

4.1 Introduction

In our study, as described in previous chapter, a variety of spore coat protein including CotY, CotE, CotZ, CotW, CotH, SafA, SpoIVA and SpoVID have been heterologously expressed, purified and analysed by SEC and EM. The preliminary results indicated that crystals formed by *B. subtilis* CotY and *B. cereus* ExsY were suitable for electron crystallographic analysis, and single particles formed by CotY and SafA are good candidates for single particle analysis. For CotV-CotW the repetitive helical fibre structure is also viable for single particle analysis. A number of the coat proteins that we investigated such as CotE, CotZ, and SpoIVA did not build up structurally ordered arrays to which we could apply further structural analysis.

4.2 CotY single particle analysis

In the previous chapter, we described the successful purification of CotY under denaturating conditions. Purified CotY was eluted in 3 main peaks folloing SEC. EM revealed the crystal pieces appeared in the first peak and abundant single particles appeared in the last peak (Fig 3.2).

For single particle analysis, to ensure adequate particles to extract information for structure determination, a substantial amount of negatively stained CotY particles micrographs were taken. One representative image is shown in (Fig 4.1), the gel filtration fraction from peak c (Fig 3.2) was appropriately diluted to give well-dispersed particles (Fig 4.1). Many of the particles appeared to have a stain-filled cavity located in the centre of the particle (e.g. circled particles in Fig. 4.1).

All the images were processed within the image processing software suite IMAGIC 5 (Vanheel and Keegstra 1981; van Heel, Harauz *et al.* 1996; van Heel, Gowen *et al.* 2000). Approximately 2,500 particles formed by CotY were manually picked out from individual micrographs. The diameter of the CotY single particles was 11-13 nm. Individual particles were extracted in boxes of 80 x 80 pixels corresponding to about 3x

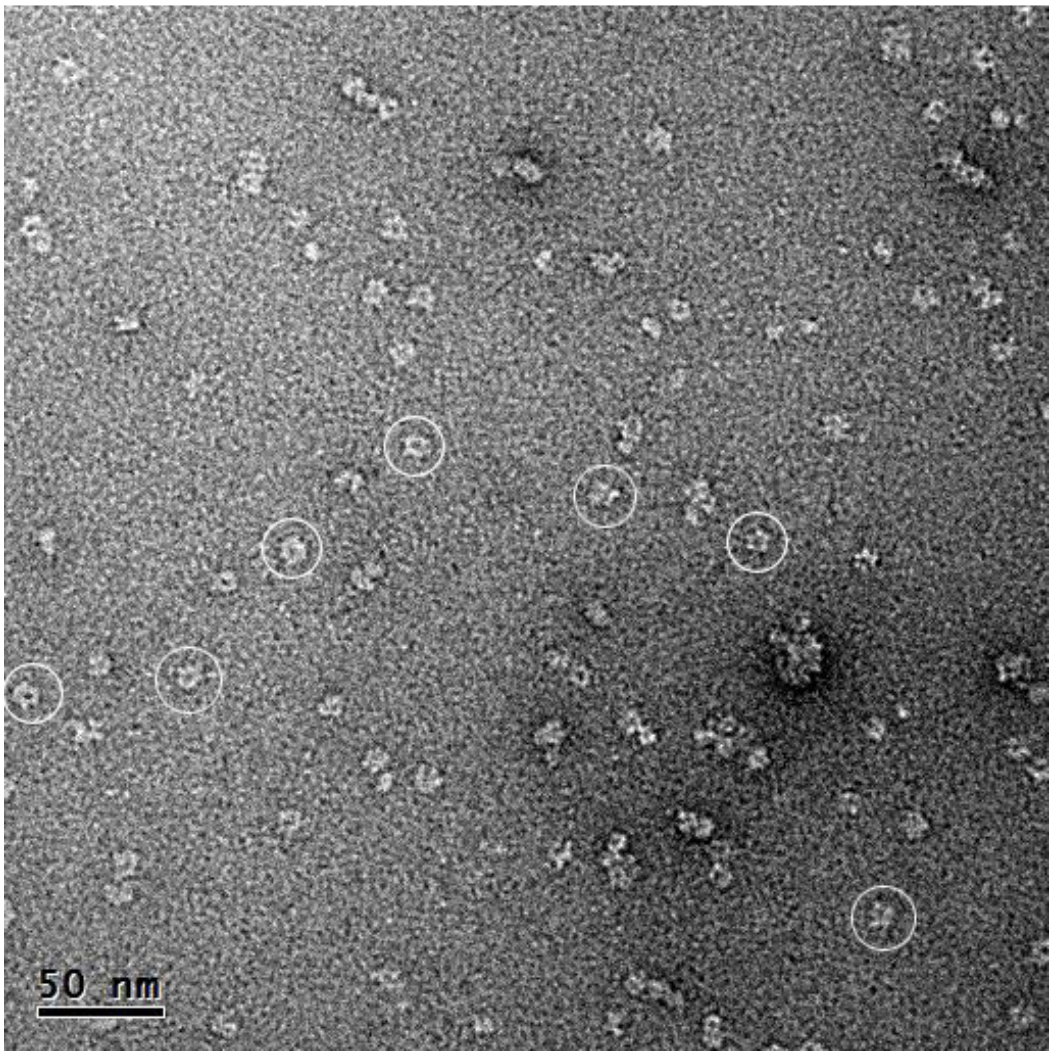

Fig 4.1 Electron micrograph of negatively stained particles from fractions of peak c (Fig 3.2 and 3.3). It shows some characteristic particles that are enclosed by white circles showing the stain-filled cavity in the centre. Scale bar was indicated on the left bottom.

of their diameter (pixel size: 0.39 nm/pixel). The particles were subjected to cycles of multi-reference alignment and multivariate statistical analysis (MSA) (Fig 4.2A). The eigenimages were output from MSA-RUN and gave an idea about the main differences found in the dataset. The first eigenimage always shows the average of all images. The third, forth and fifth eigen images revealed symmetry information, which for CotY suggests that the particle's symmetry is 6-fold (Fig 4.2A).

We started with 10 class averages and eventually reduced these to 7 stable class average images and all seven averages are shown in Fig 4.2B. The CotY particles appeared to be 6-fold rotational symmetry. An evident hole/cavity in the centre of particles was clearly visible. It is likely that the single particles of CotY appeared to assemble into oligomers with six-fold projection symmetry suggesting that they might be hexametric. This assignment was further supported by our crystallographic analysis on CotY crystal, which is depicted later.

4.3 SafA single particle analysis

The same single particle analysis procedures were applied to SafA. According to the profile of the chromatogram, and in combination with EM observation, the SafA fraction was selected and diluted to an appropriate concentration to ensure the protein particle could be well enough dispersed for particle selection in the images. Shown in Fig 4.3, is a representative particle micrograph which was used for particle selection. 2, 493 particles were manually picked and cut out by a box with size 80 x 80 pixels (Pixel size is 0.39nm/pixel). The boxed particles were normalized, band-pass filtered and aligned. The dataset was band-pass filtered and translationally aligned to a rotational averaged total sum. Iterated steps from average to alignment were run for 5 rounds and aligned output dataset for MSA. The rotational average of total sum of particles appeared to be circular structure (Fig 4.4A)

The particle projections in the micrographs were measured at approximately 13-15 nm, so we masked particle to define the interesting area. The previous aligned images were subjected to MSA. The resulting eigenimages indicated a rotational symmetry and some

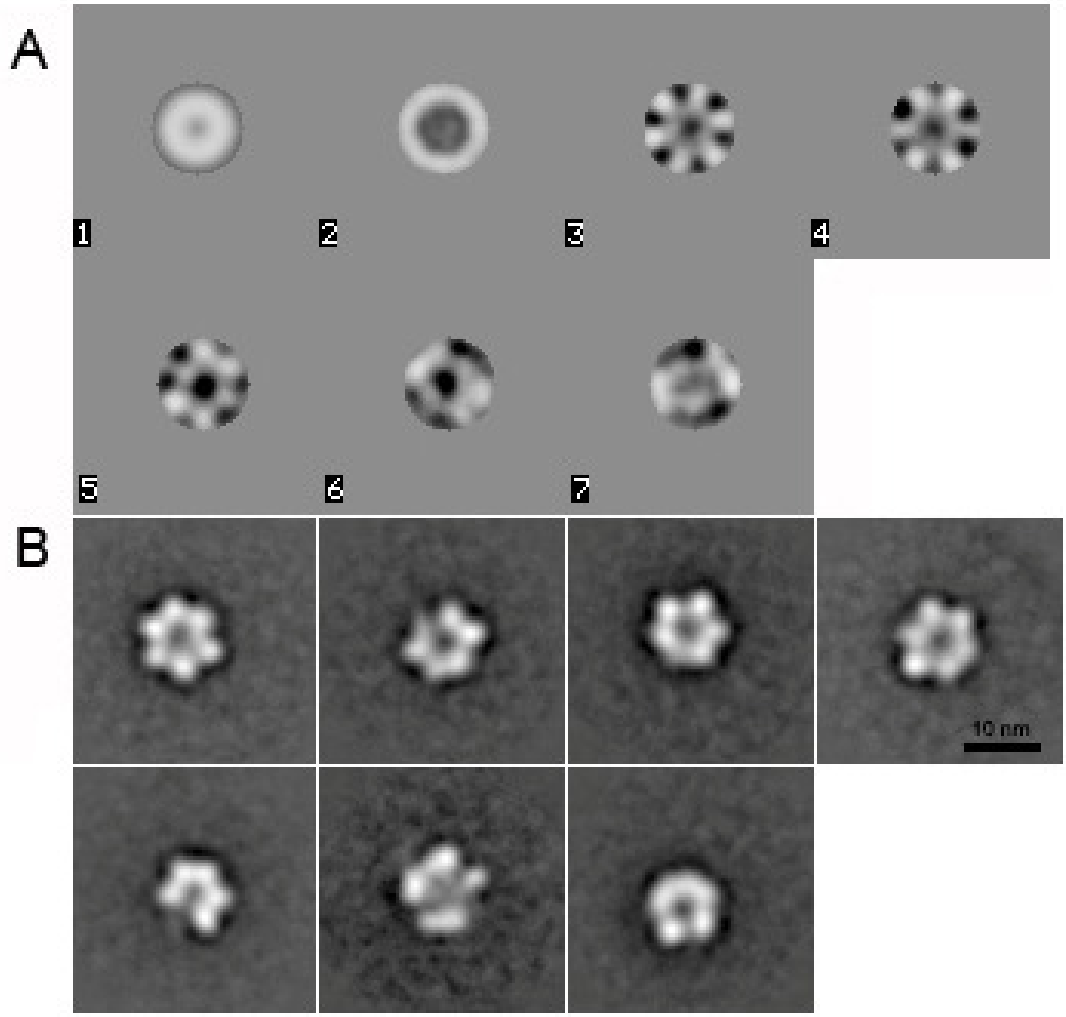

Fig 4.2 Single particle analysis of CotY. (A) Eigen images from multivariate statistical analysis; (1) is the rotational average of the particles; (2) arises from the variation in diameter, probably through staining variations; (3-5) show the information of the symmetry which indicates 6-fold symmetry; (6-7) show the stretch of particles which is caused by staining (B) Seven images of class average. Scale bar = 10 nm.

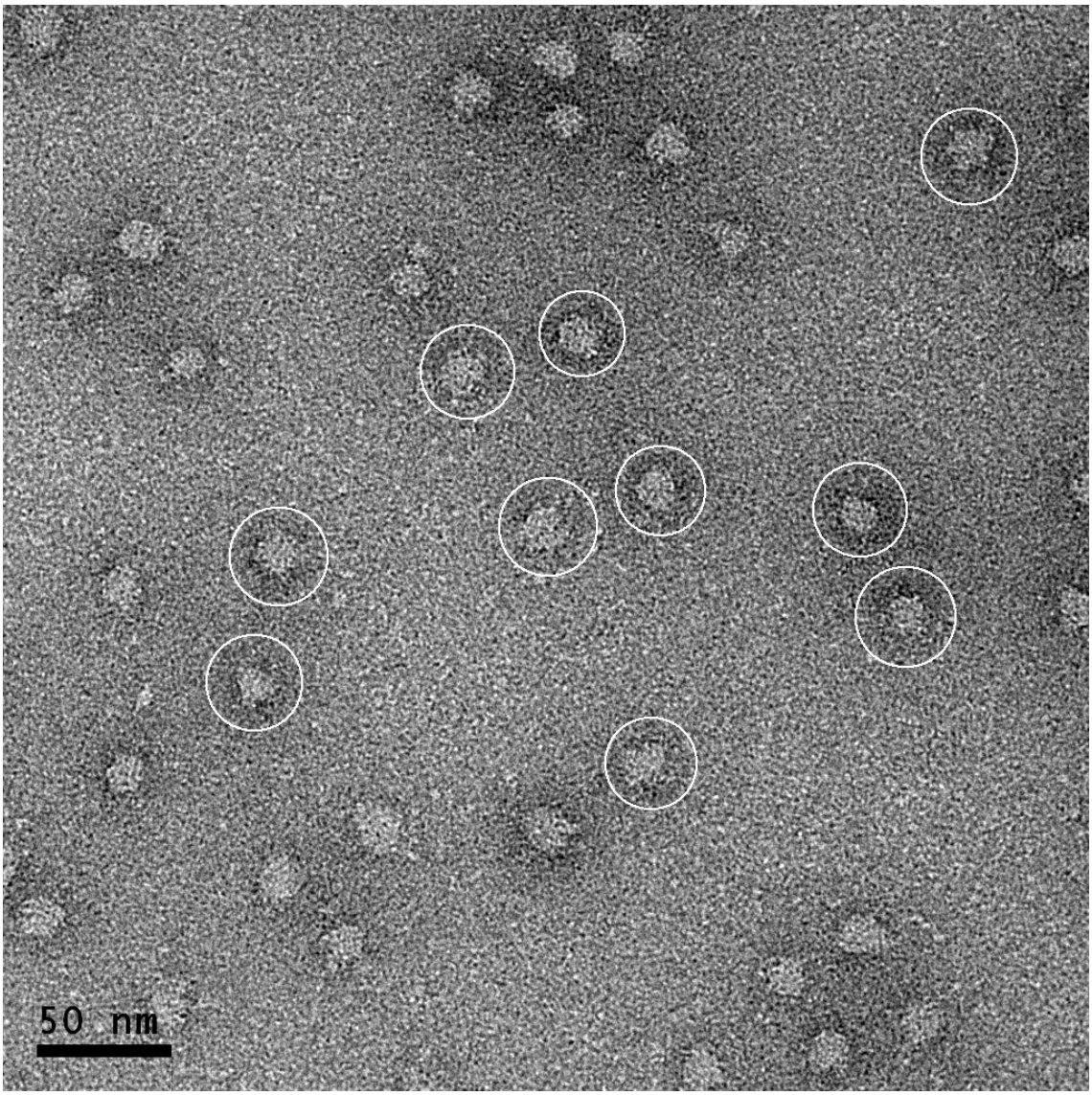

Fig 4.3 shows electron micrograph of negatively stained particles of SafA. Some representative particles were enclosed by white circles.

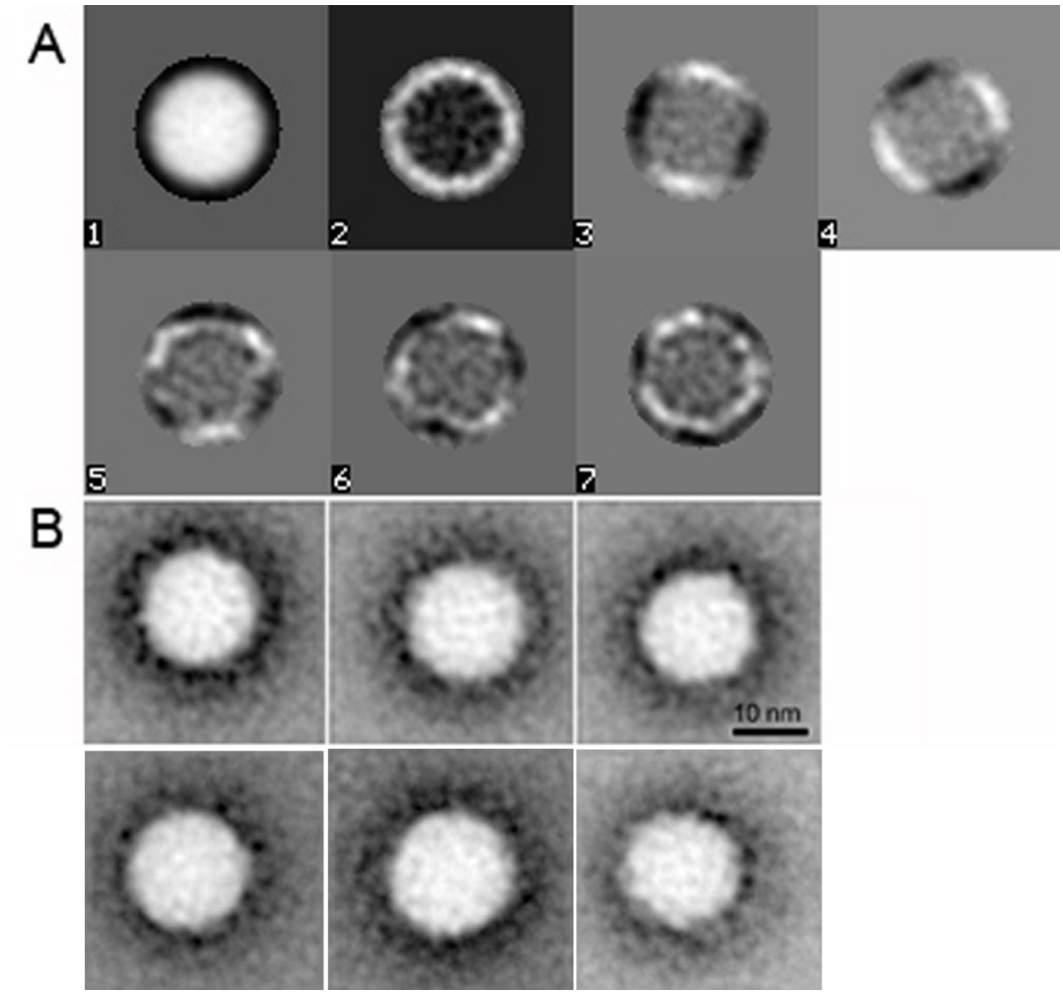

Fig 4.4 Single particle analysis of SafA. (A) Eigenimages from multivariate statistical analysis; (1) is the rotational average of the particles; (2) is the variation in diameter; (3-5) show the information of the symmetry; (6-7) show the stretch of particles which is caused by staining (B) All six images of class average. Scale bar = 10 nm.

variations in stretching in one direction (Fig 4.4A). The classification started with a 50 classes. Due to quite a few similar views, the number of classes was gradually reduced round by round. Eventually, after 5 iterations of MSA, 6 stable class average images were obtained and shown in Fig 4.4B. Six representative class averages indicated that there is no obvious and structural feature to distinguish them. The projections could arise from a sphere but this cannot be proved without a full three dimensional analysis.

4.4 TEM analysis of CotY crystal using negative stain

CotY, as described in last chapter, formed well-ordered arrays with a distinct diffraction in computer-generated Fourier transforms. To extract more information about the crystal and reconstruct 2D/3D model, we collected images from tilt series (-50° to 50°, 10° interval). Some of the images were collected from the protein fraction after size exclusion chromatography and some acquired from the elution of nickel column with imidazole (usually by 0.3M imidazole).

Fig 4.5 shows negatively stained CotY two-dimensional crystals with a distinct diffraction pattern. A number of non-tilted CotY crystal micrographs were processed and all crystals have a similar overall appearance with the same unit cell dimensions a = 86.8 ± 0.8 Å, b = 86.4 ± 1.4 Å, γ = 119.4° ± 1.1.

The optimal space group was thereby chosen and corresponding phase origin was determined (Table 4.1). For all CotY samples tested, space group determination indicated that *p*3 is consistent across all images, whilst a subset of these images were also consistent with *p321* (Table 4.1). The *p*3 plane group was therefore chosen as a conservative approach for all further processing of crystals.

In our crystal galleries, the crystal almost never fills the entire image, so it makes no sense to use the area where the crystal is not regular or no crystal exists but background. The way we processed was to mask out the crystal area from the whole image in light of the indication of correlation map that shows the cross-correlation profile generated during unbending the crystal (Fig 4.6). After masking the crystal, the standard scripts were run again. Final step of processing was the generation of the density projection map and grey-level map. An unsymmetrized map and symmetrized map were created

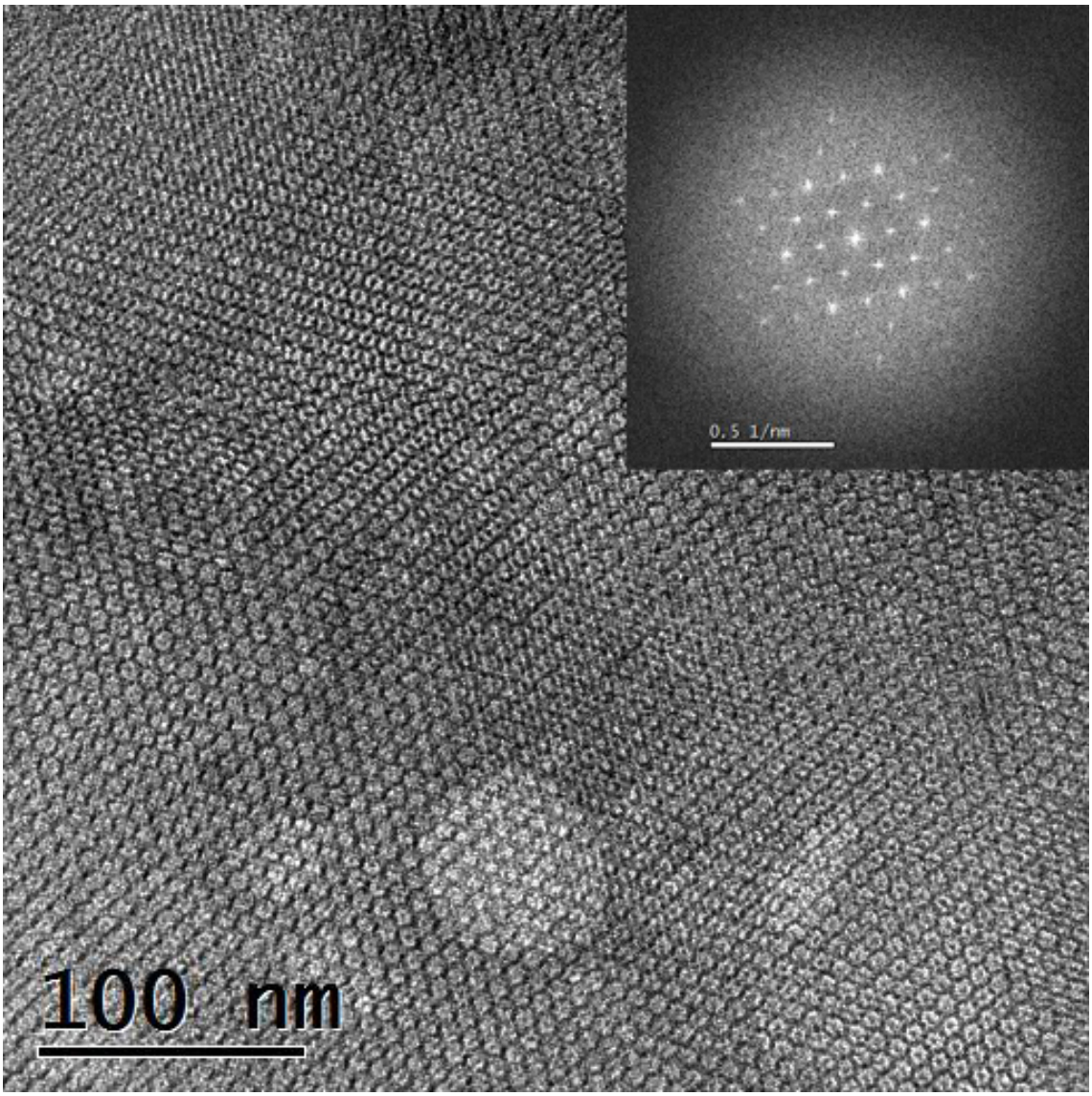

Fig 4.5 Electron micrograph of very large negatively stained crystal sheet of CotY. Computer-generated Fourier transform of crystal in a inset figure showing distinct diffraction pattern.

Table 4.1 The internal phase residuals determined after the imposition of all possible two-sided plane groups calculated from one of the micrographs of CotY crystals.

Two sided plane group	Phase residual versus with other spot (90° random)	Number of comparisons	Target residual based on statistics taking Friedel weight into account
*p*1	21.3	40	
*p*2	45.2	20	30.8
*p*12_b	37.9	11	23.9
*p*12_a	60.9	11	23.9
*p*121_a	66.8	11	23.9
*p*121_b	45.4	11	23.9
*c*12_b	37.9	11	23.9
*c*12_a	60.9	11	23.9
*p*222	58.5	42	25.8
*p*2221b	45.1	42	25.8
*p*2221a	71.0	42	25.8
*p*22121	60.8	42	25.8
*c*222	58.5	42	25.8
*p*4	55.9	48	25.3
*p*422	51.1	102	23.2
*p*4212	62.5	102	23.2
*p*3	9.5*	34	21.3
*p*312	28.0	78	22.0
*p*321	18.2*	80	22.3
*p*6	30.1	88	23.5
p622	33.7	178	22.4

Internal phase residuals were determined from spots of IQ1-1Q5 to 20Å resolution. The values marked with * are good candidates for the symmetry as the experimental phase residual is close to that expected value based on the signal-to-noise ratio.

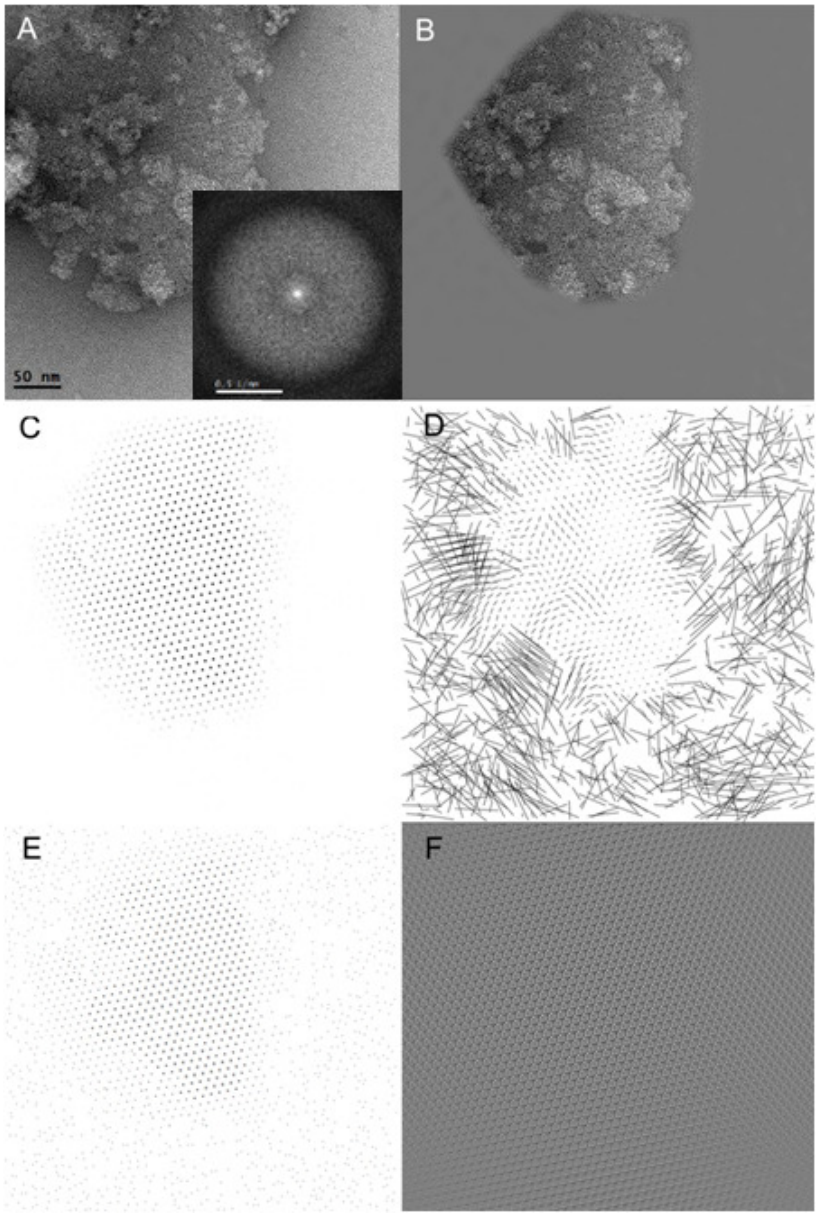

Fig 4.6 CotY crystal masking and steps of image unbending. (A) is the raw image with diffraction shown in the inset; (B) is the crystal masked out from non-crystalline areas; (C) Correlation map that shows the cross-relation profile from chosen area of (B); (D) Vector plot of distortion from the ideal crystal lattice allows the original image to be unbent. It shows deviations from the ideal crystal. Vectors are plotted as 10 times elongated; (E) Correlation map of original image. Darker symbols indicate higher correlation; (F) Unbent and Fourier-filtered image.

(Fig 4.7). In CotY crystal projection map, the most prominent feature in each case is a lattice of heavily stained pits surrounded by three distinct stain-excluding densities.

4.5 Three-dimensional reconstruction of CotY crystal

All individual images recorded by an EM are 2D projections of 3D density. Therefore to generate a 3D CotY model, it is necessary to combine a number of 2D projection maps from a range of different tilt angles, from which the tilt images provide different views of the structure. Many tilted series from different angles were collected and further merged by using UNIX scripts incorporating various MRC programs (Amos, Henderson *et al*. 1982; Henderson, Baldwin *et al.* 1986; Henderson, Baldwin *et al.* 1990; Henderson, Baldwin *et al.* 1990; Havelka, Henderson *et al*. 1993; Crowther, Henderson *et al.* 1996). Not all the images contributed to the merging since some of them had either bad drift or poor diffraction after the initial processing. Image processing was performed on the individual tilted images mostly like the way we did to non-tilted images. A couple of important parameters that were used to define the tilt geometry of the tilted images needed to be determined, such as TLTAXIS (angle from x-axis to the tilt-axis) and TLTANG (angle between tilt axis and the grid).

In CotY tilted image processing, we found that the lattice-based tilt geometry determination was only reliable for larger tilt angles, which was usually equal to or greater than 30°. Therefore, for low angle tilt data, we referred to the high angle tilt images in the same series, where they share almost the same TAXA and a known offset in TANGL.

A lattice line sinc-fitting program LATLINE was used to interpolate the observed amplitudes and phases (Agard 1983) (Fig 4.8). The output of LATLINE is a set of amplitude and phases that represent the best estimates of the structure factors from all the data. It can be seen as an interpolation of the data along the lattice line. The interpolated structure factor estimates were used in a Fourier synthesis to reconstruct the three dimensional density.

The reconstructed density appears to represent two layers of hexameric rings, staggered relative to each other (Fig 4.9). The diameter of the hole in the symmetric ring is about 3.2 nm and thickness of the crystal was estimated to be about 5.5 nm. The projection of

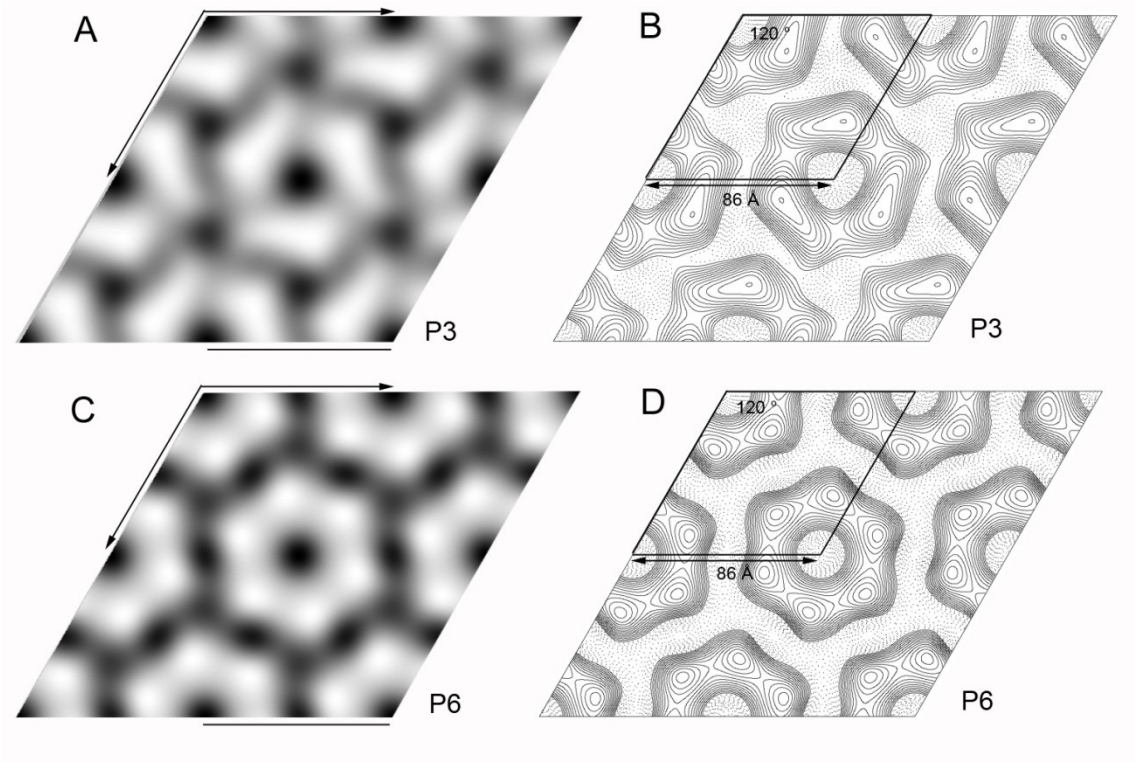

Fig 4.7 Averaged projection maps of CotY negatively stained crystal. (A) Three-fold symmetry was applied to grey-level map. Black is dense regions. White is least dense regions. Scale bar is about 86 Å; (B) and (D) Contour maps of the density from CotY crystal; (C) is a grey-level map showing *p6* symmetry from CotY crystal; (D) is the corresponding contour maps of the density from (C). Unit cell profile was drawn up by solid line and dimension was indicated as well. The upper resolution is 20 Å.

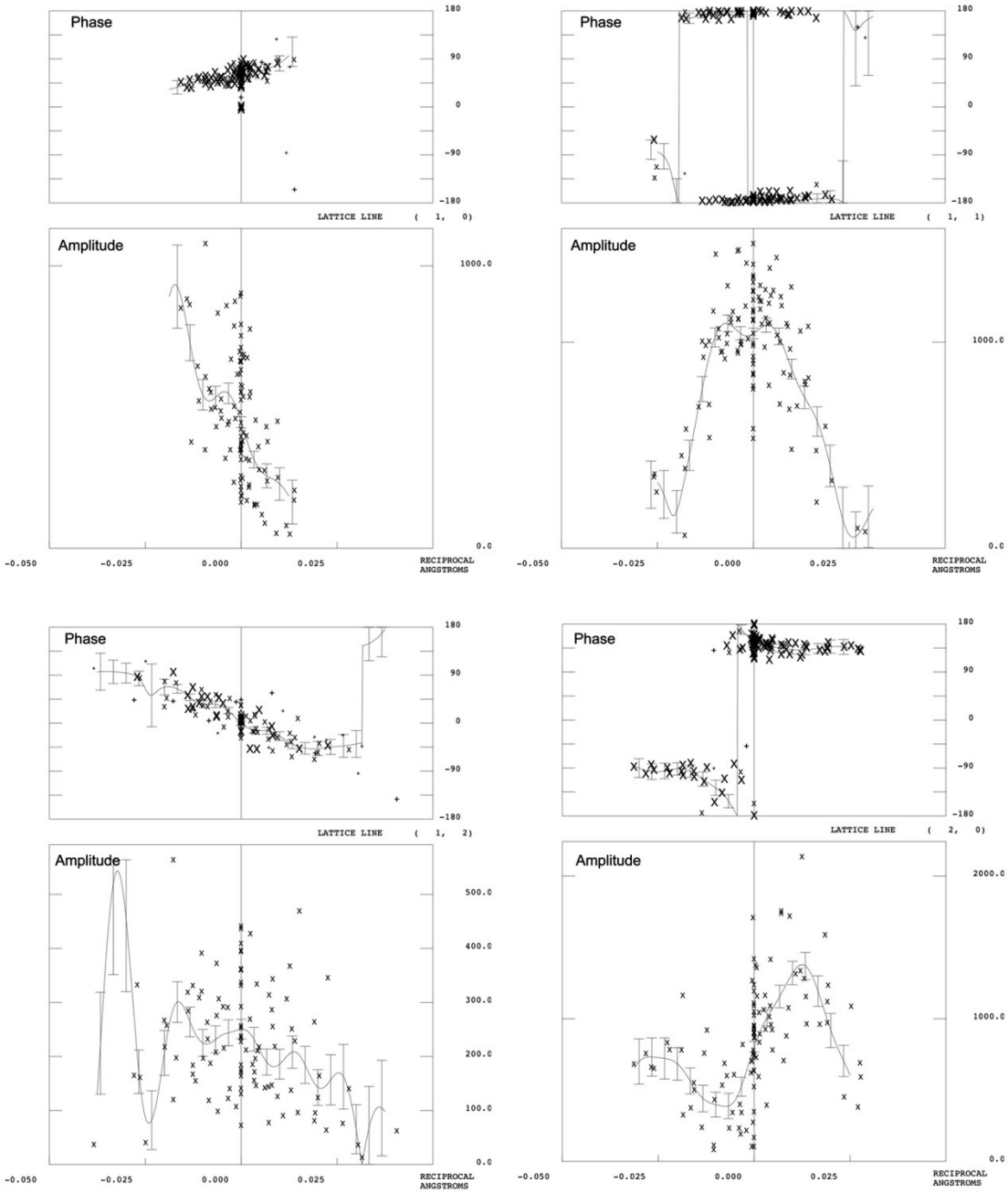
Phase
180
90
0
-90
-180
LATTICE LINE (1, 0)
Amplitude
1000.0
0.0
-0.050
-0.025
0.000
0.025
RECIPROCAL ANGSTROMS
Phase
LATTICE LINE (1, 1)
Amplitude
Phase
LATTICE LINE (1, 2)
Amplitude
500.0
400.0
300.0
200.0
100.0
Phase
LATTICE LINE (2, 0)
Amplitude
2000.0

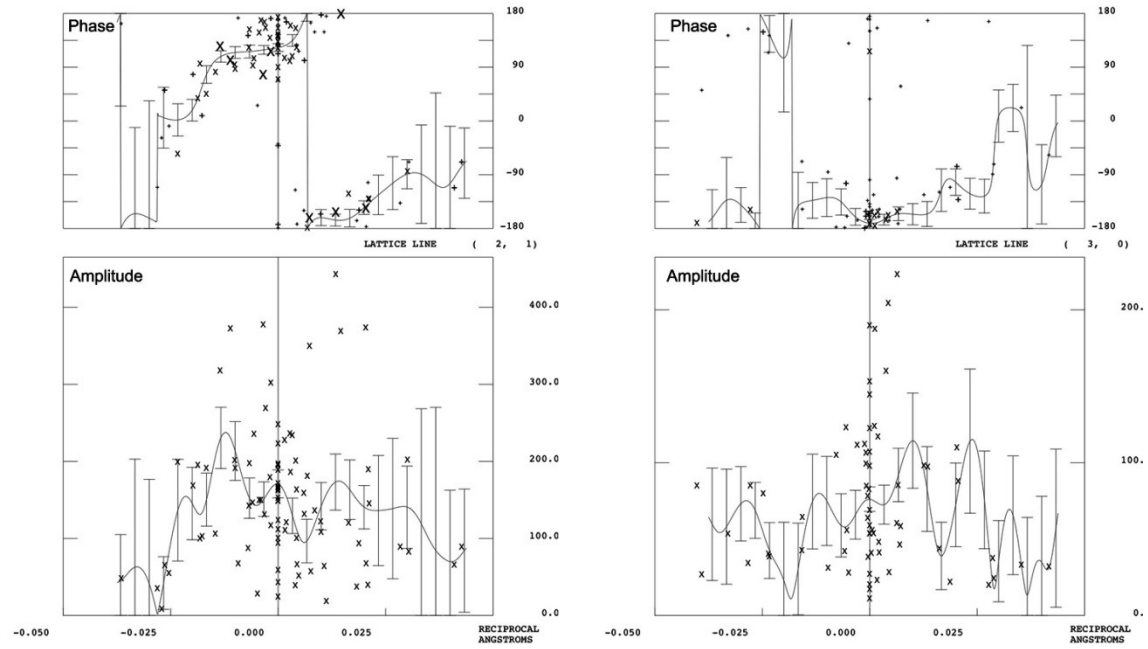

Fig 4.8 Amplitude and phase variation along z* for selected *h, k* values for the CotY crystal. The top panel for each lattice line shows the phase variation along the z* axis in degrees. The bottom panel shows the amplitude variation (in arbitrary units) along the z* axis. The horizontal z* axis is the distance from the origin of the lattice line. The error bars represent the standard error of the fitted amplitude and phase values from LATLINE.

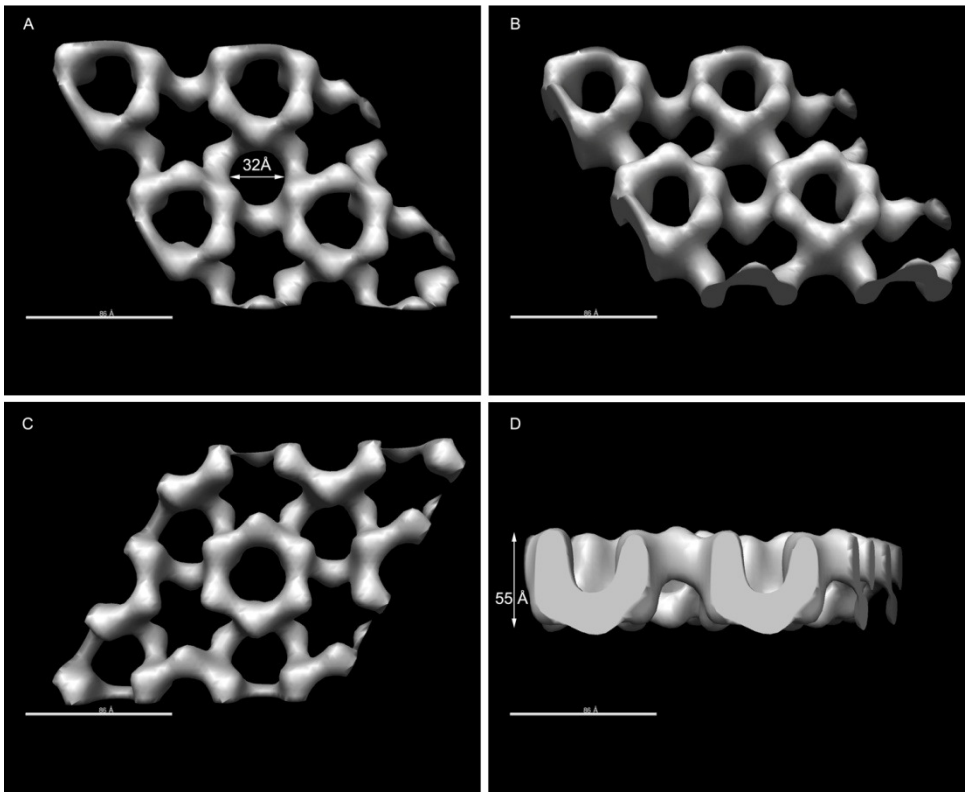

Fig 4.9 Surface representation of the CotY crystal in three dimension. (A and C) View perpendicular to the crystal plane from both surfaces; (B) Oblique views; (D) View parallel to the crystal plane. The cross length of the hole is around 32 Å and thickness of crystal is around 55 Å. The resolution is about 25 Å. The dimensions of the CotY crystals lattice are $a = b$ ~86 Å, γ ~120. Scale bar ~86 Å.

a single layer would be expected to be similar to that shown in Fig 4.7, suggesting that this rare form corresponds to a single layer of CotY hexamers, with p6 symmetry or that only one layer of a double layered crystal was stained in this instance. The 3D map answers all the questions on the structure inconsistency among the single particle profile, 2D symmetry and 3D map. In our single particle analysis, the final map presents as symmetric ring and obviously 6-fold symmetry. But 2D projection map and space group determination gave a different result: *p*3 or *p*321 symmetry. The majority of crystals were of the two-layer form where the layers superimpose to yield the projection shown in Fig 4.7 which has only *p3* symmetry. *p*321, this higher symmetry would be explained by a 'face-to-face' packing of the two layers rather than 'face-to-tail', but we require higher resolution data to confirm this.

4.6 CotY crystal forms inside the *E. coli* cells

To investigate the CotY self-assembly event taking place in *E. coli*, the cells were collected 3h following induction by 1 mM IPTG and resuspended with milli Q water or 8 M urea buffer. The cultured cells were disrupted by sonication for 45s in total (10 s and 50 s cooling). Broken cells could be seen by EM after short sonication.

Many large crystalline sheets with clear diffraction were found in both native and denaturating (8 M urea) conditions (Fig 4.10A-B). The best of the micrographs were subjected to image processing by *2dx_image*. The result including symmetry information and unit cell dimension were almost the same as that we got from CotY purified protein $a = b = 86$ Å, $\gamma = 120°$. Moreover, the result suggested that the CotY crystal was not yielded in the 8 M urea condition only. The huge crystal also existed in the milli Q water condition and also shared the same parameter in crystal unit cell dimension.

Remarkably, through the observation of broken cells, crystals could be directly seen inside the cell body (Fig 4.10C). Patchy CotY crystal grew along the contour of the *E.coli* cell envelope but from the view of micrograph, the exact site of formation was uncertain. We tried to observe the entire cell that provides native conditions for crystal growing, but unfortunately, electron beam could not fully penetrate the cell wall or only a short distance, we could not detect any detail of internal environment of whole cells. The control experiment also was done with sole pET28a plasmid inserted *E. coli* cells; no crystalline structure was detected (data now shown).

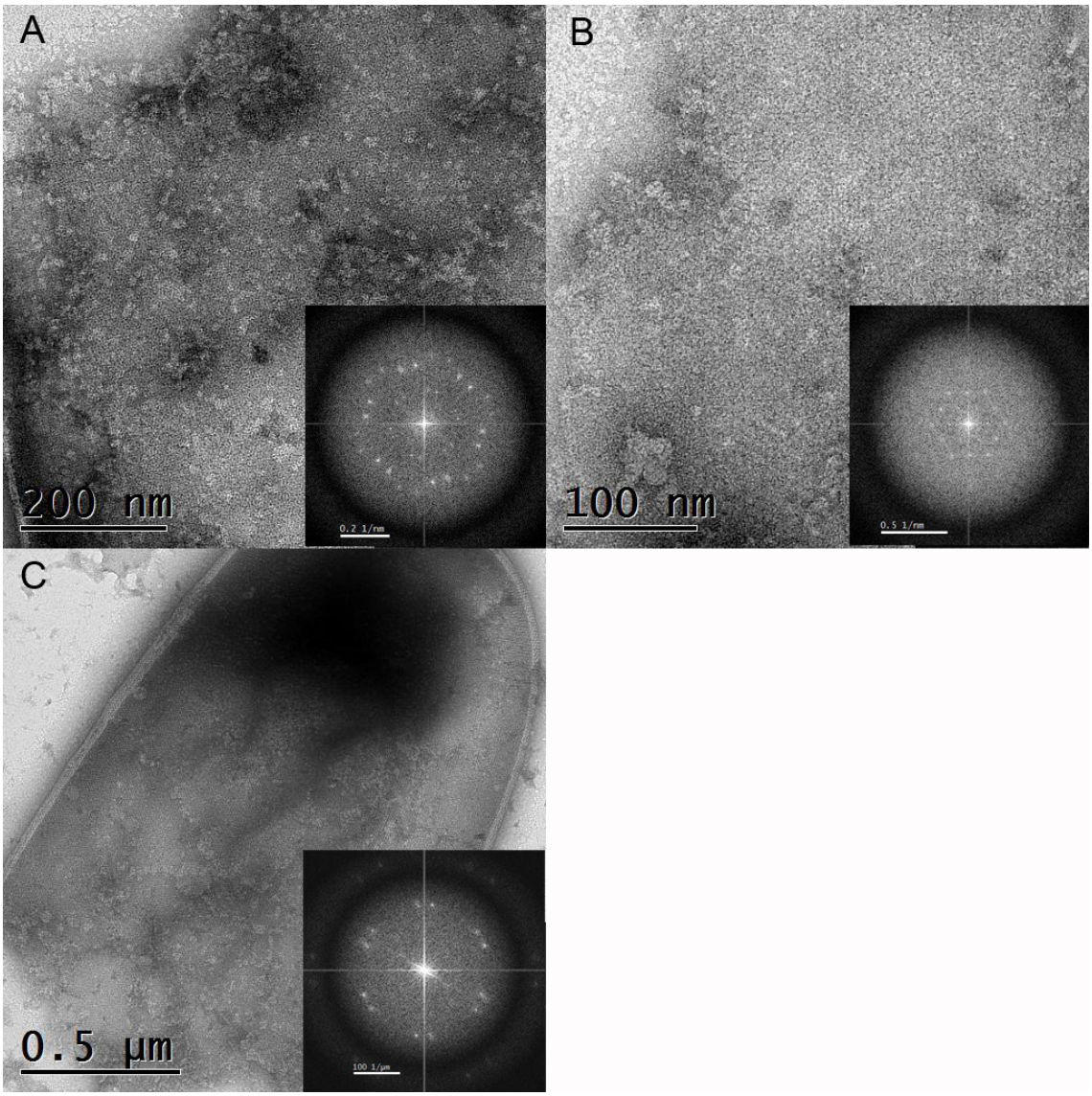

Fig 4.10 Representative images of CotY crystals collected after sonication. (A) Crystal sheet in 8M urea condition; (B) Crystal sheets seen in the milli Q water conditions; (C) Crystal found in the sonciation-disrupted *E. coli* cells. Without purification procedure, induced *E. coli* BL21 cells were spun down and resuspended in 8M urea buffer or milli Q water prior to sonication. After sonication, cells were directly loaded on the grid and observed by EM. FFT for each micrograph are shown in the insets and scale bars are indicated.

4.7 Disassembly of CotY crystals

Interestingly, when CotY (12µl, 1.12 mg/ml) was analysed on a 4-12% SDS-PAGE gel without any treatment (No heat, no DTT added), six obvious bands could be detected. Two of the densest bands, indicative of monomer and hexamer molecular weight size were evident (Fig 4.11A). Besides the evident bands, molecular weight size higher than hexamer, not only double hexamer band, a bunch of weak band indicating huge CotY multimeric complexes were detected (Fig 4.11B). These results are consistent with our speculation on CotY crystal architecture: six subunit of CotY monomers assemble into a hexameric ring which forms the basic repeating unit of the crystals. The existence of crystal produced high molecular weight species detectable in the gel. CotY samples were treated with 50 mM DTT and/or heating at 99°C for 20 min in an attempt to reduce any disulphide bonds and identify how it affects the crystal assembly. When CotY was treated with 50 mM DTT and heat, only a dense band corresponding to the monomer with slight background could be detected (Fig 4.11A). However, if CotY was treated with a reducing agent or heating alone, both monomer and hexamer species could still be detected. Denaturing and reducing effect also modified CotY motilities on the gel. As shown on the gel, four samples appeared to migrate differently (Fig 4.11).

To identify the impact of reducing agent DTT and heating on CotY crystal, all the samples treated with heating and/or 50 mM DTT were loaded on the grids and observed by EM. As expected, untreated CotY appeared as crystal sheets (Fig 4.12). A few of protein aggregations could be seen as well. On the gel, six bands between putative monomer size and hexamer. Higher molecular weight species can be explained as polymer of CotY such as aggregation or various sized crystal sheets. When CotY was treated with both DTT and heat, no crystal piece was detected (Fig 4.13). Instead of crystal, the protein aggregates and single particles significantly increased (Fig 4.13). On the corresponding profile on the gel, only one band corresponding to a monomer size (MW 28 kDa) appeared. The likely explanation is that in the presence of DTT and heat, all the intrinsic linkages were disrupted; therefore the single particle, aggregation and crystal seen in untreated CotY all fell apart into monomers.

When CotY was treated by DTT only, we could observe crystal pieces (Fig 4.14). The DDT treatment has limited impact on integrity of CotY crystal. The result is consistent

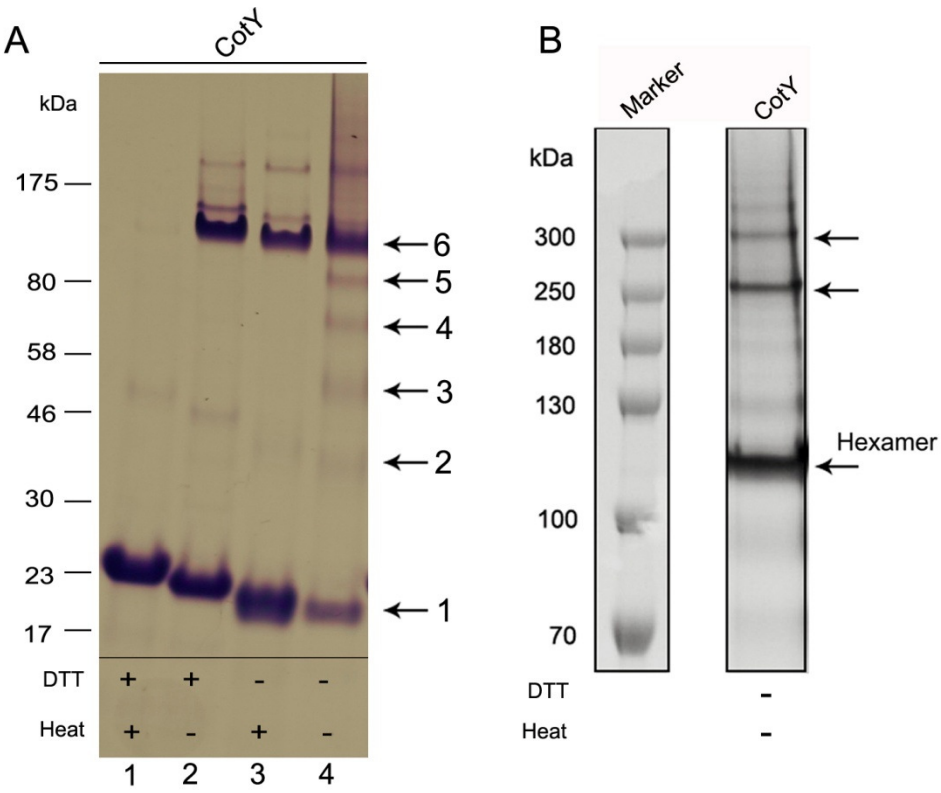

Fig 4.11 Coomassie blue stained SDS-PAGE of CotY after heat treatment and/or incubation with 50 mM DTT (Lane 1-4). (A) Four samples were analysed on a 4-12% SDS-PAGE. Six arrows indicated putative CotY monomer, dimer, trimer etc. (B) High range protein ladders were used to estimate the high molecular species. The sample used was the one without any treatment. Arrows indicate CotY hexamer and higher molecular species.

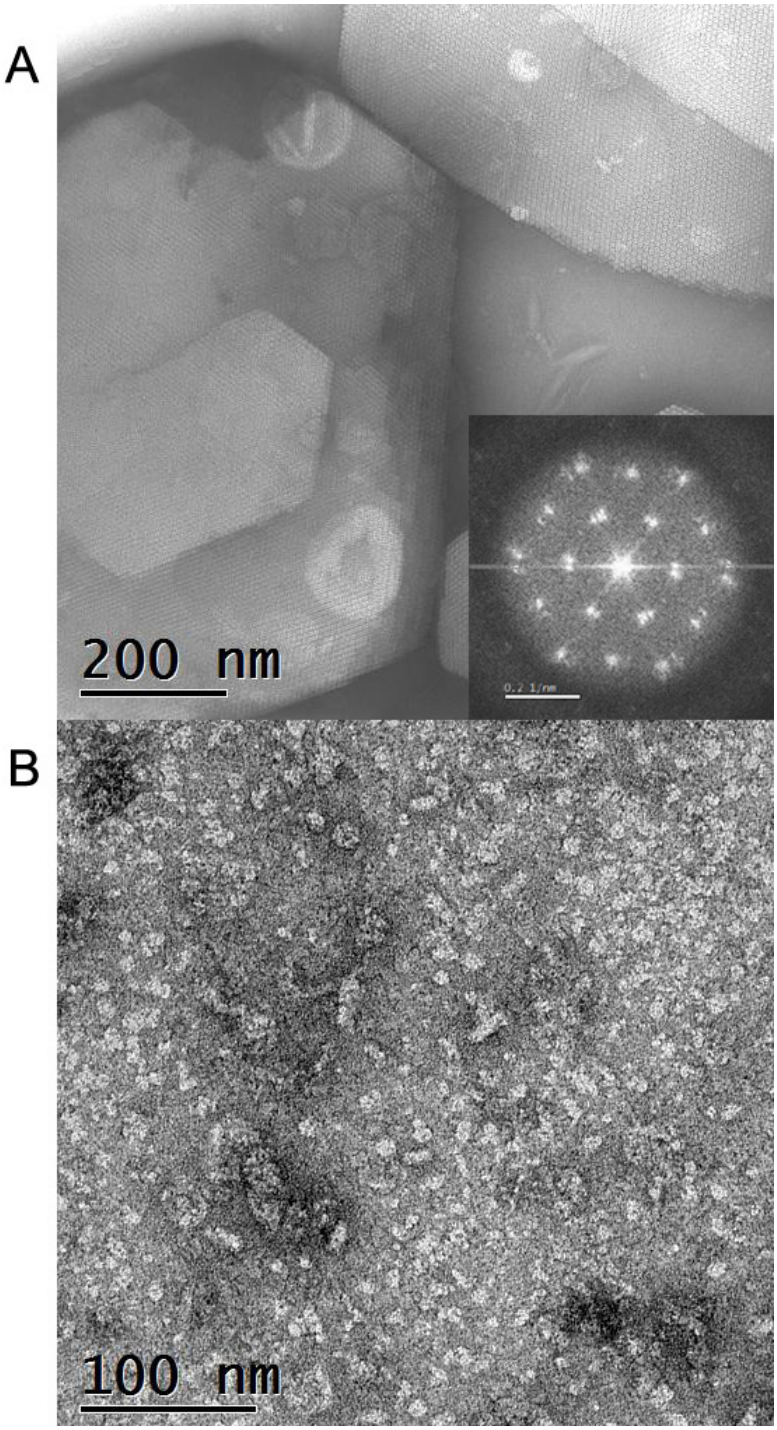

Fig 4.12 Negatively stained CotY without any treatment. Without being treated by 50 mM DTT or heat, crystal sheets (A) and single particles (B) formed by CotY could be observed, as well as few of aggregations on the background. Scale bar is on the left bottom.

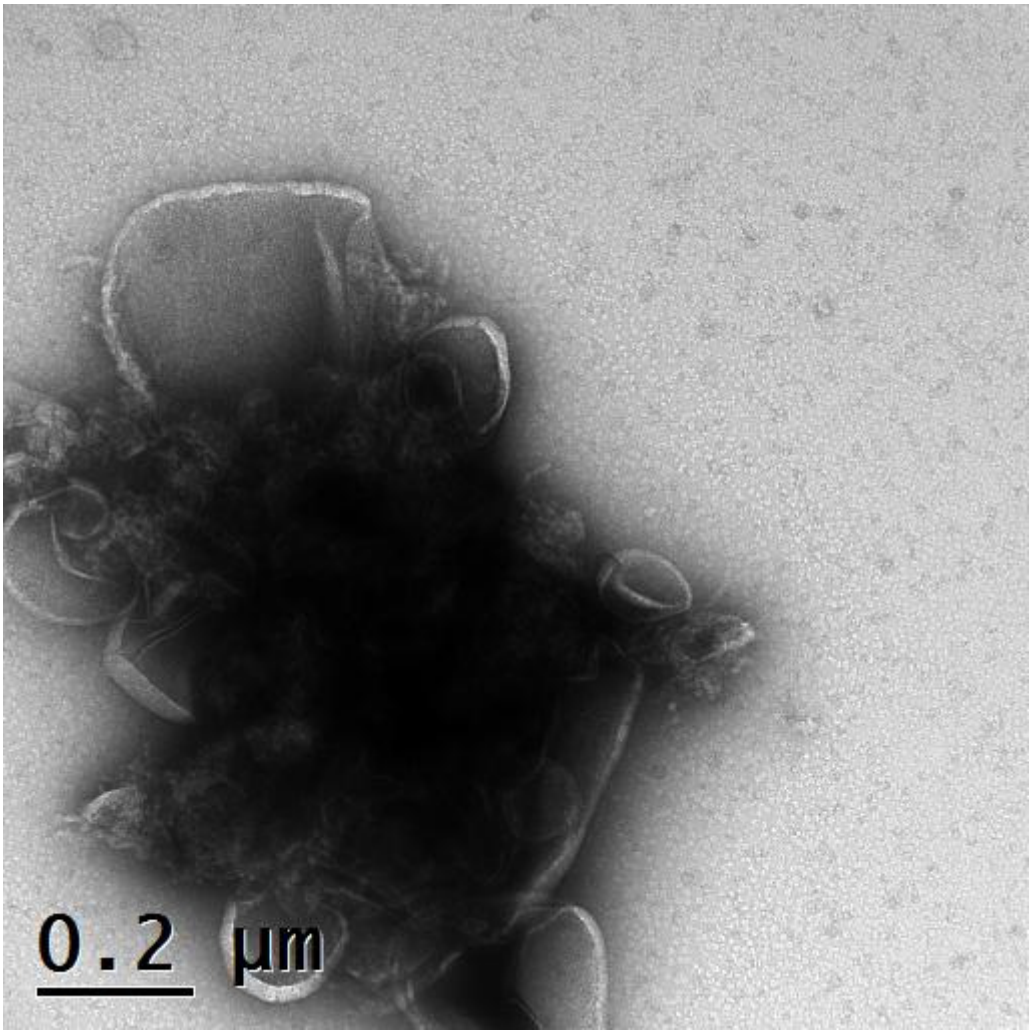

Fig 4.13 Negatively stained CotY upon treatment of 50mM DTT and 20 min heating at 99 ℃. Instead of crystal pieces, protein aggregates surrounded by a large amount of single partices appeared. Scale bar is on the left bottom.

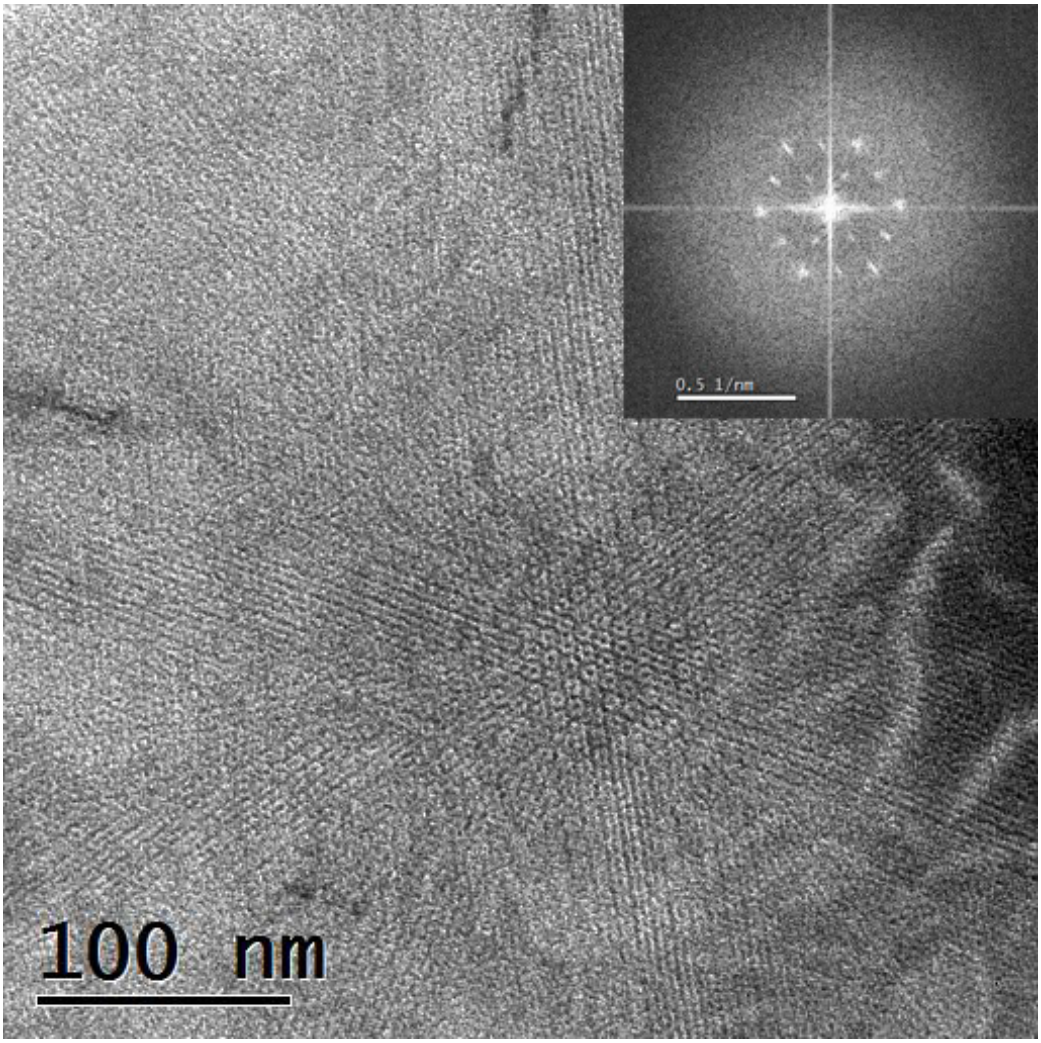

Fig 4.14 Negatively stained CotY upon treatment of 50 mM DTT. Distinct diffraction on the inset image indicated that the 50 mM DTT treatment is unable to disrupt the crystal structure.

with the protein profile on the gel, in which the putative hexamer and higher molecular weight complexes exist. In the case of heat-treated CotY but no DTT added, similar bands were detected on the gel. On the micrograph, crystal pieces were still detected and nicely dispersed single particles and few of protein aggregations could be seen as well (Fig 4.15). Heating also has limited impact on the intergrity of the crystals and only few of crystals were falled apart into single particles (hexamer). So either DTT reducing agent or denaturing caused by heating could only partially affect the integrity of the CotY crystals.

4.8 Structural analysis of CotV-CotW cylindrical complexes

The complexes of CotV-CotW generated fibrous assemblies of a consistent diameter (Fig 4.16). The projected fibres viewed by EM were consistently of about 10 nm in cross section. This ordered self-assembling structure makes it a good sample for structural analysis. Using the single particle analysis program IMAGIC 5, the straight fibres were boxed and cut for analysis. 137 of fibre sections were used for averaging and alignment processing. The average image indicated the fibres have a roughly cylindrical cross section (Fig 4.16). A Fourier transform computed from a selected length of the average fibres appeared to be strong layer line at 0.141 nm^{-1}, suggesting a helical pitch of about 7 nm (Fig 4.16). The structural analysis was done by Dr Svetomir Tzokov, University of Sheffield, Sheffield.

4.9 Discussion

The structural analysis shown here represents the next stage in our characterisation of the assembly of *B. subtilis* coat proteins (Krajcikova, Lukacova *et al.* 2009; Mullerova, Krajcikova *et al.* 2009), specifically those from the so-called “insoluble fraction” (Zhang, Fitz-James *et al.* 1993; Henriques and Moran 2007). In our study we have not attempted an exhaustive analysis of chemical interactions of spore coat components. In the previous chapter, we had screened a number of the spore coat proteins and three of them, CotY, SafA and CotV-CotW were found to present ordered self-assembly properties, and were considered to be good candidates for further structural analysis. Our findings do point to a significant role for self-assembly in this process. Evidence for this also comes from the early work of Aronson and Fitz-Jameswho demonstrated at

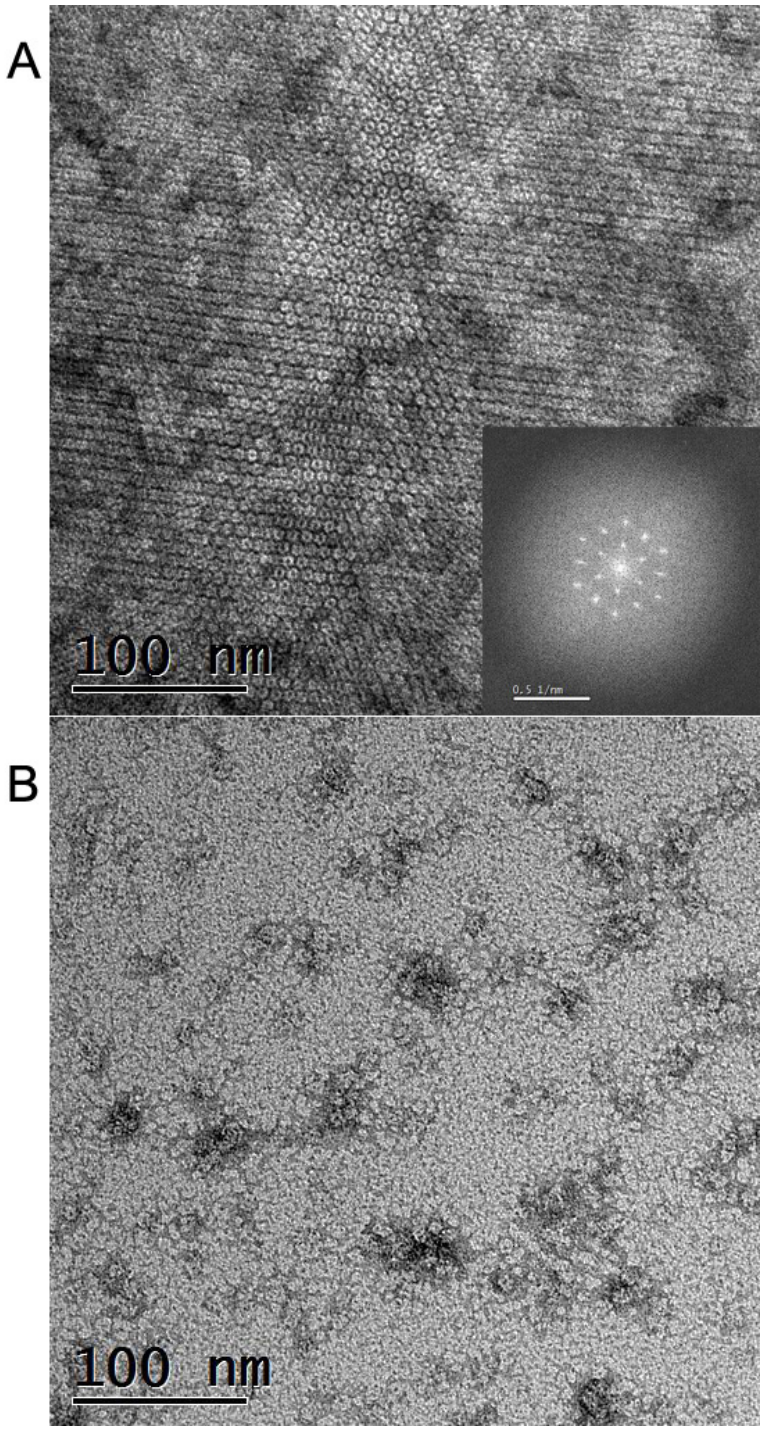

Fig 4.15 Negatively stained CotY upon heating at 99℃ for 20 min, no DTT added. (A) FTT in the inset image indicated that the crystal was not fully disrupted; (B) Single particles increased after the treatment.

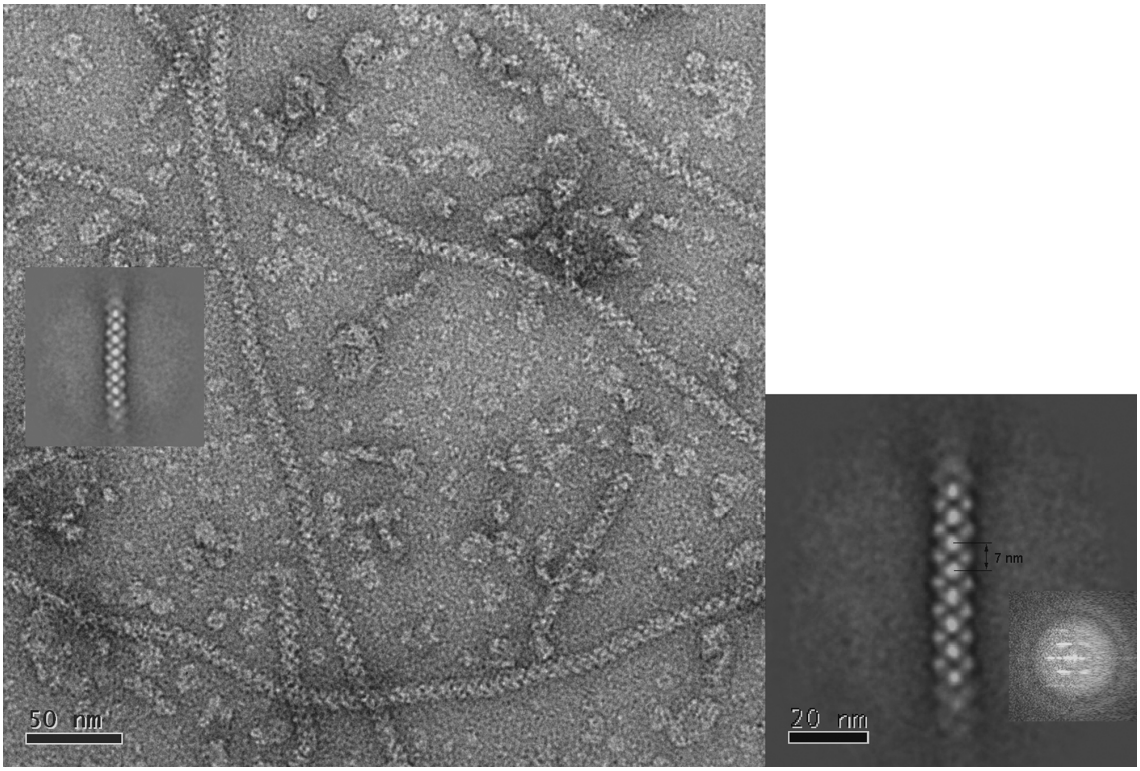

Fig 4.16 Structural analysis of CotV-CotW fibre-like complexes. The left micrograph shows the cylindrical structure observed in CotV-CotW co-expression preparation. There was also a background of amorphous material. The inset image was the average of 137 fibre sections processed by IMAGIC5. The right figure shows Fourier transforms from reconstruction (Left half) and raw fibre image (Right half). The distance between vertical pitches was estimated at around 7 nm. The structural analysis was done by Dr Svetomir Tzokov, Sheffield.

least partial reconstitution of the outer coat layers of *B. cereus* that had been treated initially with DTT and urea (Aronson and Fitz-James 1971); the presence of cystine in the dialysis buffer appeared essential for ordered layering, presumably through facilitating disulphide exchange (Aronson and Fitz-James 1976). It is therefore likely that disulphide bond formation plays an important role in cross-linking proteins of the spore coat. CotY and CotZ are homologous, tyrosine- and cystine-rich components of the *B. subtilis* outer coat or crust. The involvement of intermolecular disulphide bonds in CotY oligomerisation has already been inferred as has the cross-linking of CotY-CotZ heteromultimers in the insoluble fraction (Zhang, Fitz-James *et al*. 1993). We found CotY crystals were not fully disrupted by the 50 mM DTT or 20 min overheating, however, as DTT and overheat both performed, the crystals were fully fallen apart into single particles and protein aggregates. This strongly suggests that crystals are held together at least in part by disulphide cross-links and this could reflect the *in vivo* situation.

CotY

Recombinant CotY assembled into putative hexamers. These can then form a higher order assembly consisting of sheets one molecule thick (exhibiting *p*6 plane group symmetry) or two molecules thick (exhibiting *p*3 plane group symmetry); the thicker sheets essentially consist of two *p*6 symmetric layers staggered relative to each other and possibly packed face-to-face (Fig 4.14). We were unable to find conditions in which we could induce isolated hexamers to form two-dimensional crystals. The reasons for this might be kinetic and/or the concentration was too low- perhaps a rare nucleation event is required.

The most remarkable feature of the *p*6 crystal is its superficial resemblance to the basal layer crystal of the exosporium of members of the *B. cereus* family; the *B. subtilis* CotY array has unit cell parameters $a = b = 86$ Å whilst those of *B. cereus* exosporium which is now known to also have *p*6 symmetry are similar, with $a = b = 80$ Å (Ball, Taylor *et al.* 2008; Kailas, Terry *et al*. 2011). There is no exosporium in *B. subtilis* although the possible relatedness of the *B. subtilis* spore crust (McKenney, Driks *et a*l. 2010) and the *B. cereus* exosporium has been noted (Imamura, Kuwana *et al.* 2011). This putative relatedness is exemplified by *B. cereus* exosporium which contains two orthologues of *B. subtilis* CotY, namely ExsY and CotY. The remarkable similarity between our

synthetic CotY lattice and the native exosporium leads us to speculate that a large part of the natural two-dimensional crystals found in exosporium are made up of ExsY and/or CotY. This would imply that an inherent tendency of these proteins to form two-dimensional arrays could be part of their function. Whether or not CotY forms natural two-dimensional arrays in the *B. subtilis* spore is not yet known. However, CotY has been proposed as a component of the crust (Imamura, Kuwana *et al.* 2011) or at the very least to be involved in assembly of the crust (McKenney, Driks *et al.* 2010). Our crystals are sensitive to reducing agent and there is clear evidence that CotY forms disulphide-linked multimers in the spore coat (Zhang, Fitz-James *et al.* 1993). This would be consistent with the hexameric single particles acting as the fundamental building blocks of a disulphide-linked network within the outer spore coat/crust. It is clear that one or more coat proteins do form hexagonally symmetric arrays *in situ*; these have been revealed in freeze-etch samples of coats of a variety of spores (Holt and Leadbetter 1969; Aronson and Fitz-James 1976; Ebersold, Cordier *et al.* 1981) and more recently by AFM (Plomp, Leighton *et al*. 2005; Plomp, Leighton *et al*. 2005; Plomp, Leighton *et al*. 2007; Kailas, Terry *et a*l. 2011). These arrays have been reported to have spacing of ~90 Å, close to the 86 Å we found in our CotY assemblies. However, from the limited data available from *B. subtilis* spores (Aronson and Fitz-James 1976), it is not yet clear whether such arrays exist in the *B.cereus* species.

The exact sites which combine the unit cell of the CotY into crystal are still unknown. We have attempted to observe the crystal on the site of the broken *E. coli* BL21 cells after sonication. No special nucleation-required conditions provided, we directly detected huge sheets of crystal appearing to follow the contour of *E. coli* cell membrane under both urea and urea-free conditions. It is suggested that the event of crystal formation can occur in the condition without urea. Considering disulphide bond formation is generally not considered favourable in the cell cytoplasm (Fass 2012) and even in the presence of oxygen it is slow; in *E. coli* disulphide bond formation is normally catalysed in the periplasm (Kadokura, Katzen *et al.* 2003). This leaves intriguing questions as to where, when and how the CotY 2D crystals that we have generated could form disulphide bonds. However, perhaps self assembly of crystals first takes place through the non-covalent association of the CotY components, which is then followed by disulphide bond formation through some unknown mechanism. Similar questions arise when considering the formation of disulphides in the native *B. subtilis*

spore. The functional advantage of disulphide bonds in conferring thermal and mechanical stability (Fass 2012) to the spore coat seems clear. An exploration of which cysteine residues are involved would be the topic of future investigation.

The tendency of CotY to from thin two-dimensional arrays may be reflected in the layering structure observed in the outer coat region. Indeed this layering is almost abolished in a cotXYZ triple mutant (Zhang, Fitz-James *et al.* 1993). Imamura et al. reported that CotY and CotZ depend on each other to assemble on spores (Imamura, Kuwana *et al.* 2011). The proteins might have distinct roles in crust formation, both requiring the spore crust to localize on the spore. Alternatively, they may form heterooligomers. Nevertheless, our results demonstrate that CotY is capable of polymerizing on its own at least in a heterologous expression system.

So far for the self assembly properties and structure research of CotY, the conclusions are:

(1) We have isolated single particles formed by CotY which appeared to assemble into oligomers with six-fold projection symmetry suggesting that are hexameric. The same conclusion was also reached by analysis of CotY by SDS-PAGE without reducing agent added.

(2) CotY has a propensity to form 2D crystalline assemblies somewhat analogous to those seen for the *B. cereus* family exosporium. It is clear that the lattice is made up of six-fold symmetric rings, and two layers of hexamers held together with linkers.

(3) CotY can form 2D array inside the cytoplasm of *E. coli BL21* cells, the exact formation mechanism needs to be determined in the future.

(4) DTT can partially disrupt the crystal structure but very limited. Disulphide bonding would be the essential cross-linking to maintain the crystal. More reducing agent disruption experiments such as using much higher concentration of DTT to crystal sheets will be performed.

SafA

SafA is a morphogenetic protein of *B. subtilis* playing important role in coat assembly (Beall, Driks *et al.* 1993; Driks, Roels *et al.* 1994; Ozin, Henriques *et al.* 2000; Ozin, Samford *et al.* 2001; Costa, Isidro *et al.* 2006). We have produced SafA coat protein in the presence and absence of 8 M urea. Recombinant SafA assembled into multimers of

very high molecular weight under both native and denaturating conditions. The underlying mechanism for this behaviour is still unknown. Due to high homogeneity of the single particles, SafA was analysed by single particle analysis. The SafA appeared to be circular structure in the projection map. It was previously reported that SafA's localization is dependent on SpoVID by direct interaction and also could interact with itself (Ozin, Henriques *et al*. 2000; Ozin, Samford *et al.* 2001; Driks 2002; Costa, Isidro *et al*. 2006). A SafA ortholog protein, ExsA was found to have a role in promoting anchoring of both the coat and exosporium layer to the spore of *B. cereus* (Bailey-Smith, Todd *et al*. 2005). Moreover, SpoVID and SafA orthologues are present in all *Bacillus* species and some of mechanistic details of the functioning in coat morphogenesis are conserved. Since very limited structural information was extracted from the final proposed SafA single particle model, it is difficult to speculate how its function relates to the circular structure.

CotV-CotW

For CotV-CotW Fourier transforms of fibre images showed a layer line structure typical of helical assemblies, albeit rather diffuse. The fibres are distorted, so at this stage we have not attempted a full helical diffraction analysis. However, it is very possible that they could ultimately be amenable to the type of hybrid analysis developed for other disordered helical assemblies e.g. (Egelman 2007) At this stage we have restricted our analysis to a simple filtering of the meridian and prominent layer lines seen in Fig. 4.16 resulting in the image seen in Fig. 4.16 in which the repetitive structure is enhanced.

The polymers we have described here demonstrate the capacity for these spore coat proteins to self-assemble. These higher order assemblies bear similarities to structures already seen *in situ* and the relationship between them deserves further analysis. A deeper investigation of the chemistry driving these assemblies is also called for. Finally the prospects for higher resolution analysis, using cryo-EM techniques are very good from these ordered assemblies. These results should give an alternative way to understand the roles of spore coat protein in spore maturation and accelerate efforts to probe into high-resolution investigation of crystal structure, which might be helpful to unveil the assembly mechanism underlying the spore coat/exosporium construction.

CHAPTER 5

Electron crystallographic analysis of exosporium protein ExsY of *B. cereus*

5.1 Introduction

ExsY is one of the most important components of exosporium in *B. anthracis* and *B. thuringiensis* required for correct formation of exosporium. As a homologue protein of CotY of *B. subtilis* localizing on the natural crystalline exosporium, as described in Chapter 3, ExsY could self-assemble into crystals, in this chapter we therefore focus on its structural analysis. The data we obtained in combination with the structure information extracted from the exosporium of *Bacillus* family species (Ball, Taylor *et al.* 2008; Kailas, Terry *et al*. 2011) allows us to propose how this single component contributes to the whole structure of exosporium.

5.2 Three-dimensional merging of ExsY

The recombinant ExsY of *B. cereus* was prepared and provided by Dr. David Radford, Sheffield. *exsY* contains two his-tags, one at N-terminal and the other one at the C-terminal. ExsY was purified by the same method as CotY as previously described. EM was used to collect the micrographs of ExsY assemblies at different angles.

All non-tilted ExsY images have a similar overall appearance with the same unit cell dimension $a = b$ ~83 Å, γ ~ 120°. For most of the samples, crystallographic phases were consistent with *p*6 symmetry, although in this preliminary analysis, *p*3 was conservatively enforced (Table 5.1). The repeating unit of the structure with *p*3 symmetry applied was characterised by heavily stained central pits each surrounded by six stain-excluding densities (Fig 5.1). Notably, the density distribution was similar to that of the CotY *p*6 form (Fig 4.10).

To extract more structural detail, images of tilted ExsY crystals were recorded to build up a 3D volume. Images were recorded at 10° intervals over a range of up to -50° to 50°. Crystal pieces with sufficiently large size were picked up and eventually four good-quality tilt series contributed to the final structure. Crystals were merged together by minimising the phase residual as described for CotY images (see §4.5). A representation

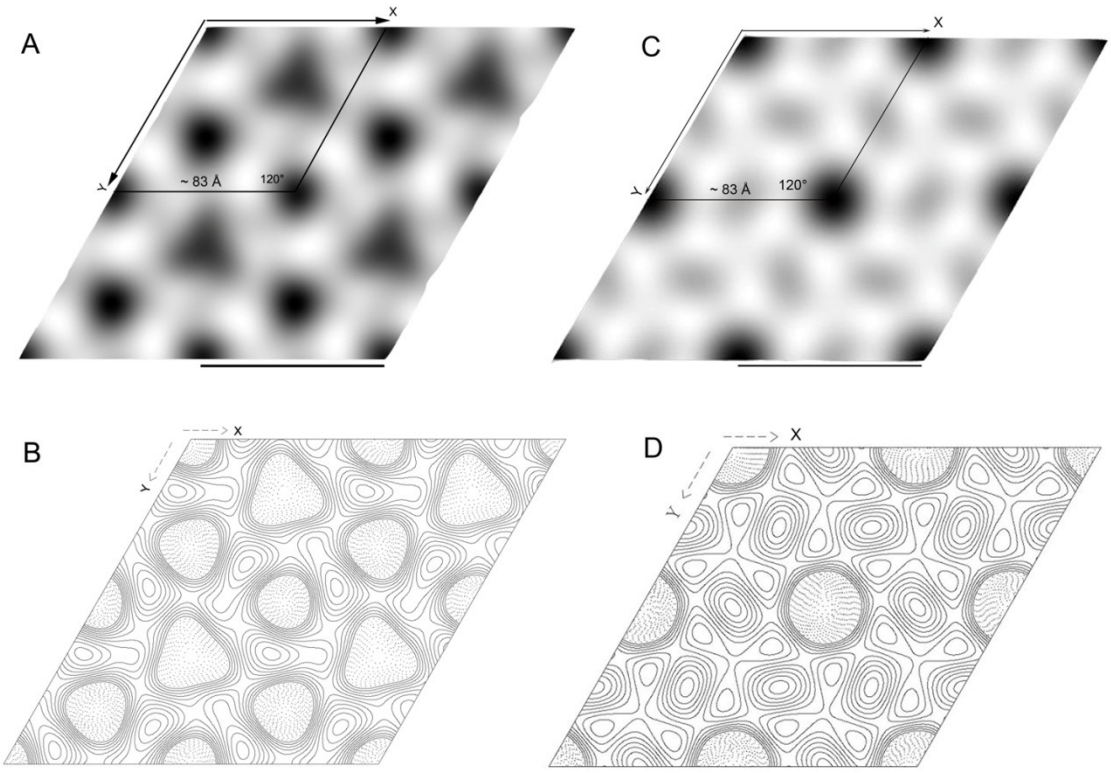

Fig 5.1 Generation of the projection map of ExsY negatively stained crystal. (A) Grey-level map of ExsY crystal. (B) Contour map of the density in (A) *p*3 symmetry has been applied to projection map; (C) Grey-level map of *B. cereus* ATCC 10876; (D) Contour map of the density in (C) *p*6 symmetry has been applied to. Unit cell profile was drawn up by solid line. The upper resolution is 20 Å. Black bar represents about 83 Å.

Table 5.1 The internal phase residuals determined after the imposition of all possible two-sided plane groups calculated from one of the micrographs of ExsY crystals.

Two sided plane group	Phase residual versus with other spot (90° random)	Number of comparisons	Target residual based on statistics taking Friedel weight into account
*p*1	29.3	34	
*p*2	43.8	17	43.3
*p*12_b	54.0	7	35.3
*p*12_a	45.1	7	35.3
*p*121_a	29.6	7	35.3
*p*121_b	62.4	7	35.3
*c*12_b	54.0	7	35.3
*c*12_a	45.1	7	35.3
*p*222	59.3	31	36.9
*p*2221b	56.9	31	36.9
*p*2221a	41.8	31	36.9
*p*22121	64.7	31	36.9
*c*222	59.3	31	36.9
*p*4	55.7	37	35.7
*p*422	53.9	75	32.5
*p*4212	60.6	75	32.5
*p*3	22.9*	28	29.3
*p*312	27.1*	64	30.2
*p*321	37.1	69	31.1
*p*6	34.1*	73	32.5
p622	36.7	150	30.9

Internal phase residuals were determined from spots of IQ1-1Q5 to 20Å resolution. The values marked with * are good candidates for the symmetry as the experimental phase residual is close to that expected value based on the signal-to-noise ratio.

of the calculated three-dimensional density distribution is shown in (Fig 5.2). Threshold Fig 5.1 level for surface contouring were set at a level close to the maximum gradient of contrast, continuous connectivity of density throughout the 3D volume could be visible (Data not shown).

Unlike the CotY case, no uniform single particle was detected in the ExsY preparation. However, a hexameric ring-like structure is obvious within the crystal lattice. In CotY the predominant crystal form consisted of two layers of hexameric rings, while in ExsY only a single layer structure was observed.

5.3 Discussion

ExsY of *B. anthracis* and *B. cereus* has been widely studied (Hachisuka, Kojima *et al*. 1966; Todd, Moir *et al.* 2003; Redmond, Baillie *et al*. 2004; Boydston, Yue *et al*. 2006; Johnson, Todd *et al.* 2006). ExsY and CotY were considered to be candidates for major components of the exosporium lattice because a *ΔexsY* strain of *B. cereus* and *B. anthracis* only produce the exosporium with a small terminal cap and *ΔexsYΔcotY* strain is devoid of exosporium (Boydston, Yue *et al*. 2006; Johnson, Todd *et al.* 2006; Steichen, Kearney *et al*. 2007). Although we have not investigated CotY of *B. cereus*, the ExsY projection map shows high similarity in design with the projection map of intact exosporium of *B. cereus* ATCC 10876 (Fig 5.2). Both of them have a cavity at the centre which surrounded by six prominent stain-excluding densities (Fig 5.2C). We speculate that a large part of the natural 2D arrays in exosporium is made up of ExsY and/or CotY. Another open question is the exact distribution of two major proteins. Thompson *et al* proposed a model for the bottle-cap assembly of the exosporium which consists of non-cap and cap protein component (Thompson, Hoelscher *et al*. 2012). CotY, anchor protein ExsFB and BxpB (ExsFA) were localized in the cap region; BclB, ExsF and BxpB, ExsY and Alr distribute throughout non-cap region. CotY was believed to be a "cap" protein which could cover the distal end of exosporium, but so far it is still unknown whether ExsY also localizes in this region (Thompson, Hoelscher *et al.* 2012). However, it is confirmed that ExsY is a "non-cap" protein, which covers the larger part of the exosporium (> 75%) (Thompson, Hoelscher *et al.* 2012).

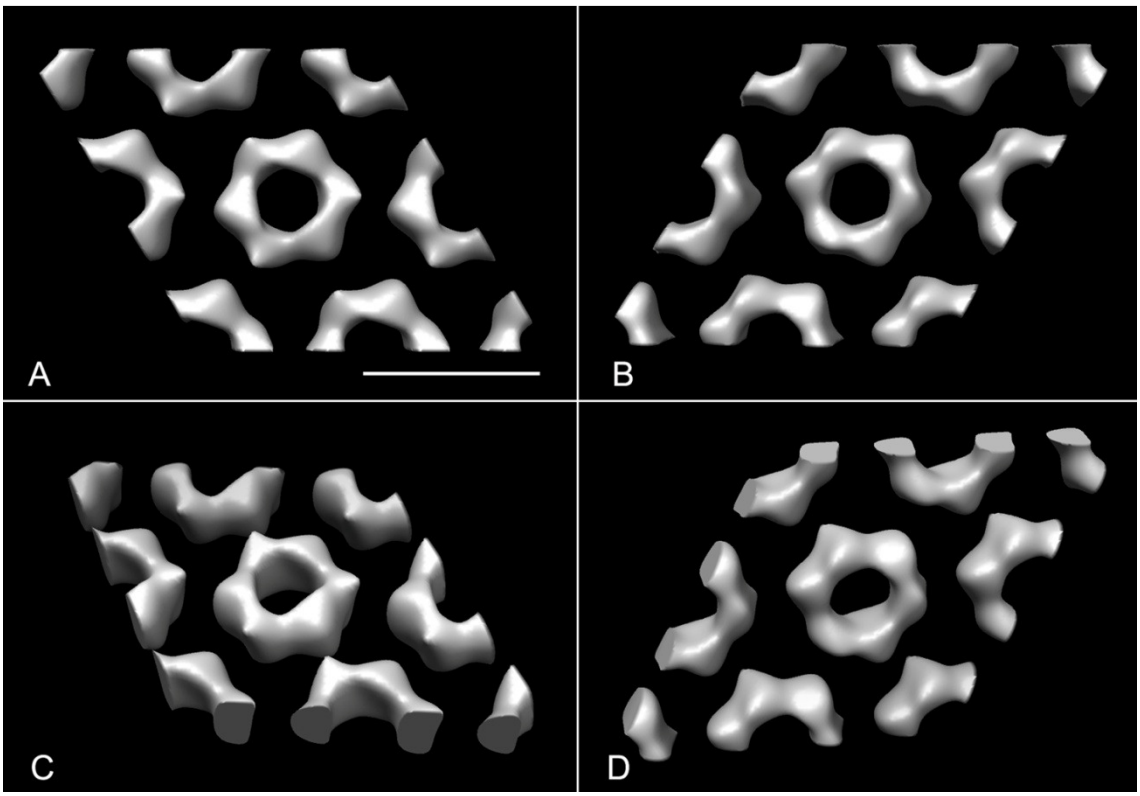

Fig 5.2 Surface representation of the ExsY crystal in three dimension. (A-B) View perpendicular to the crystal plane from both surfaces; (C-D) Oblique views. The resolution is about 25 Å. The dimensions of the ExsY crystals lattice are a=b ~83 Å, γ~120. Scale bar ~83 Å.

Based on the observed crystallinity of CotY and ExsY it seems likely that both would contribute to the crystallinity of exosporium. The unit cell dimension $a = b$ ~83 Å, γ ~ 120° indicative of type II crystal suggests that the ExsY crystal is related to the so-called type II crystal of the exosporium (Ball, Taylor *et al*. 2008) which is thought to be a major component of the basal layer (Kailas, Terry *et al*. 2011). Not only close in unit cell dimension, ExsY structure appears very similar to the interconnected lattice of CotY hexameric rings. We compared the ExsY 3D model with the 3D *B. cereus* type II crystal that was distinguished by the individual crowns with large stain-filled cavities at the centre (Fig 1.2) (Ball, Taylor *et al.* 2008; Kailas, Terry *et al*. 2011). We have not seen the crown structure in the ExsY 3D volume, instead a hole was evident in the centre (Fig 5.2). The exosporium is composed by a number of exosporium proteins that all may contribute to integrity of the structure. ExsY is just one of the components of the exosporium and it would appear to make up the bulk of the wall of the sixfold symmetric crowns. In the exosporium this must be embellished with further proteins making up the threefold symmetric linkers between crowns (Kailas, Terry *et al.* 2011). In addition there must be another protein or proteins forming the closed off base of the crowns.

CHAPTER 6

Structure of the exosporium of selected members of the *Bacillaceae*

6.1 Introduction

In our study, a number of *Bacillus* spores were screened by EM to find the most suitable for generating crystalline exosporium samples. Spores of 15 species of *Bacillus* were provided by Adam Driks (Loyola University Medical School). All spores were observed by negative stain electron microscopy and the potential ones with distinct diffraction of the exosporium layer were selected for further structural analysis. The aim was to find samples that more amenable to very high-resolution structural analysis than currently studied in our group, species from *B. cereus.* Two candidates, *B. circulans* 42G1, and *B. fusiformis* ATCC 7055 stood out from the crowd. Slight sonication (6s) was utilized to slough off the exosporium fragment. With the same data analysis that was applied to CotY, we constructed the 2D/3D model of exosporium of *B. circulans* 42G1 and *B. fusiformis* ATCC 7055 species. Moreover, to obtain finer structural details such as α-helices and accurate map to determine features such as pore or pit size, cryo-EM was employed to investigate the crystalline exosporium of *B. fusiformis* ATCC 7055.

6.2 Electron microscopy screen of spore and exosporium from *Bacillus* species

The spores screened in our study were generally from species that have received very little attention in the literature. Table 6.1 shows the list of species we identified.

Name	**Presence of crystallity on exosporium**
B. pumilus SAFR-032 611	Distinct diffraction on FFT indicated crystal structure of the exosporium.
B. badius BGSC #23A1	No diffraction detected on fragile exosporium.
B. fusiformis ATCC 7055	Distinct and sharp diffraction on exosporium.
B. lentus Gibson 165 BGSC #60A1	Poor diffraction on exosporium.
Paenibacillus alevei 1113 DT-1A	No diffraction detected.
B. vedderi NRRL B23388	Distinct diffraction detected. Natural crystal structure formed by exosporium.
B. pseudomyciodes NRRL B-617	Poor diffraction on exosporium.
B. megaterium ATCC 12872	No diffraction.
B. nianci NRRL B23384	Distinct diffraction on exosporium fragments.

B. pycnus NRRL NRS-1691	No diffraction detected.
B. neidei NRRL BD101	Distinct and sharp diffraction on exosporium. Good candidate for structural analysis.
B. odysseyi	No diffraction detected.
B. circulans 42G1	Distinct and sharp diffraction on exosporium.
B. mycoides ES-027	Poor diffraction on exosporium.
B. laterosporus ATCC 64T	No diffraction detected.

Table 6.1 List of 15 of *Bacilli* spores that were provided by Dr Adam Driks lab, Loyola University.

6.2.1 *B. pumilus* SAFR-032 611

Bacillus pumilis is commonly found in soil (Ash, Priest et al. 1993). The *B. pumilis* spore is highly resistant to environmental stresses, such as UV radiation, desiccation, and oxidizing agents.

As shown in Fig 6.1, *B. pumilus* SAFR-032 611 possesses fragile exosporium, often appearing detached from the spore core. High magnification (Fig. 6.1B) indicated some periodicity within the exosporium 2D array. Various filamentous structures were also evident. The computer generated FFT (Fig. 6.1B inset) indicated that the exosporium could be a target for EM crystallographic analysis.

6.2.2 *B. badius* BGSC #23A1

The formed spores are ellipsoidal, subterminal, sometimes paracentral or terminal, not swelling the sporangium (Ash, Priest et al. 1993). We observed the spore by EM and it appeared to have an exosporium (Fig 6.2). The exosporia in the spores are largely cracked; however, we could still observe a few intact exosporium layers that cover the spore body at one terminus of the endospore. No crystallinity so far has been detected throughout the exosporium fragments.

6.2.3 *B. lentus* Gibson 165 BGSC #60A1

The spore formed is ellipsoidal and paracentral. *B. lentus* Gibson 165 BGSC #60A1 spores were observed by EM. The darkly stained spore body is paracentral, and

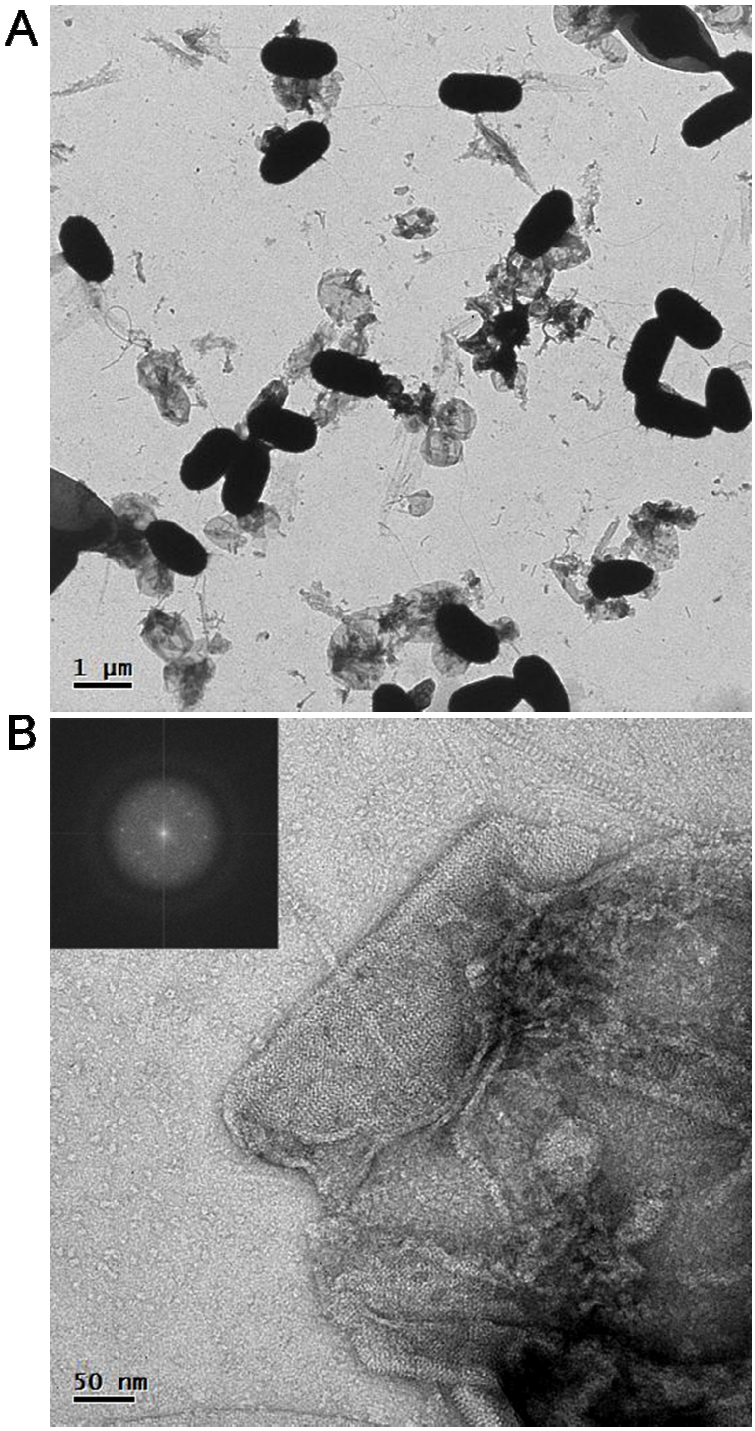

Fig 6.1 Electron micrograph of negatively stained *B. pumilus* SAFR-032 611 spores and exosporium. (A) shows entire spores with fragile exosporium. The exosporium can be seen as a large loose and well-ordered structure with distinct diffraction in the inset image shown (B).

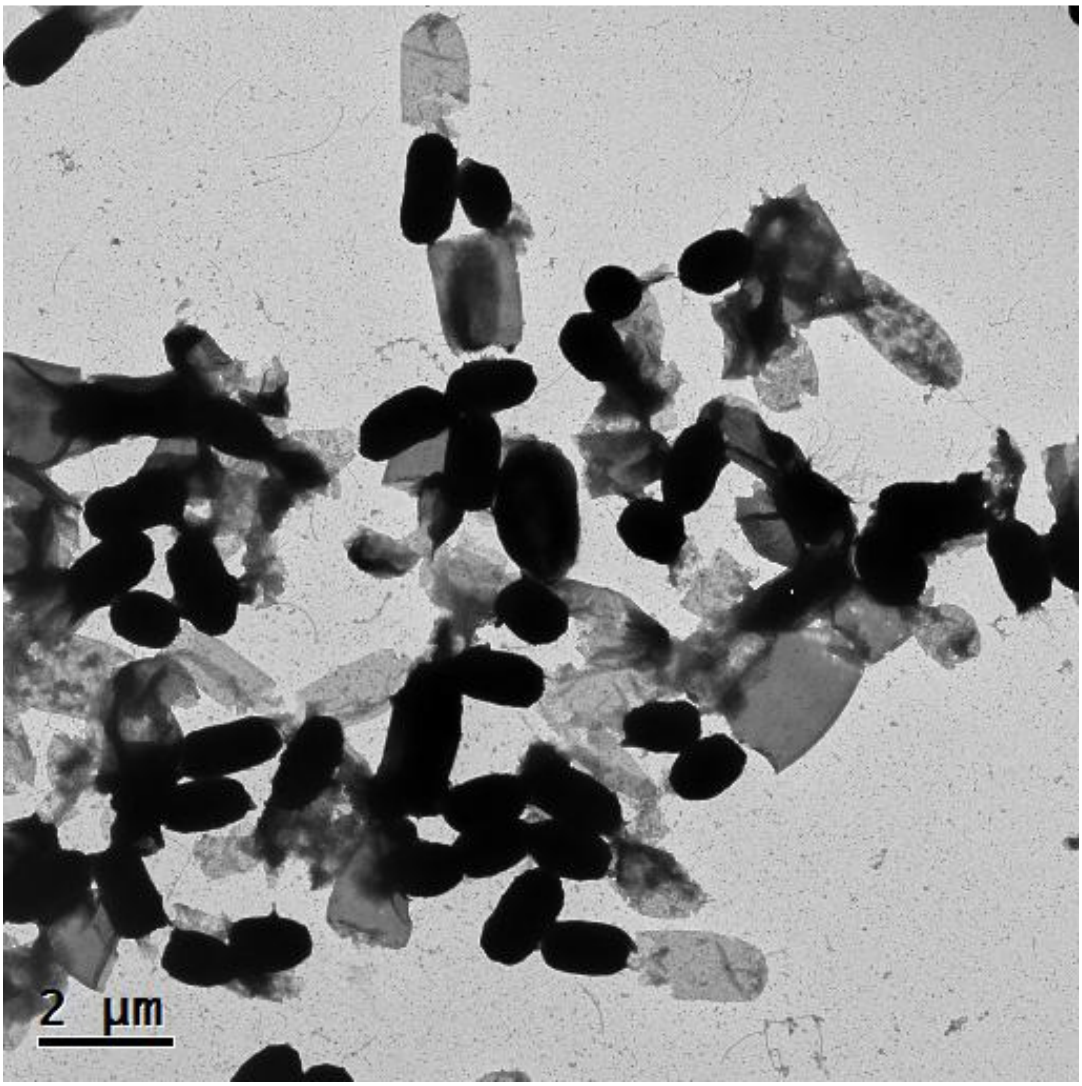

Fig 6.2 Electron micrograph of negatively stained *B. badius* BGSC #23A1 exosporia and spores. The fragile exosporium can be seen as a large loose structure.

exosporium evidently covered the spore body (Fig 6.3). It appeared to have periodic arrays with hairy nap projections (Fig 6.3). Diffraction was weak and diffuse.

6.2.4 *Paenibacillus alevei* 1113 DT-1A

Paenibacillus alevei a spore-forming bacterium, originally included within the genus *Bacillus* and then reclassified as a separate genus (Ash, Priest *et al*. 1993). By EM, spores with loose exosporium could be seen (Fig 6.4). No evident diffraction was detected from the exosporium (Fig 6.4).

6.2.5 *B. vedderi* NRRL B23388

Bacillus vedderi can produce ellipsoidal or spherical, terminal spores in swollen sporangia (N.A.Logon and Vos 2009). By EM identification, the intact spore appears to be elongated with exosporium stretched out (Fig 6.5A). The darkly stained spore body was settled in the one end of whole spore. In high magnification micrographs of exosporium of whole spores, as shown in Fig 6.5B, the obvious periodicity was detected on the surface of the exosporium layer which indicated by sharp diffraction. No hairy nap layer was seen attached but fibre-like appendages were found surrounding the exosporium.

6.2.6 *B. pseudomycoides* NRRL B-617

DNA relatedness analyses based on spectrophotometrically measured renaturation rates revealed *B. myciodes* is genetically closely related to *B. cereus* (Somerville and Jones 1972; Seki, Chung *et al*. 1978; Nakamura and Jackson 1995). *B. pseudomycoides* was separated from *Bacillus mycoides* by phylogenetic analyses and differences in fatty acid composition (Nakamura 1998). *B. psedusomycoides* is a Gram-positive, non-motile bacterium producing paracentral/subterminal, ellipsoidal endospores (N.A.Logon and Vos 2009).

By EM observation, the spore body was found relatively tightly enclosed by exosporium (Fig 6.6A). The high magnification micrograph revealed prominent exosporium with distinct diffraction (Fig 6.6B). There appears to be a ‘hairy nap’ layer visible at the exosporium outer margin (Fig 6.6B).

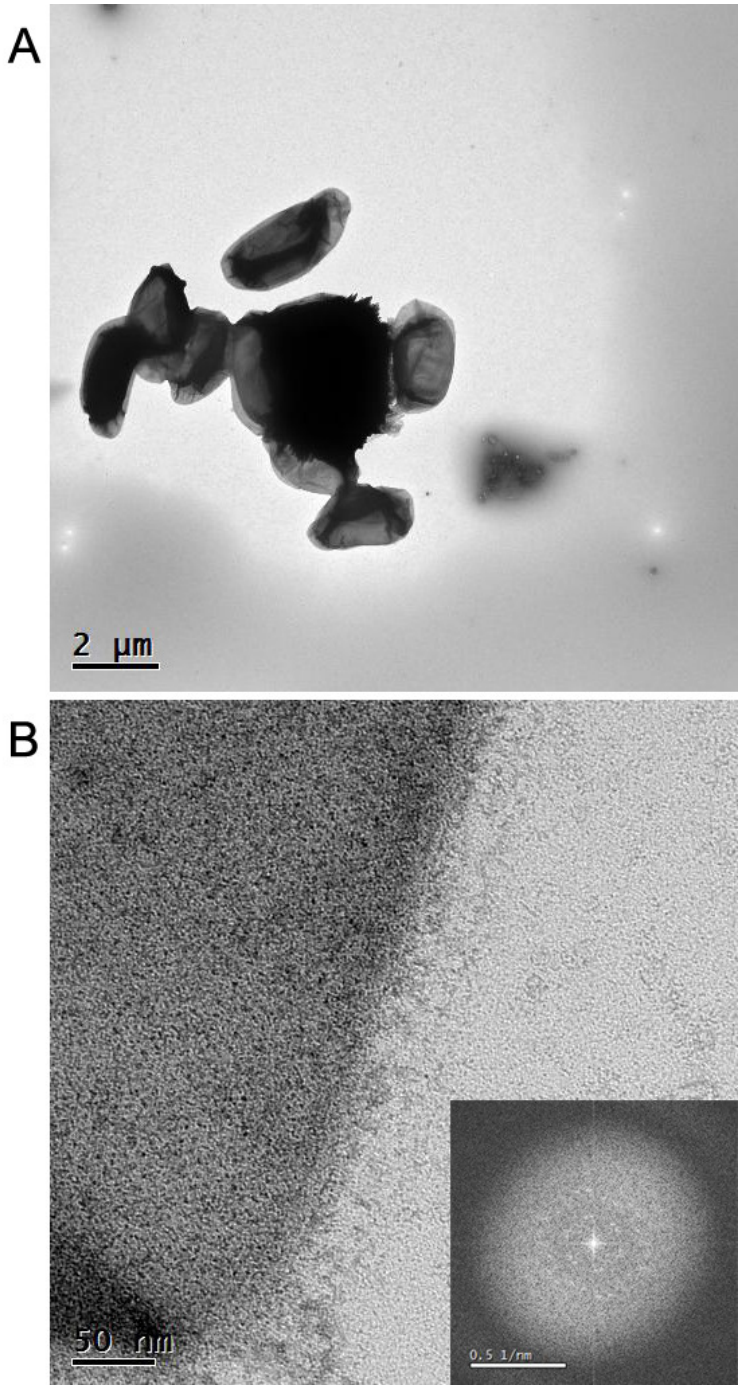

Fig 6.3 Electron micrograph of negatively stained *B. lentus* Gibson 165 BGSC #60A1 spores and exosporium. (A) the micrograph shows entire spores with distinct exosporium tightly surrounding; (B) shows the high magnification of exosporium. Hairy nap appears to attach to the thick exosporium. The generated FFT image is indicated in the inset on the right bottom.

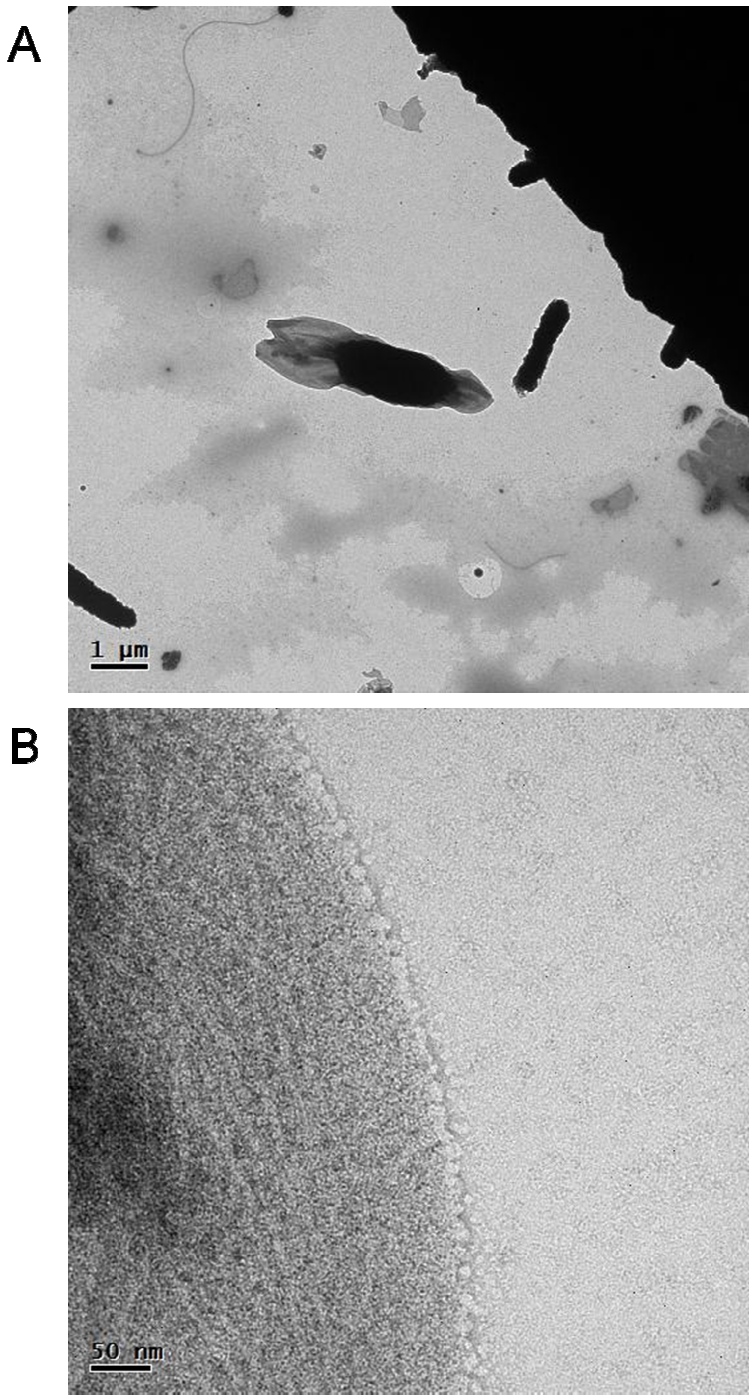

Fig 6.4 Electron micrograph of negatively stained *Paenibacillus alevei* 1113 DT-1A spores and exosporium. (A) shows entire spores with distinct exosporium. (B) shows the high magnification of exosporium. The hairy nap appears to attach to the exosporium. No diffraction was detected.

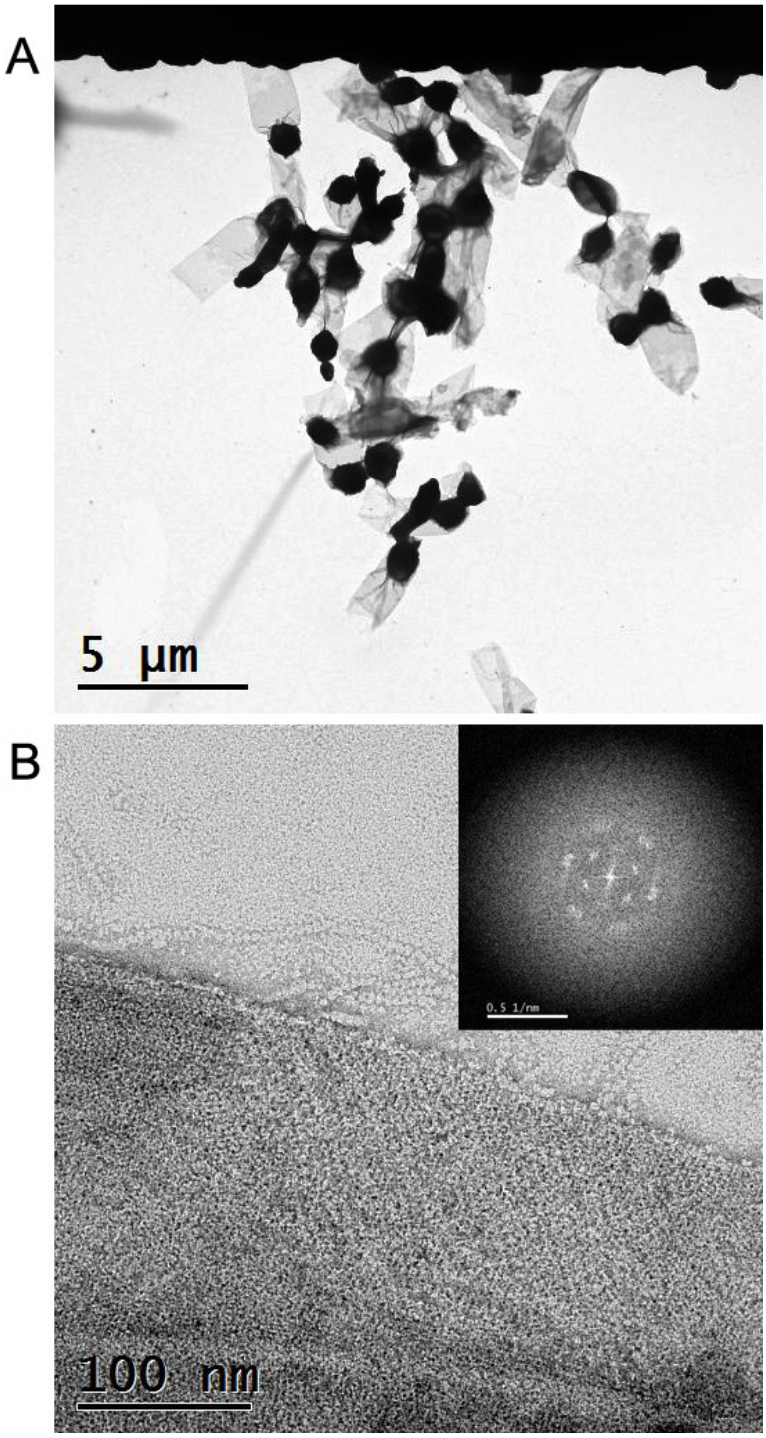

Fig 6.5 Electron micrograph of negatively stained *B. vedderi* NRRL B23388 spores and exosporia. (A) shows whole spores with distinct exosporium. The intact spore appears to be elongated with the darkly stained spore core at one pole; (B) shows the high magnification of exosporium with distinct diffraction shown in the inset. Appendages were dispersed around the exosporium but no visible hairy nap detected.

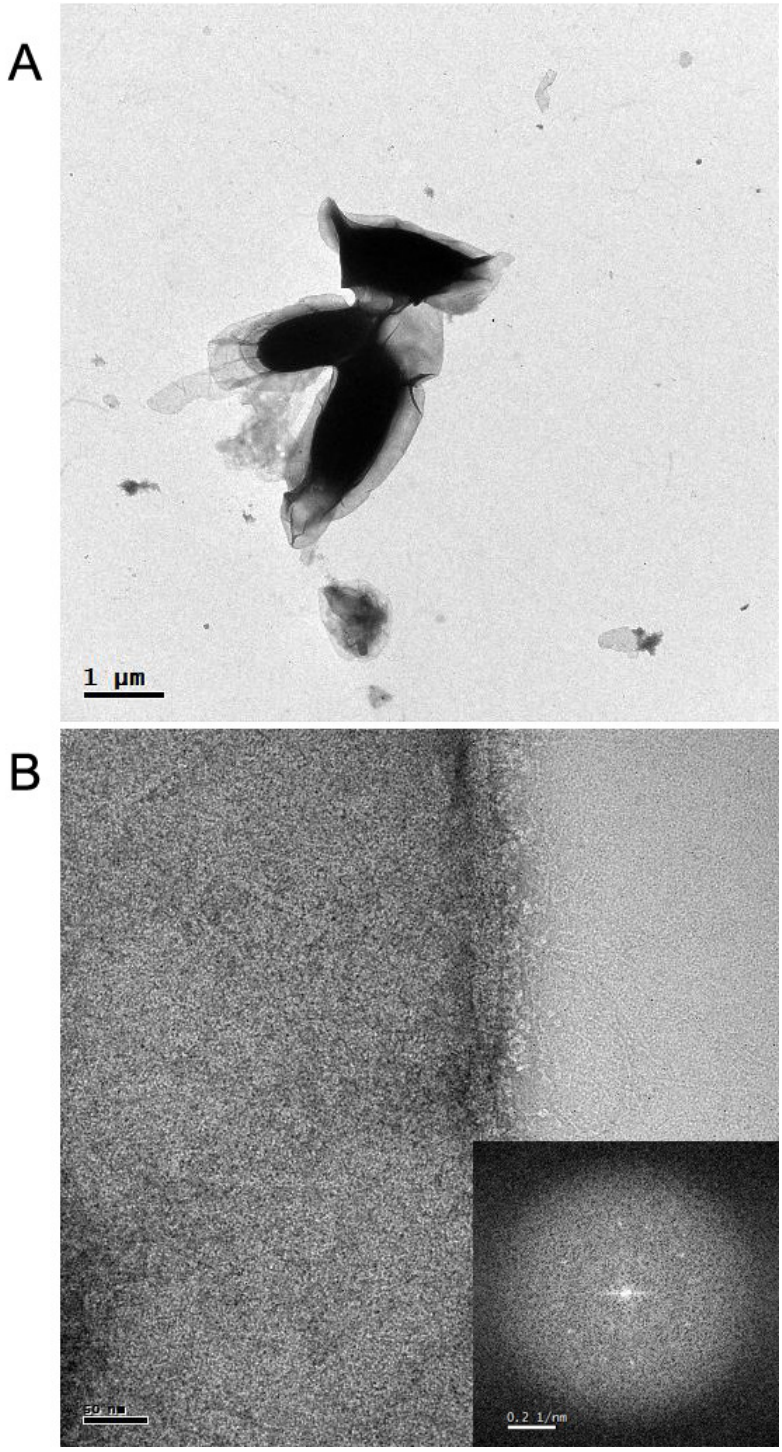

Fig 6.6 Electron micrograph of negatively stained *Bacillus pseudomyciodes* NRRL B-617 spores and exosporium. (A) shows intact spores with distinct exosporium covering. Folds are visible on the exosporium surface; (B) shows the high magnification of exosporium with distinct diffraction in the inset.

6.2.7 *B. megaterium* ATCC 12872

Bacillus megaterium is found in soil and has been extensively used as an industrial protein production host (Vary, Biedendieck *et al*. 2007). Under the electron microscope, the exosporium was heavily stained and tightly wrapped around the spore body (Fig 6.7). The exosporium layer was so dense that no structural information could be extracted from micrographs (Data not shown).

6.2.8 *B. nianci* NRRL B23384

Bacillus nianci forms a spore for which few reports are available in the literature. We observed the spore and its exosporium by EM. As shown in Fig 6.8A, the exosporium is not elongated but tightly encloses the spore body. We also detected exosporium fragments. The exosporium appeared to have well ordered arrays. A great number of well-ordered hexameric particles were found on the exosporium (Fig 6.8B). FFT indicated good crystallinity on exosporium. Preliminary image processing revealed that the unit cell dimension of crystal was $a = b$ ~91Å, γ ~120°.

6.2.9 *B. pycnus* NRRL NRS-1691

For *B. pycnus,* terminal and spherical endospores form in swollen sporangia (Nakamura, Shida *et al*. 2002; Vaishampayan, Miyashita *et al.* 2009). *B. pycnus* NRRL-NRS-1691 spores were observed by EM (Fig 6.9A). The darkly stained spore body appeared to be spherical and was localized in one terminal of spore. The exosporium was highly elongated but tightly covered the spore body at one terminus. Folds were visible at the end of spore. The high magnification micrograph appeared to show a narrow thin hairy nap fringe attached to the exosporium. Fibre-like structures could be seen on the surface (Fig 6.9). No diffraction was detected from exosporium.

6.2.10 *B. neidei* NRRL BD101

Bacillus neidei is isolated from soil (Nakamura, Shida *et al*. 2002). EM observation shows that the *B. neidei* spore appears to be a terminal spore with a loose extended exosporium (Fig 6.10). The exosporium is like a tube and the darkly stained spore body was localized at one end of the intact spore. We also looked at high magnification and ordered exosporium arrays were visible (Fig 6.10). No hairy nap was found attaching to the exosporium. Fibre-like appendages were visibly surrounding the exosporium.

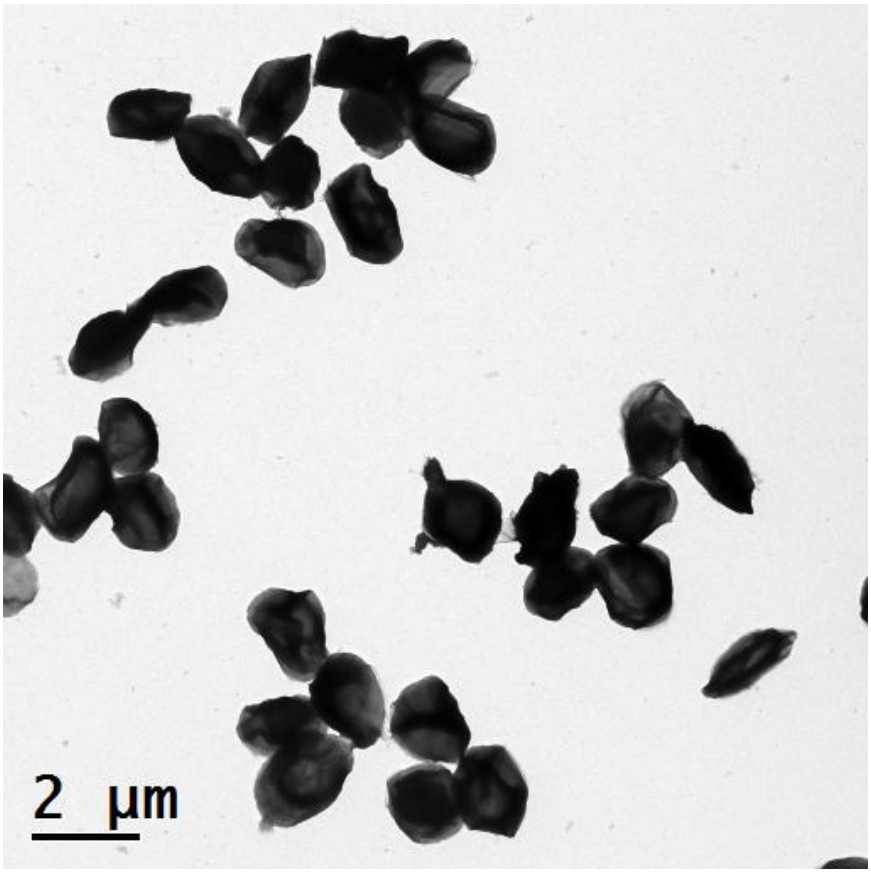

Fig 6.7 Electron micrograph of negatively stained *B. megaterium* ATCC 12872 spores.

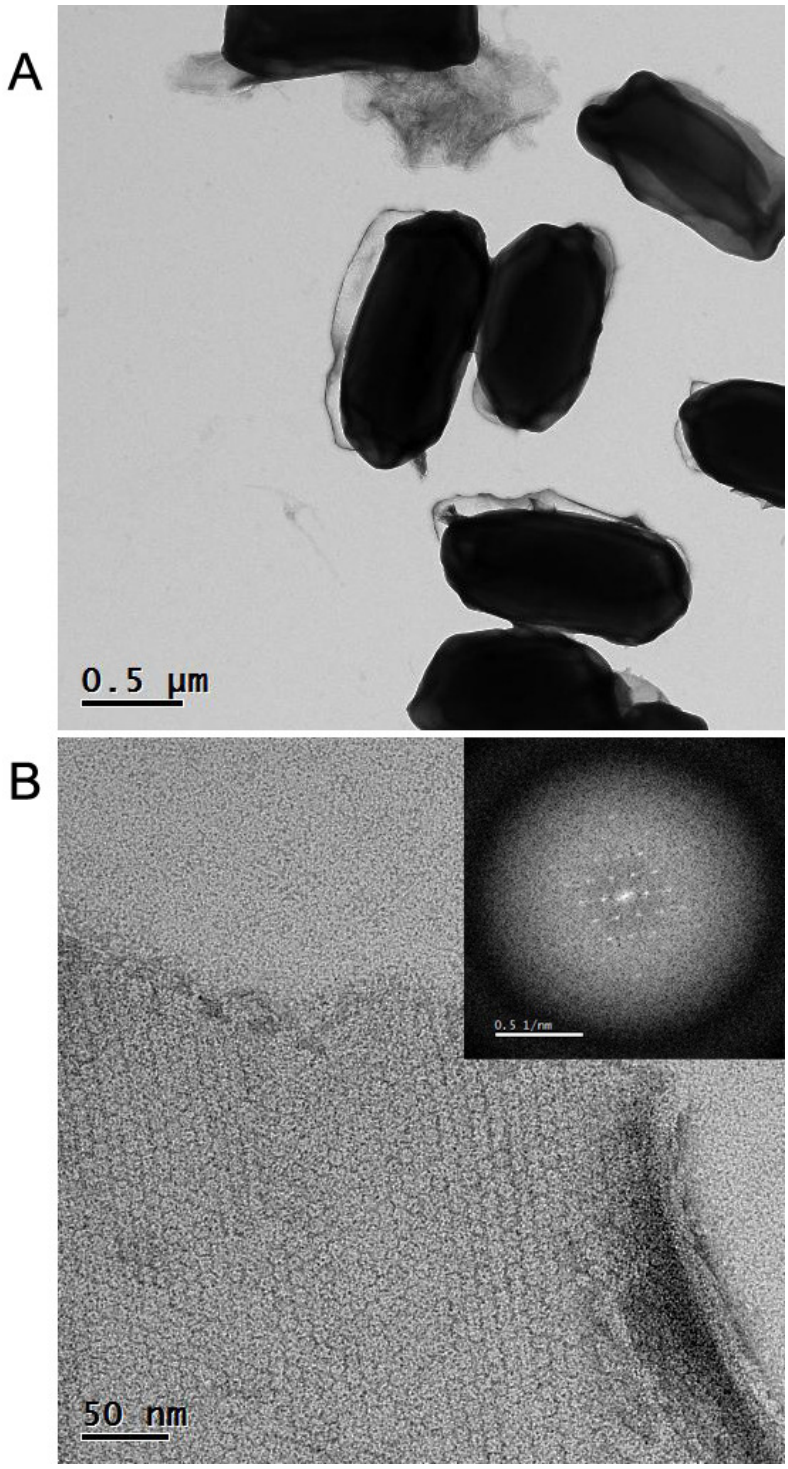

Fig 6.8 Electron micrograph of negatively stained *B. nianci* NRRL B23384 spores and exosporia. (A) shows intact spores; (B) shows the high magnification of exosporium with distinct diffraction in the inset. Apparent hexameric particles are well contrasted.

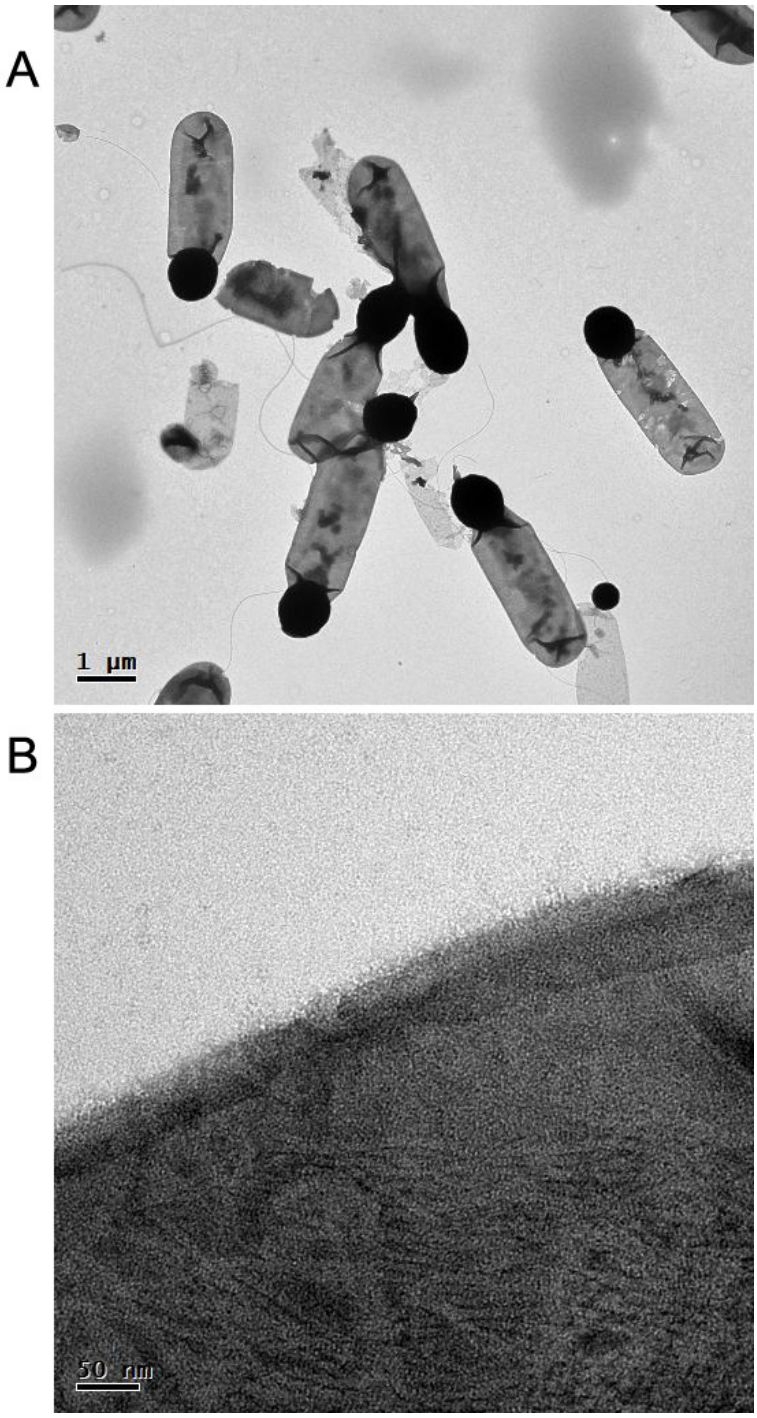

Fig 6.9 Electron micrograph of negatively stained *B. pycnus* NRRL NRS-1691 spores and exosporium. (A) shows intact spores with elongated exosporium; (B) shows the high magnification of exosporium. A short nap can be seen. No crystallinity was detected on the exosporium.

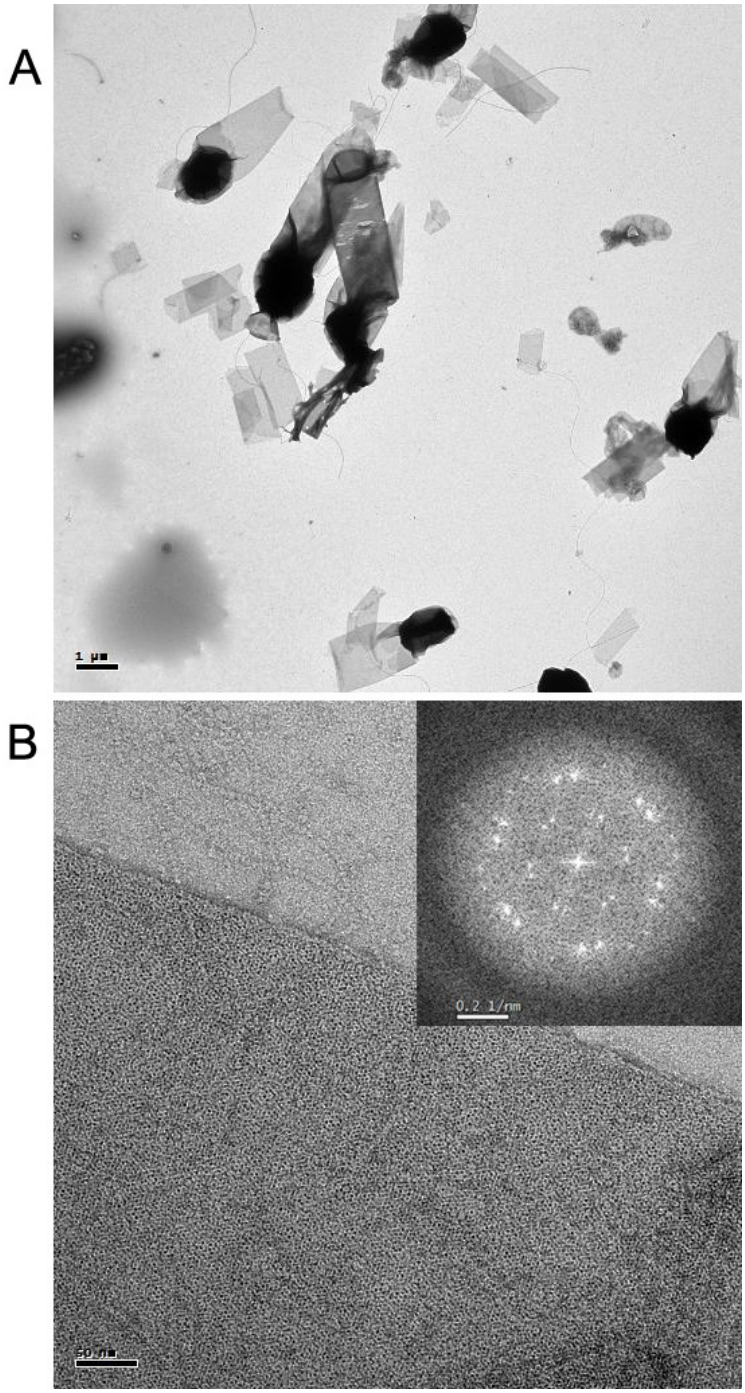

Fig 6.10 Electron micrograph of negatively stained B. neidei NRRL BD101 spores and exosporium. (A) shows intact spores with elongated exosporium. Fragments of the exosporium were dispersed around; (B) shows the high magnification of exosporium. No hairy nap was visible and crystal structure was indicated by FFT image of inset.

Preliminary image processing revealed that the unit cell dimension of crystal was $a = b$ ~63 Å, γ ~120°, whilst the distance between subunits in the fibrils was measured ~ 5 nm. This suggested that these appendages might not be sloughed off from the exosporium although they had high similarity of appearance.

6.2.11 *B. odysseyi*

B.odysseyi is an aerobic, rod-shaped bacterium forming round-spore (La Duc, Satomi *et al.* 2004). The strain was isolated from the surface of the Mars Odyssey spacecraft. The 16S rDNA sequence analysis proved the strain belonged to the genus *Bacillus* (La Duc, Satomi *et al.* 2004). Round spores were observed under EM (Fig 6.11). The loose structure of exosporium was visible wrapping the spore body. No hairy nap layer or crystal structure was found on the exosporium in high magnification micrographs (Fig 6.11).

6.2.12 *B. mycoides* ES-027

B.mycoides is a non-motile soil bacterium that was classified as a member of the *B.cereus* group (Claus and Berkeley 1986; Di Franco, Beccari *et al*. 2002). The intact spore appears similar to the *B. pseudomyciodes* NRRL B-617 spore with loose exosporium. The darkly staining spore body easily disassociates from the intact spore, and the sac-like exosporium was dispersed with intact spore as a result (Fig 6.12). We also looked at the high magnification of exosporium fragments, which presented crystallinity (Fig 6.12); the diffraction was weak. The hairy nap layer was visible on the fringe of exosporium, which is consistent with the profile of the *B. pseudomyciodes* NRRL B-617 spore we previously described.

6.2.13 *B. laterosporus* ATCC 64T

B.laterosporus is a soil based, spore-bearing bacterium that possesses a high insecticidal activity similar to the activity of *B. thuringiensis* (Favret and Yousten 1985; Smirnova, Minenkova *et al*. 1996; Orlova, Smirnova *et al*. 1998). It is distinguished by its ability to produce canoe-shaped lamellar crystal inclusions, adjacent to the spore (Smirnova, Minenkova *et al.* 1996). By EM analysis, the spore appears to be ellipsoidal with large exosporium tightly covered (Fig 6.13). No diffraction or hairy nap could be detected (Fig 6.13).

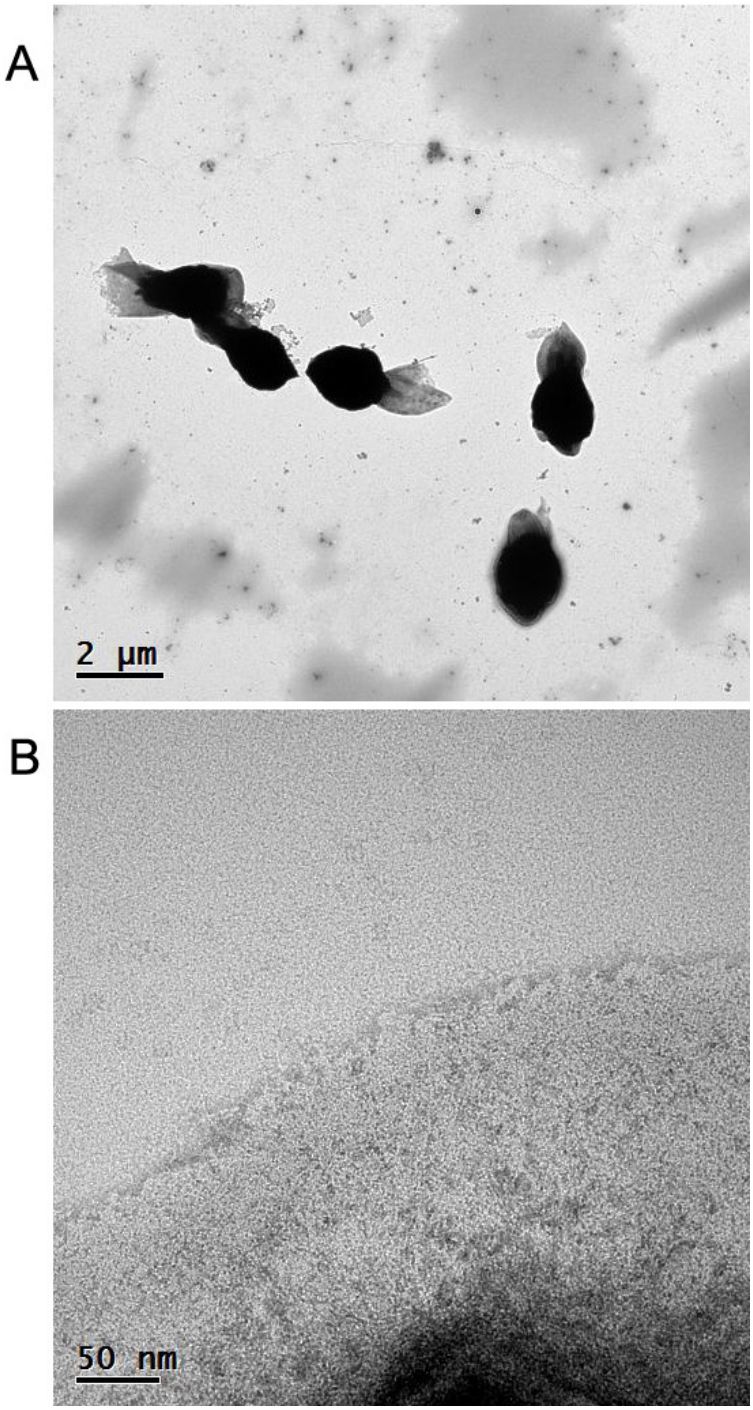

Fig 6.11 Electron micrograph of negatively stained B. odysseyi spores and exosporium fragment. (A) shows intact round-spore; (B) shows the high magnification of exosporium. No crystalline structure or hairy nap detected.

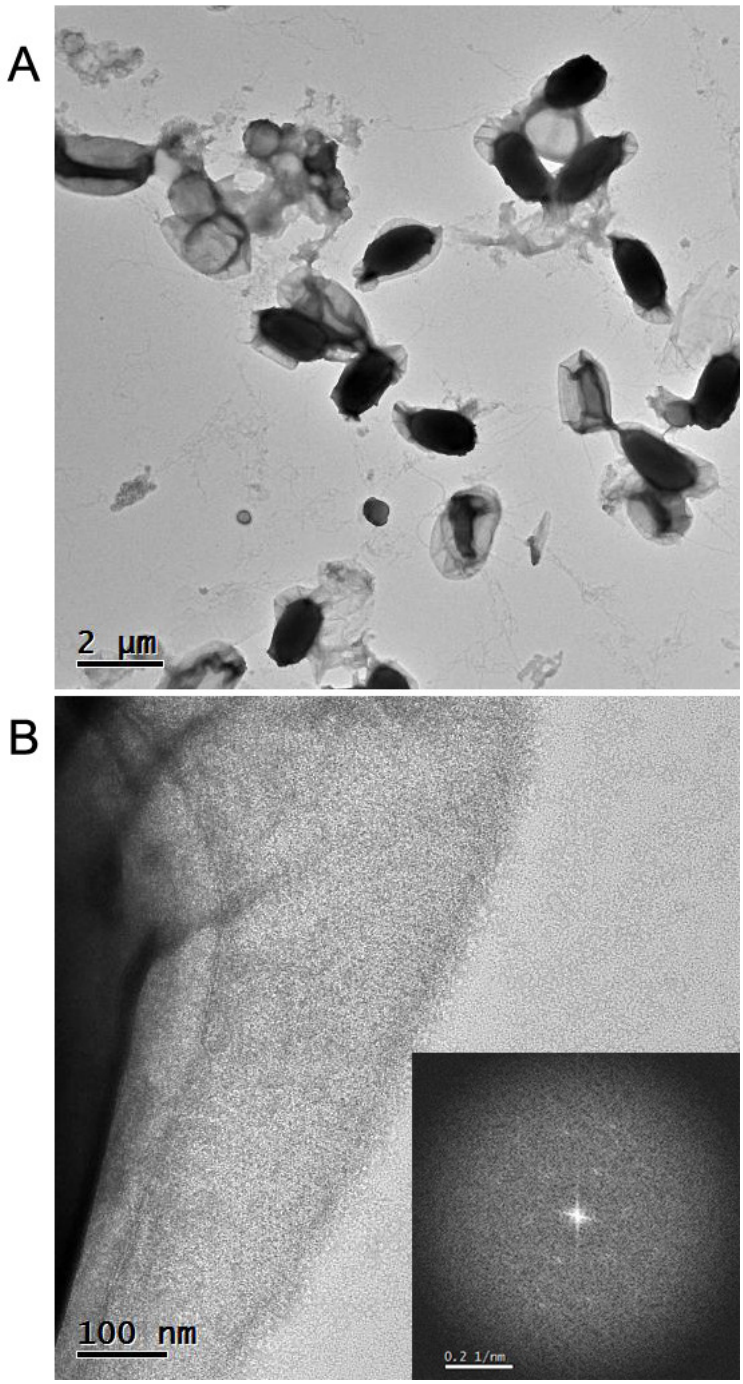

Fig 6.12 Electron micrograph of negatively stained *B. mycoides* ES-027 spores and exosporium. (A) shows intact round-spore. Some of the fragile exosporium was detached from the spore body; (B) shows the high magnification of exosporium. Weak diffraction could be detected which indicated crystal structure formed by exosporium. Hairy nap was visible attaching to the fringe of the exosporium.

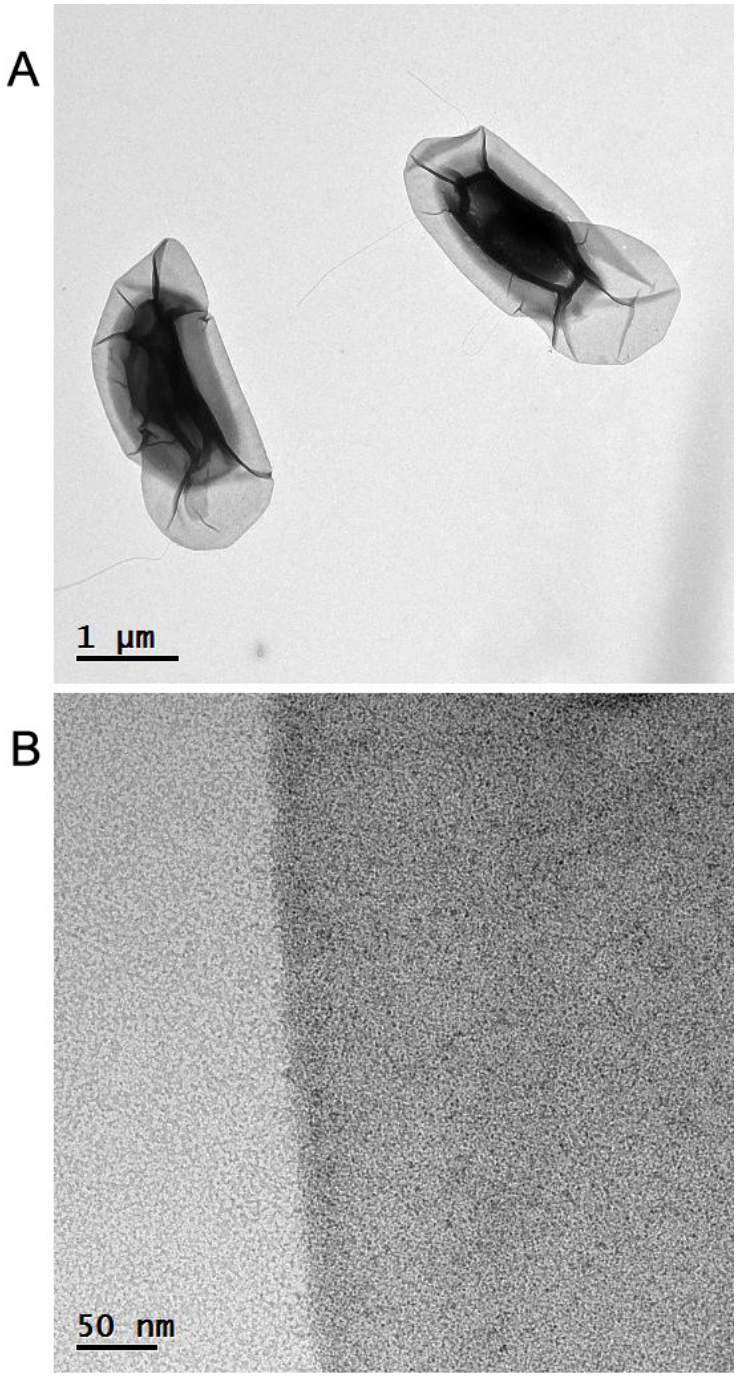

Fig 6.13 Electron micrograph of negatively stained *B. laterosporus* ATCC 64T spores and exosporium. (A) shows intact ellipsoidal spore. Large loose exosporium was clearly visible wrapping the spore body; (B) shows the high magnification of exosporium. No diffraction and hairy nap could be seen from exosporium.

6.2.14 *B. circulans* 42G1

B.circulans was first described and named by Jordan in 1890 and later isolated by Ford in 1916 (Ford 1916)**.** Its colonies displayed interior circular movement so was nominated as *B.circulans* (Ford 1916). The sporea formed by the *B. circulans* 42G1 were observed by EM. The ellipsoidal spore bodies were enclosed by a large balloon-like exosporium (Fig 6.14). Filamentous appendages were found sticking out of exospoium. High magnification of the exosporium demonstrated a clear periodicity on the surface along with a hairy nap (Fig 6.14). The well-ordered crystal structure formed by the *B. circulans* 42G1 makes it a good candidate for high-resolution 2D/3D investigation.

6.2.15 *B. fusiformis* ATCC 7055

B. fusiformis is long, rod-shaped, spore-forming bacterium of the genus *Bacillus.* The spore formed by *B. fusiformis* ATCC 7055 appeared to be a long rod shape by EM observation (Fig 6.15). The highly extended exosporium enclosed the darkly spherical spore on one end of intact spore. High magnification micrograph of exosporium showed a well-ordered periodicity (Fig 6.15) making this spore a good candidate for high-resolution 2D/3D analysis.

6.3 Structural analysis of exosporium from *Bacillus circulans* 42G1

The spore was subjected to slight sonication treatment, usually 5 second at amplitude 10 microns to isolate the fragments of the exosporium (Fig 6.16). The fragments we obtained were analysed by negative stain EM and image processing.

We found two types of crystal formed within the exosporium. The data for one type were extracted from the image of exosporium in intact spores. The crystal lattice with dimensions $a = b$ ~83Å, γ ~120°, similar to that of the type II crystal described by Ball *et al.* (Ball, Taylor *et al.* 2008) (Fig 6.17). Analysis of each individual crystal revealed that *p*3 symmetry was favoured (table 6.2).

The other type of crystal lattice displayed unit cell dimensions $a = b$ ~67Å, γ ~120°, *p*3 symmetry was favoured (table 6.3). The sample was revealed in samples subjected to light sonication; the parameters are close to those of the type I crystal described by Ball

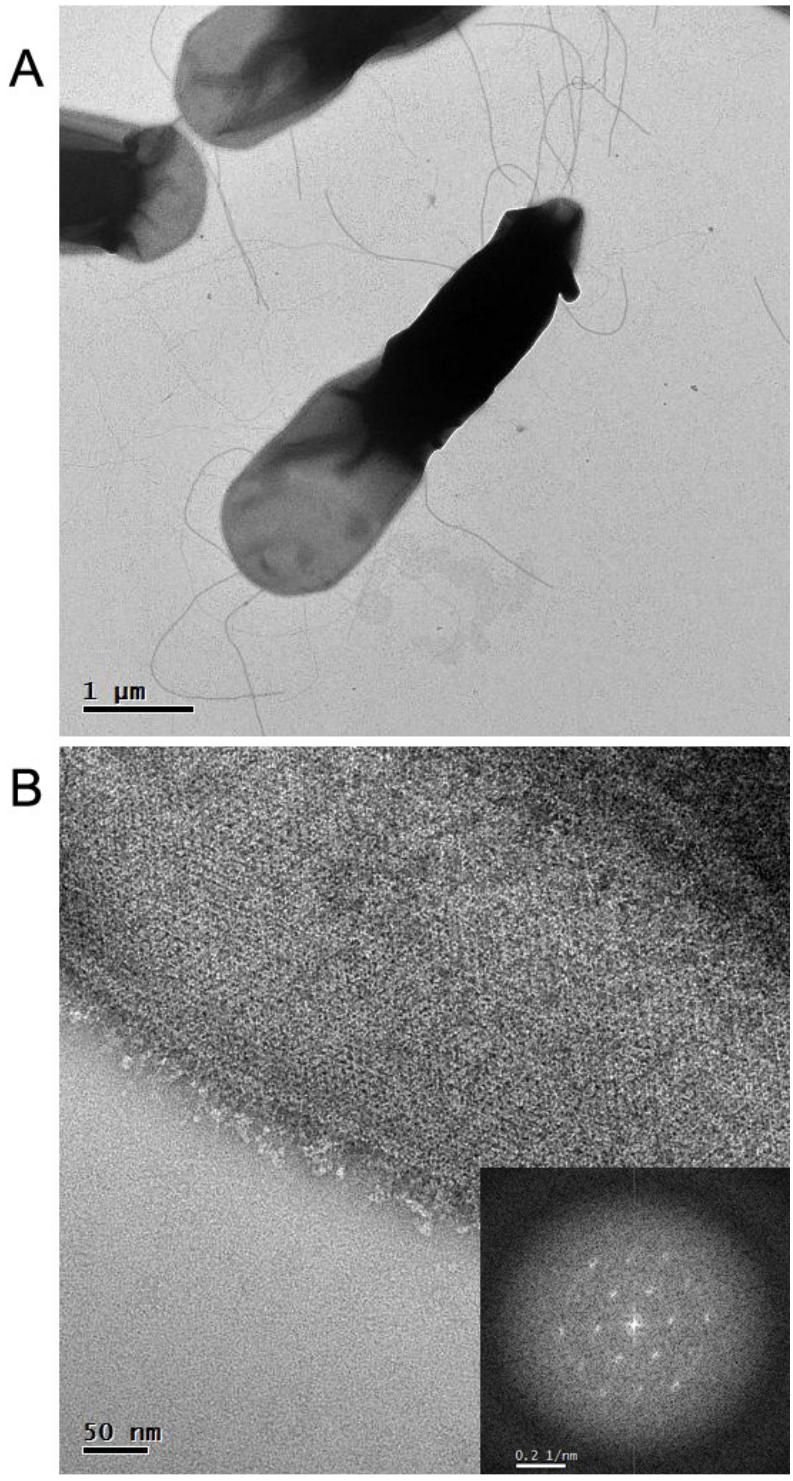

Fig 6.14 Electron micrograph of negatively stained *B. circulans* 42G1 spores and exosporium. (A) shows intact spore. Large loose exosporium was clearly visible wrapping the spore body. The filament appendages stuck out from exosporium; (B) shows the high magnification of exosporium. Highly periodicity was evident on the surface of exosporium where hairy nap apparently attached.

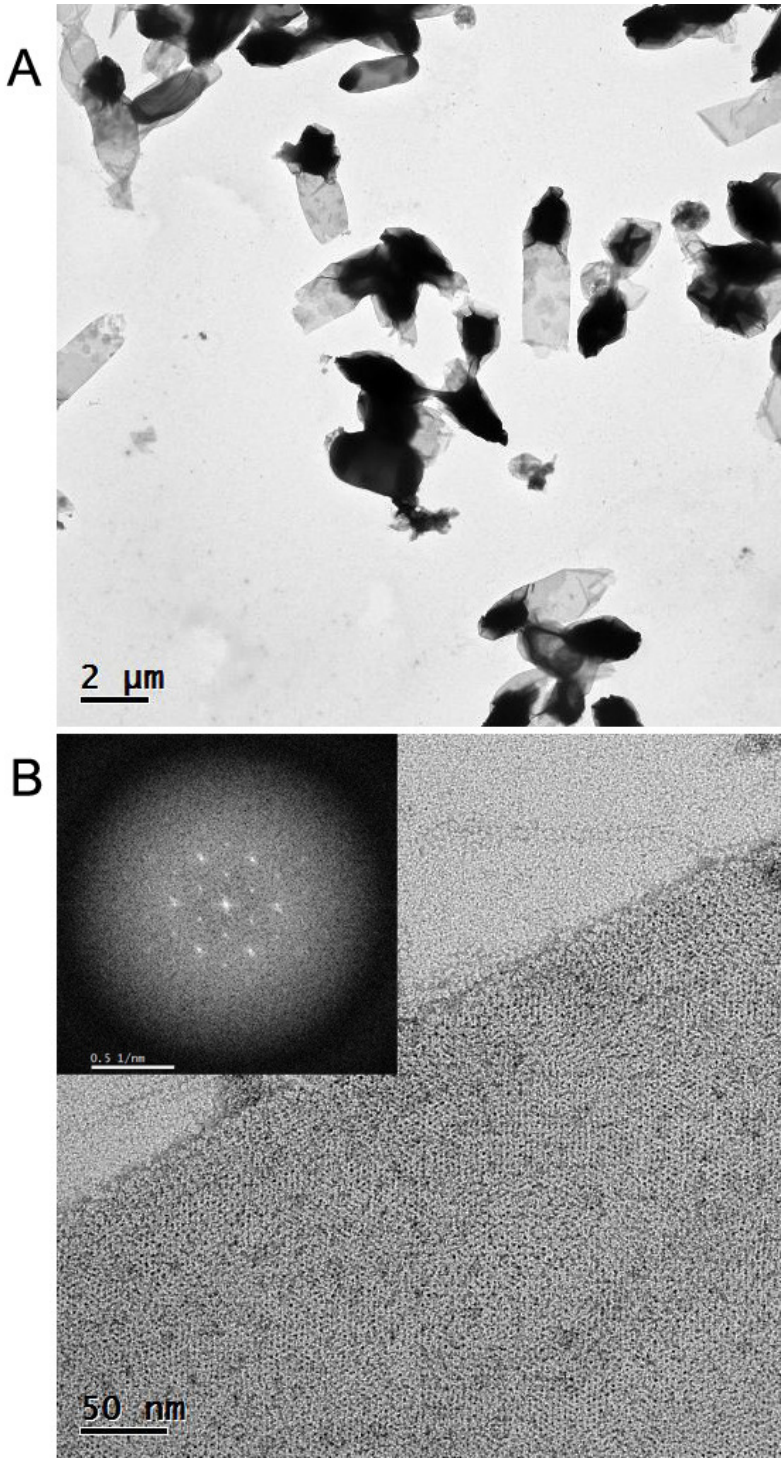

Fig 6.15 Electron micrograph of negatively stained *B. fusiformis* ATCC 7055 spores and exosporium. (A) shows intact spore. A large tubular exosporium was seen with darkly stained spore body at one pole; (B) shows the high magnification of exosporium. High periodicity was evident on the surface of exosporium. No hairy nap detected.

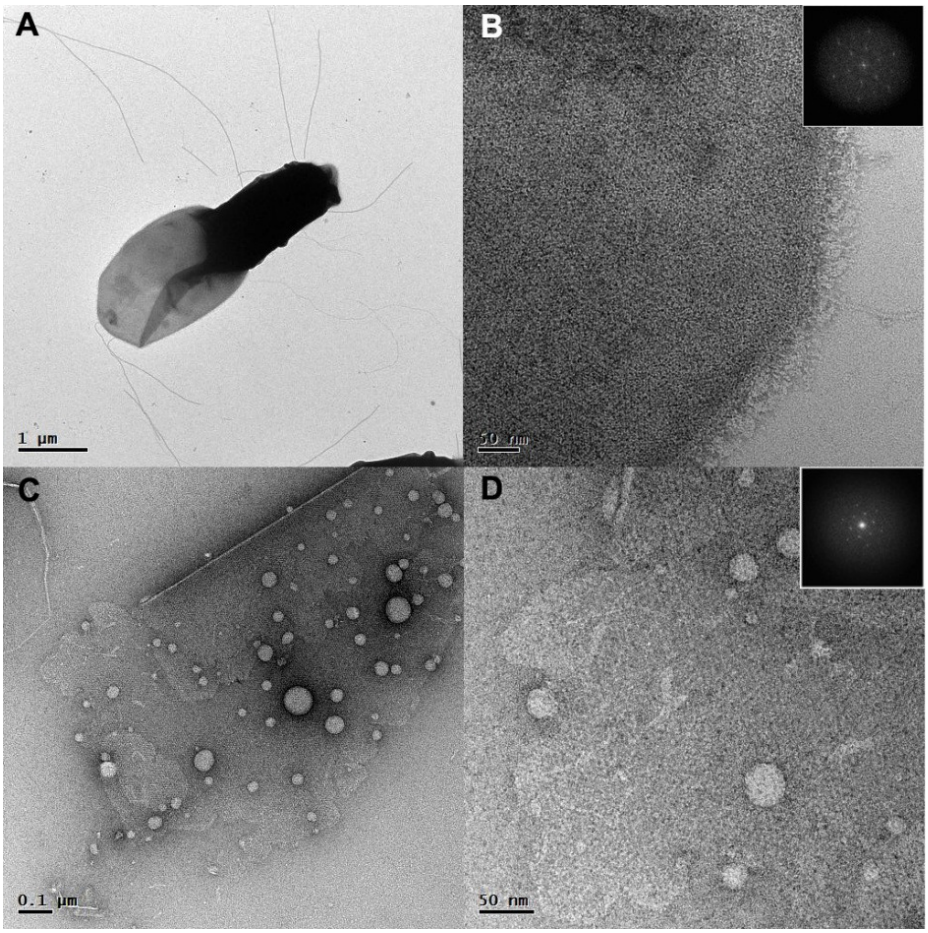

Fig 6.16 Images of spores of *B. circulans* 42G1. (A) Whole spore; (B) The exosporium on an intact spore. Inset shows a FFT image corresponding to the sample; (C) Low magnification image of crystal from exosporium upon slight sonication; (D) High magnification image of crystal sloughed off upon slight sonication. Inset shows a FFT image corresponding to the sample

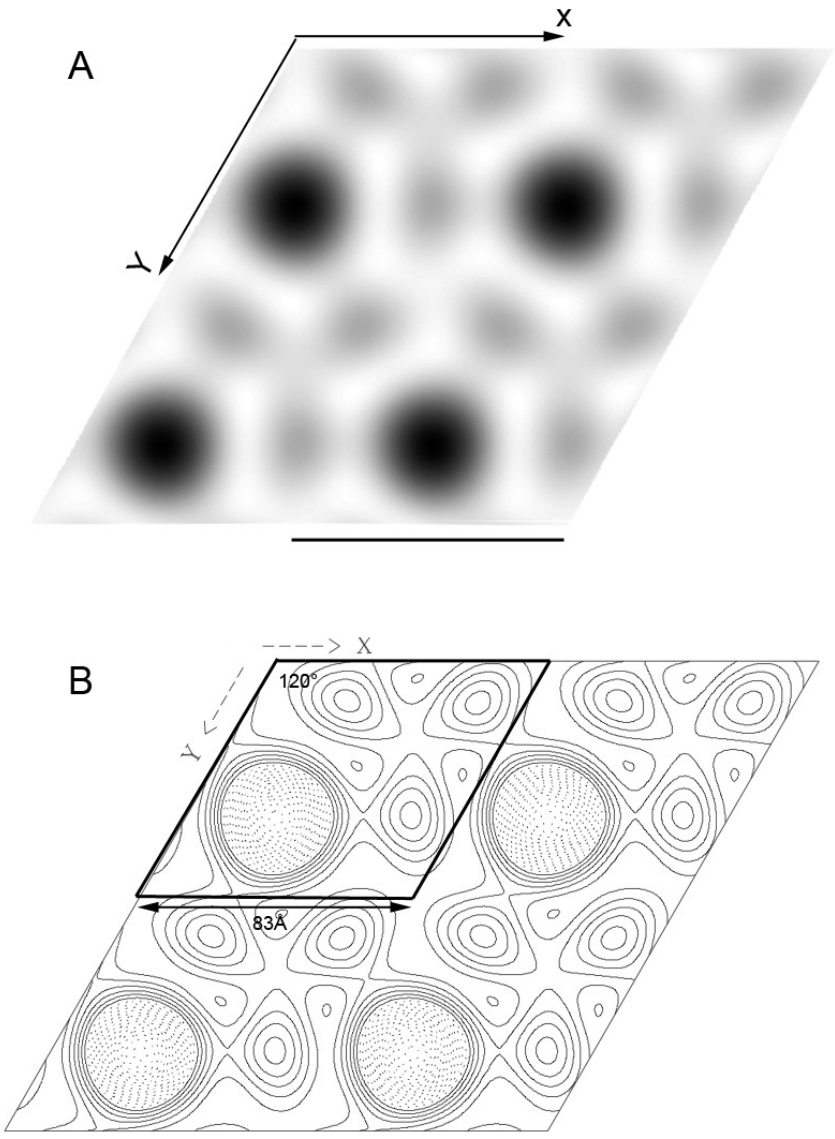

Fig 6.17 The projection map of type II crystal of *B. circulans* 42G1 exosporium. The unit cell dimensions $a=b$ ~83Å, γ ~120. (A) Grey-level maps of $p3$ map from exosporium; (B) Contour maps of the density. The upper resolution is 20 Å. Black is dense regions. White is least dense regions. Scale bar is about 83 Å.

Table 6.2 The internal phase residuals determined after the imposition of all possible two-sided plane groups calculated from one of the micrographs of *B. circulans* 42G1 exosporium Type II crystals.

Two sided plane group	Phase residual versus with other spot (90° random)	Number of comparisons	Target residual based on statistics taking Friedel weight into account
*p*1	26.0	40	
*p*2	37.2	20	29.1
*p*12_b	49.2	11	29.3
*p*12_a	74.0	11	29.3
*p*121_a	58.4	11	29.3
*p*121_b	59.0	11	29.3
*c*12_b	49.2	11	29.3
*c*12_a	74.0	11	29.3
*p*222	56.5	42	31.8
*p*2221b	67.7	42	31.8
*p*2221a	57.7	42	31.8
*p*22121	51.2	42	31.8
*c*222	56.5	42	31.8
*p*4	54.9	48	31.0
*p*422	50.5	102	28.4
*p*4212	49.2	102	28.4
*p*3	20.9*	36	26.0
*p*312	22.6*	82	26.6
*p*321	24.6*	87	27.3
*p*6	25.6*	92	28.6
p622	25.8*	189	27.3

Internal phase residuals were determined from spots of IQ1-1Q5 to 20Å resolution. The values marked with * are good candidates for the symmetry as the experimental phase residual is close to that expected value based on the signal-to-noise ratio.

Table 6.3 The internal phase residuals determined after the imposition of all possible two-sided plane groups calculated from one of the micrographs of *B. circulans* 42G1 exosporium Type I crystals.

Two sided plane group	Phase residual versus with other spot (90° random)	Number of comparisons	Target residual based on statistics taking Friedel weight into account
*p*1	23.7	32	
*p*2	59.4	16	34.4
*p*12_b	70.6	9	27.3
*p*12_a	44.1	8	26.4
*p*121_a	65.3	9	27.3
*p*121_b	54.6	8	26.4
*c*12_b	70.6	9	27.3
*c*12_a	44.1	8	26.4
*p*222	59.9	33	28.9
*p*2221b	61.9	33	28.9
*p*2221a	63.7	33	28.9
*p*22121	64.7	33	28.9
*c*222	59.9	33	28.9
*p*4	57.7	36	28.5
*p*422	66.4	80	25.8
*p*4212	66.0	80	25.8
*p*3	13.4*	30	23.7
*p*312	49.2	69	24.1
*p*321	33.3	73	24.7
*p*6	40.2	76	25.9
p622	59.1	158	24.8

Internal phase residuals were determined from spots of IQ1-1Q5 to 20Å resolution. The values marked with * are good candidates for the symmetry as the experimental phase residual is close to that expected value based on the signal-to-noise ratio.

et al. (Ball, Taylor *et al.* 2008). We collected images of nine tilt series, but data from these series proved difficult to merge into one data set. We compared projection maps for each series and found that they could be sorted into 4 types as shown in Fig 6.18.

It is noteworthy that the *B. cereus* family type I crystal was localized in a parasporal layer of the spore where no hairy nap is attached (Ball, Taylor *et al.* 2008). Similarly, in our sample, no hairy nap layer has been detected on these four various forms of crystals, nonetheless, the whole spore does have a hairy nap attached. This suggests these crystal types may also be isolated from a parasporal layer underneath the type II crystal layer we initially found on the outermost layer of the whole spore because we did not see this lattice in the extended parts of the exosporium on the intact spores. Additionally, we also directly observed multi-layers on the exosporium after being treated with sonication (Fig 6.19).

6.4 Structural analysis of exosporium from *B. fusiformis* ATCC 7055

Unlike the *B. circulans* 42G1, the spore of *B. fusiformis* ATCC 7055 has no clearly defined hair-like layer attaching on the surface of exosporium layer.

To isolate the single layer of the exosporium, the spore was subjected to slight sonication treatment. Fig 20 shows the fragments released from the whole spore. In attempting to map out the exosporium structure, image analysis was performed on micrographs of the fractioned and intact exosporium sheets. *2dx-image* was used to analyse the 2D exosporium, and up to date, we only found one type of crystal form in *B. fusiformis* ATCC 7055 with the unit cell in p3 symmetry, $a = b$ ~67 Å, γ ~120° (Fig 6.21); this is close to the type I crystal assigned described by Ball *et al*., in the parasporal layer of B. cereus spores, which also has no hairy nap attached. In comparison with the type I crystal of *B. circulans* 42G1 exosporium the appearance of *B. fusiformis* ATCC 7055 bears some similar overall appearance in 2D projection map (Fig 6.18). However, high-resolution cryo-EM is essential for a detailed comparison, as well as its protein composition exploration.

The crystals tilted by up to ± 50 degrees (10º increment) were collected to reconstruct a 3D representation of the crystal density. Due to the highly ordered and enormous exosporium pieces we isolated, the 3D map was of low noise. In the same way as we

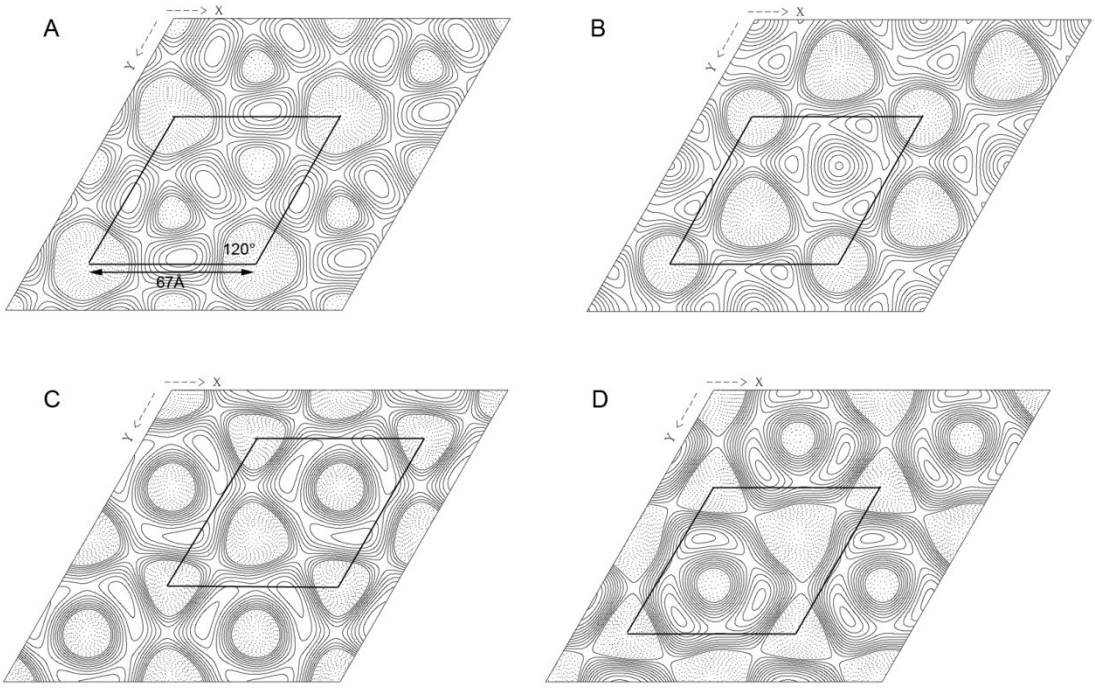

Fig 6.18 Four contour maps of density from various exosporium fragments of *B. circulans* 42G1 after slight sonciation treatment. *p*3 symmetry was applied. All four unit cell shares the same dimension $a=b$ ~67Å, γ ~120. The unit cell profile was drawn up by solid line and dimension indicated as well.

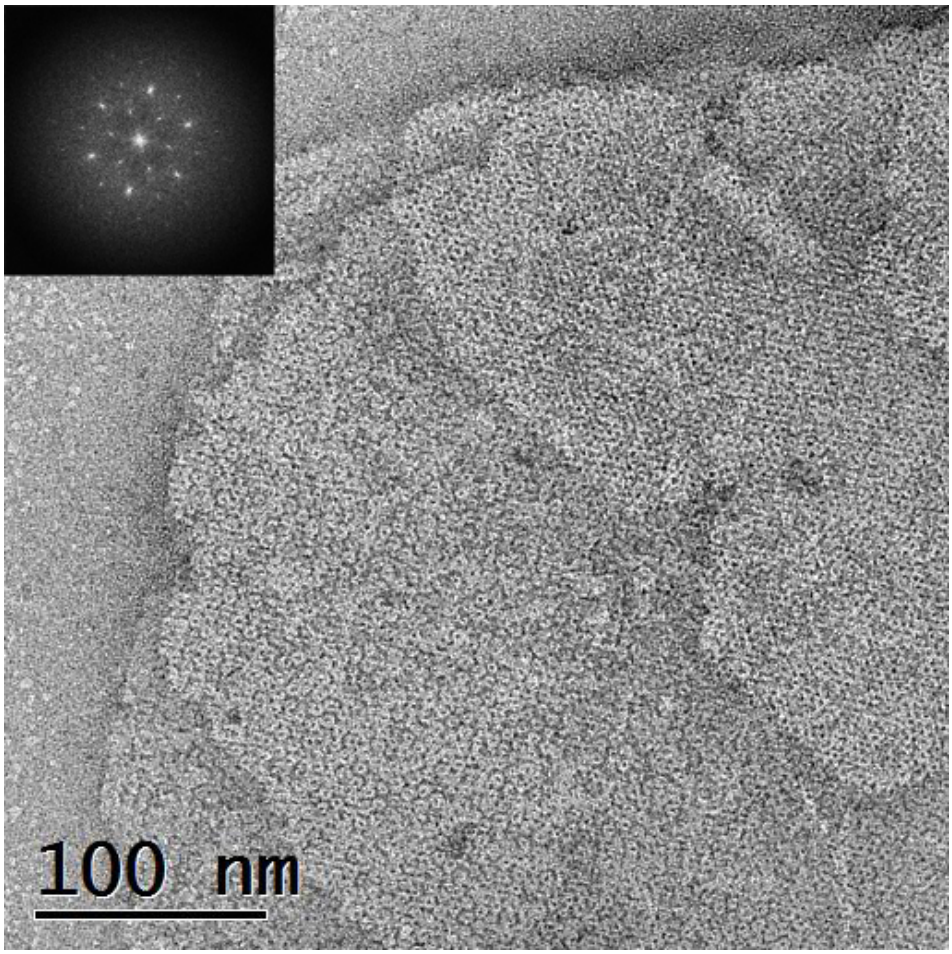

Fig 6.19 Electron micrograph of negatively stained *B. circulans* 42G1 exosporium fragments after sonication. The disrupted exosporium revealed multilayered structure. No hairy nap was visible on the surface. The unit cell dimension of whole fragment is $a = b$ ~67Å, γ ~120° indicative of type I crystal. FFT image shown in the inset.

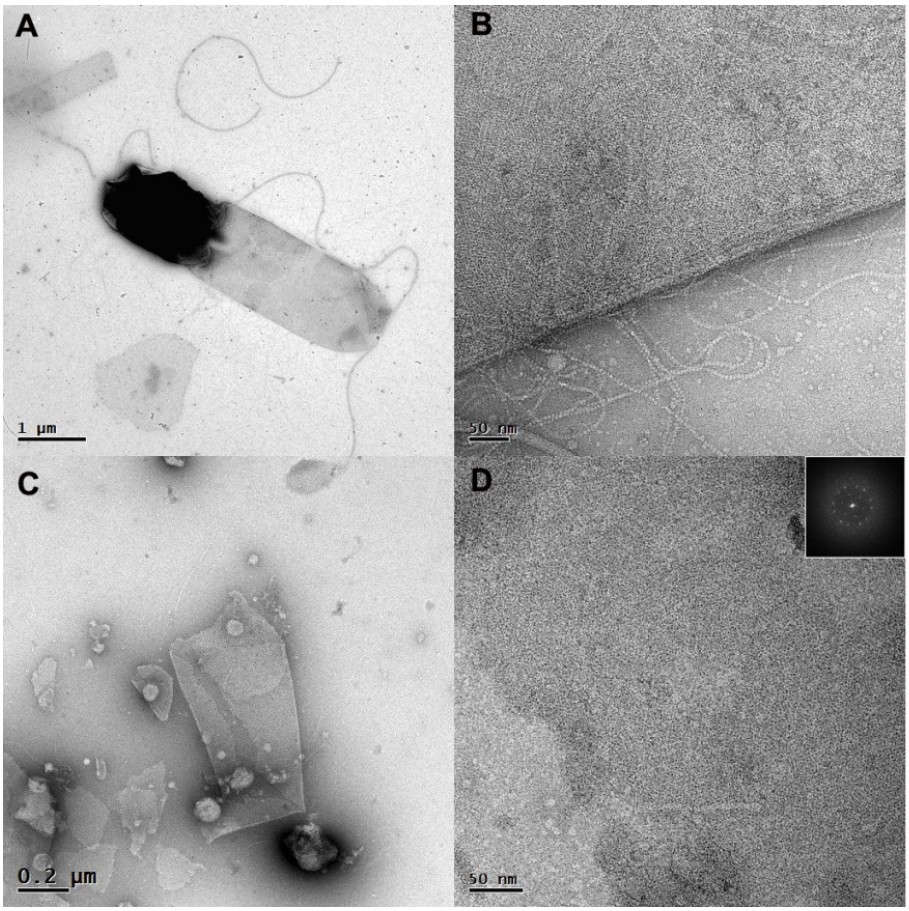

Fig 6.20 Negatively stained spores of *B. fusiformis* ATCC 7055 and exosporium fragments after sonication. (A) Whole spore; (B) The exosporium on an intact spore; (C) Low magnification image of crystal from exosporium upon slight sonication; (D) High magnification image of crystal separated out upon slight sonication. Inset shows a FFT image corresponding to the sample.

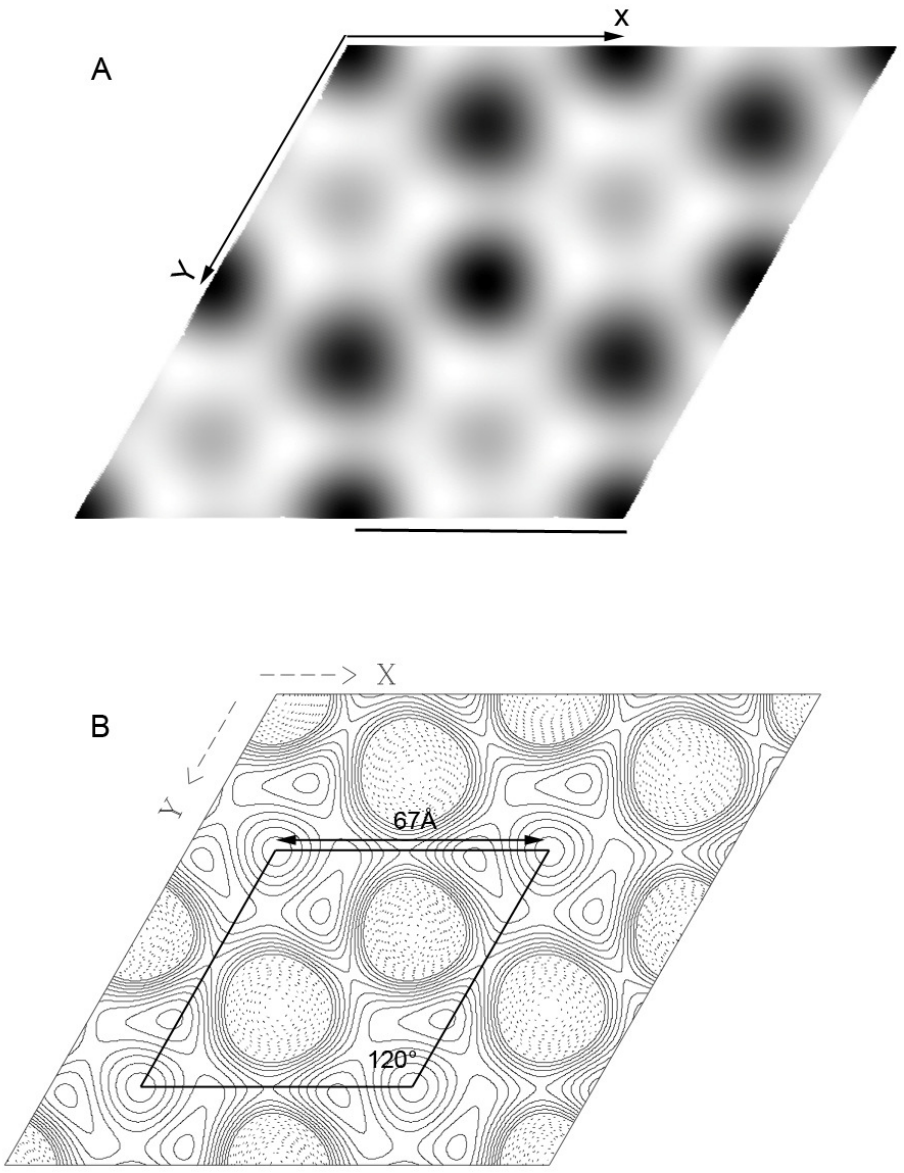

Fig 6.21 Representative density projection map of *B. fusiformis* ATCC 7055 exosporium. (A) Grey-level maps of p3 map from exosporium; (B) Contour maps of the density. The upper resolution is 20 Å. Black is dense regions. White is least dense regions. Scale bar is about 67 Å. Unit cell profile indicated by solid line.

processed the CotY crystal, the 3D map was merged by starting with non-tilted images and as shown in Fig 6.22, the pits and holes on the unit cell lattice are regularly distributed. The overall architecture appears as a two-dimensional lattice of "cup". The bulk of the molecular mass is concentrated around one of the three-fold symmetry axes to form each individual "cup" that encloses a central cavity, apparently closed at on end (Fig 6.22A) but open at the other (Fig 6.22B). The lattice appears to be connected by six connecting spokes. At the chosen threshold levels, the cups have a cross length <32 Å and <40 Å in thickness. The holes between the crowns have a triangular appearance with a diameter of < 45 Å at their widest point and the diameter of the round holes is <37 Å (Fig 6.22).

6.5 Projection structure of type I crystals of *B. fusiformis* ATCC 7055 exosporium using cryo-EM

The best of cryo-images were picked from a number of films and the majority of exosporium crystals diffract well with sharp spots in the FFT visible out as far as to 8 Å (Fig 6.23). *2dx_image* was used to process the individual cryo-images. All the acceptable plane groups after internal phase comparisons suggested phase residuals from the crystals were consistent with *p*3 symmetry (table 6.4). *p*3 was therefore applied to our processed images. To produce a detailed merged 2D map, the best three of the crystal cryo-images based on the crystal size and order by analysis of calculated Fourier transform were selected. The selected images were initially processed by *2dx_image*. The phase and amplitude data were extracted and refined to a common phase origin using ORIGTILTK by using the standard scripts for 2D plane merging based on MRC software suite. SCALEIMAMP was used to determine the temperature factor for amplitudes correction by using the bacteriorhodopsin amplitudes as reference for scaling (Havelka, Henderson *et al*. 1995; Crowther, Henderson *et al.* 1996). The fall-off in the contrast transfer function envelope for each image was restored by the application of negative temperature factors ranging from 720 to 1000Å^2. AVRGAMPHS was used to average phases and amplitudes and generate a figure-of-merit weighted projection map (Table 6.5). *p*3 symmetry was applied to the merged images. As shown in Fig 6.24, the 2D projection map indicates density features, some of which may represent α-helices at 10 Å resolution.

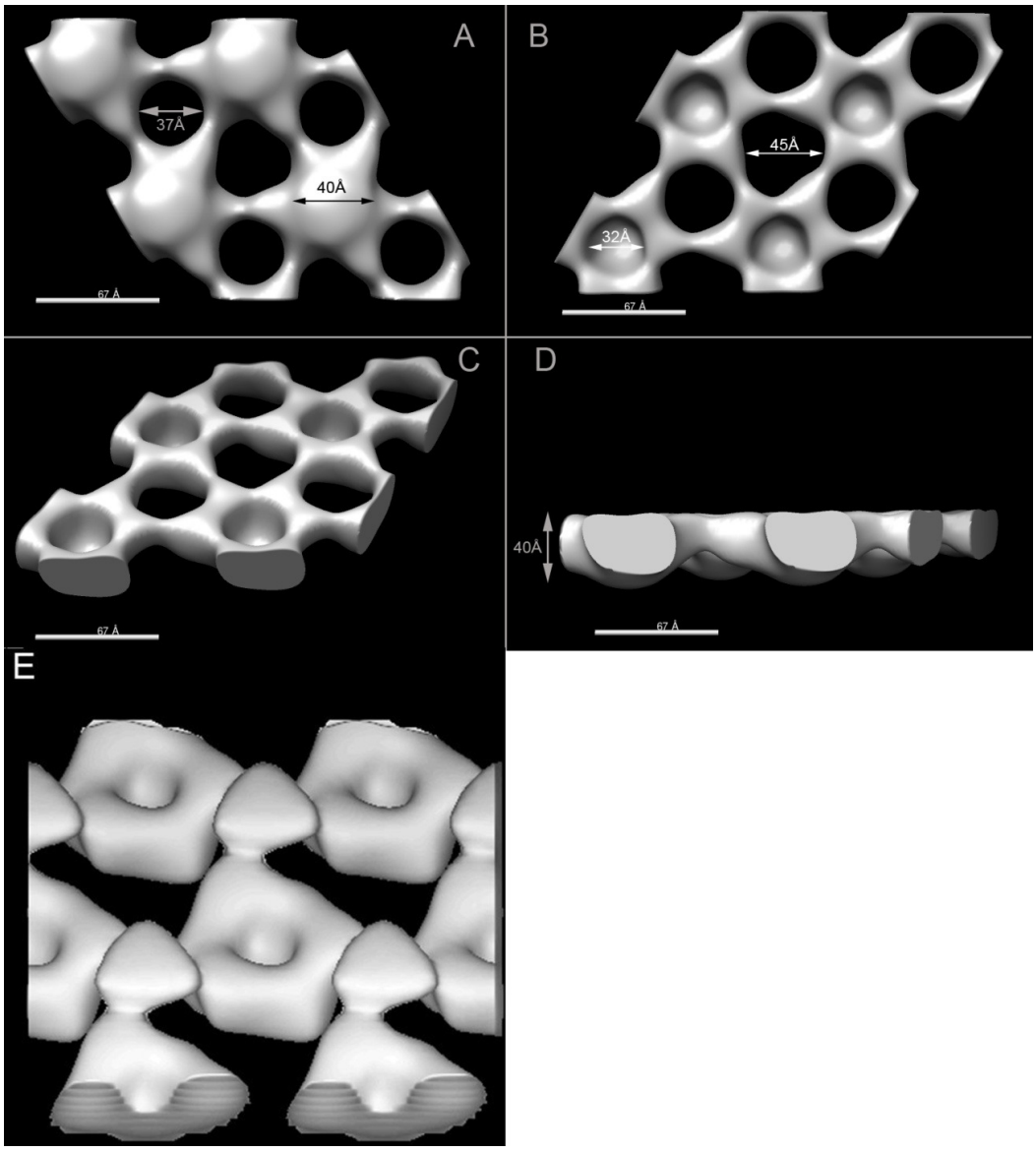

Fig 6.22 Reconstruction of negatively stained type I crystal of *B. fusiformis* ATCC 7055. (A-B) View perpendicular to the crystal plane from both surfaces; (C) Oblique view of 3D map; (D) Cross section view of 3D map. The upper resolution is about 25 Å. The dimensions of the crystals lattice are $a=b$ ~67 Å, γ ~ 120. The cross length of crystal thickness and little hole on the crystal was indicated. Scale bar ~67 Å; (E) Surface representations of the *B. thuringiensis* type I crystal in three dimensions from (Ball, Taylor *et al*. 2008).

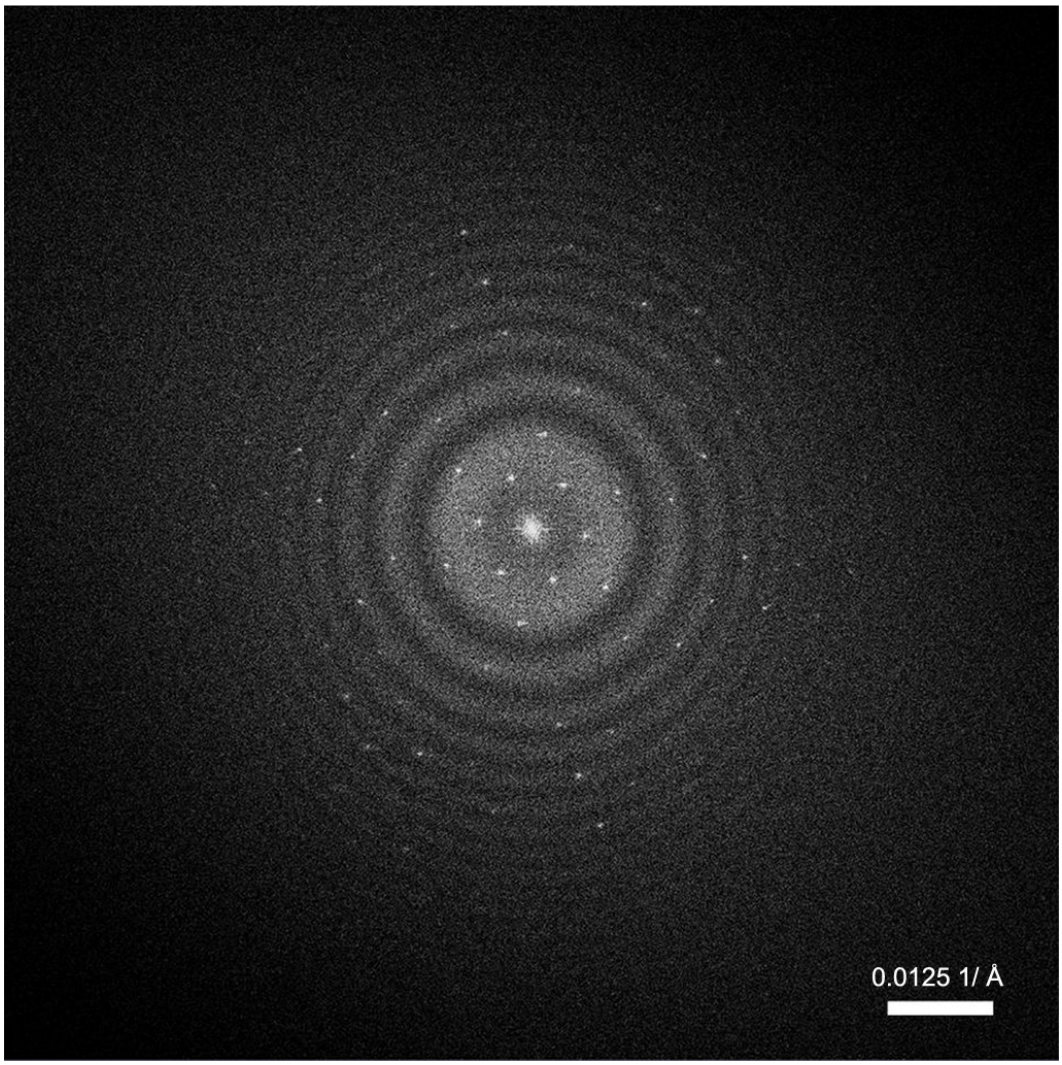

Figure 6.23 Calculated Fourier transforms from one representative Cryo-image of *B. fusiformis* ATCC 7055 exosporium.

Table 6.4 The internal phase residuals determined after the imposition of all possible two-sided plane groups calculated from one of the micrographs of *Bacillus fusiformis* ATCC 7055 exosporium Type II crystals.

Two sided plane group	Phase residual versus with other spot (90° random)	Number of comparisons	Target residual based on statistics taking Friedel weight into account
*p*1	16.3	44	
*p*2	63.8	22	23.4
*p*12_b	63.6	12	18.7
*p*12_a	62.9	12	18.7
*p*121_a	44.3	12	18.7
*p*121_b	39.3	12	18.7
*c*12_b	63.6	12	18.7
*c*12_a	62.9	12	18.7
*p*222	68.4	46	19.7
*p*2221b	61.5	46	19.7
*p*2221a	58.4	46	19.7
*p*22121	57.7	46	19.7
*c*222	68.4	46	19.7
*p*4	61.5	54	19.2
*p*422	63.2	114	17.7
*p*4212	64.2	114	17.7
*p*3	7.6*	38	16.3
*p*312	22.2	86	16.6
*p*321	39.2	93	17.2
*p*6	47.0	98	17.9
*p*622	49.4	201	17.1

Internal phase residuals were determined from spots of IQ1-1Q5 to 6Å resolution. The values marked with * are good candidates for the symmetry as the experimental phase residual is close to that expected value based on the signal-to-noise ratio.

Table 6.5 Phase residuals in resolution shells for *p*3 averaged Fourier terms

Resolution shell (Å)	Number of independent reflections	Phase residuals
1000-20.1	40	25.0
20.1-14.2	29	30.5
14.2-11.6	21	44.6
11.6-10.1	27	42.4

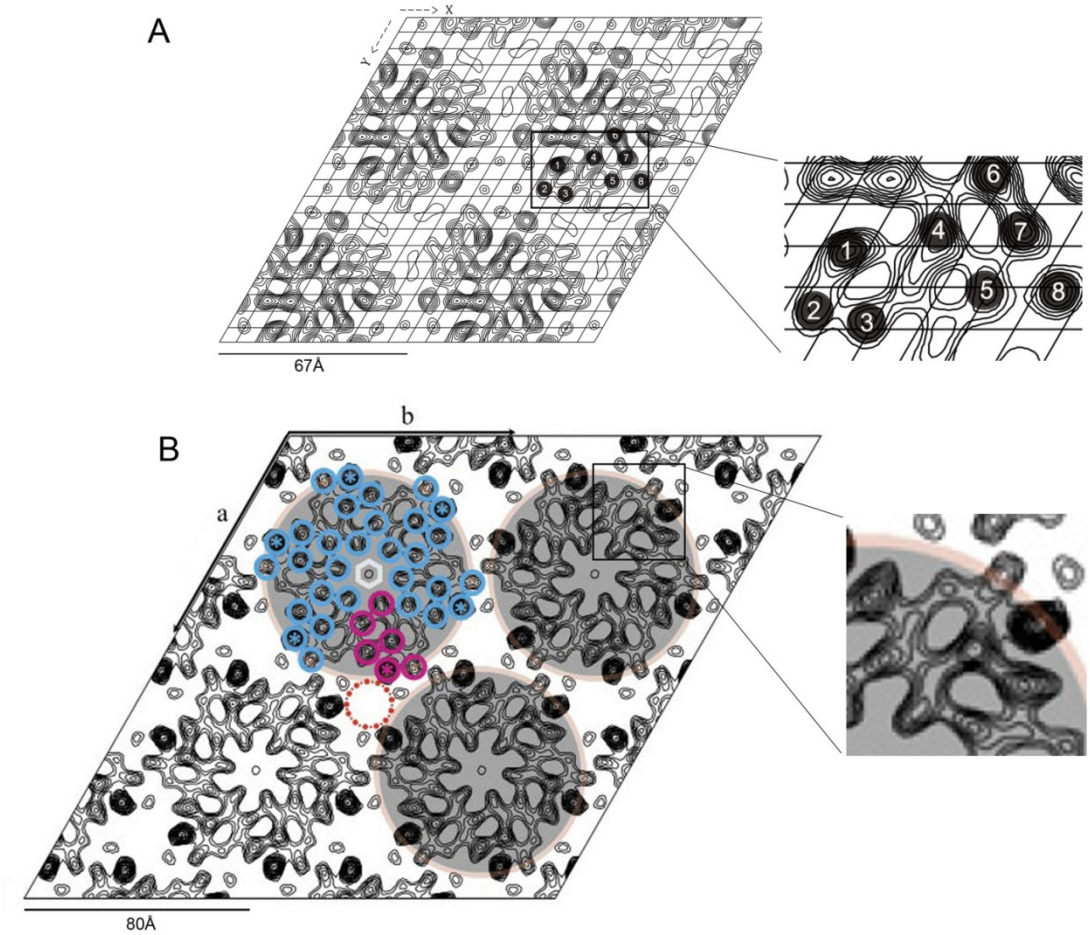

Fig 6.24 (A) Projection map for the type I crystal of *B. fusiformis* ATCC 7055 exosporium by cryo-EM. The map was merged by three crystal cryo-images and processed using MRC software. *p*3 symmetry was applied to merged map. Potential α-helices are shown within one asymmetric unit with black circles and numbers; (B) Projection map with *p*6 symmetry at 8 Å resolution for basal layer crystals by (Kailas, Terry *et al*. 2011). The area on the maps that was considered to bear similarities was boxed out and englarged for comparison.

6.6 Discussion

Historically, 2D studies of wild type exosporium crystal have focussed on *B. cereus* and *B.thuringiensis*, however, other than these, we know little about other wild type crystalline exosporium. In this study, we focused on the whole exosporium of 15 other species from genus *Bacillus*. The aims were (i) to determine if any species were intrinsically better ordered than *B. cereus* for high-resolution structural work and (ii) to see if a comparative analysis of exosporium structures might help us define the minimal core structure of the exosporium or the envelope of the fundamental monomeric exosporium basal layer subunit. Two exosporium samples from *B. circulans* 42G1 and *B. fusiformis* ATCC 7055 were chosen for structure analyses. Both of them yielded crystals with unit cell dimension $a = b$ ~67 Å, $\gamma = 120°$ and $p3$ symmetry. These parameters were remarkably close to those of the Type I crystal defined by Ball *et al.* in the *B. cereus* family. However, these crystals did yield a variety of projection densities in *B. circulans* 42G1. We could not exclude the possibility that it may be due to variable composition of multilayers and staining effects. We also found a crystals with $a = b$ ~83 Å, $\gamma = 120°$, similar parameters to those described for the *B. cereus* Type II crystals (Ball, Taylor *et al.* 2008) in *B. circulans* 42G1 spores. The multilayer *B. circulans* 42G1 exosporium shown in Fig 6.19 indicated that the emergence of Type I crystal after sonication could be that stain isn't able to penetrate the intact exosporium and only the surface type II crystals could be seen. When the spore was broken by sonication, stain solution can get in and this shows up the type I crystals underneath.

Electron microscopy revealed that members of *B. cereus* family produce spores with exosporium displaying structural similarities. They are composed of a paracystalline basal layer and hairy nap outer layer (Gerhardt and Ribi 1964; Hachisuka, Kojima *et al*. 1966; Beaman, Pankratz *et al.* 1971; Kailas, Terry *et al.* 2011). In the exosporium preparations released from spores of the *B. cereus* family, three forms of crystalline fragment with unit cell axes of ~65 Å (Type I), ~80 Å (Type II) and ~100 Å (Type III) have been identified (Ball, Taylor *et al*. 2008). Type I crystals were believed to be localized in a parasporal layer which is interior to the type II crystals that was localized in basal layer where the hairy nap is attached (Kailas, Terry *et al.* 2011). The exosporium crystal forms reflected by unit cell dimension from the two novel spore samples here seem to fit this pattern. Type II crystal from *B. circulans* 42G1 is from

intact spore where hairy nap was clearly visible. Type I crystal of exosporium fragments of *B. circulans* 42G1 and intact *B. fusiformis* ATCC 7055 are from exosporium where no hairy nap could be seen. Sonication certainly has a disruptive effect to the integrity of spore. It may disassemble the exosporium, resulting in any inner layers being exposed. It is possible that the four forms of type I crystal are concealed close to the spore core thus we did not pick this lattice up in the whole spores where only one form of type II crystal was seen.

Electron microscopy of *B. circulans* 42G1 fragmented exosporium revealed that there were at least four forms of crystalline layers localized at parasporal layer sharing same unit cell dimension but different appearance in projection maps. From the overall appearances of all the projection map solved by *2dx_image* program in the comparable same unit cell dimension, type I crystal of *B. fusiformis* ATCC 7055 has a similar overall appearance (Fig 6.21) with the one form of type I crystal of *B. circulans* 42G1 (Fig 6.18B). It is at least a hint that they may share some of common structural feature. Four forms of type I crystal density map of *B. circulans* 42G1 were compared with the other type I crystal in *Bacillus* family revealed in our lab, we found at least one form of type I crystal of *B. circulans* 42G1 (Fig 6.18B) shares high similarity type I crystal from *B. cereus* 14579 and *B. thuringiensis* HD1 (Ball, Taylor *et al*. 2008).

In the case of type II detected in intact exosporium of *B. circulans* 42G1, it shares the same unit cell dimension and overall appearance in density map with *B. cereus* 10876, *B. cereus* 14579, *B. thuringiensis kurstaki* HD1*, B. anthracis* Vollum and *B. anthracis* Ames spores' exosporium type II crystals (Ball, Taylor *et al.* 2008). Also, we roughly compared the projection map of the type II crystal from *B. circulans* 42G1 with the data we obtained from *B. cereus* family. They definitely share some common features on the projection map: a densely stained core with six stain-excluding densities surrounding it (Fig. 6.17). The diameter of the core is about 45 Å that is also identical.

We compared the 3D reconstruction of the type I crystal from *B. fusiformis* ATCC 7055 with its putative counterpart in *B. thuringiensis*. At the current resolution, both 3D negatively stained models appeared to have some similarities (Fig 6.22). They both have the "cup" that is joined together by linker domains centred on axes of threefold symmetry (Fig 6.22E). However, for a detailed comparison, high-resolution analysis on

the crystal was needed. Three good cryo-images were merged together and *p*3 symmetrised map was used to compared with the cryo-projection map of two crystal types, type I from *B. thuringiensis* kurstaki HD1 and type II from *B. cereus* 10876. At least there is a hint that we can get some of the density feature to overlap with those of the *B. cereus* p6 density although not fully overlapped (Kailas, Terry *et al.* 2011) (Fig 6.24B). It would be useful as if could provide independent verification of a monomer envelope within the respective threefold *B. fusiformis* ATCC 7055 and sixfold *B. cereu*s if it is correct. More images and more careful alignment are required.

CHAPTER 7
Discussion

As essentially specialized cells, spores have been extensively studied in the model bacterium *B. subtilis*. The motivation has been to understand the genetic control of gene expression that drives development of a unicellular organism and to better understand the spore's resistance properties which are important in food sterilisation processes. Extensive studies have been carried out in the study of molecular genetics, spore morphology, biochemical analysis, and functionality etc. However, we understand relatively little about the assembly mechanism and structure of spore, especially the structure that largely determine the robust nature of the spore coat. The aim of this study was mainly to study the spore coat proteins which build into organised macromolecular structures at the correct location and at the right time.

In this work, we analysed several spore coat proteins expressed as recombinant polyhistidine-tagged protein in *E.coli* such as CotY and CotZ. Using gel filtration, the complexes fromed by proteins were isolated corresponding to a variety of aggregation states, mostly disordered. However, a few were able to self-assemble into distinctive higher ordered structure, such as CotY, CotV-CotW, SafA and ExsY, The proteins we investigated were all expressed in a heterologous host which would be very unlikely to have specific machinary for their higher order assembly. The ordered structure we see within induced *E. coli* cells do point firmly to a propensity of these proteins for self-assembly in the *E. coli* cytosol. It is compelling to expect the self-assemblies properties of these spore coat/exosporium proteins to have biological relevance to spore coat/exosporium. The spore coat proteins offer the potential for complex heterogeneous and asymmetrical self assembly and with their inherent physical and chemical robustness should allow construct a biologically derived structuring system for novel nano-biotechnology processes.

7.1 The self-assembly properties of spore coat proteins

As we show here, the self-assembling coat proteins can generate extremely uniform structured surfaces with periodic patterns having unit distances of the order of several

nanometres and can be used to structure other functional elements. The self-organising surfaces can consist of a single arrayed unit (CotY), or a mixed unit (CotV-CotW). A number of self-assembled structures including two-dimensional crystals and helical fibres have been observed by EM. It is tempting to speculate that these assemblies are related to those found *in vivo* and that self-assembly is a critical function of the coat protein in building up the spore.

Among these protein, CotY drew much of our focus since it presented great crystallizing ability during protein preparation. Other than CotY, CotV-CotW is able to generate fibrous assemblies of one consistent diameter. For the rest of the spore coat proteins, they do present a certain ability of assembling to protein complexes. SafA is able to self-assemble to homogeneous proteinaceous particles with diameter about 20 nm. Single particle analysis has been performed to analyse the particle structure, but no structural feature could be seen. We therefore have to restrict our analysis to this point. SafA has been reported to interact with SpoVID and localization of SafA to the spore coat requires direct interaction with SpoVID (Ozin, Samford *et al.* 2001; Costa, Isidro *et al.* 2006). This is a worthwhile endeavour to look into the possible complexes formed by SafA-SpoVID. CotE-CotZ, CotE, CotH, CotZ, SpoIVA, and SpoVID yielded less compelling results in terms of self-assembly properties and will not be discussed further here.

7.2 The role of CotY self-assembly in building the spore coat of *B. subtilis*

CotY is stable enough to self-assemble under 8M urea conditions into highly ordered structures, homogeneous single particles and crystal pieces. Single particle analysis and negatively stained electron crystallography analysis were respectively applied to investigate the structure of single particles and crystal sheets. The result of single particle analysis showed heterologously expressed CotY assembled into putative hexamers. These then likely appeared to form a double-layered crystal piece. We were unable to find conditions where we could induce isolated single particles to form two-dimensional crystals. The likely reason for this might be kinetic activity perhaps a rare nucleation event is required.

The spore of *B. subtilis* does not have exosporium, the outermost layer is spore coat, which was also called spore crust. CotY has been proposed as a component of the crust (Imamura, Kuwana et al. 2011). Whether CotY forms natural two-dimensional arrays in the *B. subtilis* spore is not yet known. However, this would imply that an inherent tendency of CotY to form two-dimensional arrays might be part of their function during spore formation.

7.3 How CotY assembles?

The 3D map of the CotY raises an interesting question about what is holding the subunit together. However, the nature of bonds connecting the lattice is still unknown. Aronson and Fitzjames attempted to reconstitute the outer coat layers of *B. cereus* that had been treated with DTT and urea *in vitro* (Aronson and Fitz-James 1971); the presence of cystine in dialysis buffer promoted partial reconstruction of outer spore layer in organized structure (Aronson and Fitz-James 1971). It is very likely that disulphide bonding formation plays an important role in cross-linking proteins of the spore coat. It is worth noting that CotY and CotZ are cysteine rich protein of *B. subtilis* outer spore or crust (Zhang, Fitz-James *et al.* 1993; Imamura, Kuwana *et al*. 2011). The high content of cysteine residues in both proteins suggests that they might be cross-linked by forming intermolecular or intramolecular disulphide bridges.

DTT should disrupt the integrity of the whole structure if the crystal lattice was maintained by disulphide crosslinking. We found that CotY crystals incubated under reducing conditions with 50 mM DTT at least partially disrupted; however, crystal structure still maintained integrity. A similar phenomenon was detected as only heating at 99°C for 20 min treatment was applied. Only with a combination of heat and DTT did the crystals appeared to dismantle into single particles. The following SDS-PAGE resolution of CotY with heating or/and 50 mM DTT also strongly suggested that crystals are held together at least in part by disulphide cross-linking and this could reflect the *in vivo* situation. The likely explanation is two sets of disulphide linkages held crystal together were speculated: intermolecular disulphide bridges-a relatively accessible set holding the crystal lattice together and intramolecular disulphide bridges-a buried set responsible for holding monomers together so as to maintain the hexamer integrity. Perhaps most plausibly all these disulphide bonds are intermolecular. Single

particles are built up with 6 monomers by relatively inaccessible intramolecular disulphide bridges and then construct crystal structure by more easily accessible intermolecular disulphide bridges. As heating works with DTT, heating can denature the protein, resulting in disulphide bonds exposure to the DTT. Single particle and crystal all fall apart into monomer on the gel. While when only DTT or heating is applied, both hexamer and monomer appear on the gel: crystal organised architecture was disturbed, but single particles, which maintained by intramolecular disulphide bridges were still intact.

7.4 The role of ExsY self-assembly

The characteristic self-assembly properties of CotY sparked our interest in ExsY because ExsY and CotY are *B. subtilis* CotY homologues in the *B. cereus* family. ExsY and CotY are also cysteine rich, and also likely to be cross-linked through disulphide bonds in exosporium (Steichen, Kearney *et al.* 2005). As we had expected, ExsY was also were able to self-assemble into well-ordered arrays.

CotY and ExsY were good candidates for major components of the lattice of the exosporium. ExsY was thought to distribute throughout non-cap region and possibly in cap region of exosporium model that proposed by Thompson *et al* (Thompson, Hoelscher *et al.* 2012). We have not investigated the CotY of *B. cereus*, which is a next task for the project.

So far, no homogeneous single particles formed by ExsY have been found. Preliminary ExsY 3D reconstruction suggested a single-layered repeating unit of structure with *p*6 symmetry. Ball *et al* reconstructed *B. cereus* type II crystal in three dimensions. The type II crystal features by its individual crowns with large stain-filled cavities at their centre, whilst in our preliminary model ExsY has a hole in the centre. However, both of them appear to be connected by two sets of connecting spokes that along three-fold symmetry in projection map (Fig 5.2)

7.5 Structural features of the exosporium from novel *Bacillus* species revealed by TEM

Historically, since the spores formed by *B. subtilis* get no exosporium, the exosporium that is present as the surface layer of spores of some species, including pathogens of relevance to the agriculture and food community is poorly characterised. Up to date, the studies of exosporium have focused on members of the *B. cereus* group. The investigation into the novel species of *Bacillus* spores would screen better ordered crystal forms of exosporium for higher resolution analysis than what we are currently working on such as *B. cereus* spores. The comparative analyses among than might reveal core features common to all exosporia. We hence screened a number of *Bacillus* spores that have distinct exosporium to seek for the most suitable for generating well-ordered crystalline exosporium samples. Out of 15 species investigated, two of the best candidates, *B. circulans 42G1* and *B. fusiformis* ATCC 7055 were particularly suitable for structural analyses. *B. circulans* 42G1 has hairy nap attached, while no visible hairy nap is present in *B. fusiformis* ATCC 7055 spores. EM revealed the multilayered structure on the exosporium fragments of *B. circulans* 42G1. Two types of crystal form were found on *B. circulans* 42G1 exosporium, which belonged to Type I and Type II crystals. Type II crystal was found on the intact *B. circulans* exosporium where hairy nap attached, which is consistent with previous result describing type II crystal on the basal layer where hairy nap layer attached in the *B. cereus* family (Ball, Taylor *et al.* 2008). Other four forms of type I crystal were found on crystal pieces where no hairy nap layer was seen. This also consistent with reports of type I crystals found in the *B. cereus* family (Ball, Taylor *et al.* 2008). We compared all the 2D density of crystal form found in *B. circulans* 42G1 with corresponding ones from *B. cereus* family. *B. fusiformis* ATCC 7055 is the best one for higher resolution cryo-EM analysis in our gallery. Only one form of type I crystal was found. 3D negatively stained volume and 2D cryo-EM high-resolution map were also constructed.

7.6 Future work

The structural analysis reported here represents the next stage in our characterisation of the assembly of *B. subtilis* coat and *B. cereus* exosporium. Other than ExsY and CotY that we have explored, we could think of some other orthologues such as CotY of *B. cereus*. High-resolution cryo-EM structural analysis could also be used to help locate individual coat/exosporium components - this could include use of electron tomography for *in situ* analysis of whole spores or spore sections.

7.6.1 High-resolution analysis on CotY and ExsY crystal

The CotY 3D reconstruction revealed a double-layered architecture and single layered crystal for ExsY. Their self-assembly properties might reflect aspects of *in vivo* self-assembly behaviour that is useful for us to understand how spore coat/exosporium build up. In next stage, we will work on more related homologues, such as ExsFA ExsFB etc to see if they will co-assemble with ExsY, CotY from *B. cereus* to check if these proteins could also bear self-assembly ability. The exact bonding among the CotY crystal and single particles is not fully understood. To disassemble the CotY to single particle and set conditions to see if the crystal could be formed again may be worth a try, X-ray crystallography for high resolution as well.

So far, we have not seen ExsY's ability of forming homogeneous single particles. Thus, we will isolate ExsY by gel filtration or by other means to confirm if ExsY forms crystals in the same way as CotY. The ExsY reconstruction is still a preliminary model, more refinement work is required to optimize the model.

On the other hand, the abundant huge pieces of crystal could be obtained from the *E. coli* expression system could greatly improve the sample, which will be conducive for cryo-EM analysis. The additional knowledge of structural analysis of individual components will be used to compare with our understanding of whole spore structure, and help us elucidate how these individual components relate to the entire spore coat or exosporium structure.

7.6.2 Other spore coat proteins

CotZ is the homologue protein of CotY in *B. subtilis*. Both of them are localized in the spore crust and required for the spore coat correct formation (Imamura, Kuwana *et al.* 2010; Imamura, Kuwana *et al.* 2011). Although no self-assembling ordered species formed by CotZ has been detected, we cannot exclude the possibilty that it might possess this property. CotZ has been found to interact with CotE, and net-like structure has been found on CotE-CotZ mixure. We need to try repeating experiment to confirm if CotZ could form crystal structure by interacting with other spore coat components. CotV and CotW are able to form into helical assemblies, so it is very possible that they

could ultimately be amenable to the type of hybrid analysis developed for other disordered helical assemblies (Egelman 2007). The interaction between SafA-SpoVID makes it viable to separately prepare two proteins and mix them for electron microscopy observation (Ozin, Henriques *et al*. 2000; Ozin, Samford *et al*. 2001; Costa, Isidro *et al.* 2006).

7.6.3 Structural analysis of more novel *Bacillus* species

The initial 2D and 3D negative stain reconstruction on *B. fusiformis* ATCC 7055 exosporium has laid a firm foundation for further high-resolution cryo-EM anlysis. Except for *B. fusiformis* ATCC 7055 and *B. circulans* 42G1, there are several *Bacillus* spores such *B. vedderi* NRRL B23388 that show good crystallinity of the exosporium. We just prioritised *B. fusiformis* and *B. circulans* structural analysis; however, the other *Bacillus* species could also be great additions to our knowledge. We will therefore work on these spores, and go back to the *B. fusiformis* ATCC 7055 which is best one for cryo-EM we screened out so far. 3D high-resolution reconstructions of *Bacillus* related species would give us a true structural understanding.

References

1. **Abhyankar, W., A. T. Beek, H. Dekker, R. Kort, S. Brul, and C. G. de Koster.** 2011. Gel-free proteomic identification of the *Bacillus subtilis* insoluble spore coat protein fraction. Proteomics **11:**4541-50.
2. **Agard, D. A.** 1983. A least-squares method for determining structure factors in three-dimensional tilted-view reconstructions. J Mol Biol **167:**849-52.
3. **Amos, L. A., R. Henderson, and P. N. Unwin.** 1982. Three-dimensional structure determination by electron microscopy of two-dimensional crystals. Prog Biophys Mol Biol **39:**183-231.
4. **Anagnostopoulos, C., and J. Spizizen.** 1961. Requirements for Transformation in *Bacillus subtilis*. J Bacteriol **81:**741-6.
5. **Aronson, A. I., and P. Fitz-James.** 1976. Structure and morphogenesis of the bacterial spore coat. Bacteriol Rev **40:**360-402.
6. **Aronson, A. I., and P. C. Fitz-James.** 1971. Reconstitution of bacterial spore coat layers *in vitro*. J Bacteriol **108:**571-8.
7. **Ash, C., J. A. Farrow, M. Dorsch, E. Stackebrandt, and M. D. Collins.** 1991. Comparative analysis of *Bacillus anthracis, Bacillus cereus*, and related species on the basis of reverse transcriptase sequencing of 16S rRNA. Int J syst Bacteriol **41:**343-6.
8. **Ash, C., F. G. Priest, and M. D. Collins.** 1993. Molecular identification of rRNA group 3 *bacilli* (Ash, Farrow, Wallbanks and Collins) using a PCR probe test. Proposal for the creation of a new genus *Paenibacillus*. Antonie Van Leeuwenhoek **64:**253-60.
9. **Bailey-Smith, K., S. J. Todd, T. W. Southworth, J. Proctor, and A. Moir.** 2005. The ExsA protein of *Bacillus cereu*s is required for assembly of coat and exosporium onto the spore surface. J Bacteriol **187:**3800-6.
10. **Ball, D. A., R. Taylor, S. J. Todd, C. Redmond, E. Couture-Tosi, P. Sylvestre, A. Moir, and P. A. Bullough.** 2008. Structure of the exosporium and sublayers of spores of the *Bacillus cereus* family revealed by electron crystallography. Mol Microbiol **68:**947-58.
11. **Bauer, T., S. Little, A. G. Stover, and A. Driks.** 1999. Functional regions of the *Bacillus subtilis* spore coat morphogenetic protein CotE. J Bacteriol **181:**7043-51.
12. **Beall, B., A. Driks, R. Losick, and C. P. Moran, Jr.** 1993. Cloning and characterization of a gene required for assembly of the *Bacillus subtilis* spore coat. J Bacteriol **175:**1705-16.
13. **Beaman, T. C., and P. Gerhardt.** 1986. Heat resistance of bacterial spores correlated with protoplast dehydration, mineralization, and thermal adaptation. Appl Environ Microbiol **52:**1242-6.
14. **Beaman, T. C., H. S. Pankratz, and P. Gerhardt.** 1989. Low heat resistance of *Bacillus sphaericus* spores correlated with high protoplast water content. FEMS Microbiol Lett **49:**1-4.
15. **Beaman, T. C., H. S. Pankratz, and P. Gerhardt.** 1971. Paracrystalline sheets reaggregated from solubilized exosporium of *Bacillus cereus*. J Bacteriol **107:**320-4.
16. **Boydston, J. A., P. Chen, C. T. Steichen, and C. L. Turnbough, Jr.** 2005. Orientation within the exosporium and structural stability of the collagen-like glycoprotein BclA of *Bacillus anthracis*. J Bacteriol **187:**5310-7.

17. **Boydston, J. A., L. Yue, J. F. Kearney, and C. L. Turnbough, Jr.** 2006. The ExsY protein is required for complete formation of the exosporium of *Bacillus anthracis*. J Bacteriol **188:**7440-8.
18. **Bravo, A., S. S. Gill, and M. Soberon.** 2007. Mode of action of *Bacillus thuringiensis* Cry and Cyt toxins and their potential for insect control. Toxicon **49:**423-35.
19. **Cangiano, G., A. Mazzone, L. Baccigalupi, R. Isticato, P. Eichenberger, M. De Felice, and E. Ricca.** 2010. Direct and indirect control of late sporulation genes by GerR of *Bacillus subtilis*. J Bacteriol **192:**3406-13.
20. **Cano, R. J., and M. K. Borucki.** 1995. Revival and identification of bacterial spores in 25- to 40-million-year-old Dominican amber. Science **268:**1060-4.
21. **Catalano, F. A., J. Meador-Parton, D. L. Popham, and A. Driks.** 2001. Amino acids in the *Bacillus subtilis* morphogenetic protein SpoIVA with roles in spore coat and cortex formation. J Bacteriol **183:**1645-54.
22. **Chen, G., A. Driks, K. Tawfiq, M. Mallozzi, and S. Patil.** 2010. *Bacillus anthracis* and *Bacillus subtilis* spore surface properties and transport. Colloids Surf B Biointerfaces **76:**512-8.
23. **Claus, D., and R. C. W. Berkeley.** 1986. Genus *Bacillus* Cohg 1982. Bergey's Manual of Systematic Bacteriology, The Williams & Wilkins Co., Baltimore 2**:**1105-1139.
24. **Claus, D., and R. C. W. Berkeley.** 1986. Genus *Bacillus* Cohn 1872, 174. Bergey's manual of systematic bacteriology **2:**1105-1139.
25. **Costa, T., A. L. Isidro, C. P. Moran, Jr., and A. O. Henriques.** 2006. Interaction between coat morphogenetic proteins SafA and SpoVID. J Bacteriol **188:**7731-41.
26. **Cowan, A. E., E. M. Olivastro, D. E. Koppel, C. A. Loshon, B. Setlow, and P. Setlow.** 2004. Lipids in the inner membrane of dormant spores of *Bacillus* species are largely immobile. Proc Natl Acad Sci U S A **101:**7733-8.
27. **Crowther, R. A., R. Henderson, and J. M. Smith.** 1996. MRC image processing programs. J Struct Biol **116:**9-16.
28. **Cutting, S., A. Driks, R. Schmidt, B. Kunkel, and R. Losick.** 1991. Forespore-specific transcription of a gene in the signal transduction pathway that governs Pro-sigma K processing in *Bacillus subtilis*. Genes Dev **5:**456-66.
29. **Cutting, S., S. Panzer, and R. Losick.** 1989. Regulatory studies on the promoter for a gene governing synthesis and assembly of the spore coat in *Bacillus subtilis*. J Mol Biol **207:**393-404.
30. **Daubenspeck, J. M., H. Zeng, P. Chen, S. Dong, C. T. Steichen, N. R. Krishna, D. G. Pritchard, and C. L. Turnbough, Jr.** 2004. Novel oligosaccharide side chains of the collagen-like region of BclA, the major glycoprotein of the *Bacillus anthracis* exosporium. J Biol Chem **279:**30945-53.
31. **Dawes, I. W., D. Kay, and J. Mandelstam.** 1969. Sporulation in *Bacillus subtilis.* Establishment of a time scale for the morphological events. J Gen Microbiol **56:**171-9.
32. **de Francesco, M., J. Z. Jacobs, F. Nunes, M. Serrano, P. T. McKenney, M. H. Chua, A. O. Henriques, and P. Eichenberger.** 2012. Physical interaction between coat morphogenetic proteins SpoVID and CotE is necessary for spore encasement in *Bacillus subtilis*. J Bacteriol **194:**4941-50.
33. **de Hoon, M. J., P. Eichenberger, and D. Vitkup.** 2010. Hierarchical evolution of the bacterial sporulation network. Curr Biol **20:**R735-45.

34. **Dean, D. H.** 1984. Biochemical genetics of the bacterial insect-control agent *Bacillus thuringiensis*: basic principles and prospects for genetic engineering. Biotechnol Genet Eng Rev **2:**341-63.
35. **Deatherage, J. F., K. A. Taylor, and L. A. Amos.** 1983. Three-dimensional arrangement of the cell wall protein of *Sulfolobus acidocaldarius*. J Mol Biol **167:**823-48.
36. **Desrosier, J. P., and J. C. Lara.** 1984. Synthesis of the Exosporium during Sporulation of *Bacillus Cereus*. Journal of General Microbiology **130:**935-940.
37. **Di Franco, C., E. Beccari, T. Santini, G. Pisaneschi, and G. Tecce.** 2002. Colony shape as a genetic trait in the pattern-forming *Bacillus mycoides*. BMC Microbiol **2:**33.
38. **Driks, A.** 1999. *Bacillus subtilis* spore coat. Microbiol Mol Biol Rev **63:**1-20.
39. **Driks, A.** 2004. From rings to layers: surprising patterns of protein deposition during bacterial spore assembly. J Bacteriol **186:**4423-6.
40. **Driks, A.** 2002. Maximum shields: the assembly and function of the bacterial spore coat. Trends Microbiol **10:**251-4.
41. **Driks, A., S. Roels, B. Beall, C. P. Moran, Jr., and R. Losick.** 1994. Subcellular localization of proteins involved in the assembly of the spore coat of *Bacillus subtilis*. Genes Dev **8:**234-44.
42. **Driks, A., and P. Setlow.** 1999. Morphogenesis and properties of the bacterial spore. in Y. Brun and L. Shimkets (ed.), Prokaryotic development. American Society for Microbiology, Washington, D.C**:**191-218.
43. **Ebersold, H. R., J. L. Cordier, and P. Luthy.** 1981. Bacterial mesosomes: method dependent artifacts. Arch Microbiol **130:**19-22.
44. **Egelman, E. H.** 2007. The iterative helical real space reconstruction method: surmounting the problems posed by real polymers. J Struct Biol **157:**83-94.
45. **Eichenberger, P., M. Fujita, S. T. Jensen, E. M. Conlon, D. Z. Rudner, S. T. Wang, C. Ferguson, K. Haga, T. Sato, J. S. Liu, and R. Losick.** 2004. The program of gene transcription for a single differentiating cell type during sporulation in *Bacillus subtilis*. PLoS Biol **2:**e328.
46. **Eichenberger, P., S. T. Jensen, E. M. Conlon, C. van Ooij, J. Silvaggi, J. E. Gonzalez-Pastor, M. Fujita, S. Ben-Yehuda, P. Stragier, J. S. Liu, and R. Losick.** 2003. The sigmaE regulon and the identification of additional sporulation genes in *Bacillus subtilis*. J Mol Biol **327:**945-72.
47. **Errington, J.** 1993. *Bacillus subtilis* sporulation: regulation of gene expression and control of morphogenesis. Microbiol Rev **57:**1-33.
48. **Errington, J.** 2003. Regulation of endospore formation in *Bacillus subtilis*. Nat Rev Microbiol **1:**117-26.
49. **Fairhead, H., B. Setlow, and P. Setlow.** 1993. Prevention of DNA damage in spores and in vitro by small, acid-soluble proteins from *Bacillus* species. J Bacteriol **175:**1367-74.
50. **Fass, D.** 2012. Disulfide bonding in protein biophysics. Annu Rev Biophys **41:**63-79.
51. **Favret, M. E., and A. A. Yousten.** 1985. Insecticidal activity of *Bacillus laterosporus*. J Invertebr Pathol **45:**195-203.
52. **Feucht, A., L. Evans, and J. Errington.** 2003. Identification of sporulation genes by genome-wide analysis of the sigmaE regulon of *Bacillus subtilis*. Microbiology **149:**3023-34.
53. **Ford, W. W.** 1916. Studies on Aerobic Spore-bearing Non-pathogenic Bacteria: Part I. Introduction. J Bacteriol **1:**273-6.

54. **Francesconi, S. C., T. J. MacAlister, B. Setlow, and P. Setlow.** 1988. Immunoelectron microscopic localization of small, acid-soluble spore proteins in sporulating cells of *Bacillus subtilis*. J Bacteriol **170:**5963-7.
55. **Freer, J. H., and H. S. Levinson.** 1967. Fine structure of *Bacillus megaterium* during microcycle sporogenesis. J Bacteriol **94:**441-57.
56. **Gerhardt, P., and R. E. Marquis.** 1989. Spore thermoresistance mechanisms. Regulation of Procaryotic Development: 43-63. In I. Smith, R. A. Slepecky, and P. Setlow (ed.), Regulation of procaryotic development. American Society for Microbiology, Washing-ton, D.C.
57. **Gerhardt, P., and E. Ribi.** 1964. Ultrastructure of the Exosporium Enveloping Spores of *Bacillus Cereus*. J Bacteriol **88:**1774-89.
58. **Giorno, R., M. Mallozzi, J. Bozue, K. S. Moody, A. Slack, D. Qiu, R. Wang, A. Friedlander, S. Welkos, and A. Driks.** 2009. Localization and assembly of proteins comprising the outer structures of the *Bacillus anthracis* spore. Microbiology **155:**1133-45.
59. **Gipson, B., X. Zeng, and H. Stahlberg.** 2007. 2dx_merge: data management and merging for 2D crystal images. J Struct Biol **160:**375-84.
60. **Gipson, B., X. Zeng, Z. Y. Zhang, and H. Stahlberg.** 2007. 2dx--user-friendly image processing for 2D crystals. J Struct Biol **157:**64-72.
61. **Goldman, R. C., and D. J. Tipper.** 1978. *Bacillus subtilis* spore coats: complexity and purification of a unique polypeptide component. J Bacteriol **135:**1091-106.
62. **Gordon, R. E., and W. C. Haynes.** 1973. The Genus *Bacillus*. United States Department of Agriculture, Washington, D. C.
63. **Grantcharova, N., U. Lustig, and K. Flardh.** 2005. Dynamics of FtsZ assembly during sporulation in *Streptomyces coelicolor* A3(2). J Bacteriol **187:**3227-37.
64. **Graumann, P. L.** 2007. Bacillus: cellular and molecular biology. Academic Press, Wymondham, United Kingdom.
65. **Hachisuka, Y., K. Kojima, and T. Sato.** 1966. Fine filaments on the outside of the exosporium of *Bacillus anthracis* spores. J Bacteriol **91:**2382-4.
66. **Hall, C. E.** 1955. Electron densitometry of stained virus particles. J Biophys Biochem Cytol **1:**1-12.
67. **Han, C. S., G. Xie, J. F. Challacombe, M. R. Altherr, S. S. Bhotika, N. Brown, D. Bruce, C. S. Campbell, M. L. Campbell, J. Chen, O. Chertkov, C. Cleland, M. Dimitrijevic, N. A. Doggett, J. J. Fawcett, T. Glavina, L. A. Goodwin, L. D. Green, K. K. Hill, P. Hitchcock, P. J. Jackson, P. Keim, A. R. Kewalramani, J. Longmire, S. Lucas, S. Malfatti, K. McMurry, L. J. Meincke, M. Misra, B. L. Moseman, M. Mundt, A. C. Munk, R. T. Okinaka, B. Parson-Quintana, L. P. Reilly, P. Richardson, D. L. Robinson, E. Rubin, E. Saunders, R. Tapia, J. G. Tesmer, N. Thayer, L. S. Thompson, H. Tice, L. O. Ticknor, P. L. Wills, T. S. Brettin, and P. Gilna.** 2006. Pathogenomic sequence analysis of *Bacillus cereus* and *Bacillus thuringiensis* isolates closely related to *Bacillus anthracis*. J Bacteriol **188:**3382-90.
68. **Havelka, W. A., R. Henderson, J. A. Heymann, and D. Oesterhelt.** 1993. Projection structure of halorhodopsin from *Halobacterium halobium* at 6 A resolution obtained by electron cryo-microscopy. J Mol Biol **234:**837-46.
69. **Havelka, W. A., R. Henderson, and D. Oesterhelt.** 1995. Three-dimensional structure of halorhodopsin at 7 Å resolution. J Mol Biol **247:**726-38.

70. **Henderson, R.** 1975. The structure of the purple membrane from *Halobacterium hallobium*: analysis of the X-ray diffraction pattern. J Mol Biol **93:**123-38.
71. **Henderson, R., J. M. Baldwin, T. A. Ceska, F. Zemlin, E. Beckmann, and K. H. Downing.** 1990. An atomic model for the structure of bacteriorhodopsin. Biochem Soc Trans **18:**844.
72. **Henderson, R., J. M. Baldwin, T. A. Ceska, F. Zemlin, E. Beckmann, and K. H. Downing.** 1990. Model for the structure of bacteriorhodopsin based on high-resolution electron cryo-microscopy. J Mol Biol **213:**899-929.
73. **Henderson, R., and P. N. Unwin.** 1977. Structure of the purple membrane from *Halobacterium halobium*. Biophys Struct Mech **3:**121.
74. **Henriques, A. O., B. W. Beall, and C. P. Moran, Jr.** 1997. CotM of *Bacillus subtilis,* a member of the alpha-crystallin family of stress proteins, is induced during development and participates in spore outer coat formation. J Bacteriol **179:**1887-97.
75. **Henriques, A. O., and C. P. Moran, Jr.** 2000. Structure and assembly of the bacterial endospore coat. Methods **20:**95-110.
76. **Henriques, A. O., and C. P. Moran, Jr.** 2007. Structure, assembly, and function of the spore surface layers. Annu Rev Microbiol **61:**555-88.
77. **Hoffmaster, A. R., J. Ravel, D. A. Rasko, G. D. Chapman, M. D. Chute, C. K. Marston, B. K. De, C. T. Sacchi, C. Fitzgerald, L. W. Mayer, M. C. Maiden, F. G. Priest, M. Barker, L. Jiang, R. Z. Cer, J. Rilstone, S. N. Peterson, R. S. Weyant, D. R. Galloway, T. D. Read, T. Popovic, and C. M. Fraser.** 2004. Identification of anthrax toxin genes in a *Bacillus cereus* associated with an illness resembling inhalation anthrax. Proc Natl Acad Sci U S A **101:**8449-54.
78. **Holser, W. T.** 1958. Point Groups and Plane Groups in a Two-Sided Plane and their Subgroups. Zeitschrift für Kristallographie **110:**266-281.
79. **Holt, S. C., J. J. Gauther, and D. J. Tipper.** 1975. Ultrastructural studies of sporulation in *Bacillus sphaericus*. J Bacteriol **122:**1322-38.
80. **Holt, S. C., and E. R. Leadbetter.** 1969. Comparative ultrastructure of selected aerobic spore-forming bacteria: a freeze-etching study. Bacteriol Rev **33:**346-78.
81. **Horneck, G., H. Bucker, and G. Reitz.** 1994. Long-term survival of bacterial spores in space. Adv Space Res **14:**41-5.
82. **Ichikawa, H., R. Halberg, and L. Kroos.** 1999. Negative regulation by the *Bacillus subtilis* GerE protein. J Biol Chem **274:**8322-7.
83. **Imamura, D., R. Kuwana, H. Takamatsu, and K. Watabe.** 2010. Localization of proteins to different layers and regions of *Bacillus subtilis* spore coats. J Bacteriol **192:**518-24.
84. **Imamura, D., R. Kuwana, H. Takamatsu, and K. Watabe.** 2011. Proteins involved in formation of the outermost layer of *Bacillus subtilis* spores. J Bacteriol **193:**4075-80.
85. **Inglesby, T. V.** 1999. Anthrax as a biological weapon: Medical and public health management Jama-J Am Med Assoc **281**.
86. **Isticato, R., A. Pelosi, M. De Felice, and E. Ricca.** 2010. CotE binds to CotC and CotU and mediates their interaction during spore coat formation in *Bacillus subtilis*. J Bacteriol **192:**949-54.
87. **Ivanova, N., A. Sorokin, I. Anderson, N. Galleron, B. Candelon, V. Kapatral, A. Bhattacharyya, G. Reznik, N. Mikhailova, A. Lapidus, L. Chu, M. Mazur, E. Goltsman, N. Larsen, M. D'Souza, T. Walunas, Y. Grechkin,**

G. Pusch, R. Haselkorn, M. Fonstein, S. D. Ehrlich, R. Overbeek, and N. Kyrpides. 2003. Genome sequence of *Bacillus cereus* and comparative analysis with *Bacillus anthracis*. Nature **423:**87-91.

88. **Johnson, M. J., S. J. Todd, D. A. Ball, A. M. Shepherd, P. Sylvestre, and A. Moir.** 2006. ExsY and CotY are required for the correct assembly of the exosporium and spore coat of *Bacillus cereus*. J Bacteriol **188:**7905-13.
89. **Kadokura, H., F. Katzen, and J. Beckwith.** 2003. Protein disulfide bond formation in prokaryotes. Annu Rev Biochem **72:**111-35.
90. **Kailas, L., C. Terry, N. Abbott, R. Taylor, N. Mullin, S. B. Tzokov, S. J. Todd, B. A. Wallace, J. K. Hobbs, A. Moir, and P. A. Bullough.** 2011. Surface architecture of endospores of the *Bacillus cereus/anthracis/ thuringiensis* family at the subnanometer scale. Proc Natl Acad Sci U S A **108:**16014-9.
91. **Katz, E., and A. L. Demain.** 1977. The peptide antibiotics of *Bacillus*: chemistry, biogenesis, and possible functions. Bacteriol Rev **41:**449-74.
92. **Kay, D., and S. C. Warren.** 1968. Sporulation in *Bacillus subtilis*. Morphological changes. Biochem J **109:**819-24.
93. **Kim, H., M. Hahn, P. Grabowski, D. C. McPherson, M. M. Otte, R. Wang, C. C. Ferguson, P. Eichenberger, and A. Driks.** 2006. The *Bacillus subtilis* spore coat protein interaction network. Mol Microbiol **59:**487-502.
94. **KJ, R., and R. CG.** 2004. Sherris Medical Microbiology (4th ed). McGraw Hill.
95. **Koch, R.** 1876. Untersuchungen über Bakterien. V. Die Aetiologie der Milzbrand Krankheit, begrandet auf Entwicklurgs geschichte des *Bacillus anthracis.* Beiträge zur Biologie der Pflanzen 2.
96. **Koni, P. A., and D. J. Ellar.** 1994. Biochemical characterization of *Bacillus thuringiensis* cytolytic delta-endotoxins. Microbiology **140 (Pt 8):**1869-80.
97. **Kotiranta, A., K. Lounatmaa, and M. Haapasalo.** 2000. Epidemiology and pathogenesis of *Bacillus cereus* infections. Microbes Infect **2:**189-98.
98. **Kozuka, S., and K. Tochikubo.** 1985. Properties and origin of filamentous appendages on spores of *Bacillus cereus*. Microbiol Immunol **29:**21-37.
99. **Krajcikova, D., M. Lukacova, D. Mullerova, S. M. Cutting, and I. Barak.** 2009. Searching for protein-protein interactions within the *Bacillus subtilis* spore coat. J Bacteriol **191:**3212-9.
100. **Kroos, L.** 2007. The *Bacillus* and *Myxococcus* developmental networks and their transcriptional regulators. Annu Rev Genet **41:**13-39.
101. **Kroos, L., B. Kunkel, and R. Losick.** 1989. Switch protein alters specificity of RNA polymerase containing a compartment-specific sigma factor. Science **243:**526-9.
102. **Kuhlbrandt, W., D. N. Wang, and Y. Fujiyoshi.** 1994. Atomic model of plant light-harvesting complex by electron crystallography. Nature **367:**614-21.
103. **Kunkel, B., L. Kroos, H. Poth, P. Youngman, and R. Losick.** 1989. Temporal and spatial control of the mother-cell regulatory gene spoIIID of *Bacillus subtilis*. Genes Dev **3:**1735-44.
104. **Kunst, F., N. Ogasawara, I. Moszer, A. M. Albertini, G. Alloni, V. Azevedo, M. G. Bertero, P. Bessieres, A. Bolotin, S. Borchert, R. Borriss, L. Boursier, A. Brans, M. Braun, S. C. Brignell, S. Bron, S. Brouillet, C. V. Bruschi, B. Caldwell, V. Capuano, N. M. Carter, S. K. Choi, J. J. Codani, I. F. Connerton, A. Danchin, and et al.** 1997. The complete genome sequence of the gram-positive bacterium *Bacillus subtilis.* Nature **390:**249-56.

105. **Kuwana, R., Y. Kasahara, M. Fujibayashi, H. Takamatsu, N. Ogasawara, and K. Watabe.** 2002. Proteomics characterization of novel spore proteins of *Bacillus subtilis*. Microbiology **148:**3971-82.
106. **La Duc, M. T., M. Satomi, and K. Venkateswaran.** 2004. *Bacillus odysseyi* sp. nov., a round-spore-forming *bacillus* isolated from the Mars Odyssey spacecraft. Int J Syst Evol Microbiol **54:**195-201.
107. **Lai, E. M., N. D. Phadke, M. T. Kachman, R. Giorno, S. Vazquez, J. A. Vazquez, J. R. Maddock, and A. Driks.** 2003. Proteomic analysis of the spore coats of *Bacillus subtilis* and *Bacillus anthracis*. J Bacteriol **185:**1443-54.
108. **Lapidus, A., E. Goltsman, S. Auger, N. Galleron, B. Segurens, C. Dossat, M. L. Land, V. Broussolle, J. Brillard, M. H. Guinebretiere, V. Sanchis, C. Nguen-The, D. Lereclus, P. Richardson, P. Wincker, J. Weissenbach, S. D. Ehrlich, and A. Sorokin.** 2008. Extending the *Bacillus cereus* group genomics to putative food-borne pathogens of different toxicity. Chem Biol Interact **171:**236-49.
109. **Little, S., and A. Driks.** 2001. Functional analysis of the *Bacillus subtilis* morphogenetic spore coat protein CotE. Mol Microbiol **42:**1107-20.
110. **Losick, R., and P. Stragier.** 1992. Crisscross regulation of cell-type-specific gene expression during development in *B. subtilis.* Nature **355:**601-4.
111. **Lutkenhaus, J., and S. G. Addinall.** 1997. Bacterial cell division and the Z ring. Annu Rev Biochem **66:**93-116.
112. **Makino, S.** 2002. Anthrax as a biological weapon. J Food Hyg Soc Jpn **43:**228-232.
113. **McKenney, P. T., A. Driks, H. A. Eskandarian, P. Grabowski, J. Guberman, K. H. Wang, Z. Gitai, and P. Eichenberger.** 2010. A distance-weighted interaction map reveals a previously uncharacterized layer of the *Bacillus subtilis* spore coat. Curr Biol **20:**934-8.
114. **McKenney, P. T., and P. Eichenberger.** 2012. Dynamics of spore coat morphogenesis in *Bacillus subtilis.* Mol Microbiol **83:**245-60.
115. **Morlot, C., T. Uehara, K. A. Marquis, T. G. Bernhardt, and D. Z. Rudner.** 2010. A highly coordinated cell wall degradation machine governs spore morphogenesis in *Bacillus subtilis*. Genes Dev **24:**411-22.
116. **Mullerova, D., D. Krajcikova, and I. Barak.** 2009. Interactions between *Bacillus subtilis* early spore coat morphogenetic proteins. FEMS Microbiol Lett **299:**74-85.
117. **N.A.Logon, and P. D. Vos.** 2009. Genus I. *Bacillus* Cohn 1872. In: (Eds) P.D. Vos, G. Garrity, D. Jones, N.R. Krieg, W. Ludwig, F.A. Rainey, K.-H. Schleifer, W.B. Whitman. Bergey's manual of systematic bacteriology 3(The Firmicutes, Springer)**:**21-127.
118. **Naclerio, G., L. Baccigalupi, R. Zilhao, M. De Felice, and E. Ricca.** 1996. Erratum. *Bacillus subtilis* spore coat assembly requires *cotH* gene expression. J Bacteriol **178:**6407.
119. **Nakamura, L. K.** 1998. *Bacillus pseudomycoides* sp. nov. Int J syst Bacteriol **48 Pt 3:**1031-5.
120. **Nakamura, L. K., and M. A. Jackson.** 1995. Clarification of the Taxonomy of *Bacillus Mycoides*. International Journal of Systematic Bacteriology **45:**46-49.
121. **Nakamura, L. K., O. Shida, H. Takagi, and K. Komagata.** 2002. *Bacillus pycnus* sp. nov. and *Bacillus neidei* sp. nov., round-spored bacteria from soil. Int J Syst Evol Microbiol **52:**501-5.

122. **Nicholson, W. L., N. Munakata, G. Horneck, H. J. Melosh, and P. Setlow.** 2000. Resistance of Bacillus endospores to extreme terrestrial and extraterrestrial environments. Microbiol Mol Biol Rev **64:**548-72.
123. **Nicholson, W. L., B. Setlow, and P. Setlow.** 1990. Binding of DNA in vitro by a small, acid-soluble spore protein from *Bacillus subtilis* and the effect of this binding on DNA topology. J Bacteriol **172:**6900-6.
124. **Oggioni, M. R., G. Pozzi, P. E. Valensin, P. Galieni, and C. Bigazzi.** 1998. Recurrent septicemia in an immunocompromised patient due to probiotic strains of *Bacillus subtilis*. J Clin Microbiol **36:**325-6.
125. **Ohye, D. F., and W. G. Murrell.** 1973. Exosporium and spore coat formation in *Bacillus cereus* T. J Bacteriol **115:**1179-90.
126. **Orlova, M. V., T. A. Smirnova, L. A. Ganushkina, V. Y. Yacubovich, and R. R. Azizbekyan.** 1998. Insecticidal activity of *Bacillus laterosporus*. Appl Environ Microbiol **64:**2723-5.
127. **Ozin, A. J., A. O. Henriques, H. Yi, and C. P. Moran, Jr.** 2000. Morphogenetic proteins SpoVID and SafA form a complex during assembly of the *Bacillus subtilis* spore coat. J Bacteriol **182:**1828-33.
128. **Ozin, A. J., C. S. Samford, A. O. Henriques, and C. P. Moran, Jr.** 2001. SpoVID guides SafA to the spore coat in *Bacillus subtilis*. J Bacteriol **183:**3041-9.
129. **Pandey, N. K., and A. I. Aronson.** 1979. Properties of the *Bacillus subtilis* spore coat. J Bacteriol **137:**1208-18.
130. **Piggot, P. J., and D. W. Hilbert.** 2004. Sporulation of *Bacillus subtilis*. Curr Opin Microbiol **7:**579-86.
131. **Plomp, M., T. J. Leighton, K. E. Wheeler, H. D. Hill, and A. J. Malkin.** 2007. In vitro high-resolution structural dynamics of single germinating bacterial spores. Proc Natl Acad Sci U S A **104:**9644-9.
132. **Plomp, M., T. J. Leighton, K. E. Wheeler, and A. J. Malkin.** 2005. Architecture and high-resolution structure of *Bacillus thuringiensis* and *Bacillus cereus* spore coat surfaces. Langmuir **21:**7892-8.
133. **Plomp, M., T. J. Leighton, K. E. Wheeler, and A. J. Malkin.** 2005. The high-resolution architecture and structural dynamics of *Bacillus* spores. Biophys J **88:**603-8.
134. **Pogliano, J., N. Osborne, M. D. Sharp, A. Abanes-De Mello, A. Perez, Y. L. Sun, and K. Pogliano.** 1999. A vital stain for studying membrane dynamics in bacteria: a novel mechanism controlling septation during *Bacillus subtilis* sporulation. Mol Microbiol **31:**1149-59.
135. **Pogliano, J., M. D. Sharp, and K. Pogliano.** 2002. Partitioning of chromosomal DNA during establishment of cellular asymmetry in *Bacillus subtilis*. J Bacteriol **184:**1743-9.
136. **Popham, D. L.** 2002. Specialized peptidoglycan of the bacterial endospore: the inner wall of the lockbox. Cell Mol Life Sci **59:**426-33.
137. **Price, K. D., and R. Losick.** 1999. A four-dimensional view of assembly of a morphogenetic protein during sporulation in *Bacillus subtilis.* J Bacteriol **181:**781-90.
138. **Ramamurthi, K. S., K. R. Clapham, and R. Losick.** 2006. Peptide anchoring spore coat assembly to the outer forespore membrane in *Bacillus subtilis*. Mol Microbiol **62:**1547-57.
139. **Rasko, D. A., M. R. Altherr, C. S. Han, and J. Ravel.** 2005. Genomics of the *Bacillus cereus* group of organisms. FEMS Microbiol Rev **29:**303-29.

140. **Rasko, D. A., J. Ravel, O. A. Okstad, E. Helgason, R. Z. Cer, L. Jiang, K. A. Shores, D. E. Fouts, N. J. Tourasse, S. V. Angiuoli, J. Kolonay, W. C. Nelson, A. B. Kolsto, C. M. Fraser, and T. D. Read.** 2004. The genome sequence of *Bacillus cereus* ATCC 10987 reveals metabolic adaptations and a large plasmid related to *Bacillus anthracis* pXO1. Nucleic Acids Res **32:**977-88.
141. **Ravel, J., L. Jiang, S. T. Stanley, M. R. Wilson, R. S. Decker, T. D. Read, P. Worsham, P. S. Keim, S. L. Salzberg, C. M. Fraser-Liggett, and D. A. Rasko.** 2009. The complete genome sequence of *Bacillus anthracis* Ames "Ancestor". J Bacteriol **191:**445-6.
142. **Read, T. D., S. N. Peterson, N. Tourasse, L. W. Baillie, I. T. Paulsen, K. E. Nelson, H. Tettelin, D. E. Fouts, J. A. Eisen, S. R. Gill, E. K. Holtzapple, O. A. Okstad, E. Helgason, J. Rilstone, M. Wu, J. F. Kolonay, M. J. Beanan, R. J. Dodson, L. M. Brinkac, M. Gwinn, R. T. DeBoy, R. Madpu, S. C. Daugherty, A. S. Durkin, D. H. Haft, W. C. Nelson, J. D. Peterson, M. Pop, H. M. Khouri, D. Radune, J. L. Benton, Y. Mahamoud, L. Jiang, I. R. Hance, J. F. Weidman, K. J. Berry, R. D. Plaut, A. M. Wolf, K. L. Watkins, W. C. Nierman, A. Hazen, R. Cline, C. Redmond, J. E. Thwaite, O. White, S. L. Salzberg, B. Thomason, A. M. Friedlander, T. M. Koehler, P. C. Hanna, A. B. Kolsto, and C. M. Fraser.** 2003. The genome sequence of *Bacillus anthracis* Ames and comparison to closely related bacteria. Nature **423:**81-6.
143. **Redmond, C., L. W. Baillie, S. Hibbs, A. J. Moir, and A. Moir.** 2004. Identification of proteins in the exosporium of *Bacillus anthracis*. Microbiology **150:**355-63.
144. **Rety, S., S. Salamitou, I. Garcia-Verdugo, D. J. Hulmes, F. Le Hegarat, R. Chaby, and A. Lewit-Bentley.** 2005. The crystal structure of the *Bacillus anthracis* spore surface protein BclA shows remarkable similarity to mammalian proteins. J Biol Chem **280:**43073-8.
145. **Riesenman, P. J., and W. L. Nicholson.** 2000. Role of the spore coat layers in *Bacillus subtilis* spore resistance to hydrogen peroxide, artificial UV-C, UV-B, and solar UV radiation. Appl Environ Microbiol **66:**620-6.
146. **Roels, S., A. Driks, and R. Losick.** 1992. Characterization of *spoIVA*, a sporulation gene involved in coat morphogenesis in *Bacillus subtilis*. J Bacteriol **174:**575-85.
147. **Roels, S., and R. Losick.** 1995. Adjacent and divergently oriented operons under the control of the sporulation regulatory protein GerE in *Bacillus subtilis*. J Bacteriol **177:**6263-75.
148. **Rothfield, L. I., and S. S. Justice.** 1997. Bacterial cell division: the cycle of the ring. Cell **88:**581-4.
149. **Sacco, M., E. Ricca, R. Losick, and S. Cutting.** 1995. An additional GerE-controlled gene encoding an abundant spore coat protein from *Bacillus subtilis*. J Bacteriol **177:**372-7.
150. **Sandman, K., L. Kroos, S. Cutting, P. Youngman, and R. Losick.** 1988. Identification of the promoter for a spore coat protein gene in *Bacillus subtilis* and studies on the regulation of its induction at a late stage of sporulation. J Mol Biol **200:**461-73.
151. **Schoeni, J. L., and A. C. Wong.** 2005. *Bacillus cereus* food poisoning and its toxins. J Food Prot **68:**636-48.

152. **SEKI, T., C.-K. CHUNG, H. MIKAMI, and Y. OSHIMA.** 1978. Deoxyribonucleic Acid Homology and Taxonomy of the Genus *Bacillus*. Int J syst Bacteriol **28:**182-189.
153. **Setlow, B., D. Sun, and P. Setlow.** 1992. Interaction between DNA and alpha/beta-type small, acid-soluble spore proteins: a new class of DNA-binding protein. J Bacteriol **174:**2312-22.
154. **Setlow, J. K., M. Randesi, J. G. Adams, B. Setlow, and P. Setlow.** 1992. Mutation and killing of Escherichia coli expressing a cloned *Bacillus subtilis* gene whose product alters DNA conformation. J Bacteriol **174:**2943-50.
155. **Setlow, P.** 1992. I will survive: protecting and repairing spore DNA. J Bacteriol **174:**2737-41.
156. **Setlow, P.** 2003. Spore germination. Curr Opin Microbiol **6:**550-6.
157. **Setlow, P.** 2006. Spores of *Bacillus subtilis*: their resistance to and killing by radiation, heat and chemicals. J Appl Microbiol **101:**514-25.
158. **Shaw, P. J., and G. J. Hills.** 1981. Tilted Specimen in the Electron-Microscope - a Simple Specimen Holder and the Calculation of Tilt Angles for Crystalline Specimens. Micron **12:**279-282.
159. **Smirnova, T. A., I. B. Minenkova, M. V. Orlova, M. M. Lecadet, and R. R. Azizbekyan.** 1996. The crystal-forming strains of *Bacillus laterosporus*. Res Microbiol **147:**343-50.
160. **Smith, J. M.** 1999. Ximdisp--A visualization tool to aid structure determination from electron microscope images. J Struct Biol **125:**223-8.
161. **Smith, N. R., R. E. Gordon, and F. E. Clark.** 1952. Aerobic sporeforming bacteria. United states, Department of argriculture, Washington D. C **16**.
162. **Soberon, M., J. A. Lopez-Diaz, and A. Bravo.** 2013. Cyt toxins produced by *Bacillus thuringiensis*: A protein fold conserved in several pathogenic microorganisms. Peptides **41:**87-93.
163. **Somerville, H. J., and M. L. Jones.** 1972. DNA competition studies within the *Bacillus cereus* group of *bacilli*. J Gen Microbiol **73:**257-65.
164. **Steichen, C., P. Chen, J. F. Kearney, and C. L. Turnbough, Jr.** 2003. Identification of the immunodominant protein and other proteins of the *Bacillus anthracis* exosporium. J Bacteriol **185:**1903-10.
165. **Steichen, C. T., J. F. Kearney, and C. L. Turnbough, Jr.** 2005. Characterization of the exosporium basal layer protein BxpB of *Bacillus anthracis*. J Bacteriol **187:**5868-76.
166. **Steichen, C. T., J. F. Kearney, and C. L. Turnbough, Jr.** 2007. Non-uniform assembly of the *Bacillus anthracis* exosporium and a bottle cap model for spore germination and outgrowth. Mol Microbiol **64:**359-67.
167. **Stenfors Arnesen, L. P., A. Fagerlund, and P. E. Granum.** 2008. From soil to gut: *Bacillus cereus* and its food poisoning toxins. FEMS Microbiol Rev **32:**579-606.
168. **Stevens, C. M., R. Daniel, N. Illing, and J. Errington.** 1992. Characterization of a sporulation gene, spoIVA, involved in spore coat morphogenesis in *Bacillus subtilis*. J Bacteriol **174:**586-94.
169. **Stragier, P., and R. Losick.** 1996. Molecular genetics of sporulation in *Bacillus subtilis*. Annu Rev Genet **30:**297-41.
170. **Sun, D. X., P. Stragier, and P. Setlow.** 1989. Identification of a new sigma-factor involved in compartmentalized gene expression during sporulation of *Bacillus subtilis*. Genes Dev **3:**141-9.

171. **Sylvestre, P., E. Couture-Tosi, and M. Mock.** 2002. A collagen-like surface glycoprotein is a structural component of the *Bacillus anthracis* exosporium. Mol Microbiol **45:**169-78.
172. **Sylvestre, P., E. Couture-Tosi, and M. Mock.** 2005. Contribution of ExsFA and ExsFB proteins to the localization of BclA on the spore surface and to the stability of the *bacillus anthracis* exosporium. J Bacteriol **187:**5122-8.
173. **Sylvestre, P., E. Couture-Tosi, and M. Mock.** 2003. Polymorphism in the collagen-like region of the *Bacillus anthracis* BclA protein leads to variation in exosporium filament length. J Bacteriol **185:**1555-63.
174. **Takamatsu, H., T. Kodama, T. Nakayama, and K. Watabe.** 1999. Characterization of the yrbA gene of *Bacillus subtilis*, involved in resistance and germination of spores. J Bacteriol **181:**4986-94.
175. **Tan, L., M. Li, and C. L. Turnbough, Jr.** 2011. An unusual mechanism of isopeptide bond formation attaches the collagenlike glycoprotein BclA to the exosporium of *Bacillus anthracis*. MBio **2:**e00084-11.
176. **Teleman, A. A., P. L. Graumann, D. C. Lin, A. D. Grossman, and R. Losick.** 1998. Chromosome arrangement within a bacterium. Curr Biol **8:**1102-9.
177. **Thompson, B. M., B. C. Hoelscher, A. Driks, and G. C. Stewart.** 2012. Assembly of the BclB glycoprotein into the exosporium and evidence for its role in the formation of the exosporium 'cap' structure in *Bacillus anthracis*. Mol Microbiol **86:**1073-84.
178. **Thompson, B. M., B. C. Hoelscher, A. Driks, and G. C. Stewart.** 2011. Localization and assembly of the novel exosporium protein BetA of *Bacillus anthracis*. J Bacteriol **193:**5098-104.
179. **Todd, S. J., A. J. Moir, M. J. Johnson, and A. Moir.** 2003. Genes of *Bacillus cereus* and *Bacillus anthracis* encoding proteins of the exosporium. J Bacteriol **185:**3373-8.
180. **Tokieda, K., Y. Morikawa, K. Maeyama, K. Mori, and K. Ikeda.** 1999. Clinical manifestations of *Bacillus cereus* meningitis in newborn infants. J Paediatr Child Health **35:**582-4.
181. **Unger, V. M.** 2000. Assessment of electron crystallographic data obtained from two-dimensional crystals of biological specimens. Acta Crystallogr D Biol Crystallogr **56:**1259-69.
182. **Vaishampayan, P., M. Miyashita, A. Ohnishi, M. Satomi, A. Rooney, M. T. La Duc, and K. Venkateswaran.** 2009. Description of *Rummeliibacillus stabekisii* gen. nov., sp. nov. and reclassification of *Bacillus pycnus* Nakamura et al. 2002 as Rummeliibacillus pycnus comb. nov. Int J Syst Evol Microbiol **59:**1094-9.
183. **Valpuesta, J. M., J. L. Carrascosa, and R. Henderson.** 1994. Analysis of electron microscope images and electron diffraction patterns of thin crystals of phi 29 connectors in ice. J Mol Biol **240:**281-7.
184. **van Heel, M., B. Gowen, R. Matadeen, E. V. Orlova, R. Finn, T. Pape, D. Cohen, H. Stark, R. Schmidt, M. Schatz, and A. Patwardhan.** 2000. Single-particle electron cryo-microscopy: towards atomic resolution. Q Rev Biophys **33:**307-69.
185. **van Heel, M., G. Harauz, E. V. Orlova, R. Schmidt, and M. Schatz.** 1996. A new generation of the IMAGIC image processing system. J Struct Biol **116:**17-24.
186. **Vanheel, M., and W. Keegstra.** 1981. Imagic - a Fast, Flexible and Friendly Image-Analysis Software System. Ultramicroscopy **7:**113-130.

187. **Vary, P. S., R. Biedendieck, T. Fuerch, F. Meinhardt, M. Rohde, W. D. Deckwer, and D. Jahn.** 2007. Bacillus megaterium--from simple soil bacterium to industrial protein production host. Appl Microbiol Biotechnol **76:**957-67.
188. **Veening, J. W., H. Murray, and J. Errington.** 2009. A mechanism for cell cycle regulation of sporulation initiation in *Bacillus subtilis*. Genes Dev **23:**1959-70.
189. **Waller, L. N., N. Fox, K. F. Fox, A. Fox, and R. L. Price.** 2004. Ruthenium red staining for ultrastructural visualization of a glycoprotein layer surrounding the spore of *Bacillus anthracis* and *Bacillus subtilis*. J Microbiol Methods **58:**23-30.
190. **Wang, K. H., A. L. Isidro, L. Domingues, H. A. Eskandarian, P. T. McKenney, K. Drew, P. Grabowski, M. H. Chua, S. N. Barry, M. Guan, R. Bonneau, A. O. Henriques, and P. Eichenberger.** 2009. The coat morphogenetic protein SpoVID is necessary for spore encasement in *Bacillus subtilis*. Mol Microbiol **74:**634-49.
191. **Warren, S. C.** 1968. Sporulation in *Bacillus subtilis*. Biochemical changes. Biochem J **109:**811-8.
192. **Webb, C. D., A. Decatur, A. Teleman, and R. Losick.** 1995. Use of green fluorescent protein for visualization of cell-specific gene expression and subcellular protein localization during sporulation in *Bacillus subtilis*. J Bacteriol **177:**5906-11.
193. **Welkos, S. L.** 1991. Plasmid-associated virulence factors of non-toxigenic (pX01-) *Bacillus anthracis.* Microb Pathog **10:**183-98.
194. **Wiencek, K. M., N. A. Klapes, and P. M. Foegeding.** 1990. Hydrophobicity of *Bacillus* and *Clostridium* spores. Appl Environ Microbiol **56:**2600-5.
195. **Wu, L. J., and J. Errington.** 1994. *Bacillus subtilis* SpoIIIE protein required for DNA segregation during asymmetric cell division. Science **264:**572-5.
196. **Wu, L. J., and J. Errington.** 1998. Use of asymmetric cell division and *spoIIIE* mutants to probe chromosome orientation and organization in *Bacillus subtilis*. Mol Microbiol **27:**777-86.
197. **Yudina, T. G., A. V. Konukhova, L. P. Revina, L. I. Kostina, I. A. Zalunin, and G. G. Chestukhina.** 2003. Antibacterial activity of Cry- and Cyt-proteins from *Bacillus thuringiensis* ssp. israelensis. Can J Microbiol **49:**37-44.
198. **Zhang, J., P. C. Fitz-James, and A. I. Aronson.** 1993. Cloning and characterization of a cluster of genes encoding polypeptides present in the insoluble fraction of the spore coat of *Bacillus subtilis*. J Bacteriol **175:**3757-66.
199. **Zheng, L., R. Halberg, S. Roels, H. Ichikawa, L. Kroos, and R. Losick.** 1992. Sporulation regulatory protein GerE from *Bacillus subtilis* binds to and can activate or repress transcription from promoters for mother-cell-specific genes. J Mol Biol **226:**1037-50.
200. **Zheng, L. B., W. P. Donovan, P. C. Fitz-James, and R. Losick.** 1988. Gene encoding a morphogenic protein required in the assembly of the outer coat of the *Bacillus subtilis* endospore. Genes Dev **2:**1047-54.
201. **Zheng, L. B., and R. Losick.** 1990. Cascade regulation of spore coat gene expression in *Bacillus subtilis*. J Mol Biol **212:**645-60.
202. **Zilhao, R., G. Naclerio, A. O. Henriques, L. Baccigalupi, C. P. Moran, Jr., and E. Ricca.** 1999. Assembly requirements and role of CotH during spore coat formation in *Bacillus subtilis*. J Bacteriol **181:**2631-3.

203. **Zilhao, R., M. Serrano, R. Isticato, E. Ricca, C. P. Moran, Jr., and A. O. Henriques.** 2004. Interactions among CotB, CotG, and CotH during assembly of the *Bacillus subtilis* spore coat. J Bacteriol **186:**1110-9.
204. **Zolock, R. A., G. Li, C. Bleckmann, L. Burggraf, and D. C. Fuller.** 2006. Atomic force microscopy of *Bacillus* spore surface morphology. Micron **37:**363-9.

Publications

Qiang Wan*, Daniela Krajcikova*, Svetomir Tzokov, Imrich Barak, Per A. Bullough (2013). Supramolecular assemblies of *Bacillus subtilis* spore coat proteins (in preparation)

Presentation of research

The International *Bacillus anthracis*, *B. cereus*, and *B. thuringiensis* Conference. Bruges, Belgium. Awarded Best student poster.
Poster Presentation: **Qiang Wan,** A., Bullough, P. (2011). "Characterisation of Self-assembly Properties of *Bacillus* Spore Coat Proteins"

5th European Spore Conference. Royal Holloway, University of London, UK
Poster Presentation: **Qiang Wan**, A., Bullough, P. (2012). "Characterisation of Self-assembly Properties of *Bacillus* Spore Coat Proteins"